OPTICAL APERTURE SYNTHESIS

A COMPARISON OF TECHNIQUES FOR WIDE-FIELD INTERFEROMETRIC IMAGING

Proefschrift

ter verkrijging van de graad van doctor
aan de Technische Universiteit Delft,
op gezag van de Rector Magnificus prof.dr.ir. J.T. Fokkema,
voorzitter van het College voor Promoties,
in het openbaar te verdedigen op

dinsdag 9 mei 2006 om 12u30

door

Casper van der Avoort

werktuigbouwkundig ingenieur
geboren te Tilburg.

Dit proefschrift is goedgekeurd door de promotor:
prof.dr.ir. J.J.M. Braat

Toegevoegd promotor: dr. S.F. Pereira

Samenstelling promotiecommissie:

Voorzitter	
Rector Magnificus,	Technische Universiteit Delft
Promotoren	
prof.dr.ir. J.J.M. Braat,	Technische Universiteit Delft
dr. S.F. Pereira,	Technische Universiteit Delft
Leden	
prof.dr. M.W.M. de Graauw,	Rijksuniversiteit Groningen
prof.dr. J. Surdej,	Université de Liège
prof.dr.ir. L.J. van Vliet,	Technische Universiteit Delft
dr. L.A. d'Arcio,	ESA/ESTEC
dr. J.W.A. den Herder,	SRON

This work was supported by the Technische Universiteit Delft and mainly funded by the *stichting Nederlands Wetenschappelijk Onderzoek* (NWO), of which the *Stichting Ruimtevaart Onderzoek Nederland* (SRON) is a part.

Cover: *Interference*, January 2005

ISBN 90-78314-03-6

Summary

Optical long baseline stellar interferometry is an observational technique in astronomy that already exists for over a century, but is truly blooming during the last decades. The undoubted value of stellar interferometry as a technique to measure stellar parameters beyond the classical resolution limit is more and more spreading to the regime of synthesis imaging. With optical aperture synthesis imaging, the measurement of parameters is extended to the reconstruction of high resolution stellar images. A number of optical telescope arrays for synthesis imaging are operational on Earth, while space-based telescope arrays are being designed. For all imaging arrays, the combination of the light collected by the telescopes in the array can be performed in a number of ways. In this thesis, methods are introduced to model these methods of beam combination and compare their effectiveness in the generation of data to be used to reconstruct the image of a stellar object.

One of these methods of beam combination is to be applied in a future space telescope. The European Space Agency is developing a mission that can valuably be extended with an imaging beam combiner. This mission is labeled Darwin, as its main goal is to provide information on the origin of life. The primary objective is the detection of planets around nearby stars—called exoplanets—and more precisely, Earth-like exoplanets. This detection is based on a signal, rather than an image. With an imaging mode, designed as described in this thesis, Darwin can make images of, for example, the planetary system to which the detected exoplanet belongs or, as another example, of the dust disk around a star out of which planets form. Such images will greatly contribute to the understanding of the formation of our own planetary system and of how and when life became possible on Earth.

The comparison of beam combination methods for interferometric imaging occupies most of the pages of this thesis. Additional chapters will treat related subjects, being experimental work on beam combination optics, a description of a novel formalism for aberration retrieval and experimental work on nulling interferometry. The Chapters on interferometric imaging are organized in such a way that not only the physical principles behind a stellar interferometer are clear, but these chapters also form a basis for the method of analysis applied to the interferometers—or rather beam combination methods—under consideration. The imaging process in a stellar interferometer will be treated as the inversion of a linear system of equations.

The definition of interferometric imaging in this thesis can be stated to be the reconstruction of a luminosity distribution function on the sky, that is, in angular measure, larger than the angular diffraction limited spot size—or Point-Spread Function (PSF)—of a single telescope in the array and that contains, again in angular measure, spatial structure that is much smaller than the PSF of a single telescope. This reconstruction has to

be based on knowledge of the dimensions of the telescope array and the detector. The detector collects intensity data that is formed by observation of the polychromatic luminosity distribution on the sky and is deteriorated by the quantum-nature of light and an imperfect electronic detection process. Therefore, the imaging study presented in this thesis can be regarded to be a study on the signal characteristics of various interferometers while imaging a polychromatic wide-field stellar source.

The collection of beam combination methods under consideration consists of four types. Among these are two well-known types, having either co-axially combined beams as in the Michelson–Morley experiment to demonstrate the existence of ether, or beams that follow optical paths as if an aperture mask were placed in front of a telescope, making the beams combine in the focus of that telescope, as suggested by Fizeau. For separated apertures rather than an aperture mask, these optical paths are stated to be homothetic. In short, these two types will be addressed as the Michelson or the Homothetic type. The other two types are addressed as Densified and Staircase. The first one is short for densified pupil imaging, an imaging technique very similar to the Homothetic type, be it that the natural course of light after the aperture mask is altered. However, the combination of the beams of light is again in focus. The Staircase method is an alternative to the co-axial Michelson method and lends its name from the fact that a staircase-shaped mirror is placed in an intermediate focal plane after each telescope in the array, before combining the beams of light co-axially. This addition allows stellar imaging as with the Michelson type, with the advantage of covering a large field-of-view. The details of these methods will intensively be discussed in this thesis, but the introduction of them at this point allows a short list of results, found by comparing them for equal imaging tasks.

►► **Homothetic** imagers are best suited for covering a wide field-of-view, considering the information content of the interferometric signals these arrays produce. The large number of detectors does not seem to limit the imaging performance in the presence of noise, due to the high ratio of coherent versus incoherent information in the detector signal. The imaging efficiency of a **Michelson** type array is also high, although—considering only polychromatic wide-field imaging tasks—the ratio of coherent versus incoherent information in the detected signals is very low. This results in very large observation times needed to produce images comparable to those obtained with a Homothetic array. A detailed presentation of the characteristics of the detected signals in a co-axial Michelson array reveal that such signals, obtained by polychromatic observation of extended sources, have fringe envelope functions that do not allow Fourier-spectroscopy to obtain high-resolution spectroscopic information about such a source.

►► For the **Densified** case, it is found that this method can indeed provide an interferometric PSF that is more favorable than a homothetic PSF, but only for narrow-angle observations. For polychromatic wide-field observations, the Densified-PSF is field-dependent, for which the image reconstruction process can account. Wide-field imaging using the favorable properties of the Densified-PSF can be performed, by using special settings of the delay or optical path length difference between interferometer arms and including observations with several settings of delay in the observation data. The **Staircase** method is the second best method for the imaging task under consideration. The discontinuous nature of the staircase-shaped mirrors does not give rise to a discontinuous reconstructed luminosity distribution or non-uniformly covered spatial frequencies. The intrinsic efficiency of the interferometric signal in this type of interferometer is worse than that of the other co-axial method, although the ratio of coherent versus incoherent signal in the data—the length of the fringe packet in one intensity trace—is

nearly ultimate. The inefficiency is overwhelmingly compensated for by the very short observation time needed.

Besides numerical studies of interferometer arrays, one interferometric imager was also studied experimentally. A homothetic imager was built, comprising three telescopes with fully separated beam relay optics. The pointing direction, the location and the optical path length of two of the three beams are electronically controllable. The beams can be focused together to interfere, via a beam combiner consisting of curved surfaces. This set-up allows to measure the required accuracies at which certain optical elements have to be positioned. Moreover, this set-up demonstrates that without knowledge of the initial pointing directions, locations and optical path lengths of the beams, the situation of homothesis can be attained, solely based on information from the focal plane of the set-up. Further experiments show that the approximation of exact homothesis is limited by the optical quality of the beam combiner optics.

Parallel to the experiments on homothesis, a study was performed to evaluate the use of the Extended Nijboer–Zernike (ENZ) formalism for analysis of multiple aperture optical systems. It is envisaged that an aberration retrieval algorithm, provided with the common focus of a homothetic array, can be used to detect misalignment of or even aberrations in the sub-apertures of the sparse synthetic aperture. The ENZ formalism is a powerful tool to describe the focal intensity profile in an optical imaging system, imaging a monochromatic point source through a pupil that is allowed to have a certain transmission profile and phase aberration function over the pupil. Moreover, the formalism allows calculation of intensity profiles outside the best-focus plane. With the intensity information of several through-focus planes, enough information is available to reconstruct the pupil function from it. The formalism is described, including the reconstruction algorithm. Although very good results are obtained for general pupil functions, the results for synthetic pupil functions are not very promising. The detailed description of the ENZ-aberration retrieval reveals the origin of the breakdown of the retrieval process.

Finally, a description of experiments on nulling interferometry is given, starting with the presentation of an experimental set-up for three-beam nulling. A novel strategy for polychromatic nulling is treated here, with the goal of relieving the tight phase constraint on the spectra in the individual beams. This theoretically allows broad band-nulling with a high rejection ratio without using achromatic phase shifters. The disappointing results led to an investigation of the spectra of the individual beams. The origin of the unsatisfactory level of the rejection ratio is found in the spectral unbalance of the beams. Before branching off, the beams have an equal spectrum. Then, the encounter of different optical elements with individually applied coatings, the control of beam-power per beam and finally the beam coupling into a single-mode fiber, apparently alter the spectra in such a way that the theoretically achievable level of the rejection ratio cannot be reached.

The research described in this thesis provides onsets for research in several areas of interest related to aperture synthesis and guidelines concerning the design of synthetic telescopes for imaging. As such, this research contributes to the improvement of instrumentation for observational astronomy, in particular for stellar interferometry. While nulling interferometry is the detection technique that allows a space telescope array such as ESA's Darwin to identify exoplanets, optical aperture synthesis imaging is the technique that can make images of the planetary systems to which these exoplanets belong. Moreover, many objects can be observed that represent earlier versions of our planetary system, our Sun and even our galaxy, the Milky Way. Observing these objects might an-

swer questions about the origins of the Earth itself and the life on it.

Casper van der Avoort, spring 2006

Samenvatting

Optische apertuur synthese is geen nieuw onderwerp binnen de sterrenkunde. Al meer dan een eeuw geleden werd de techniek toegepast om de diameter van sterren te meten. Zelfs professionele telescopen konden de sterren niet beter afbeelden dan een vlekje waarvan de grootte niet gerelateerd was aan de werkelijke grootte van een ster. Een stel samenwerkende telescopen bleek wél een nauwkeurige meting aan deze ster te kunnen verrichten. De waarneem-nauwkeurigheid hing niet langer af van de afmetingen van een enkele telescoop, maar van de afstand tussen de onderlinge telescopen. Dit is het hart van het waarnemingsprincipe waarover dit proefschrift gaat. Wanneer een telescoop simpelweg gezien wordt als een opening waardoor het licht naar binnen komt, een zogenaamde *apertuur*, is het begrijpelijk dat meerdere samenwerkende telescopen gezien kunnen worden als een samengestelde of *synthetische* apertuur. De beschreven metingen aan diameters van sterren werden gedaan met zichtbaar licht; de astronoom deed zijn waarnemingen 'op het oog'. De toevoeging 'optisch' aan de titel van dit proefschrift vind zijn oorsprong dan ook niet in de beschreven vroege astrometrie, maar juist in de astronomie van de laatste jaren, aangezien apertuur synthese als waarnemingstechniek pas echt een vlucht nam in de tweede helft van de vorige eeuw, waarbij juist straling van radio-golflengten werd gemeten. Met reeksen van radiotelescopen werden zeer gedetailleerde afbeeldingen geproduceerd. De mogelijkheid zulke afbeeldingen te maken met zichtbaar of bijna zichtbaar licht verklaart de aanduiding optische apertuur synthese.

Apertuur synthese als afbeeldingstechniek kenmerkt zich ten eerste in het feit, dat geen plaatjes worden opgenomen, maar metingen, waaruit een afbeelding gereconstrueerd dient te worden. Ten tweede staat de techniek weliswaar bekend als een techniek waarmee afbeeldingen van een zeer hoge resolutie geconstrueerd kunnen worden, maar tegelijkertijd ook als een techniek die slechts een zeer klein deel van het blikveld van een telescoop zo nauwkeurig kan afbeelden. Het grootste deel van het onderzoek dat beschreven wordt in dit proefschrift heeft tot doel de mogelijkheden in kaart te brengen, waarmee dit hoge-resolutie blikveld vergroot kan worden. Deze mogelijkheden zijn varianten van de architectuur van de optiek die de lichtbundels van de telescopen samen moet brengen. Voor deze zogenaamde 'beam combiners' worden vier varianten aangedragen, waaronder twee klassieke methoden, lijkend op de instrumenten van een eeuw terug danwel op de radio-telescoop varianten, en twee afgeleide methoden. De namen van de methoden, die in de tekst uitgebreid behandeld worden, zijn: Michelson (vernoemd naar de Nobelprijs winnaar Albert A. Michelson), Homothesis (naar de griekse benaming voor een exact gelijke plaatsing), Densified (omdat er een *vernauwde* synthetische apertuur gecreëerd wordt) en tenslotte Staircase, een in Delft ontwikkelde methode die vernoemd is naar het optische element dat een cruciale rol speelt: een trapvormige spiegel.

Alle technieken zullen in staat blijken een groot blikveld te kunnen reconstrueren met hoge resolutie. Wanneer echter zeer lichtzwakke hemellichamen worden bestudeerd, zijn de benodigde observatietijd en het aantal benodigde pixels in de camera achter de samengestelde telescoop factoren van belang. De vier methoden worden vergeleken op de gemaakte fout bij het reconstrueren van een uitgebreide bron aan de hemel, als functie van de hoeveelheid licht die ze daarvan opvangen. Hieruit blijkt dat de methoden Homothesis en Staircase veruit het best presteren. Deze methodes zijn echter in technische realisatie vele male complexer dan de andere twee methoden.

Twee andere onderwerpen van onderzoek, beschreven in dit proefschrift, zijn 'nulling interferometry' en het meten van afbeeldingsfouten in een afbeeldend optisch systeem. Dit laatste onderwerp werd aanvankelijk gezien als een manier om fouten in de samenvoeging van lichtbundels van uit elkaar geplaatste telescopen te meten. Helaas bleek dit doel onhaalbaar met de gekozen techniek. Deze techniek biedt echter wel zeer uitgebreide mogelijkheden om delen van een synthetische telescoop—hetzij in de afzonderlijke telescopen, hetzij in de samenvoegende optiek—te analyseren op uitlijnfouten.

Nulling interferometry is een techniek waarbij ook het licht van meerdere telescopen gecombineerd wordt, maar waar niet het verkrijgen van een afbeelding het doel is, maar juist het uitdoven (nulling) van sterrenlicht. Dit is zinvol, aangezien een kleine planeet niet meetbaar is rondom een stralende ster, maar wel rondom een gedoofde ster. Op deze manier kunnen metingen verricht worden aan planeten rondom nabijgelegen sterren—de zogenaamde exo-planeten—aangaande de chemische samenstelling van hun atmosfeer en zelfs de leefbaarheid. Een cruciale rol is weggelegd voor de architectuur van de optiek die voor de uitdoving zorgdraagt. In dit proefschrift wordt een mogelijkheid voor deze architectuur beschreven en worden tevens enkele tegenvallende resultaten gepresenteerd. Het vinden van de oorzaak van deze tegenvallende resultaten is de belangrijkste bijdrage van dit deel van het onderzoek. Het blijkt, dat kleine verschillen in de benodigde halfdoorlatende spiegels en de inkoppeling van de afzonderlijke lichtbundels een goede werking van deze techniek verhinderen. Hoewel dit geldt voor alle experimenten in nulling interferometry, blijkt de gekozen uitdovings-strategie meer gevoelig dan andere voor deze afwijkingen.

Hoewel de onderwerpen in dit proefschrift ver uit elkaar lijken te liggen, behoren ze allemaal tot het arsenaal van de astronomen van deze eeuw. De beschreven waarnemingstechnieken hebben reeds gezorgd voor belangwekkende ontdekkingen in de astronomie en de astrofysica, waaronder de ontdekkingen van exo-planeten de meest bekende zijn. Afbeeldingsfout-vrije synthetische aperturen, gebaseerd in de ruimte, uitgerust voor zowel ster-uitdovende als beeldvormende taken, worden reeds voorbereid en zullen in de komende jaren waarnemingen van ongeëvenaarde resolutie naar de Aarde gaan sturen.

Casper van der Avoort, voorjaar 2006

Wat is wetenschap? Wetenschap is de titanische poging van het menselijk intellect zich uit zijn kosmische isolement te verlossen door te begrijpen.

W.F. Hermans

Contents

Chapter 1

Introduction

1.1 Background

As far back as any possible source of human information goes, celestial events occurring on the nightly skies have been recorded. This means they have been observed, marveled at and found interesting, inexplicable or even terrifying enough to report about. These reports have been stories, drawings or tedious and detailed writings. In an attempt to understand them, uncommon events where devoted to the willing of Gods, but also the common presence of those innumerable peaceful shiny dots tempted early scientists to give answers to the Why of their presence and to the What of their nature.

Astronomy is not only an old, but also a very pure science. The experiments are set-up and running far away in the universe, and they can not be disturbed by measuring them. An astronomer merely needs to find the ongoing experiment matching his interest, rather than to set one up. To ensure a proper understanding of the events, a trustworthy observation of it is a necessity. The astronomer needs instruments that convert the emitted information from the event to interpretable information on earth. Visible light, but also infra-red and ultra-violet light, are forms of radiation that can carry great amounts of information from a celestial body to the Earth. One way to transfer the received radiation into intelligible information, is to use *optics*.

The general term for the optics in use when dealing with radiation sources very far away, is a telescope. In general, a telescope is an instrument that provides information—currents, numbers or even images—that we can interpret. The information answers questions, and human nature drives us to formulate new questions out of these answers. The telescopes need to provide more information, in shorter time. Or, weaker sources need to be analyzed. And when it comes to images, more detail is needed.

The need for images with great information content has driven this research. An invented technique to obtain a high resolution needed to be combined with a large image extent. The proposed solutions are combinations of piecewise solutions that were already known, combined with new ways of processing the recorded radiation into information. As is often the case, several solutions to the same problem exist. They are compared here and their specific advantages and drawbacks are listed.

1.2 Telescopes and interferometry

Observational astronomy is limited by a number of factors. Without good lenses or mirrors, only blurred images are obtained. For perfectly shaped optical surfaces, the blurring is minimal and decreases as the diameter of the telescope increases. However, the practical production issues to arrive at such near perfectly-shaped elements increase in complexity for increasing diameters. But even if the production would be perfect, still blurring occurs. The Earth's atmosphere is not placid nor homogeneous. The constant twinkling of stars is a demonstration of this effect. A larger collecting surface on a telescope means that a larger 'column' of turbulent atmosphere is affecting the light from a stellar source. In the past century, two separate technologies were invented and developed to facilitate observational astronomy at high resolution. Adaptive Optics aims at correcting the atmospheric disturbances after the light is collected with a larger telescope. Stellar Interferometry relies on the fact that small collectors are less affected by the atmosphere, and that the light they collect can be processed in such a way that the set of collectors act as being part of a large synthetic telescope. The oldest of the two techniques is Stellar Interferometry, but this technique was not initially intended for imaging. Large telescopes with the aid of Adaptive Optics do have this aim. The two subjects hence are complementary for studying stellar sources with a high level of detail.

1.2.1 Early stellar interferometry

A very good description of the history of stellar interferometry can be found in Selected Papers on Long Baseline Stellar Interferometry (Lawson, 1997). Stellar interferometry started just after 1867 when Fizeau proposed to the Académie des Sciences that interference could be used to measure stellar diameters (Fizeau, 1868). He realized that there was a relationship between the dimensions of the interference fringes and the size of the light source, in this case being a star and he wrote that *extremely fine fringes can only be brought into existence when the source of the light has but angular dimensions that are almost undetectable.* He hoped that this principle would allow to obtain new data on the angular diameters of stars. Five years later, Stéphan conducted the first experiments according to this proposal (Stéphan, 1874). At the Observatoire de Marseille, he masked the large Foucault telescope to define two apertures spaced 50 centimeters apart. Stéphan reported to observe interference fringes on all stars but Sirius. The measurements on Sirius were uncertain, but he expressed his hope that Sirius' diameter could eventually be measured. Later he reported again the results of observations with a 65 cm aperture separation. All the stars he observed produced fringes, including Sirius, making him retract his prior comments. He concluded that the stars must have angular diameters less than 0.158 arcsec—the angular diameter for which fringes would disappear using a 65 cm baseline—and possibly only a fraction of it[1].

Around 1890 the American Michelson also got interested in using interferometry for the observation of stars (Michelson, 1890). He succeeded in performing measurements with much larger aperture separations, no longer limited by the principal size of the telescope. In December 1920 he performed the first measurement of a stellar diameter, which resulted in headlines in the newspapers. The measured star was the red supergiant Betelgeuse. Later, it became evident that only the largest stars could be measured by this method using Michelson's instrument, a 20 ft interferometer (Fig. 1.1). The

[1] The angular diameter of Sirius is 0.007 arcsec, or about 30 nrad.

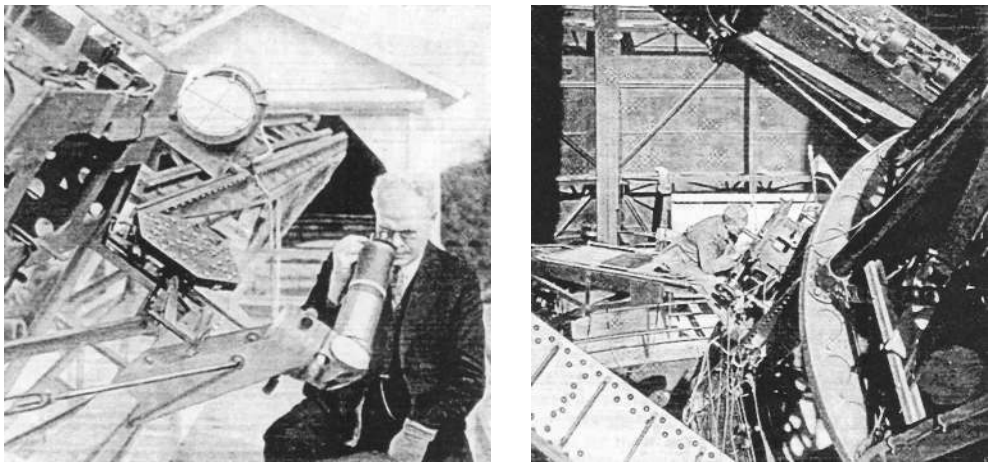

Figure 1.1: Reproduction of photographs accompanying Pease's article on Interferometer Methods in Astronomy (Michelson and Pease, 1921). Both images show an observer at the 20 ft interferometer, a periscope mounted on a 100 inch telescope.

larger 50 ft version operated by Pease (†1938) was only marginally successful and mainly demonstrated the very high degree of optical and mechanical stability needed for these measurements.

Radio astronomy was born in 1933 when it was discovered that the Milky Way emitted radiation at radio wavelengths. After World War II, radar technology was embedded and the field of radio interferometry was started. Optical interferometry revived again in the 50s and 60s, partially due to the success of its radio equivalent. The intensity interferometer developed by Hanbury Brown and Twiss brought renewed interest in high resolution optical interferometry. Modern long-baseline interferometry started in the early 1970s. Theoretical understanding of turbulence had progressed, sensitive photoelectric detectors had been developed and controllable servo systems could be employed. Pease's mechanical and optical problems now seemed surmountable. After performing interferometry with two apertures, fringes were eventually obtained from two separated telescopes by Labeyrie (Labeyrie, 1976) in 1974 at the Observatoire de Nice. Still, stellar interferometry consisted in measuring properties of stars or binary stars. Not until 1995, the first images were produced by COAST, the Cambridge Optical Aperture Synthesis Telescope, using 3 or more separated telescopes and reconstructing from closure phases (Baldwin *et al.*, 1996).

The resolving power and image quality of single dish telescopes also evolved during the past decades. Currently, several optical stellar interferometers exist (see Fig. 1.2), comprising multiple very large telescopes equipped with systems like adaptive optics to defeat the resolution limits posed by the atmosphere. Telescope arrays are even being designed for space operation, with typical high resolution missions such as to directly observe planets around nearby stars.

1.2.2 Adaptive optics and large telescopes

A field of research related to long-baseline interferometry, but originating from a very different point of interest is the study of Multiple Aperture Optical Telescopes. These are

Figure 1.2: Telescopes around the world. From left to right: Telescopes and lab of GI2T in France, four 8m telescopes of VLTI in Chile, the faceted 10m primary of one Keck telescope in Hawaii, the LBT at a construction site in Italy.

also referred to as Multiple Mirror Telescopes or faceted telescopes. A traditional telescope is limited to sizes of 10 meters, due to production accuracies for these sizes of optical surfaces. Atmospheric blurring also increases for larger areas of collecting surface, but that is not even considered here. For space applications, sizes of telescopes are typically limited to the size of the compartment in which they have to be transported to space. The famous Hubble Space Telescope had to fit in the Space Shuttle. Since resolution is related to the size of the primary mirror, the idea arose to build telescope primaries consisting of several separately produced parts. With production facilities of high accuracy and with the aid of computer controlled alignment while operating, Extremely Large Telescopes should be possible to build. Currently, several multi-telescope Earth observers are being designed for space operation and the feasibility of the OverWhelmingly Large telescope (OWL) is being studied for operation on the atmospherically favorable continent Antarctica.

The synthetic apertures can now either be (hexagonal) parts of a big curved surface or be finished (small) telescope primaries placed close together. This type of telescopes is dedicated to imaging, although plans also exist for huge coronographs based on such a synthetic primary. Unlike the example given for long-baseline interferometry, these imaging arrays or faceted primaries are typically *compact* and *filled*. The spatial frequencies that are covered have a cut-off related to the size of the synthetic aperture. Nearly all frequencies within are covered. This means that a single snapshot of a scenery contains information for nearly all spatial frequencies, in nearly all directions. For some arrays, the collecting area is compact, but not filled. The Golay configurations (Golay, 1971) for N telescopes provide a full frequency coverage, if snapshots are taken for a number of rotations of the whole array. Only the collective set of snapshots of the same scenery will produce a high resolution image. A single observation by LBT (Bertero and Boccacci, 2000) would produce an image with detail resolution in one direction as if the scenery were observed with an 8 m telescope, while in the direction of the dual dish placement (the primary baseline) the resolution relates to that of a 22 m telescope.

The arrays for long-baseline optical interferometry are all non-compact and hence far from filled. These *diluted* or sparse arrays hence seem less apt for acquiring snapshot images of a scenery. Placed at large separations, the array would collect very high spatial frequency information for only a few directions, without all lower frequency components. Moreover, the field-of-view (FOV) considerations for long-baseline arrays on one side and multiple-telescope imagers on the other side are very different, reflecting in the methods of beam transportation and detection, as will be detailed in Chapter 3. Generally speaking, both fields—stellar interferometry and multi-aperture imaging—allow to make images with an array of telescopes, delivering fine structure much smaller than the

resolution limit of a single telescope in the array.

1.3 Spectroscopy and high-resolution imaging from space

Arrays of telescopes can also be used in a different way to detect information from distant stars. Nulling interferometry is a field that is mainly focusing on detecting faint signals from planets around other stars than the Sun by attenuating or *nulling* the stellar light. The high intensity contrast ratio between a star and a planet (10^6 – 10^9, depending on the wavelength) would otherwise prohibit detection and analysis of a planetary signal, since it would be outshined by the star. The European Space Agency (ESA) started a concept study for an infrared space interferometer in 1995 and labeled it *Darwin*, to be operated in the year 2015.

As formulated in the Darwin Imaging study (De Vries *et al.*, 2005), the Darwin nulling array would make a great number of very interesting imaging observations possible. Some objects will be presented, together with the requirements they pose on the telescope array. The requirements will be discussed. The drivers for Darwin observations are both spatial and spectral resolution. The present study on optical aperture synthesis largely deals with the spatial resolution. Spectral issues shall be addressed only shortly in this thesis.

1.3.1 Science topics

Darwin will operate in an infrared wavelength range largely inaccessible for ground-based astronomy because of the Earth's temperature. In this wavelength range, the spectra of interstellar and circumstellar dust show many features, as listed in Table 1.1. These spectral features allow characterization of the physical and chemical properties of a stellar object. Such a characterization (Röttgering, 2003) is the main science driver for the imaging mode. An example of an observation for which both high spatial and spectral resolution was required, is the study of the building blocks of planets within proto-planetary disks (Van Boekel *et al.*, 2004). Figure 1.3 was taken from this publication. Although full feature imaging did not take place in this study, it provided information that could prove and alter parts of the models on proto-planetary disks. Visible and infrared interferometry have proved their value for astronomy (Quirrenbach, 2001; Baldwin and Haniff, 2002; Saha, 2002). To provide *images* rather than single interferometric measurements is the next desire of the interferometry-community (Paresce *et al.*, 2005).

Resolving spectral features is a subject rather left out of this research. However, high spatial resolution over an interferometrically large field-of-view is another necessity. The combination of modest spectral resolution and very high spatial resolution by using an interferometric array, would allow dust characterization as a function of location and would therefore *give crucial information about formation and destruction of dust around old and young stellar objects* (De Vries *et al.*, 2005). Big questions in the scientific domains of star formation, planet formation and galaxy formation, could be answered. So far, only models and indirect observations provide information on these subjects. For the same reasons, central regions of active galaxies are also interesting objects for observation with the Darwin array. Table 1.1 provides a list of spectral features to be expected in the Darwin wavelength range. To be able to perform spectrometry in these bands, high spectral resolution is needed. However, not all objects of interest pose this requirement,

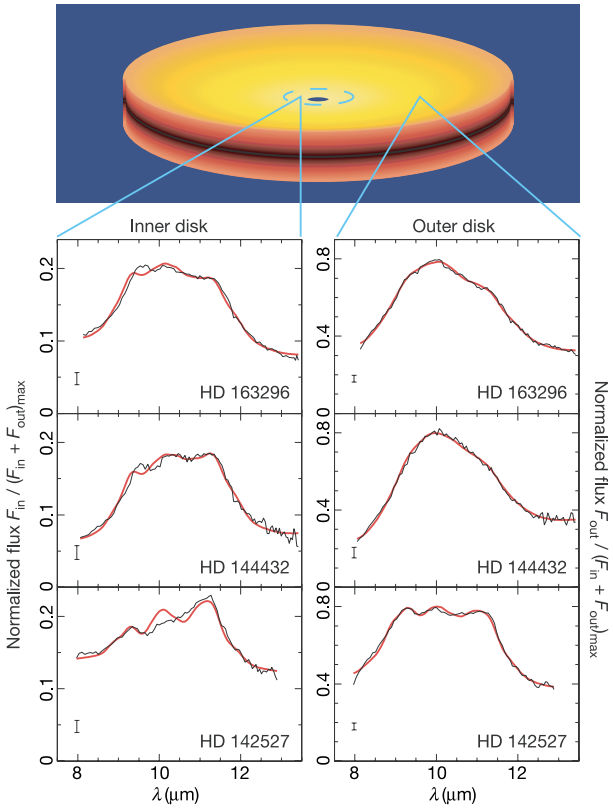

Figure 1.3: Infrared spectra of the inner (1–2 AU) and outer (2–20 AU) disk regions of three Herbig Ae-class stars (named HD *number*). The inner disk spectrum is obtained from an interferometric observation, the outer disk spectrum is the result of subtracting the inner disk spectrum from a low spatial resolution spectrum of the total disk. The spectra are fit to a model, describing the amount of crystallinity, the fraction of large grains and the crystalline olivine to pyroxene ratio. The latter two materials are dust components, of which spectra could be measured in laboratories. The differences in shape between the inner- and outer-disk spectra indicate a difference in dust mineralogy. The star HD 142527 is the youngest one and the observations indicate that, as was the case in the early Solar System, the silicate dust in the inner regions of proto-planetary disks is highly crystalline before planet formation occurs (Van Boekel *et al.*, 2004).

as will be detailed. The spatial issues such as structure and dimensions are detailed in (De Vries *et al.*, 2005) and result in a list of top-level imaging requirements.

Example objects for observation

Figures 1.4 and 1.5 show models of a few objects for observation. Star formation and the development of a planetary system have been modeled (Meyer *et al.*, 1998), but direct observations of such systems have never been performed to verify the theory behind the models. Indirect observations of exo-planets are reported frequently nowadays (Mayor & Queloz, 1995) but for direct observations, resolution is needed that is unattainable

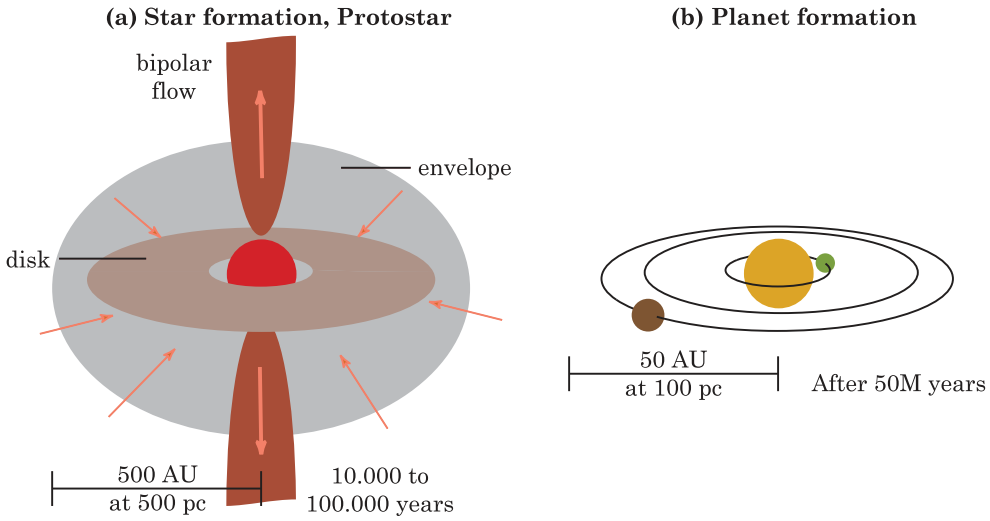

Figure 1.4: Science topics star formation and planet formation. (a) Star formation takes place in dark dust clouds, but the bright core and the violent outflow can be studied. To study the dust itself however, high spectral and spatial resolution are needed, at low light levels in the infrared. (b) A central star forms and heats the gas-rich dust globule to make it contract and form a disk. Planets form in this debris dust disk. Investigation of the disk itself will reveal details about planet formation. The indicated times are years since star formation.

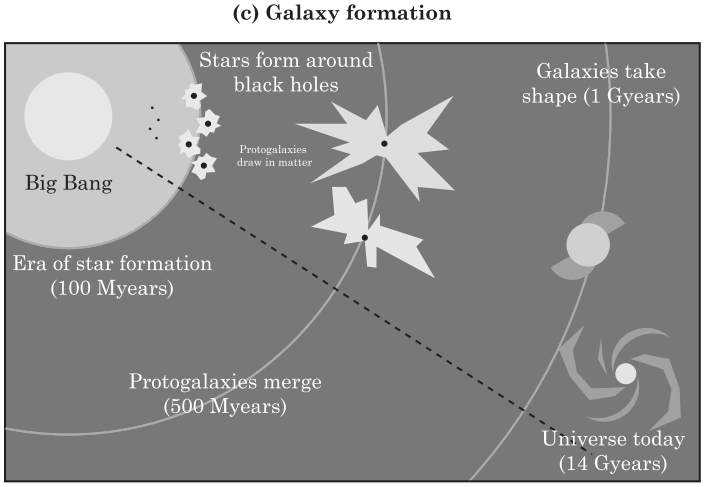

Figure 1.5: Galaxies form from smaller clumps of primordial galaxies. Spatial resolution is needed to detect these building blocks. Interacting galaxies produce stars, leading to significant infrared output.

Table 1.1: List of most important spectral features in the Darwin wavelength band. Taken from (De Vries *et al.*, 2005).

Category	λ (μ**m**)	**Species**	**Diagnostic**
PAHs[a]	6.2		Carbonaceous material
	7.7		
	8.6		
	11.3		
	12.7		
	14.2		
	16.2		
Silicates	9.7		Bulk of dust
(amorphous)	18.0		
Silicates	10.0	Mg_2SiO_4	Mineralogy
(crystalline)	11.3		
	16.3		
	19.5		
	23.5		
	27.5		
	18.5	$(Mg,Fe)SiO_3$	
	21.5		
	24.5		
	10.7	SiC	
Oxides	11.6	Al_2O_3	
	23	FeO	
Ice	6.0	H_2O	
H_2	28.2		

[a]PAHs: Polycyclic Aromatic Hydrocarbons

with present telescopes. While the key science goal of the Darwin mission is detection and characterization of Earth-like planets, the questions of planet formation can be answered by studying relatively young planetary systems with an unobscured central star (Fig. 1.4b), where nearly all gas has been removed and a so-called 'debris' dust disk with just formed planets is present around the star. The interesting area is within the 'Kuiper' belt, about 20 AU[2]. The distances to these objects range from 10 pc[3] for older evolved disks to over 100 pc for young disks in star forming regions.

In star formation (Fig. 1.4a), the interest of observation also lies in dust. More specifically, the transportation and formation or destruction of dust around a protostar reveals information about the star formation process. Inside a dark cloud, a protostar is still a bright infrared point source. The thick dust cloud causes a strong temperature gradient and hence a changing optical spectrum across the cloud. The nearest star forming regions are at a distance of about 100 pc. The clouds are thought of to have sizes of about 500 AU.

[2]Astronomical Unit (AU), the distance Earth–Sun.

[3]Parsec (pc), distance at which an object's parallax would be one arcsecond. 1 pc = 3.26 light years.

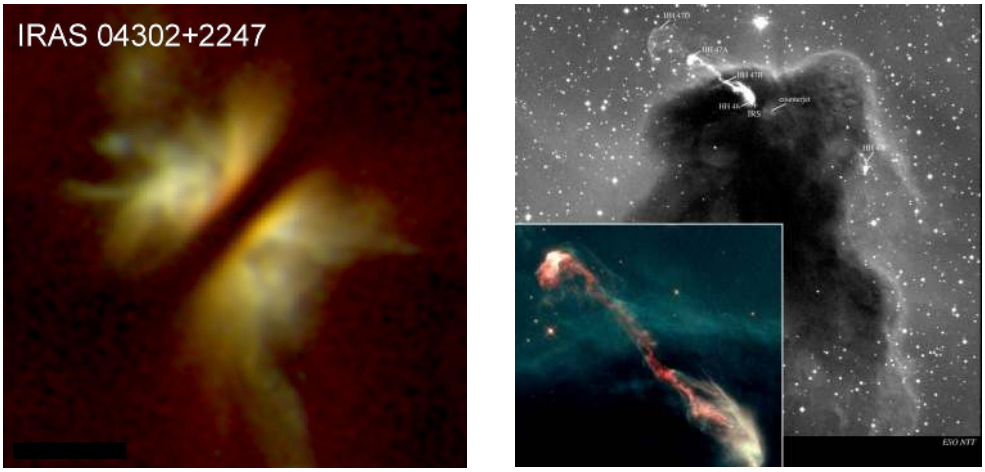

(a) (b)

Figure 1.6: Example images of the objects of interest. (a) A dust disk partly blocks the light from the bright central core, a protostar (IRAS 04302+2247). This object is very much like the early Solar system (b) Of the Herbig–Haro object no. 47, not the disk nor core, but the powerful jets are visible. The images are taken from the collections of NASA's Spitzer Space Telescope and ESO's New Technology Telescope (NTT) at La Silla.

Galaxy formation (Fig. 1.5) in the universe takes place at redshifts[4] $z = 3$–5. Smaller clumps of primordial galaxies merge. Very high resolution will be needed to discriminate these clumps in a distant young galaxy. Interacting galaxies are subject to massive star formation, leading to significant infrared output. This emission is around 1–2 μm, but at redshifts $z = 3$–5, this emission is shifted to the Darwin regime of 4–28 μm. Observation of the most distant and young galaxies is most interesting. These will be faint, hence small spectral resolution (a few channels) is favorable. Photometry will then enable characterization of distance and stellar population. Examples of the objects of interest—observed with other instruments—are depicted in Fig. 1.6.

1.3.2 Instrumental requirements

Table 1.2 presents a list of requirements necessary to collect information that can be processed to images of the astronomical objects of interest, as a result of the Darwin study (De Vries *et al.*, 2005). The imaging issues 'Spatial Resolution' and the Field-of-View (FOV) are the driving elements for this research. The FOV is depending on various parameters of the interferometer and hence the list contains no requirement on the FOV; issues related to the FOV are discussed in more detail in Sec. 3.3. The listed accuracies for path length control and the required point source sensitivity are not incorporated into the modeling and simulation of imaging interferometers in this thesis. Mechanical actuation and optical throughput are left out of the model. Concerning the detector or cam-

[4]Redshift (z) is the amount of Doppler-shift of the frequency of light from a stellar source, $z = (f_{\text{emit}} - f_{\text{obs}})/f_{\text{obs}}$. Due to the expansion of the Universe, objects further away from Earth move with a larger relative speed and are hence more reddish than objects nearby. The amount of redshift is a measure for distance.

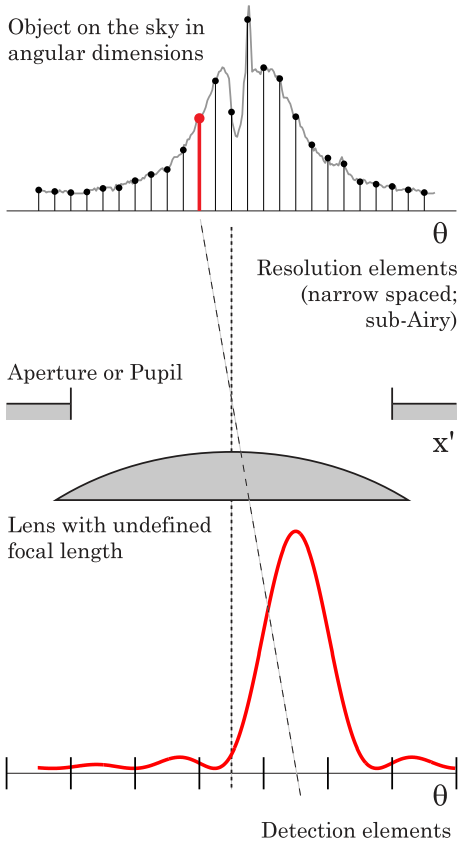

Figure 1.7: Sketch of the general imaging process. The spacing and size of the *spatial* resolution elements (on the sky) is governed by the spatial resolution of the synthetic aperture. Ultimately, the desired *spectral* resolution is to be obtained in each spatial resolution element on the sky. However, interferometric detection allows at best one spectrum estimate per spatial detection element, where it should be noted that light from several spatial resolution elements can end up in the same spatial detector element.

era, only a very limited simulation of imperfect detection is incorporated. The Dynamic Range of the obtained images will be evaluated. The requirements on an off-axis reference star and the specification of channels for the fringe tracking on the reference star are details that do not principally differ for either of the types of interferometer under consideration. Details can be found in the PRIMA reference (Quirrenbach *et al.*, 1998).

In the end, an image is to be synthesized that is a discrete and sampled rendition of a luminosity distribution on the sky, as seen in Fig. 1.7. The relative intensity of every **resolution element** has to be estimated from observations. The observations are collected with a number of **detector elements** which can be arrays of photosensitive sensors or lenslet-fiber couplers that transport the incoming light elsewhere for detection. The observation itself, as depicted here for a conventional non-interferometric imaging process, is in terms of **snapshot resolution** limited to the size of the diffraction limited point-spread-function (PSF), which is governed by the diameter of the lens (one telescope) and can on the detector array be as large as one or several detector elements,

Table 1.2: Darwin imaging requirements

Objective	**Requirement**	**Target**	**Comment**
Spectral Range	6 – 18 μm	5 – 30 μm	See list of key spectral features
Spatial Resolution	0.005"	0.001"	At 10 μm wavelength
Maximum Baseline	400 m	2000 m	For the given spatial resolution
Spectral Resolution	$R = 300$	$R = 1000$	For dust characterization
Path length Control	100 nm	10 nm	Depends on brightness
Sensitivity	40 nJy		For 48 hours integration at SNR=5
Dynamic Range	100	1000	
Off-axis Reference[a]	1 arcmin		To have a $m_v < 18^{\text{th}}$ reference star[b]
Ref. Fringe Track	0.4 – 2.5 μm		Separated range from science channels

1 Jy (Jansky) = $10^{-26} W m^{-2} Hz^{-1}$

[a] To maintain a cophased array of telescopes, the principle of *Phase Referencing* is applied, as proposed for the PRIMA-instrument (Phase Referenced Imaging and Microarcsecond Astrometry) on ESO's VLTI (Quirrenbach *et al.*, 1998). A guide star has to be picked that is bright enough and placed near the object of interest. The requirement of 1 arcmin ensures a $m_v < 18$ star available for 95% of the sky (Zombeck, 1990).

[b] Visual Magnitude m_v is a measure for the brightness of a star on a logarithmic scale, where the Sun has $m_v \equiv 1$ and higher numbers indicate weaker objects.

depending on the observation method. These methods will be detailed further. A number of low-resolution observations—the detector grid might also be consisting of a single sensor—is then numerically gathered to produce a single high-resolution synthetic image. The **Field-of-View** (FOV) that is pursued here, is generally *a few PSFs*, although the desirable FOV would be as many single-dish PSFs wide as possible. It may seem that 'a few' is still a small FOV and therefore a minor issue. However, the very high spatial resolution attainable with aperture synthesis classically manifests itself only *within* a single PSF, in that case also within a single detector element. This technique then is limited to a very narrow FOV that is in large contrast with the FOV of a single telescope. Extension of the interferometric FOV is not trivial, as will be discussed in the next chapter.

The discussed *spectral* resolution would be a desirable observable for every resolution element. Given a detector array with a high number of sensors, even obtaining the spectral resolution element per pixel would already be interesting. However, spectral issues have not been pursued here. A discussion of retrieval of spatially variant spectra will follow after the full presentation of methods for detection and imaging.

The **observation time** is in interferometric imaging closely related to the desired spatial resolution. Since the resolution rises with a growing telescope diameter, increasing the resolution can be pictured as demanding a telescope to encircle the already existing synthetic aperture. The path it has to fly will get very long and hence the observation time will increase, since snapshots or measurements will have to be made along the flown path. As a result, desired resolution can be balanced against desired observation

time.

1.3.3 Means to reach these goals

The discussed observational targets cannot be observed and characterized with currently available instruments. The 'classical' aperture synthesis known from radio astronomy can only be applied to a very narrow field. Fine spatial structure is produced, but only within one single Airy-spot. The multi-aperture optical telescopes (MAOTs) do have the capability to observe extended scenes, but these MAOTs have a fixed and compact configuration. For the very high resolution, very long extendable baselines are a necessity. A combination of the imaging strategies—measuring fringe parameters as in long baseline interferometry in combination with snapshot imaging as with a compact and fixed array—will arise. In the following research, multiple telescope arrays will be considered, where two or more telescopes will be placed at variable distances from each other. The optical surfaces will be assumed to be perfectly produced and no atmospheric disturbances are considered, since the goal application is situated in space. By combining and detecting the light collected by these telescopes in a certain way, it will be investigated whether the set targets on both spatial and spectral resolution can be achieved.

1.4 Research objective

The goal of this research can be summarized as a comparison of the performance of different types of stellar interferometers for the specific task of imaging an extended source and retrieving spectral information from that source within a limited observation time.

1.5 Outline of this thesis

The next two chapters, Chapter 2 and Chapter 3, will describe in detail how four different types of stellar interferometers work and how they produce an image. The production of an image relies on the inversion of collected interferometric data, which is an ill-posed inverse problem. In Chapter 4, solution strategies for this type of problem are discussed. With algorithms to describe the detection and to reconstruct an image out of detected signals, the complete imaging process can be simulated. Chapter 5 contains a detailed comparison of simulated results, obtained for the various possible interferometer setups. A description of experimental work on one type of stellar interferometer is given in Chapter 6. After these chapters related to interferometric imaging, Chapter 7 describes a method for general aberration retrieval, based on the Nijboer–Zernike diffraction theory of aberrations. The final topic in this thesis is nulling interferometry, on which experimental work was done. These experiments are described in Chapter 8. Finally, Chapter 9 concludes all the presented research and found results.

Chapter 2

Principles of optics and interferometry

Interferometers for imaging are able to produce high-resolution images. These images contain more spatial information than an image that would be produced by a single telescope, instead of an array of telescopes. The higher resolution is a result of the fact that the light of the telescopes is made to interfere. There are several ways to make beams of light interfere. To understand the boundary conditions on beam combination, the imaging principle of a single telescope is presented in Sec. 2.1. The distinctions in imaging interferometers, as well as the common name for such an interferometer deserves attention, which is given in Sec. 2.2. Then, using the same image formation theory as for the single telescope, the response of an interferometer to an elementary light source is derived in Sec. 2.3. This response is generalized, so that interferometers with different types of beam combination can be described with it. For one type of beam combination, the derived response is compared to another way of predicting the response, based on complex visibilities. This will show that the derived, generalized response is not only valid, but also a necessity to describe the information output of an interferometer for the task of imaging a wide-field source with very high angular resolution in the case of a polychromatic observation.

2.1 Light and radiation

In this section, the physical background of imaging is described. Starting with a point source emitting electromagnetic radiation and ending with a description of what this point source will look like for the observer, the total process of imaging a star with a conventional telescope can be described. For imaging with co-operating telescopes, the actual image retrieval is completely different, but the imaging process by a single telescope remains important, as will be shown. Therefore, the imaging by a single telescope is treated first.

2.1.1 Electromagnetic waves

The usual denomination for electromagnetic radiation of a certain wavelength, not too far from the visible domain, is *light*. Instead of mentioning wavelength, also *photon en-*

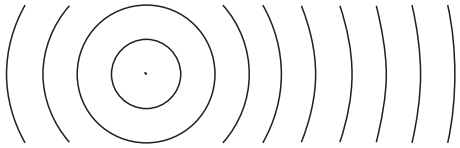

Figure 2.1: A spherical wave eventually results in a planar wave.

ergy could have been mentioned as the discriminating parameter. These two entities are in fact interchangeable, but refer to the two complementary natures of light. Instead of considering radiation as particles with a certain energy, the radiation is in this section treated as waves of a certain wavelength. Moreover, in this section only continuous harmonic waves will be considered.

In this framework, a one-dimensional wave can be approximated mathematically by the scalar wave function

$$\psi(x,t) = Ae^{i(kx-\omega t+\epsilon)} = Ae^{i\phi}. \tag{2.1}$$

In this expression, A is the amplitude of the wave, t and x represent time and location, respectively, k is the *wavenumber* and ϵ is some phase off-set. The circular wavenumber k is inversely proportional to the wavelength and could be described as 'the number of waves that fits in one meter'. The *phasor* expression $Ae^{i\phi}$ gives the amplitude and phase of the radiation of a certain wavelength at some point in time and space, given by the full expression for $\psi(x,t)$. In the case of multiple waves crossing the same point in time and space—while all waves have the same wavelength—summation of all the corresponding phasors for this point is allowed. Here, the vector character of the electro-magnetic field is neglected and the scalar model is adhered to.

Extending the wave equation from one dimension to more is most easily done for the case of a *plane wave*. This is the case when for a certain moment in time t, the phasors at different locations x have the same phase and this set of locations forms a plane. This plane is then perpendicular to the propagation direction $\vec{\mathbf{k}}$, so that the wavenumber now is a vector with a certain length and direction in space. The location in space can now generally be expressed by the position vector $\vec{\mathbf{r}}$ so that the wave equation becomes

$$\psi(\vec{\mathbf{r}},t) = Ae^{i\left[\left(\vec{\mathbf{k}}\cdot\vec{\mathbf{r}}\right)-\omega t\right]}, \tag{2.2}$$

where the minus sign originates from the convention about the time-dependence of the harmonic wave $\exp[-i\omega t]$. Plane waves, however, can not directly be associated with point sources of radiation. It is well known that an acoustic source in air or a stone thrown in a pond will produce *spherical* waves. The harmonical spherical wave is described as

$$\psi(r,t) = \left(\frac{\mathscr{A}}{r}\right)e^{ik(r-vt)}, \tag{2.3}$$

where now the speed v is used to describe the wave emanating from the origin at $r = 0$ and the source strength is denoted by $\mathscr{A}$. Plotting a few contours (Fig. 2.1) of this function shows how the radiation from a point source can be eventually considered as a plane wave, propagating in space.

For further description of the imaging process, it is useful to take notice of Huygens' Principle: *every point on a propagating wavefront serves as the source of secondary wavelets, such that the wavefront at some later time is the envelope of these wavelets.*

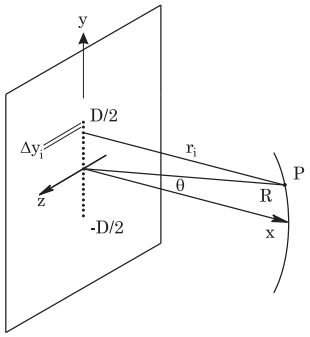

Figure 2.2: Co-ordinate system used for the example in the text, a coherent line source.

These secondary wavelets have the same period and travel at the same speed as the original propagating wavefront. This Principle is a useful tool, but the idea (dated 1678) has some shortcomings that are made up for in the concept of the diffraction integral.

2.1.2 Diffraction integral

As stated, Huygens' Principle is a useful tool to describe the evolution of waves through time and space in the case of obstructions. However, it does not take wavelength and relative phases into account. The fact that sound bends around a tree, whereas sunlight produces a shadow behind it, can not be clarified by it. By adding interference, Fresnel proposed the Huygens–Fresnel theory. The modification is that *the secondary wavelets make that the amplitude of the optical field at any point beyond it is the superposition of all these wavelets, considering their amplitudes and relative phases.* This results in regions of constructive and destructive interference. It also accounts for the wavelength, since after a propagation over distance d, the relative phase fluctuations $\phi(\lambda) = 2\pi d/\lambda$ are taken into account.

This theory can describe both the near- and far-field. However, in the far-field, the relative phase fluctuations vary not that rapidly and the pattern that will be observed is more easily described by the Fraunhofer diffraction pattern. This description is roughly valid when

$$R > \frac{a^2}{2\lambda}, \tag{2.4}$$

where a is the size of an obstacle or aperture, λ is the wavelength and R is the distance between the obstacle and the observational plane. Considering infinitesimally small point sources distributed along a slit-like aperture (see Fig. 2.2), the summation of point sources can be expressed as an integral over the slit and this results in the Fraunhofer diffraction integral, as described in *Optics* (Hecht, 1995).

Consider a monochromatically lit line opening of length D, illustrated in Figure 2.2. Numerous point sources can be imagined to be located at the line opening. Each point emits a spherical wavelet so that the electric field E is given as

$$E = \left(\frac{\mathscr{E}_0}{r}\right) \exp[i(kr - \omega t)], \tag{2.5}$$

where $\mathscr{E}_0$ is the source strength. The number of sources is N and for a very large number,

the source strength becomes

$$\mathscr{E}_L \equiv \frac{1}{D} \lim_{N\to\infty} (\epsilon_0 N) \tag{2.6}$$

which is the source strength per unit length. The electric field is then the integral over the slit

$$E = \mathscr{E}_L \int_{-D/2}^{D/2} \frac{\exp[i(kr(y) - \omega t)]}{r(y)} \mathrm{d}y. \tag{2.7}$$

When the Fraunhofer condition is met—so that in Fig. 2.2 the distance R from the slit to the point P is much larger than the slit length D—the distance r is linear with respect to y, or the phases of all contributing secondary wavefronts can be expressed linearly, so that in a direction θ

$$E = \frac{\mathscr{E}_L}{R} \int_{-D/2}^{D/2} \exp\left[k(R - y\sin\theta) - \omega t\right] \mathrm{d}y, \tag{2.8}$$

and finally

$$E = \frac{\mathscr{E}_L D}{R} \frac{\sin[(kD/2)\sin\theta]}{(kD/2)\sin\theta} \sin(kR - \omega t). \tag{2.9}$$

For ease of notation, let

$$\beta \equiv (kD/2)\sin\theta. \tag{2.10}$$

The quantity that will be measured is the *irradiance*[1], which is, apart of the factor $\epsilon_0 c$ (the permittivity of vacuuum times the speed of light in vacuum), the time average of the squared electric field, $I = \langle E^2 \rangle_T$ or

$$I(\theta) = \frac{1}{2}\left(\frac{\mathscr{E}_L D}{R}\right)^2 \left(\frac{\sin\beta}{\beta}\right)^2. \tag{2.11}$$

In its most general form, the irradiance resulting from an idealized coherent line source in the Fraunhofer approximation is then

$$I(\theta) = I(0)\left(\frac{\sin\beta}{\beta}\right)^2 \tag{2.12}$$

where $\beta = (\pi D/\lambda)\sin\theta$ and $D \gg \lambda$.

To describe what the image of a point source in the sky looks like, the tools are now in place. A point source will produce spherical wavefronts, but for large distances, these can be considered to be flat. Waves encountering an object or aperture will diffract. The plane wave will coherently illuminate that aperture. The intensity pattern in the far-field can be described with the Fraunhofer diffraction integral in a general two-dimensional version of Eq. (2.8).

For a circular aperture, an extension is needed to two dimensions and because of circular symmetry, polar coordinates are introduced. The expression for the electric field then becomes

$$E = \frac{\mathscr{E}_A e^{i(kR-\omega t)}}{R} \int_{\rho=0}^{a} \int_{\phi=0}^{2\pi} e^{i(k\rho q/R)\cos(\phi-\Phi)} \rho \mathrm{d}\rho \mathrm{d}\phi, \tag{2.13}$$

the surface integral over the circular aperture with area A and with $\mathscr{E}_A$, the field strength per unit area. To simplify this expression, the *Bessel functions* (of the first kind) are introduced. They are defined as

$$J_m(u) = \frac{i^{-m}}{2\pi} \int_0^{2\pi} e^{i(mv + u\cos v)} \mathrm{d}v, \tag{2.14}$$

[1]The generally used word *intensity* means the flow of energy per unit area per unit time. In optics, this word is by convention replaced by the word *irradiance*.

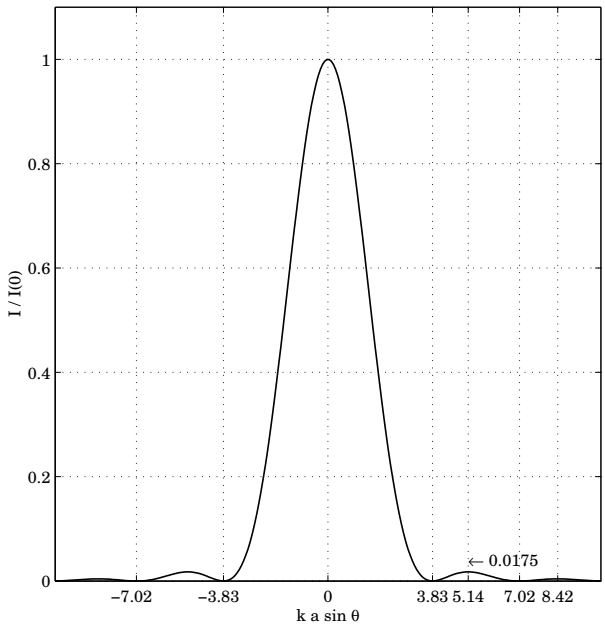

Figure 2.3: A cross section of the Airy pattern. For an aberration free system, the intensity of the first bright ring is roughly 2% of the peak intensity.

where m denotes the order of the function and (u,v) form a transform pair. Using the Bessel function J_1 and following the steps as in the line-source case, the irradiance at a point P after the circular aperture can be derived to be

$$I = \frac{2\mathscr{E}_A^2 A^2}{R^2}\left[\frac{J_1(kaq/R)}{kaq/R}\right]^2. \tag{2.15}$$

When normalized, this expression poses the description of the circular spot that can be observed when a point source is imaged. It is known as the *Airy pattern*—see Figs. 2.3 and 2.4—after the physicist Sir George Biddell Airy. The central bright region is surrounded by a dark ring, occurring at a radius corresponding to the first zero of the function $J_1(u)$. This corresponds to $kaq/R = 3.83$. The radius for the first dark ring q_1 is often called the Airy-radius and is given by

$$q_1 = 1.22\frac{R\lambda}{2a}. \tag{2.16}$$

The size of the central 'disk' is thus linearly proportional to the wavelength and inversely proportional to the diameter of the aperture.

2.1.3 Resolution of an imaging system

An extended stellar source can be considered to be self-luminous, meaning that it is made up of independently radiating point sources. For incoherent sources, the image that a lens system will form of them, will be a distribution of partially overlapping Airy patterns. It should be stated here that this is true only for aberration-free lens systems.

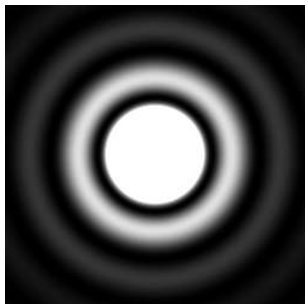

Figure 2.4: Airy rings with a saturated central peak.

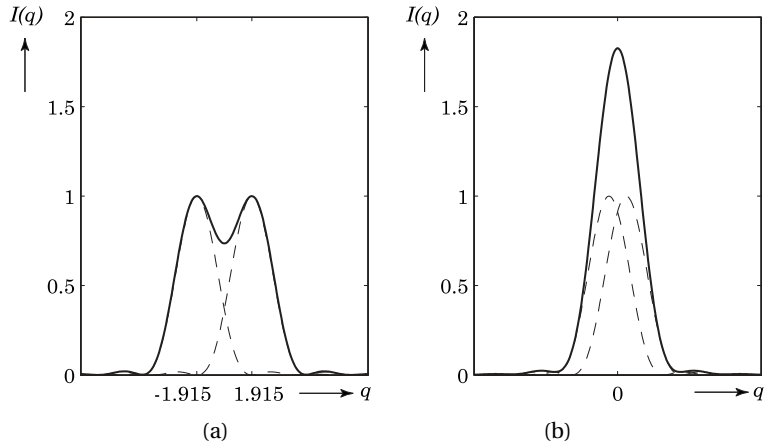

Figure 2.5: An example of imaging two point sources at the Rayleigh limit of separation (a) and two point sources that are unresolved (b). The radius of the first dark ring in the Airy pattern is at $q_1 = 1.915$.

In the presence of aberrations, the pattern of a point source will be Airy-like, but has less amplitude in the central area and most likely a broader waist. But also for the aberration-free case, the fact that the Airy pattern has a certain extent, limits the resolution of the formed image.

For two independent point sources, a criterion for resolvability or resolution can be produced. The center-to-center distance of two Airy patterns could be one criterion. But more precise definitions also exist, like the Rayleigh criterion (Fig. 2.5) which states that two equally luminous point sources are resolvable if their separation is at least half the diameter of the first dark ring of the diffraction pattern. Clearly, the resolving power of an optical system for some fixed wavelength is inversely related to the diameter D of the primary diffracting aperture. This is why—stated in a very simplified way—a larger telescope will see more detail. This large diameter however, has practical limits.

2.1.4 Need for interferometry

A very large primary mirror (or dish) would have to be supported by an enormous amount of concrete and steel, in order to keep the surface aberration-free in the presence of wind or seismic actuation. Moreover, a larger dish at the Earths surface would collect light rays that have clearly traveled through different parts of the atmosphere. Since the atmosphere is not placid and of constant density, this will result in varying optical path lengths and hence phases among the rays from one source reaching the telescope at different positions in the primary mirror. Adaptive Optics (Hardy, 1998) are able to compensate these effects partially, but before this technique had evolved, other solutions were found to surpass the limitations in resolution. Stellar Interferometry, the joint observation of a star via two separated apertures, could be performed with smaller apertures that basically did not suffer from atmospheric aberrations. The wavefronts of the beams from these smaller apertures show relatively smaller aberrations, but do need to be de-tilted and cophased by 'pistoning' them. As described in the section about history (Sec.1.2.1), this is still a difficult task, but it requires less complicated hardware than the implementation of full Adaptive Optics does. The next section will further specify the working principles of Stellar Interferometry and address the resolution limit in more detail, after a treatment of the subject of coherence.

2.1.5 Coherent and incoherent radiation

In the following chapters, as well as in the preceding sections, the terms *coherent* and *incoherent* occur frequently. The discussion on the diffraction integral and the properties of light as a wave phenomenon, assumed mostly **monochromatic** radiation. In most cases, one deals then with coherent radiation: the complex representation or phasor of any wave in time and space can be added to another one. However, as was also already pointed out, it might be possible that a source is in fact a collection of point sources emitting at the same wavelength, but that they are still incoherent. This can be understood by assuming that the phase of each point source changes randomly to different phases at very short timescales. Branched-off rays from one such point source will at recombination still interfere and are hence coherent, since their *phase difference* at the point of detection remains the same. Interference with other point sources of exactly the same color however, is not possible anymore—consider the combination of light emitted by two identical lasers—and the sources are considered to be incoherent, although they are monochromatic. The same effect can be observed in laser interferometers where the path length difference is that large, that all phase correlation at recombination is lost and the beams do not interfere, although they originated from the same monochromatic source. The coherence under consideration here, is often called *temporal coherence* and relates to the quantum nature of light. For the treatment of stellar interferometry, complete understanding of this definition of coherence is not necessary.

If the point sources are now considered to be **polychromatic**, another definition of coherence arises. Rays coming from this source are not allowed to have a too large path length difference for interference phenomena to occur. For a certain spectral bandwidth of radiation at the source, there exists a *coherence length* to which path lengths or traveling times can be compared. Rays with a path length difference larger than this coherence length are considered to be incoherent, although stemming from the same single point source. This definition of coherence is totally explicable by regarding light as a wave phenomenon. If two rays of monochromatic light are combined and observed, the intensity

as a function of path length difference can mathematically be described with a cosine function. Many colors—or polychromatic light—cause many cosines with the same origin. Mathematically, summing these cosines results in a function that still shows oscillations near the origin, but has a constant value far away from the origin. The distance at which the oscillations disappear is a function of the spectrum of the source.

A third definition of coherence occurs when **interferometry** is considered. As will be detailed in further chapters, a single polychromatic point source on the sky will produce a fringe packet as a function of an applied path length difference. This fringe packet has an extent referred to as the coherence length, as declared before. But in the case of interferometry, two separated polychromatic self-luminous point sources are often considered to be *spatially coherent* if the fringe packets that they produce on a detector fall in the same scanning region of the applied path length difference. This coherence is in the literature referred to as *partial coherence*, which applies to non-point-like sources. The resulting observed fringe packet will then generally have a non-optimal modulation, as will be detailed further; the observation principle in stellar interferometry is based on the measurement of this modulation.

Where applicable, different terms for the coherence will have to be used to avoid confusion. Where present in an example or experiment, coherence will be mentioned as either applying to *monochromatically coherent* electric fields, *polychromatically coherent* path length differences or *interferometrically coherent* separated point sources on the sky.

2.2 Interferometer labeling

Special attention should be drawn to the confusing labeling of interferometers in the literature. Very often, arrays are simply and confusingly classified as being 'Michelson-type' or 'Fizeau-type' (G. Rousset *et al.*, 2001; Loreggia *et al.*, 2004). The description of several interferometers will show that there are more flavors than just two. To be able to address and discuss all features of each interferometer correctly, a list of distinctions is made. Some confusion arises from the work by Michelson. In the 'Michelson Stellar Interferometer', a periscope system was mounted on a telescope, so that two beams of diameter D were combined side-by-side with a separation B_0, for which $D < B_0 < B$, and B is the separation of the mirrors on the outer end of the periscope. In contrast, a general 'Michelson Interferometer' has the optical lay-out of the interferometer used in the Michelson–Morley experiment, to prove the existence of ether and its motion relative to the Earth. Here, two beams are combined via a half-silvered glass plate and hence the side-by-side separation at combination is $B_0 = 0$.

The following list not only pinpoints the features to label an interferometer either 'Fizeau' or 'Michelson', but also aims to add other distinctions. These (hardware-) distinctions naturally play a role in the design of a beam combiner. It should be noted that the list of classifications relates to all optical synthetic aperture arrays, both for astronomy (diluted arrays, very long baselines) as well as for earth observation (compact, non-redundant arrays with fixed baselines).

- **Method of collection**. In many European papers, the distinction between Fizeau and Michelson-types relates to the method of wavefront collection. Fizeau and Stéphan (Sec. 1.2.1) used an aperture mask in front of the primary collector. Hence, from the beginning of the 'transport' of the partial wavefronts to the point of com-

bination, the wavefronts are curved. An interferometer with separated collection elements should therefore have telescopes with curved primaries, having the radius of curvature corresponding to the synthetic aperture in which they are positioned, to be called an array of Fizeau-type. Plans to build such an interferometer exist (Loreggia *et al.*, 2004) but none have been built. The experiments by Michelson and Pease (see historic overview, Sec. 1.2.1) took place by collecting parts of the same wavefront and transporting them while still collimated to the beam combiner, being a regular telescope. For a mirror (or siderostat) the beam compression or magnification is $M = 1$, while a telescope as collector can be configured to produce any beam compression ratio. Collecting and transporting flat partial wavefronts is a feature of both the Michelson-type and the Michelson Stellar-type. Nearly all optical long-baseline interferometers are of this type.

- **Method of combination**. In other papers, the possibility of either pupil-plane combination or image-plane combination is often addressed as Michelson or Fizeau-mode. Pupil-plane fringe detection (rather than pupil-plane beam combination) is not considered, since in all cases the energy in the beams will be focused onto one or more detectors. *In this thesis, the combination of the beams will be referred to as being co-axial or not.* When combined co-axially, a beam splitter is used to combine two beams pairwise, of which one or both beams was already the combination of two others. The co-axially combined beam will then be focused onto one or more detectors for intensity readout. The COAST array (Baldwin *et al.*, 1996) is an example. Combining non-co-axially means that the beams are placed side-by-side (Michelson Stellar, densification) or have a general magnification, position and orientation (general non-homothesis) or are homothetic with the entrance pupil configuration so that before focusing, the partial wavefronts are arranged as an exactly scaled copy of the partial wavefronts before the collectors (for example in the Large Binocular Telescope and in Multiple Aperture Optical Telescopes). The focusing optics are larger in diameter than a single beam cross-section, unlike for co-axial beam combination.

- **Method of fringe encoding**. These options are temporal or spatial encoding or a combination of both and are coupled to the method of collection or the method of combination. Operating a masked aperture (Fizeau collection) will result in spatial fringes in focus. Co-axial combination will need temporal (varying path length of a beam pair) encoding to produce fringes. For general non-homothetic, non-co-axial combination (exit baseline $0 < B_0 < B$), fringes for a part of the field-of-view will be spatially encoded. The full field-of-view can be covered by adding temporal encoding. Generally, interferometric imaging provides high resolution images for regions of the field-of-view in which fringes (encoded in some way) can be observed.

- **Method of detection**. The signal from which an image is to be reconstructed is a summation of electrical fields (partial wavefronts) superimposed in focus. Of this optical signal, only the intensity can be measured. The method of fringe encoding makes that this intensity in focus varies with position (spatial encoding) or with time (the path length difference between a pair of beams is made a function of time). To obtain all encoded information, the detection should be able to measure this time- and position-dependent intensity. The detector should consist of a

sufficient number of small enough elements to sample the spatially varying intensity. The spatial frequency is principally determined by the combination method and can possibly vary with array dimensions and the detector should be able to collect multiple intensity sets when temporal encoding is applicable. Additional restrictions for the dimension of each detection element lie in the size of a single collector and as mentioned in the separation distance of collectors. The overall dimension of the detector should (angularly) cover the desired field-of-view. The elements can be either photosensitive devices or optical fibers, feeding the local electric field to an intensity detector elsewhere. The detector can consist of one, a few, or a very large number of detection elements and will produce one or a few readouts per array configuration.

When designing an optical interferometer for certain stellar observations, the subject or class of objects to be observed determines the desirable basic lay-out of the interferometer array. The methods of collecting and combining the partial wavefronts pose constraints on the hardware of the array. The software needed is determined by the method of fringe encoding and the detector. It should be clear that both domains of hardware and software impose restrictions on each other. This may limit compatibility of available software with desirable hardware for example, but it should also be clear that hybrid combination and detection schemes are possible. For this reason, simulation based on response functions was chosen. All interferometers provide differently structured polychromatic fringes for the extended source. For a fair comparison, all detected information is post-processed with the same software for reconstruction of the image. No method-specific software is used.

2.3 Theory of interferometric imaging

As stated, several solutions exist to image a stellar objects with more than one telescope, in such a way that the resulting image contains more details than the best possible image from each single telescope could provide. Using the Fraunhofer diffraction calculation that was used for a single-dish telescope, the point-source response can be calculated for the image plane or combined focus of an array of co-phased telescopes. With this parametric response function, the transfer of the information on the sky into measureable signals can be given for four types of interferometric beam combination. For one specific combination type—co-axial combination, the most popular type—this prediction of the measureable signal is compared to the prediction based on the Zernike–Van Cittert theorem, which will be detailed. This comparison will then show how the derived nature of the response signal is not only valid for all beam combiners under consideration, but also allows extension to wide-field observations and polychromatic observations.

2.3.1 General interferometer model

In the following paragraphs, the point-source response function is derived for every possible beam combination type for imaging interferometers. The calculation is based on the fact that a wavefront originating from a stellar source at an angle θ_0 with the zenith direction, arrives as a flat wave front, exciting secondary wavelets in the collecting pupil plane, as illustrated in Figs. 2.6 and 2.7. These wavelets have equal amplitudes, but differ in phase given the slope with angle θ_0. The partial wave fronts are relayed with unit

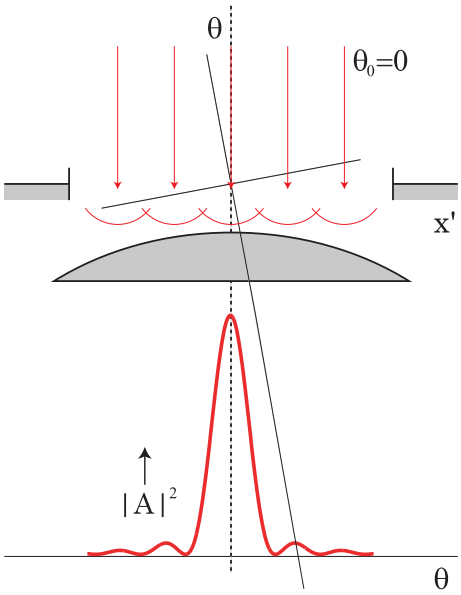

Figure 2.6: The principle of Fourier Optics to calculate a far-field or Fraunhofer diffraction pattern. A flat wavefront excites secondary wavelets across an aperture, with relative phases depending on the angle of incidence of the wavefront (here, $\theta_0 = 0$). The amplitude of the field propagating in a certain direction θ is proportional to the sum of the complex amplitudes of all secondary wavelets when these originate on a plane at an angle θ with the aperture.

magnification to the exit pupil plane (see Fig. 2.8 for general examples), where the partial wavefronts will be combined again and focused on a detector plane. This example considers only two apertures and is one-dimensional for ease of illustration and calculation.

The wavelets in the exit pupil plane generate a wave front expanding identically in all directions, as described for a regular elementary telescope in Section 2.1 and illustrated in Fig. 2.6. For a planar wavefront with an angle θ with respect to the exit pupil plane, the complex electrical field amplitude A in focus can be described as the sum of all wavelet contributions by

$$A(\theta) = \int_{\text{pupil}} e^{i(2\pi x\theta/\lambda)} \mathrm{d}x, \tag{2.17}$$

where the elementary wavelets all have amplitude 1 and equal phase, for the case $\theta_0 = 0$. The distance from exit plane to the plane at an angle θ is linearized, because $\sin(\theta) \simeq \theta$. For a point source at direction θ_0 on the sky, there will be a phase slope across the elementary wavelets, so that the phases in the plane at an angle θ have an extra slope, resulting in

$$A(\theta) = \int_{\text{pupil}} e^{i(2\pi x\theta/\lambda)} e^{i(2\pi[-x\theta_0]/\lambda)} \mathrm{d}x. \tag{2.18}$$

Figure 2.7 illustrates the phases of secondary wavelets in an exit pupil plane x; the partial wavefronts were initially collected in another plane x'. Because of the length difference $|B - B_0|$, the phase in the exit pupil is not necessarily part of a continuous function. In the case of co-axial combination, there is even a co-existence of two partial wavefronts at the same location. An expression for the in-focus amplitude is again derived, but now separately for both exit pupils. As known, every interferometer is equipped with a delay line.

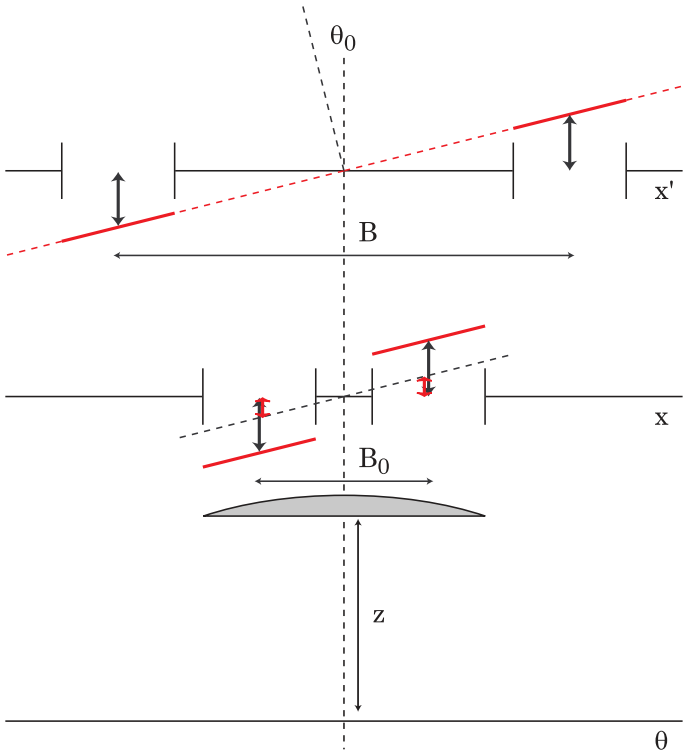

Figure 2.7: This illustration indicates the coordinates used in the derivation of the point-source response functions for all possible types of beam combination, based on the combination baseline B_0. B_0 is greater than or equal to zero. The not indicated beam paths from plane x' to plane x are the relay of pupils, symmetrically around the optical axis (dashed line). The beams, without magnification, fall on a lens to be focused (not indicated). The phase difference at the collecting apertures (black arrows) is maintained on propagating from pupil plane x' to x. For symmetry in the diffraction integral, these physical phases are compared to the phase slope at x for the same angle of incidence θ_0 at the aperture positions corresponding to the chosen value of B_0 (gray arrows).

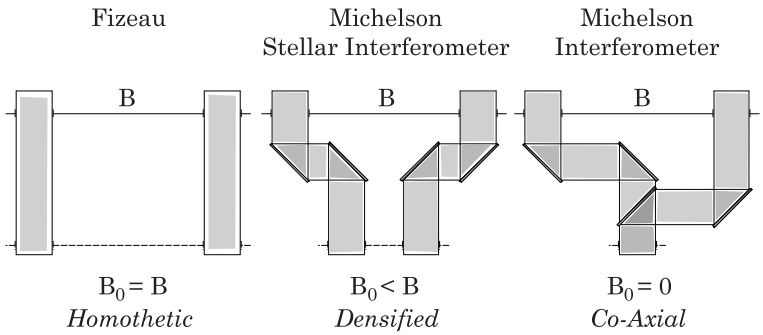

Figure 2.8: This illustration indicates the possibilities for exit pupil placement, for a general exit-baseline B_0.

In this model, one beam experiences an extra path length of d meters. The amplitude in focus is

$$A(\theta,d)=\int_{-B_0/2-D/2}^{-B_0/2+D/2} e^{i(2\pi x\theta/\lambda)}e^{i(2\pi[-x\theta_0+\frac{1}{2}(B-B_0)\theta_0]/\lambda)}\mathrm{d}x+ \\ e^{i(2\pi d/\lambda)}\int_{B_0/2-D/2}^{B_0/2+D/2} e^{i(2\pi x\theta/\lambda)}e^{i(2\pi[-x\theta_0-\frac{1}{2}(B-B_0)\theta_0]/\lambda)}\mathrm{d}x. \tag{2.19}$$

The integral expression in Eq. (2.19) describes the output for interferometers having any combination baseline $0\le B_0\le B$. The first exponentional factor $e^{i(2\pi x\theta/\lambda)}$ generates a field envelope, which is the Airy function for a circular aperture and a sinc-function for the (theoretical) one-dimensional aperture in the example. The first term $(-x\theta_0)$ of the second exponential factor indicates the phase front being tilted, and this essentially only shifts the origin of the envelope from θ to $\theta-\theta_0$. The last term containing $(B-B_0)$ covers the θ_0-dependent optical path length difference due to the choice of combination baseline length B_0, canceling for the case $B=B_0$. This is the case of homothesis. Using trigonometry and the definition of the sinc-function,

$$\mathrm{sinc}(x)=\begin{cases}1 & \text{for } x=0\\ \frac{\sin(x)}{x} & \text{otherwise}\end{cases}, \tag{2.20}$$

the integral in Eq. (2.19) can be expressed as

$$A(\theta,d)_{\text{general}}=2D\mathrm{sinc}[D\pi(\theta-\theta_0)/\lambda]\cos[\pi(d+B_0\theta-B\theta_0)/\lambda]e^{id\pi/\lambda}. \tag{2.21}$$

Two well-known responses, for a homothetic and a co-axial interferometer, can be derived from this general expression. Since $d=0$ for homothetic arrays and $B=B_0$, it is clear that the point source response is only a function of $(\theta-\theta_0)$, given B_0 and D:

$$A(\theta)_{\text{homothetic}}=\frac{\sin[\pi(\theta-\theta_0)D/\lambda]}{\pi(\theta-\theta_0)D/\lambda}\cos[\pi(\theta-\theta_0)B_0/\lambda]\,2D. \tag{2.22}$$

The envelope-with-fringes, constituted by the D-dominated sinc and the B_0-dominated cos functions, is field-invariant since both the modulation function and the envelope are functions of θ and have the same origin θ_0.

For co-axial combination, the exit baseline B_0 is zero and the path length of the second interferometer arm d is variable. To arrive at an envelope only, without extra phase additions, it is clear that when $d=B\theta_0$ there are no other terms than the shifted $(\theta-\theta_0)$ envelope. However, for a collection of point sources—since no physical source is a true point-source—at different values of θ_0, there can be only one d, so all point source responses from different θ_0 have phase shifts of $B\theta_0-d$ which results in a baseline-dependent modulation contrast. Indeed, inserting only $B_0=0$ into Eq. (2.21) results in

$$A'(\theta,d)_{\text{co-axial}}=\frac{\sin[\pi(\theta-\theta_0)D/\lambda]}{\pi(\theta-\theta_0)D/\lambda}\cos[\pi(d-B\theta_0)/\lambda]2D, \tag{2.23}$$

where A' indicates that the phase factor $\exp[id\pi/\lambda]$ in Eq. (2.21) is neglected. This factor 'rotates' the phase of the complete response and would only be of interest if this field was to be combined with another. The co-axial result is again familiar, being constituted by an envelope in direction θ with origin θ_0, that is totally modulated by a function of delay d with field-dependent origin $B\theta_0$.

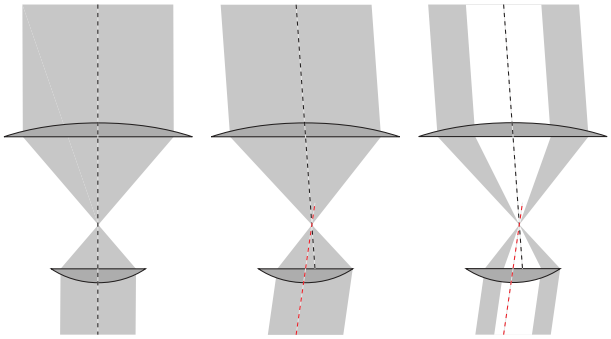

Figure 2.9: From left to right: the sketches display a telescope objective and an eyepiece, to illustrate the effects of a-focal beam compression. The first sketch clearly shows a compression ratio of $M = 2$, the ratio of the focal lengths of the two lenses. The second sketch shows that the primary direction in and out (and hence the tilts of the incoming and outgoing phase fronts) are scaled as $\theta_{\text{out}} = M\theta_{\text{in}}$. The third sketch shows the beam paths for the case of a masked primary aperture.

Including magnification

In general, a telescope can be regarded as an afocal beam compressor. The incoming and outgoing beams are collimated. Compressing the beam results in an angular magnification and higher electrical field amplitudes in the outgoing beam. As indicated in the sketches in Fig. 2.9, the beam compression factor is governed by the ratio of the focal lengths of the collecting lens (primary) and the eyepiece. For a compression factor M, this results in $\theta_{\text{out}} = M\theta_{\text{in}}$, $A_{\text{out}} = MA_{\text{in}}$ and the relations that are related to interferometry $D_{\text{out}} = D_{\text{in}}/M$ and $B_{\text{out}} = B_{\text{in}}/M$, where D and B are the diameter of each beam and the separation of them, respectively, in the collimated regions.

A telescope array where all collected beams are first compressed and then relayed to a beam combiner, is now depicted in Fig. 2.10. This is a more general version of Fig. 2.7. Having studied the method of beam compression for a masked aperture (Fig. 2.9), it is clear that the calculation of the fringe pattern after focusing the light out of a beam combiner with general exit baseline B_0 (again co-axial $B_0 = 0$, homothetic $B_0 = B/M$ or any other B_0) obeys the laws $D_0 = D/M$ and $\theta_1 = M\theta_0$ that the masked aperture example in Fig. 2.9 shows. Stating that both beams individually are compressed by the same factor M, the scaling for θ_0, A and D are fixed. Furthermore, each collector can be equipped with a field de-rotator, so that the exit beams need not be placed mirrored with respect to the optical axis. With these assumptions, an expression can now be derived, describing the focal field of a two-element interferometer with arbitrary magnification M and arbitrary exit baseline length B_0. For ease of construction of the diffraction integral, the differential phases in the partial wave fronts around B_0 have to be compared to those around the *natural* compressed baseline length B_M, instead of to the original B, as in the previous calculation. To calculate the fringed output, the magnification is introduced and the integration boundaries are changed, according to

$$A(\theta, d) = \int_{-B_0/2-\frac{D}{M}/2}^{-B_0/2+\frac{D}{M}/2} e^{i(2\pi x\theta/\lambda)} M e^{i(2\pi[-xM\theta_0+\frac{1}{2}(\frac{B}{M}-B_0)M\theta_0]/\lambda)} \mathrm{d}x + e^{i(2\pi d/\lambda)} \int_{B_0/2-\frac{D}{M}/2}^{B_0/2+\frac{D}{M}/2} e^{i(2\pi x\theta/\lambda)} M e^{i(2\pi[-xM\theta_0-\frac{1}{2}(\frac{B}{M}-B_0)M\theta_0]/\lambda)} \mathrm{d}x. \tag{2.24}$$

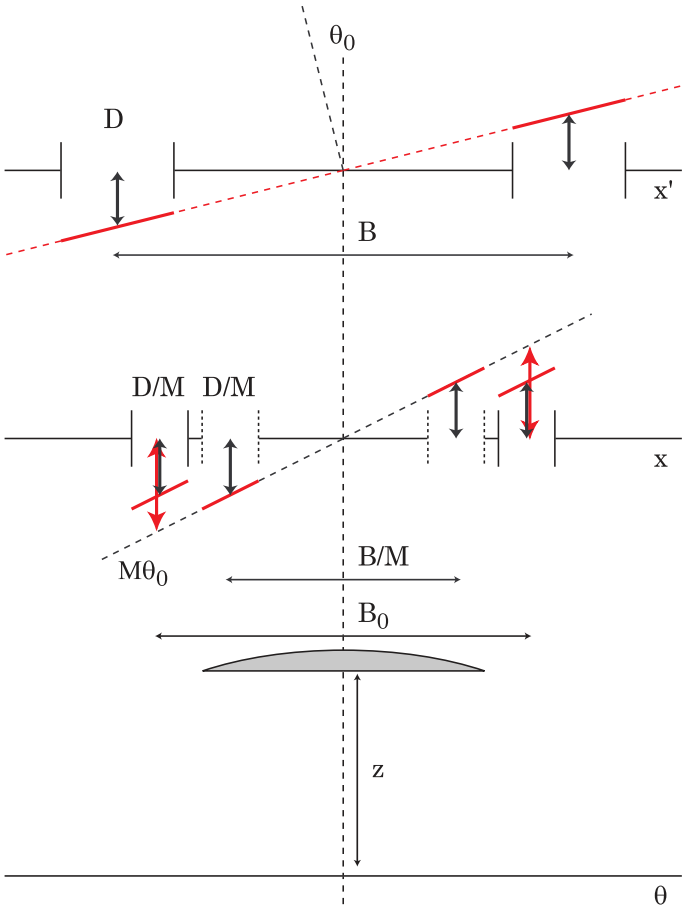

Figure 2.10: This illustration indicates the coordinates used in the derivation of the point-source response functions for all possible types of beam combination (any $B_0 \geq 0$), when a general beam compression by a factor M is applied in each arm. Again, the diffraction integral is symmetric and the phases of the wavefronts placed at B_0 separation in the plane x, proportional to $-xM\theta_0$, are compared (gray arrows, proportional to $\frac{1}{2}B_0M\theta_0$) to the 'physical' phase differences (black arrows, proportional to $\frac{1}{2}B\theta_0$) when the natural (see Fig. 2.9) path of a masked aperture was followed. Using these coordinates, the diffraction integral of Eq. 2.24 can be constructed, in which the phases proportional to $[-xM\theta_0 \pm \frac{1}{2}(\frac{B}{M} - B_0)M\theta_0]$ are used.

The first exponential factor in the integrals again constitutes the pupil-to-image relationship known from Fourier optics, see Fig. 2.6. The second exponential comprises the phases in the exit apertures; the amplitudes of the secondary sources are scaled by a factor of M. For symmetry and ease of calculation, the term is primarily a function of $\theta_0 x$ (the dashed wave front in Fig. 2.10), to which a phase offset is added (the length of the gray arrow in Fig. 2.10). Carrying out the integrations in Eq. 2.24 results in

$$A(\theta, d) = 2M\lambda \frac{\sin\left[D\pi(\theta - M\theta_0)/M\lambda\right]}{\pi(\theta - M\theta_0)} \cos\left[\pi(d + B_0\theta - B\theta_0)/\lambda\right] e^{id\pi/\lambda}. \tag{2.25}$$

The exponential factor for the delay d, outside of the cos-term, would only be of impor-

tance when this calculated field is combined with another one since all other factors are real. To calculate the intensity $I(\theta) = |A(\theta)|^2$, this exponential factor can be left out and the sinc-function can be used again, leading to

$$I(\theta, d) = 4D^2 \mathrm{sinc}^2 \left[D\pi(\theta - M\theta_0)/M\lambda \right] \cos^2 \left[\pi(d + B_0\theta - B\theta_0)/\lambda \right]. \tag{2.26}$$

If there is no internal delay ($d = 0$), the expression can be written as

$$I(\theta) = 4D^2 \mathrm{sinc}^2 \left[\frac{D\pi}{M\lambda}(\theta - M\theta_0) \right] \cos^2 \left[\frac{\pi B_0}{\lambda}(\theta - \frac{B}{B_0}\theta_0) \right]. \tag{2.27}$$

A number of features shows up nicely. The width of the envelope function is governed by the factor $\frac{D\pi}{M\lambda}$, which includes the primary diameter, the wavelength and the angular magnification, or beam compression M. The angular period of the fringes is $\frac{\lambda}{2B_0}$, implying that the exit baseline B_0 governs the fringe spacing for the observer, and is independent of the magnification M.

Equation (2.27) also shows whether the envelope-with-fringes function is field-variant or not. Both the sinc and cos-functions depend on θ. Their offset differs and is $M\theta_0$ for the sinc function and $\frac{B}{B_0}\theta_0$ for the cos function. Immediately, it is clear that when $B_0 = B/M$, these offsets are equal and hence the center of the envelope will coincide with the central fringe peak, for all values of the sky direction θ_0. Including the delay d again results in

$$I(\theta, d) = 4D^2 \mathrm{sinc}^2 \left[\frac{D\pi}{M\lambda}(\theta - M\theta_0) \right] \cos^2 \left[\frac{\pi B_0}{\lambda} \left(\theta - \left[\frac{B}{B_0}\theta_0 \right] + \frac{d}{B_0} \right) \right], \tag{2.28}$$

where for the modulation the angular period remains the same $[\lambda/(2B_0)]$ and only the offset changes. This general response function is the same expression as Eq. (2.26) and therefore the result for co-axial combination ($B_0 = 0$) is

$$I(\theta, d) = 4D^2 \mathrm{sinc}^2 \left[D\pi(\theta - M\theta_0)/M\lambda \right] \cos^2 \left[\pi(d - B\theta_0)/\lambda \right], \tag{2.29}$$

so that the cos-term is only a function of d (given a point-source direction θ_0) and that the period of the cos-modulation is not related to the magnification M.

With the general expression for $I(\theta, d)$ in Eq. (2.28), the intensity output of *any* two-element interferometer is obtained, for a single point source at θ_0 producing a uniform unity amplitude at entrance pupils of diameter D. With the assumption that both beams have an equal beam compression M, the correctly scaled envelope intensity pattern with fringes depending on either θ or d or both can be calculated.

Polychromatic response and imaging

For a polychromatic response, the expression for the intensity should be integrated over the spectral range, with a weighting factor according to the intensity spectrum of the source, for which in this case a function $L(\theta_0, \lambda)$ is taken. The detected signal then equals

$$I(\theta, d) = \int_{\theta_0} \int_{\lambda} L(\theta_0, \lambda) I(\theta, d, \theta_0, \lambda) \mathrm{d}\lambda \mathrm{d}\theta_0. \tag{2.30}$$

The superposition of the wavelength-dependent cosines will result in a fringe function with finite extent. However, the origins of the cosine functions are wavelength-independent. The envelope will not exactly be a sinc-function when summed over all wavelengths. All in all, the features of Eq. (2.28) that remain are the fact that the general polychromatic response is the product of an envelope and a fringe function with the shifted

origins $M\theta_0$ and $B\theta_0/B_0$, respectively. The envelope width can be approximated by

$$r_0 \sim \frac{D}{M\lambda_c}, \tag{2.31}$$

with λ_c the central wavelength. The angular period of the fringe function in the θ-direction remains

$$p_\theta(B_0) = \frac{\lambda_c}{2B_0}. \tag{2.32}$$

With these scaling factors, realistic field- and delay-dependent intensity response functions can be calculated for an interferometer with any magnification M and exit baseline length given by $0 \leq B_0 \leq B/M$ or even $B/M < B_0 < \infty$.

'Imaging' is recording in any way the weighted sum of point source responses of an object on the sky. Considering again the monochromatic expression of Eq. (2.26) for a very small source $L(\theta_0)$ of which all $\theta_0 \ll r_0$, then all the cosines in the weighted sum have an equal period p_θ, but different phases and amplitudes. Therefore, the varying part of the resulting intensity sum can be described with a cosine function of the same period, but with a different phase offset $\phi_{B,L}$ and modulation amplitude $C_{B,L}$:

$$\begin{aligned} I(\theta,d)_{B,L} &= \int_{\theta_0} L(\theta_0) I(\theta,d,\theta_0)_\lambda \mathrm{d}\theta_0 \\ &\simeq \mathrm{sinc}^2\left[\frac{D\pi}{M\lambda_c}(\theta - M\theta_0)\right]\left(1 + C_{B,L}\cos\left[\phi_{B,L}\right]\right). \end{aligned} \tag{2.33}$$

Conventional interferometric imaging is reduced to measuring sets of $C_{B,L}$ and $\phi_{B,L}$ for various baseline lengths B, in order to obtain information about the source L. This will be addressed in the next Section.

For wide-field observations ($\theta_0 > r_0$), the response cannot be treated as an envelope with cosine-like modulation on it, but the response over the full (θ,d)-area has to be measured to obtain information of the function $L(\theta_0)$. Observing the argument of the cosine in Eq. (2.28), it is clear that the baseline dependent response or rather the *fringe encoding* can be spatial (only a function of θ), 'temporal' (only a function of d) or a mixture of both. Interferometric imaging makes use of the fact that this collective response is a function of the entrance baseline B. Careful choice of B_0 and/or setting several d (or scanning continuously over d) ensure that the differences related to changing B are measurable and can be related to the luminosity distribution $L(\theta_0)$ on the sky.

In terms of 'sampling spatial frequencies', the monochromatic spatial frequency coverage of a source $L(\theta_0)$ arises from the full expression of the detected signal:

$$I(\theta,d)_L = \int_{\theta_0} 4D^2 L(\theta_0)\mathrm{sinc}^2\left[\frac{D\pi(\theta-\theta_0)}{M\lambda}\right]\cos^2\left[\pi/\lambda(d + B_0\theta - B\theta_0)\right]\mathrm{d}\theta_0. \tag{2.34}$$

The sinc^2 can better be written as a sin-function again. Then, both the $\sin^2$ and the $\cos^2$ terms can be written as cos-functions:

$$\begin{aligned} I(\theta,d)_L = &\int_{\theta_0} D^2 L(\theta_0)\frac{M^2\lambda^2}{D^2\pi^2(\theta-\theta_0)^2}\cdot \\ &\left\{1-\cos\left[\frac{2\pi D}{M\lambda}(\theta-\theta_0)\right]\right\}\left\{1+\cos\left[\frac{2\pi}{\lambda}(d+B_0\theta-B\theta_0)\right]\right\}\mathrm{d}\theta_0. \end{aligned} \tag{2.35}$$

Further factorization yields

$$I(\theta,d)_L = \int_{\theta_0} L(\theta_0)\frac{M^2\lambda^2}{\pi^2(\theta-\theta_0)^2} \left\{1-\cos\left[\frac{2\pi D}{M\lambda}(\theta-\theta_0)\right]+\cos\left[\frac{2\pi}{\lambda}(d+B_0\theta-B\theta_0)\right]- \cos\left[\frac{2\pi D}{M\lambda}(\theta-\theta_0)\right]\cos\left[\frac{2\pi}{\lambda}(d+B_0\theta-B\theta_0)\right]\right\}\mathrm{d}\theta_0. \tag{2.36}$$

This resembles a Fourier frequency analysis. The observed intensity pattern $I(\theta,d)_L$ resulting from a source $L(\theta_0)$ will provide information for certain spatial frequencies governed by D and B_0 in the direction of θ, provided by the first two cosine factors.

Should the exit baseline not exist ($B_0 = 0$), and the collecting apertures be pinholes ($D = 0$), the integral reduces to

$$I(\theta,d)_L = I(d)_L = \int_{\theta_0} L(\theta_0)\left\{\frac{1}{2}+\frac{1}{2}\cos\left[2\pi/\lambda(d-B\theta_0)\right]\right\}\mathrm{d}\theta_0. \tag{2.37}$$

The resulting signal, depending on baseline length B and source L, is a function of only d and will have a period $p_d = \lambda$, and represents the spatial frequency content of the source according to the harmonics of the cos-expression, since the trigonometric relation

$$\cos(a-b) = \cos(a)\cos(b)+\sin(a)\sin(b), \tag{2.38}$$

turns the integral

$$I(d)_L = \int_{\theta_0}\frac{1}{2}L(\theta_0)\left\{1+\cos\left[2\pi/\lambda(d-B\theta_0)\right]\right\}\mathrm{d}\theta_0 \tag{2.39}$$

into the signal

$$I(d)_L = \int_{\theta_0}\frac{1}{2}L(\theta_0)\cdot \left\{1+\cos\left(\frac{2\pi d}{\lambda}\right)\cos\left(\frac{2\pi B}{\lambda}\theta_0\right)+\sin\left(\frac{2\pi d}{\lambda}\right)\sin\left(\frac{2\pi B}{\lambda}\theta_0\right)\right\}\mathrm{d}\theta_0. \tag{2.40}$$

This expression resembles the Zernike–Van Cittert theorem that relates the unresolved source to the observable baseline-dependent fringe contrast, since in the measurement domain d, on top of a carrier frequency d/λ (see first cos factor and first sin factor), the value of the inner product of the source $L(\theta_0)$ with a harmonic function in θ_0 of angular spatial frequency B/λ can be measured, what comes down to measuring a single Fourier component of the spatial frequency spectrum of the source. The classical derivation of the Zernike–Van Cittert theorem is given in Section 2.3.2. With the general interferometer response of Eq. (2.36) however, in which $D \neq 0$, the more general relationship between source and detection is given for the case of finite telescopes ($D > 0$) and a wide-field or partially resolved source $L(\theta_0)$, imaged with an arbitrary exit baseline B_0. For this general case, a derivation of an expression for the sampled spatial frequencies governed by λ, D, B_0 and B, would be required, but this is not relevant at this point. The derivation of an expression for the sampled spatial frequencies (Eq. 2.40) for the co-axial case served one purpose. It shows the equivalence of the approach of deriving first a point-source intensity function and using that, an extended source intensity response, to the approach of partial coherence theory and the Zernike–Van Cittert theorem, to be explained in the next Section.

2.3.2 Relation to complex visibilities

In this section, the classical derivation of the response of an interferometer will be presented. Starting with the theory of partial coherence and the Zernike–Van Cittert theorem, the measurable signal relating to the image of the sky will be derived. Special attention is given to the desired field extension, the size of the apertures and the finite coherence length. All these factors define a huge difference between optical aperture synthesis and synthesis at radio wavelengths. Treatment of the classical theorem will show the need for a different approach. With the approach given in the previous Section, the response can even be predicted when non-standard optical elements—such as a discontinuous staircase mirror—are inserted in the optical train.

The quasi-monochromatic theory of partial coherence is used to describe the phenomenon that in stellar interferometry, the measurable interference fringes have a baseline dependent contrast. However, for wide-field interferometry it shows two shortcomings that will be detailed here. Basically, the theory assumes point-like collectors (resulting in an infinitely extended focus) and (quasi-) monochromatic radiation (resulting in an infinite coherence length). Both these assumptions are in order for radio interferometry (where a PSF is much larger than a detector and where correlation of the signals can be done at very narrow passbands) and even for very narrow angle optical interferometry (where the stellar object is highly unresolved by a single telescope). For broadband, wide-field interferometric imaging, this will result in a non-accurate prediction of the observables.

The assumption of quasi-monochromaticity results in a simplification of expressions that is not allowed for sources spanning more than a single-dish-PSF on the sky. The theory assumes that the source is sufficiently not point-like, but indeed highly unresolved, meaning that it is extended, but smaller than the diffraction limited spot size of a single telescope. It will be shown how the response of a very extended source (of a size equal to multiple single-dish-PSFs) will deviate from the quasi-monochromatic response, disqualifying the quasi-monochromatic theory to predict the interferometer response for a very extended object.

The quasi-monochromatic theory of partial coherence essentially treats the collectors or telescopes as pinholes, apertures with a diameter in the order of a few wavelengths. A true telescope has a certain extent (millions of wavelengths) which will result in a very localized presence of radiation in focus. It is clear that when the directions on the sky where the radiation comes from have a larger angular range than the angular size of the PSF in focus, one cannot treat the stellar object as a whole to predict the fringe contrast in one single detection point. The extension to wide-field objects is again not compatible with the theory. If the single detector (for which the fringe contrast should be predicted) is sized such that several PSFs next to each other can be integrated into one intensity signal, the measured fringe contrast does not relate to the whole source, since the radiation was mainly added incoherently.

Theory of partial coherence

Partial coherence relates to the correlation of electrical field vibrations at two arbitrary points in the wave field produced by a source with either a finite spectral range, a finite size, or both (Born and Wolf, 1980). Although initially developed to be able to account for light source-induced effects in microscopy, the theory also describes observable phenomena in stellar interferometers. The text in this section is based on (Beran and Par-

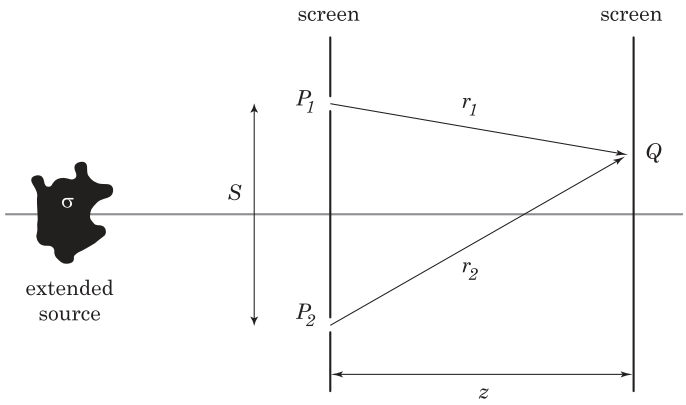

Figure 2.11: Scheme of Young's interferometer. An opaque screen with two small pinholes P_1 and P_2 separated by a distance S is placed in front of a radiating source σ. The secondary wavefronts generated at the pinholes interfere. The resulting intensity pattern can be observed at a plane, situated at an axial distance z from the pinholes.

rent, 1974) and (Montilla, 2004) with some additions.

A suitable measure for this correlation is suggested by a two-beam interference experiment, analogue to Young's interferometer (Fig. 2.11). An extended polychromatic source σ, produces an electro-magnetic wave field represented by the analytic signal $\Psi(P,t)$ which is a function of position P and time t and which neglects polarization so that it is a scalar quantity. The observable intensity or power $I(P)$ is proportional to the mean value of $\Psi(P,t)\Psi^*(P,t)$, where $()^*$ denotes the complex conjugate. Two points in the wave field are considered, P_1 and P_2. In order to study the interference effects arising from the superposition of the electrical fields from these points, a screen with pinholes at positions P_1 and P_2 is placed across the field. The complex disturbance produced at a point Q on a second screen, with an axial distance z is

$$\Psi(Q,t) = K_1\Psi(P_1, t-t_1) + K_2\Psi(P_2, t-t_2), \tag{2.41}$$

where t_1 and t_2 respectively are the times needed for the light to travel from P_1 and P_2 to Q and K_1 and K_2 are complex constants,[2] inversely proportional to the distance z. The observed power at the second screen is now

$$I(Q,t) = \langle \Psi(Q,t)\Psi^*(Q,t)\rangle. \tag{2.42}$$

Assuming that the radiation from the source is stationary,[3] the superposition can be written as

$$I(Q) = \|K_1\|^2 I_1 + \|K_2\|^2 I_2 + 2\mathrm{Re}\left\{\mathrm{K_1K_2^*}\langle\Psi(\mathrm{P_1,t-t_1})\Psi^*(\mathrm{P_2,t-t_2})\rangle\right\}, \tag{2.43}$$

where I_1 and I_2 are the powers associated to the radiation generated at the secondary sources P_1 and P_2, respectively. The averaged term is

$$\langle \Psi(P_1,t-t_1)\Psi^*(P_2,t-t_2)\rangle = \lim_{T\to\infty}\frac{1}{T}\int_{-T/2}^{T/2}\Psi(P_1,t-t_1)\Psi^*(P_2,t-t_2)\mathrm{d}t. \tag{2.44}$$

[2] In a more elaborate version of the theory, these constants K_1 and K_2 develop into integral expressions when the finite size of the collectors and their optical transmission factor are taken into account (Born and Wolf, 1980).

[3] The stationarity assumption implies that in an ensemble of functions, the averages are independent of the origin of time.

By changing variables according to $t' = t - t_2$ and introducing the time delay $\tau = t_2 - t_1$, Eq. (2.44) can be written as

$$\langle \Psi(P_1, t - t_1)\Psi^*(P_2, t - t_2)\rangle = \lim_{T\to\infty} \frac{1}{T}\int_{-T/2+t_2}^{T/2+t_2} \Psi(P_1, t' + \tau)\Psi^*(P_2, t')\mathrm{d}t'. \tag{2.45}$$

Equation (2.45) is called the *mutual coherence function* and represents a temporal complex cross-correlation between the functions $\Psi(P_1, t - t_1)$ and $\Psi(P_2, t - t_2)$ during the time interval T. The mutual coherence depends on the time delay τ and on the separation S of P_1 and P_2. Therefore, it is defined as

$$\Gamma_{12}(\tau) = \Gamma(S, \tau) = \langle \Psi(P_1, t - t_1)\Psi^*(P_2, t - t_2)\rangle. \tag{2.46}$$

Equation (2.43) can be rewritten in terms of $\Gamma_{12}(\tau)$ so that

$$I(Q) = \|K_1\|^2 I_1 + \|K_2\|^2 I_2 + 2\mathrm{Re}\left\{\mathrm{K_1 K_2^* \Gamma_{12}(\tau)}\right\}. \tag{2.47}$$

To drop the complex factors K_1 and K_2, the expression can be normalized by observing the result of placing the two pinholes at either P_1 or P_2. When $P_2 = P_1$ and hence $t_2 = t_1$, there results

$$\langle \Psi(P_1, t - t_1)\Psi^*(P_1, t - t_1)\rangle = \Gamma(S = 0, \tau = 0) = \Gamma_{11}(0), \tag{2.48}$$

which is the detected optical power associated with secondary source P_1. Likewise, $\Gamma_{22}(0)$ is associated to source P_2. Using these definitions, there arise

$$\begin{aligned} I^{(1)}(Q) &= \|K_1|^2 I_1 = \|K_1|^2 \Gamma_{11}(0) \text{ and} \\ I^{(2)}(Q) &= \|K_2|^2 I_2 = \|K_2|^2 \Gamma_{22}(0). \end{aligned} \tag{2.49}$$

After introduction of

$$\gamma_{12}(\tau) = \frac{\Gamma_{12}(\tau)}{\sqrt{\Gamma_{11}(0)\Gamma_{22}(0)}}, \tag{2.50}$$

Eq. (2.47) can now be normalized to

$$I(Q) = I^{(1)}(Q) + I^{(2)}(Q) + 2\sqrt{I^{(1)}(Q)I^{(2)}(Q)}\mathrm{Re}[\gamma_{12}(\tau)]. \tag{2.51}$$

The function $\gamma_{12}(\tau)$ is denominated the first-order *complex degree of coherence* and is characterized by the following properties:

- The function has a maximum value at the origin for $\tau = 0$
- As a consequence of the Cauchy–Schwartz inequality[4], the value of the function $\gamma_{12}(\tau)$ is $0 \le \|\gamma_{12}(\tau)\| \le 1$
- The function is a complex analytic signal
- The modulus of the complex degree of coherence is proportional to the fringe contrast of the interference fringes.

[4]The modulus of the inner product of two vectors is smaller than or equal to the product of the norms of these vectors.

The last item makes that measuring the fringe contrast while knowing the position of and the power at the pinholes, one can obtain information about the quality of the illumination source of the interference system (for the case of microscopy) or about the spatial structure of the 'illumination source', being a stellar object in the case of stellar interferometry.

In the context of partial coherence, three regimes are defined for operation of the interference system as a function of $\|\gamma_{12}(\tau)\|$. If $\|\gamma_{12}(\tau)\| = 1$, the system is operating in the *coherent limit* and the electric field vibrations at P_1 and P_2 are said to be coherent. This means that the source is sufficiently point-like and the light nearly monochromatic. If $\|\gamma_{12}(\tau)\| = 0$, the system operates at the *incoherent limit* and the superposition of the beams does not give rise to any interference effect. If $0 \leq \|\gamma_{12}(\tau)\| \leq 0$, the vibrations are partially coherent and the source is observed with *partial degree of coherence*. In general, this last condition applies to a natural source, since exact point-sources and natural monochromatic sources do not exist.

The observable fringe contrast for a wide-field source, measured with a certain bandwidth, will be lower than predicted by the quasi-monochromatic theory of partial coherence[5]. This is important when for example the flight paths of telescopes of a space based array are optimized for a certain target. Since for extended sources, in general, the fringe contrast drops with the baseline length, the maximum baseline length at which fringes can be measured at all may be shorter than expected. This effect limits the maximum resolution.

To extend the theory for the case of large telescopes and possibly a staircase mirror in the optical train, the complex functions K_1 and K_2 should be extended to incorporate the location-dependent field strength according to the Airy function. Moreover, instead of pinholes, large apertures and focusing behavior should be included, so that resolving the source partially (since it sizes a few PSFs) is accounted for in the detection of $I(Q)$. Compensation of external OPD by a staircase mirror should then be found back in a sawtooth-like behavior of the parameter τ, relating to the position Q.

Instead of extending the general theory of partial coherence to polychromatic wide-field stellar interferometry, another point of view was chosen to predict the response of an optical interferometer, as described in Sec. 2.3.1. The following section however, continues the quasi-monochromatic theory, and relates the measureable fringe visibility to the morphology of the stellar source. This will lead to a measurement–source relationship that is similar to the one derived by the approach of Sec. 2.3.1, which is easily extended to polychromatic wide-field observations, as opposed to the relationship based on partial coherence, that would require elaborate extensions to the theory presented in the current section.

Source and visibility

When the light emitted by a source σ is quasi-monochromatic with a mean frequency ν_0, it has a spectral range $\delta\nu \ll \nu_0$. The complex coherence is now

$$\gamma_{12}(\tau) = \|\gamma_{12}(\tau)\| \exp\left[i\left(\alpha_{12}(\tau) - 2\pi\nu_0\tau\right)\right], \tag{2.52}$$

where

$$\alpha_{12}(\tau) = 2\pi\nu_0\tau + \arg\left[\gamma_{12}(\tau)\right], \tag{2.53}$$

[5]The mutual intensity theory for a temporally incoherent source exists, see (Born and Wolf, 1980), pp. 606–610.

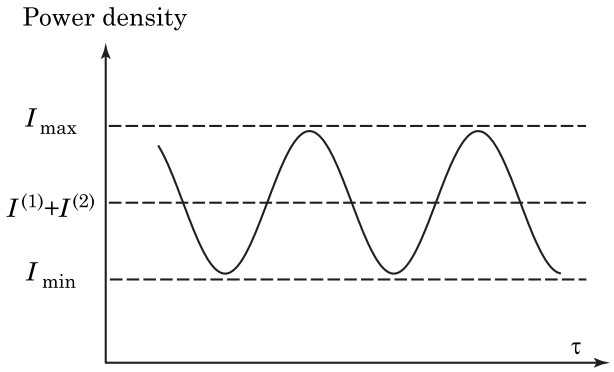

Figure 2.12: Power distribution of the interference pattern of two quasi-monochromatic beams of power $I^{(1)}$ and $I^{(2)}$ in partially coherent superposition.

and Eq. (2.51) becomes

$$I(Q) = I^{(1)}(Q) + I^{(2)}(Q) + 2\sqrt{I^{(1)}(Q)I^{(2)}(Q)}\|\gamma_{12}(\tau)\|\cos\left(\alpha_{12}(\tau) - 2\pi\nu_0\tau\right). \tag{2.54}$$

The quasi-monochromatic condition states that $\|\gamma_{12}(\tau)\|$ is nearly constant (amplitude of fringe envelope) and $\alpha_{12}(\tau)$ varies slowly with τ compared to $\cos 2\pi\nu_0\tau$. If the openings at P_1 and P_2 are sufficiently small, the intensity distribution at the vicinity of Q will consist of an almost uniform background (no intensity envelope due to diffraction by a finite aperture) $I^{(1)}(Q) + I^{(2)}(Q)$ with a superimposed sinusoidal intensity distribution, as shown in Fig. 2.12. From this fringe pattern, the primary observable for this type of interferometer can be deduced. The fringe contrast is defined as

$$\mathcal{V}(Q) = \frac{I_{max} - I_{min}}{I_{max} + I_{min}}, \tag{2.55}$$

where I_{max} and I_{min} are the intensity maximum and minimum near Q. Using expression 2.54, the fringe contrast $\mathcal{V}(Q)$ can be related to the degree of coherence of the interfering light beams by

$$\mathcal{V}(Q) = \frac{2\sqrt{I^{(1)}(Q)I^{(2)}(Q)}}{I^{(1)}(Q) + I^{(2)}(Q)}\|\gamma_{12}(\tau)\|. \tag{2.56}$$

For the special case that both openings transmit an equal power and $I^{(1)}(Q) = I^{(2)}(Q)$, the contrast $\mathcal{V}(Q) = \|\gamma_{12}(\tau)\|$ is equal to the degree of coherence of the source, with secondary sources at P_1 and P_2. Although this expression provides a contrast as a function of the location Q, it should be noted that this contrast is not a function of the size and shape of the collectors. If the path length differences between the light paths (for vacuum) $c\|\tau\|$ are small compared to the coherence length $l_{coh} = c/\delta\nu$ of the light, so that the fringe pattern shows no envelope, the function $\|\gamma_{12}(\tau)\|$ is hardly different from $\|\gamma_{12}(0)\|$. The *complex coherence factor* μ_{12} is now defined as $\mu_{12} = \gamma_{12}(0)$ and the interference expression (2.54) can be written as

$$I(Q) = 2I^{(1,2)}(Q) + 2I^{(1,2)}(Q)\|\mu_{12}\|\cos\left[\arg(\mu_{12})\right]. \tag{2.57}$$

Equation (2.57) represents the basic formula of the quasi-monochromatic theory of partial coherence. The complex coherence factor μ_{12} is usually called the *complex visibility*. Although complex, it can be measured from recorded intensities by varying τ. Given

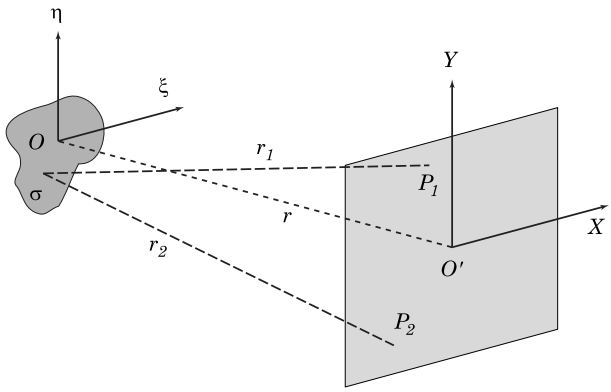

Figure 2.13: Illustration accompanying the derivation of the Zernike–Van Cittert theorem.

the positions of the secondary point sources, the complex visibility holds information about the light source. But this is only valid when the assumptions of quasi-chromaticity and point-like collectors or pinholes are satisfied.

The Zernike–Van Cittert theorem relates the complex visibility function to the source. To determine the complex coherence factor for two points P_1 and P_2 on a screen illuminated by an extended but unresolved quasi-monochromatic source σ (see Fig. 2.13), the source is divided into small elements $d\sigma_i$ centered at C_i. These elementary sources are mutually incoherent and of small dimensions compared to the mean wavelength λ_0. The complex electrical field due to element $d\sigma_i$ at a point P_m in the screen is

$$\Psi_{mi}(t) = A_i\left(t - \frac{r_{mi}}{c}\right)\frac{\exp\left[-2\pi j\nu_0(t-\frac{r_{mi}}{c})\right]}{r_{mi}}, \tag{2.58}$$

where the strength and phase of the radiation coming from element $d\sigma_i$ are respectively characterized by $\|A_i\|$ and $\arg(A_i)$, and r_{mi} is the distance from the element $d\sigma_i$ to the point P_m.

No extended astronomical source is known that is spatially coherent (Anantharamaiah *et al.*, 1994) and the case of scintillation is not considered, so the elements are mutually incoherent. The distance $r_{i2} - r_{i1}$ is small compared to l_{coh}. The mutual coherence function of P_1 and P_2 is then

$$\Gamma_{12}(\tau = 0) = \sum_i \langle A_i^*(t)A_i(t)\rangle \frac{\exp\left[2\pi j\nu_0(r_{1i} - r_{2i})/c\right]}{r_{1i}r_{2i}}. \tag{2.59}$$

Considering a source with a total number of elements so large that it can be regarded to be continuous, the sum can be replaced by the integral

$$\Gamma_{12}(\tau = 0) = \int_\sigma I(C)\frac{\exp\left[j\kappa_0(r_1 - r_2)\right]}{r_1 r_2}\mathrm{d}C, \tag{2.60}$$

where $\kappa_0 = 2\pi\nu_0/c$ and $\mathrm{d}C$ is a surface element on the planar source. The complex coherence factor is therefore

$$\mu_{12} = \frac{1}{\sqrt{I(P_1)I(P_2)}}\int_\sigma I(C)\frac{\exp\left[j\kappa_0(r_1 - r_2)\right]}{r_1 r_2}\mathrm{d}C, \tag{2.61}$$

where the power $I(P_m)$ again is the total transmitted power by the pinhole as secondary source and is defined as

$$I(P_m) = \Gamma_{mm}(0) = \int_\sigma \frac{I(C)}{r_m^2} \mathrm{d}C. \tag{2.62}$$

This result is known as the *Zernike–Van Cittert theorem* (Van Cittert, 1934; Zernike, 1938).

Assuming that the linear dimensions of the source and the distance between P_1 and P_2 are small compared to the distance of the pinholes to the source, the relative distance $r_1 - r_2$ can be approximated as

$$r_1 - r_2 \simeq \frac{(X_1^2 + Y_1^2) - (X_2^2 + Y_2^2)}{2r} - \frac{(X_1 - X_2)\xi + (Y_1 - Y_2)\eta}{r}. \tag{2.63}$$

With the definitions

$$\frac{X_1 - X_2}{r} = p, \quad \frac{Y_1 - Y_2}{r} = q \quad \text{and} \tag{2.64}$$

$$\phi = \frac{\kappa_0 \left[(X_1^2 + Y_1^2) - (X_2^2 + Y_2^2)\right]}{2r}, \tag{2.65}$$

expression (2.61) can be rewritten as

$$\mu_{12} = \frac{\exp(j\phi) \int\int_\sigma I(\xi,\eta) \exp\left[-j\kappa_0(p\xi + q\eta)\right] \mathrm{d}\xi \mathrm{d}\eta}{\int\int_\sigma I(\xi,\eta) d\xi d\eta}. \tag{2.66}$$

This equation shows that the degree of coherence is equal to the normalized Fourier transform of the intensity function of the source. This form of the Zernike-Van Cittert theorem is widely used in stellar interferometry, since the stellar sources are supposed to be at very large distances compared to the telescopes and the size of the source itself. Moreover, the source is supposed to be two dimensional. The limit of applicability of the two dimensional Fourier transform is studied in (Perley, 1994), to arrive at a Field-of-View within which the Fourier relationship holds.

Equivalence of approaches

The Fourier relationship is equivalent to the relationship described in Eq. (2.36), derived by regarding the intensity response of point sources and considering a stellar object to be a collection of such point sources at slightly varying angles. As described in the literature (Young and Hale, 1995), the approach of summing intensity responses provides physical insight into imaging in the partially coherent regime. With the provided analytical expression for the focal field, the evaluation of the imaging process—to construct the response of the extended stellar source—can be performed quickly. Moreover, it does not need adaptation to be applicable to wide-field imaging. In addition, an optical interferometric transfer matrix can be constructed, of which certain properties are readily comparable among different interferometric beam combination schemes. The construction of this transfer matrix is detailed in the next section, that also relates this matrix to other well-known imaging and reconstruction processes.

2.3.3 Inverse problems in imaging science

Image deblurring and image reconstruction (or tomography) are both well-studied inverse problems. The inverse problem of deblurring has been treated in the domain of

optical astronomy, even with space-variant convolution kernels, as in the case where images from the Hubble Space Telescope were improved (Nagy and O'Leary, 1998) or for image reconstruction with a homothetic array by joint deconvolution of multiple snapshots (Bertero and Boccacci, 2000). The tomography approach (image construction from other data rather than a degraded version of that image) is most resembled by radio imaging techniques (Cornwell, 1994) where fringe visibilities are related to the source brightness function. When only treating complex visibilities, the limited extent of the *convolution kernel* (both in finite coherence length as well as limited spatial extent of the PSF) is not taken into account in the way that wide-field optical interferometry requires. Therefore, a space-variant, multi-dimensional convolution kernel should be implemented in the convolution model for interferometric imaging.

A paper on algorithms for image reconstruction with the Large Binocular Telescope (LBT) (Bertero and Boccacci, 2000) compares some linear and iterative algorithms to each other. Maximum Entropy and CLEAN are two very popular, but intentionally omitted algorithms in that paper. It is stated that both algorithms perform better in the case of point-like objects or scenes that are mainly black except for a few pixels. For the examples given in that paper and in this thesis of recovering a wide-field extended source with unknown distribution or discontinuities, the most simple linear inverse method was chosen. It is known that iterative or non-linear approaches will perform better in retrieving sharp edges of the object (Geman and Yong, 1995) but the non-linear approaches are not as easily implemented as linear methods. The goal in this thesis is to simply demonstrate the inversion of the wide-field fringe data, for various interferometric beam combination schemes.

In the following sections, the described fringe responses at all pixels for various baseline lengths are taken as 'measured' data to be put into a linear system of equations that is inverted by applying Tikhonov regularization, a very popular method for inverting linear systems of equations. Chapter 4 will clarify this regularization process. The following sections describe the construction of the linear system of equations. For illustration, only two interferometric beam combination configurations are described in detail. These are co-axial Michelson interferometry ($B_0 = 0$) and Homothesis ($B_0 = B$). The first description illustrates the reduction of the interferometric imaging process based on point-source intensity responses to a matrix-vector multiplication. The latter description then shows how this approach resembles in notation the well-known image blurring problem.

Response and inverse problem—Michelson

The luminosity distribution on the sky (the stellar object) $L(\theta_0)$ is a positive one-dimensional function of the angular coordinate θ_0. On the one-dimensional detector in-focus, with coordinate θ, this will produce a recordable intensity $I(\theta, d)$ that will change with the applied path length difference d. In discretized form,

$$I(\theta, d) = \sum_i L_i(\theta_0) R_i(\theta, d)_{\theta_0}, \tag{2.67}$$

where $R_i(\theta, d)_{\theta_0}$ is a baseline dependent point source *response function*, measured in intensity and scaled by the source L. The index i is a running integer corresponding to all possible point source locations, in this case one per evenly spaced synthetic resolution element. Essentially, R is the product of an envelope function or diffraction pattern (PSF) in direction θ, with a normalized fringe intensity pattern in direction d. This allows to

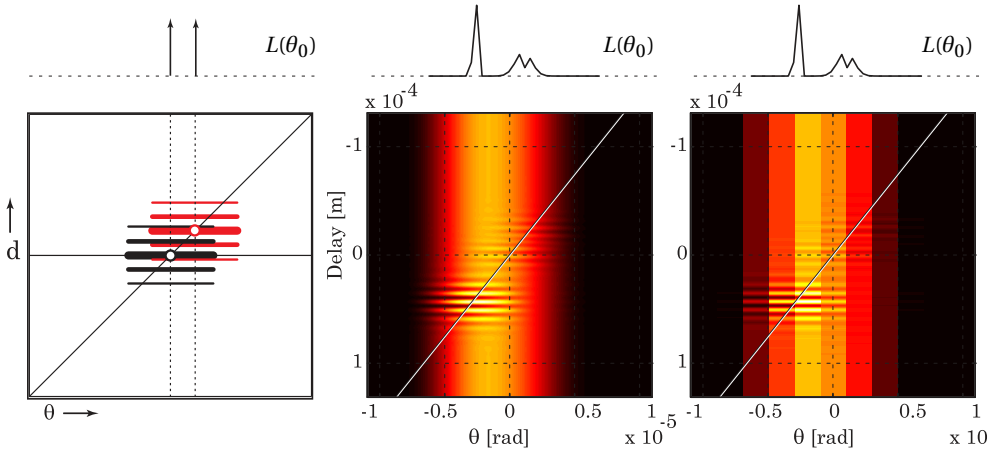

(a) Two schematic $R(\theta, d; B_k)$ (b) weighted sum $I(\theta, d; B_k)$ (c) pixelized $I_{jk}(d)$

Figure 2.14: The co-axial detection space, illustrated for two point sources (a) and an extended source (b,c). (a) Diagram of the co-axial (θ, d) detection space, for two point sources. Intensity patterns from the two point sources on the sky are summed. Per response function, the cross-section in direction θ is a sinc-function. In the other direction d, the cross-section is the polychromatic fringe pattern. The diagonal indicates the centroid locations of the response functions at $(\theta, d) = (theta_0, d_0)$ where $d_0 = B_k\theta_0$. The total—*baseline dependent*—response will be a sum of these response functions, as depicted for an extended object in (b). The steepness of the diagonal is a function of baseline length and therefore the fringe contrast (as in narrow field interferometry) of the sum $I(\theta, d; B_k)$ is baseline dependent. In (c) the pixelized example $I_{jk}(d)$ of the same extended scene is shown.

write a polychromatic $R(\theta, d)_{\theta_0}$ according to

$$R(\theta, d; B_k; \theta_0) = L(\theta_0) \int_{\lambda_{\min}}^{\lambda_{\max}} w(\lambda) 4D^2 \mathrm{sinc}^2 \left[D\pi(\theta - \theta_0)/\lambda\right] \cos^2 \left[\pi(d - d_0)/\lambda\right] \mathrm{d}\lambda, \quad (2.68)$$

where $d_0 = B_k \sin(\theta_0) \approx B_k \cdot \theta_0$ for small angles and λ indicates the wavelength. The various baseline lengths are indicated by B_k. Of the polychromatic function, the cross-section is a sinc-like function and the integrated interference term (wavelength dependent weighting with $w(\lambda)$[6]) can be implemented as a lookup-function in a polychromatic fringe packet, instead of the mentioned cos-function. The summation of point sources or integration over the sky (Eq. 2.67) is depicted for two point sources in Fig. 2.14a and for a continuous source in 2.14b,c.

The response on the detector is not measured continuously, but integrated on a few pixels with index $j = 1, 2, \ldots J$. Moreover, the summation in Eq. (2.67) is performed for every baseline setting with index $k = 1, 2, \ldots K$. As a result, the recorded intensities can be denoted as

$$I_{jk}(d) = \int_{\theta_j - \frac{1}{2}\beta}^{\theta_j + \frac{1}{2}\beta} I(\theta, d; B_k) \mathrm{d}\theta, \quad (2.69)$$

where β is the angular width on the sky of one pixel. The number of pixels J on the detector and the angular dimension β are chosen such that the detector is as large as the

[6]The relative weights $w(\lambda)$ can be chosen to be a Gaussian bandpass shape spanning the specified operation wavelengths.

Field-of-View and that a pixel is half the size of the angular PSF, related to dish diameter D. The choice of the baseline lengths B_k relates to the desirable angular resolution and will be specified at the imaging simulations.

The forward process described here can be seen as a multi-dimensional convolution (Eq. 2.68) and an integration (Eq. 2.69). Convolution and integration are two processes that cause the inversion process—finding the luminosity function $L(\theta_0)$ from recorded $I_{jk}(d)$—to be ill-posed. The solution of this inverse problem can only be estimated. If the forward problem is denoted with operator g as

$$I_{jk}(d) = g\left[L(\theta_0); B_k, \theta_j\right], \tag{2.70}$$

then the inverse problem is found by g^{-1} in

$$L(\theta_0) = g^{-1}\left[I_{jk}(d)\right], \tag{2.71}$$

so that the sky distribution $L(\theta_0)$ can be calculated from the measured $I_{jk}(d)$ given the parameters B_k and θ_j, the lengths of the baselines at which the data were taken and the central locations of the pixels.

In discrete form, this inverse problem is ill-conditioned since the response functions $R(\theta, d; B_k; \theta_0^{(i)})$ and $R(\theta, d; B_k; \theta_0^{(i\pm1)})$ of neighboring point sources within the object $L(\theta_0)$ on the sky differ only slightly in both directions θ and d. To estimate possible solutions $\hat{L}(\theta_0)$, routines by Hansen (Hansen, 1992) for Tikhonov regularization (Tikhonov and Goncharsky, 1977) are applied, based on Singular Value Decomposition (SVD). To do so, the problem has to be written in the form

$$\begin{aligned} \mathbf{A}\cdot\mathbf{x} &= \mathbf{b} \\ \mathbf{x} &= \mathbf{A}_{\mathrm{reg}}^{-1}\cdot\mathbf{b}, \end{aligned} \tag{2.72}$$

obtained by discretizing the 'source grid' and 'detection grid' as

$$\begin{aligned} \boldsymbol{\theta}_0 &= (\theta_0^{(1)}, \theta_0^{(2)}, \ldots, \theta_0^{(n)}), \\ \mathbf{d} = (d_1, d_2, \ldots, d_p) \text{ and } \boldsymbol{\theta} &= (\theta_1, \theta_2, \ldots, \theta_j), \end{aligned} \tag{2.73}$$

for every baseline length B_k. Then, column vector $\mathbf{x} \simeq L(\boldsymbol{\theta}_0)$ of length n is the sought function. The data are stored in column vector $\mathbf{b} \simeq \left[\ldots; I_{jk}(\mathbf{d}); \ldots\right]$ of length $m = p \cdot j \cdot k$, so that all data (for all pixels as well as for all baselines) are represented by one *measurement-vector*. This means that operator $\mathbf{A}$ performs the addition of response functions (the convolution), weighted by $L(\theta_0)$ and the integration over the pixels. The forward problem of obtaining a multi-baseline intensity measurement in (θ, d)-space is reduced to a matrix-vector multiplication.

Response and inverse problem—Homothesis

For the case of Homothesis, where $B_0 = B$ if $M = 1$, the imaging process is mathematically a straightforward convolution. For every baseline length, there is one space-invariant convolution kernel that is only a function of θ, not of d. With the delay $d = 0$, all point sources on the sky will produce a fringed intensity pattern on the detector. Complicated optics make this possible. The response functions (compare with Eq. 2.68) can now be expressed as

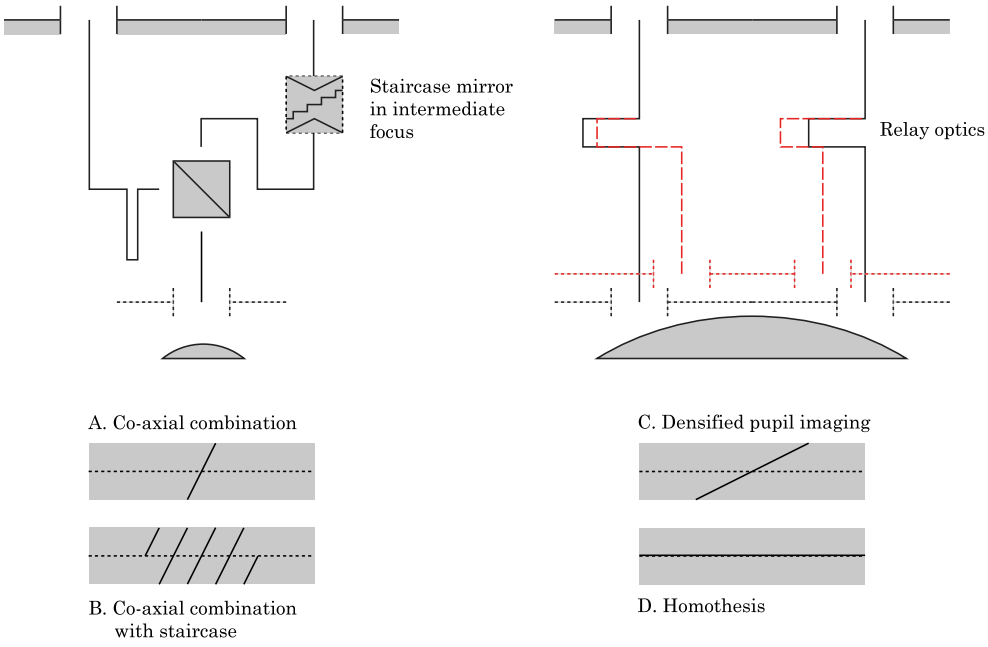

Figure 2.15: The four possible beam combination schemes, co-axial Michelson ($B_0 = 0$), Homothesis ($B_0 = B$), Densified ($0 \leq B_0 \leq B$) and Staircase, a modified co-axial scheme (to be explained). For clarity, there is no beam compression, so $M = 1$. The diagrams A,B,C and D indicate the intrinsic width of the Field-of-View for these schemes. For the co-axial schemes, the diagram is a plot of $(d - d_0)$ versus θ_0, limited to a delay scan range $d_{\min}$ to $d_{\max}$ over which fringe information is collected. For the other two schemes (image plane combination methods), the diagram indicates $(\theta - \frac{B}{B_0}\theta_0)$ versus θ_0, indicating the 'drift' of a polychromatic fringe packet off the diffraction envelope for off-axis angles.

$$R(\theta; B_k; \theta_0) = L(\theta_0) \int_{\lambda_{\min}}^{\lambda_{\max}} w(\lambda) 4D^2 \operatorname{sinc}^2 [D\pi(\theta - \theta_0)/\lambda] \cos^2 [\pi B_k(\theta - \theta_0)/\lambda] \, \mathrm{d}\lambda. \quad (2.74)$$

This function is only dependent on θ_0, the point-source location. Again, the response on the detector is not measured continuously, but integrated on a large number of pixels. Since this number is large, the continuous coordinate θ remains in use but is denoted as $\hat{\theta}$:

$$I_k(\hat{\theta}) = \int_{\theta_j - \frac{1}{2}\beta}^{\theta_j + \frac{1}{2}\beta} I_k(\theta) \mathrm{d}\theta, \quad (2.75)$$

where β is the angular width on the sky of one pixel and k is the index indicating the observation at baseline length B_k.

Four imaging methods

The remainder of this thesis shall deal with the intensity response of four types of interferometric imagers (see Fig. 2.15), of which the detector responses to a polychromatic wide-field source are calculated as a summation of elementary point-source response

functions. The calculation of the detector signals $I_{jk}(d)$ and $I_k(\hat{\theta})$ for respectively the Michelson and the Homothetis case is a straightforward summation of all response functions, weighted by the sky luminosity function $L(\theta_0)$ (Eq. 2.67). The same can be stated for the cases Densified (where $B_0 < B$ if $M = 1$) and Staircase. However, these two have small complications, compared to the given two problem formulations for co-axial and homothetic imaging. In the Densified case, the measured intensities are neither a function of only d, as in the Michelson signals $I_{jk}(d)$ per pixel, nor of only (the discretized) $\hat{\theta}$, as in the Homothesis signals $I_k(\hat{\theta})$. This image plane method has fringe encoding in both d and θ directions, and hence the measured signals per baseline configuration will be denoted as $I_k(\hat{\theta}, d)$. In the end, this only results in a different ordering of vectors in the measurement vector $\mathbf{b}$. Also the Staircase situation will finally result in the imaging operation $\mathbf{A} \cdot \mathbf{x} = \mathbf{b}$. However, in this case the measurement signals are discontinuous. A description of the complete Staircase imaging approach in Chapter 3 will clarify this.

Chapter 3

Interferometer arrays for imaging

In this chapter, examples of four possible interferometers or rather their beam combiners are discussed. In the class 'image plane combination' there are Homothesis and Densified Pupil Imaging. The class of co-axial interferometers consists of the Michelson interferometer and the Staircase imaging method. The latter is the same co-axial interferometer as the first one, but with a staircase-shaped mirror in the intermediate focal planes. For each interferometer, the specific hardware issues will be discussed and the methods to derive images from observations are presented. At the end of the chapter, an analysis is presented, to be able to quantitatively compare the reconstructed images by all interferometers, in order to provide the reconstruction quality as a function of observation time in a photon 'starved' regime.

The following sections discuss the implications of the beam combination methods, as well as the detector arrays, for their wide field-of-view operation. An excellent treatment of the methods Michelson, Homothesis and Densified is given in the work of Tallon and Tallon–Bosc (Tallon & Tallon-Bosc, 1994). There, these methods are compared to the correlator type of interferometric imaging, as encountered in radio astronomy. However, the FOV limitations discussed in that paper remain based on sampling Fourier components of the object $L(\theta_0)$, by analysis of (the complex visibility of) the central fringe. The following discussion will treat the wide FOV performance of all methods, considering them as imagers, with a (θ, d) detection space. In addition, the Staircase method will be discussed.

3.1 Image plane combination

A masked telescope combines the beams from the individual apertures in focus (see Figure 3.1). At this point, interferometer arrays are considered that, although consisting of separated apertures, imitate a masked telescope and hence should have the FOV of the full telescope. In order to imitate a mask correctly, beams from the collecting telescopes should be combined of course in a common focus. And moreover, when the beams are transported in between collection and focusing (as will be the case for a baseline longer than the diameter of the combining telescope) all beams will need a proper (and equal) beam compression, pointing and positioning (Beckers, 1990). The collecting telescopes of an array are considered as *entrance pupils* in a certain configuration. The beams just before being focused together on a detector are running through imaginary *exit pupils*,

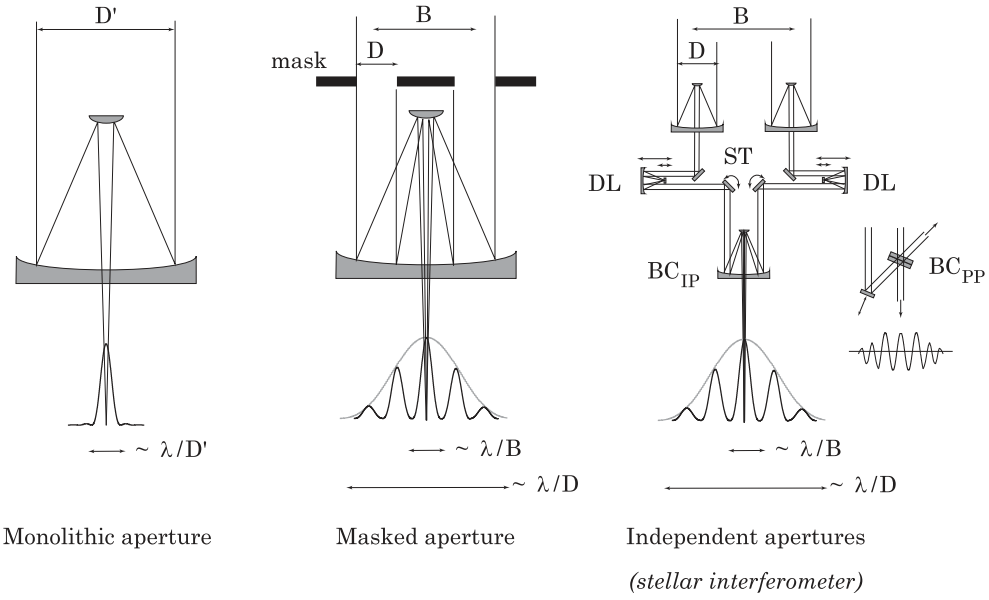

Figure 3.1: Imaging with a monolithic aperture and a masked aperture (left and central). On the right: conceptual equivalence of a synthetic aperture telescope with the masked aperture case. The indications BC_{IP} and BC_{PP} denote an Image-Plane Beam Combiner and a Pupil-Plane Beam Combiner. Legend: DL Delay Line, ST Steering mirrors, D and D' diameter, B baseline. With courtesy from L.A. d'Arcio, "Selected aspects of wide-field stellar interferometry," Thesis, Delft, 1999.

that, because of separate beam transport per beam, are adjustable. To *place* them *in the same way* (but scaled) as the entrance pupils, means there is *homothesis*. This would ensure a proper imaging system, where the diameters and separations of the individual beams have a constant ratio, as they would have in a large masked telescope. This proper imaging systems is then obeying the *Golden rules of imaging* (Traub, 1986).

3.1.1 Homothetic arrays

Considering an imaging system with beam compression M, masking the entrance pupil with a mask with separation of holes B, would place the exit beams at a hole separation B/M. The exit baseline is thus taken $B_0 = B/M$. As derived in Chapter 2, focusing the beams out of such a homothetic optical system with telescope diameter D, telescope separation B and magnification M, would produce the focal intensity

$$I(\theta) = 4D^2 \mathrm{sinc}^2\left[\frac{D\pi}{M\lambda}(\theta - M\theta_0)\right]\cos^2\left[\frac{B\pi}{M\lambda}(\theta - M\theta_0)\right]. \tag{3.1}$$

for a point source at direction θ_0, emitting light of wavelength λ. The sinc and the cos functions have the same origin, which is wavelength independent. Therefore, a fringed envelope will result, one for every point source on the sky, as depicted in Fig. 3.2. The derivation of this function consisted in applying a Fourier analysis to a masked aperture. In fact, for a homothetic array, the Fourier Transform (FT) is a quick and easy tool to predict the Point Spread Function (PSF) of the common focus of the array. Assuming the array is homothetic, implies assuming that, in the case of perfect individual collectors,

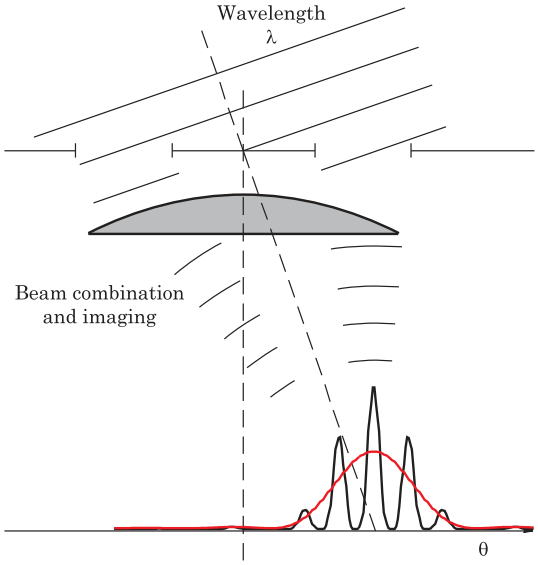

Figure 3.2: A sketch of the imaging process in a Fizeau interferometer. The sketch illustrates a masked aperture, but the incoming parallel wavefronts can also be considered to be separated and brought to this point according to the rules of homothesis. An aberration-free masked aperture will produce a fringed Airy profile in focus. The diameter of the envelope is governed by the aperture diameter D, whereas the fringe width is a function of the separation of apertures B.

the PSF is constant with respect to the field. For a field-invariant PSF it is known that the imaging process of an optical system is in fact a convolution of the intensity distribution on the sky with the intensity distribution of the optical system, which is the PSF. For one dimension θ, this can be expressed as

$$I(\theta)_{\mathrm{rec}} = I(\theta)_{\mathrm{PSF}} \otimes I(\theta)_{\mathrm{sky}}. \tag{3.2}$$

The convolution theorem states that a convolution of functions can be expressed as a multiplication in Fourier-space

$$\mathscr{I}(\omega)_{\mathrm{rec}} = \mathscr{I}(\omega)_{\mathrm{PSF}} \cdot \mathscr{I}(\omega)_{\mathrm{sky}}, \tag{3.3}$$

where ω denotes a spatial frequency and $\mathscr{I}$ is the FT of the intensity distribution. As stated, the PSF is the FT of the pupil configuration. The inverse FT of the PSF is, apart from constants, again representing the pupil function. A pupil function of a masked aperture would be zero everywhere, except for locations inside a sub-aperture. Hence, the function $\mathscr{I}(\omega)_{\mathrm{PSF}}$ will have the same property that it is zero nearly everywhere, except for regions related to the configuration of the telescopes. The multiplication with all these zeros in Eq. (3.3) results in the loss of these spatial frequencies in $\mathscr{I}(\omega)_{\mathrm{rec}}$ and hence in the recorded image $I(\theta)_{\mathrm{rec}}$. To collect all image information from $\mathscr{I}(\omega)_{\mathrm{sky}}$, several array configurations are needed to cover all spatial frequencies.

Therefore, a homothetic array can only deliver full-feature images if the telescope configuration (or baseline length B and its orientation) is variable by repositioning or array rotation.

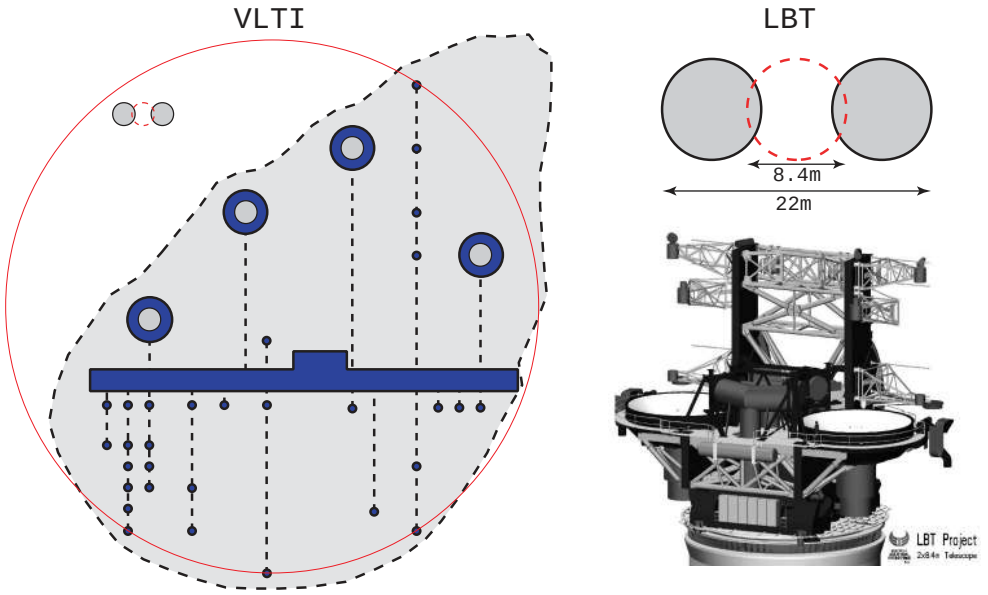

Figure 3.3: Illustrations showing the possible pupil geometries of the Very Large Telescope Interferometer VLTI (left) and the Large Binocular Telescope LBT (right). **VLTI:** The area enclosed by the dashed line is the cut-off part of Mount Paranal in Chile, on which four 8.2m Unit Telescopes have a fixed location and four 1.8m Auxilary Telescopes can be stationed at the indicated positions. The complete array is rotated by Earth rotation. The circle in the VLTI sketch is 200m in diameter, the LBT dimensions are indicated within this circle. **LBT:** The LBT comprises two 8.4m telescopes on a common mount, spanning 22m edge-to-edge. The dashed circle indicates that the spatial frequencies covered by each telescope separately partially overlap with those covered by the synthetic aperture.

Building a homothetic array

Two homothetic arrays for observational astronomy have been conceived, whereas one array is up until today not capable of operating in the wide-field imaging mode for which is was once designed. The Large Binocular Telescope (LBT, first light 2006) and the Very Large Telescope Interferometer (VLTI, first light 2001) share the capability of performing wide-field interferometry, but there are many differences between them (see Fig. 3.3). The LBT comprises two 8.4m-telescopes mounted on a common structure. The geometry is not changeable but chosen such that a continuous range of spatial frequencies is covered; the rotation of the Earth allows coverage of more spatial frequencies than a single snapshot by the array provides. The array is equipped with adaptive optics systems on each telescope and flexure compensation to ensure a co-phased and aberration-free common focus. At the site of VLTI, reconfigurability of the array is allowed. Four 8m Unit Telescopes have fixed locations, but the four 1.8m Auxiliary Telescopes can be placed at a number of different locations, indicated in Fig. 3.3. In this way, and with the aid of Earth rotation, a well sampled spatial frequency coverage of the sky can be obtained. However, only homothetic beam combination can then ensure a large field-of-view. So far, only less complicated co-axial beam combination facilities are installed at the VLTI, which disqualifies the array to be homothetic.

As described in literature (Beckers, 1990; d'Arcio, 1999), obtaining homothesis for a reconfigurable array requires stringent control of all beam properties, such as orientation, placement and magnification. These mechanical parameters influence the interferometric field-of-view and the complex fringe contrast. The stringent control of parameters, however, is based on the desire to be able to perform interferometry over a field-of-view as large as that of a single telescope. As discussed in Chapter 1, this is not a necessity for the observational targets specified. The demands on stringent *control* can be 'relaxed' to stringent *knowledge* of them, and simpler and more robust hardware can then be installed to reach 'weakly-homothetic' beam combination. There is another reason why such beam combination is favorable, arising from the analysis of information processing.

Information processing

As depicted in Fig. 3.2 and clarified by the Fourier relationship, the signal in focus will be a convolution with an envelope whose diameter is inversely scaled by dish diameter D/M in which fringes appear with width related to $B_0 = B/M$. The information in this intensity distribution can only be stored for joint processing if it is adequately sampled, i.e. if the detector pixel spacing is smaller than half (Nyquist sampling limit) or rather a quarter of the fringe period. For long baselines, the angular fringe period gets short, which would imply a very long focal length and very small detectors to be able to exploit that long baseline for resolution in the observation. In other words, a homothetic array requires a focal length and detector that match the intended resolution of the *synthetic* aperture. Although the snapshots taken with this detector can be of lower resolution than the final image, the resolution of the detector limits the resolution of the final image. A non-homothetic array decouples the detector resolution and the ultimate reconstruction resolution completely. The detector dimensions also pose a limit to the field-of-view, but this statement is true for any—even monolithic—imager.

3.1.2 Pupil Densification

Since the snapshots have to be processed to obtain an image anyway and since there are gaps in the spatial frequency coverage of these snapshots, the idea arose to *densify* (Labeyrie, 1996) the exit pupil configuration, so that the fringes in focus are wider and hence a detector grid of less resolution is required to obtain all information out of a snapshot. The snapshot however, is no longer a convolution of the sky with one point spread function. Figure 3.4 shows an example of a densified pupil imager (Pedretti *et al.*, 2000). In this demonstrator, the two lenslet arrays affect the exit-pupil baseline and individual beam diameter. The output baseline B_0 is maintained after densification, so the fringe period is still the same. However, D_0, the beam diameter after modification, is relatively larger, which makes the envelope around the fringe function narrower. With more difficulty, the demonstrator could have maintained D_0 and shortened B_0, which would meet the discussed detector requirements more illustratively.

Obviously, this technique narrows the interferometric field-of-view. The polychromatic fringe function shall in practice consist of only a few fringes, unlike the monochromatic cosine factor in

$$I(\theta, d) = 4D^2 \mathrm{sinc}^2\left[D\pi(\theta - M\theta_0)/M\lambda\right] \cos^2\left[\pi(d + B_0\theta - B\theta_0)/\lambda\right]. \tag{3.4}$$

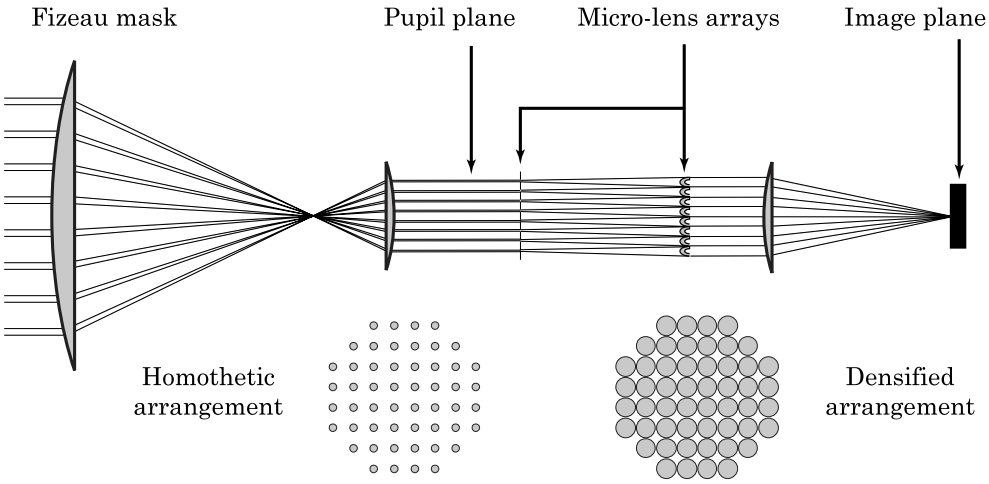

Figure 3.4: Illustration explaining the laboratory set-up for demonstration of pupil densification. Taken from (Pedretti *et al.*, 2000). The homothetic part simulates the collection with separated telescopes and outputting a compressed version. Then two micro-lens arrays apply a beam expansion to each beam, so that homothesis is lost.

Still, this expression points out that the origins of the sinc and the cos functions have origins that are differently scaled to the point source direction θ_0. This means that for the off-axis parts of the sky, the polychromatic point spread function is different. The imaging process can no longer be expressed as a straightforward convolution. For small targets, much smaller than the angular dimension of the envelope function, the assumption of a constant PSF might be made (Labeyrie, 1996). For a wide-field observation of several PSFs in diameter however, one should not only process the snapshots with field-variant kernel deconvolution (Nagy and O'Leary, 1998) but even ensure that the PSF at the edges still contains fringes. The fringes carry the information on the high spatial frequencies, hence loss of fringes directly means loss of resolution. It is assumed that for angles close to the optical axis, the optical path length in the interferometer arms is equalized. However, applying an intentional extra path length d might be useful to 'drag' lost fringes at one edge of the field-of-view back into the snapshot again, at the cost of loss of detail at the opposite edge. Sequential snapshots with the same telescope separation, but with different d can be stored and all processed jointly to arrive at the high resolution image. A straightforward numerical algorithm to incorporate the use of a space-variant PSF and the use of multiple d per array configuration is implemented in the numerical simulations in Chapter 5. Note that in Fig. 3.4, the use of lenslet arrays (or other diffractive elements such as pinholes) poses a limit on the field of view, since they act as aperture stops for each individual beam. This effect is not further considered in the simulations, where over-sized beam compressors are considered, so that unvignetted beams of arbitrary D_0 and B_0 are feasible.

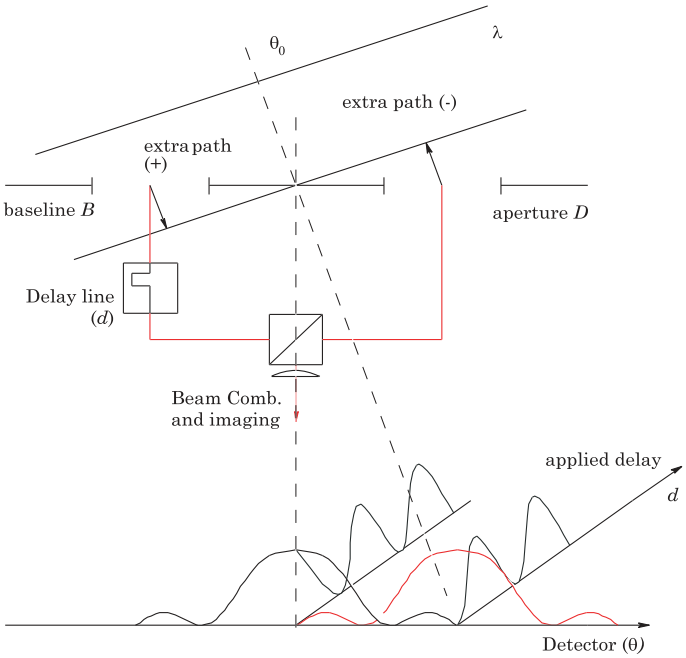

Figure 3.5: Schematic of the imaging process in a co-axial Michelson interferometer. Two response functions in (θ, d)-space are indicated, characterized by a shift of the diffraction envelope and a different origin of the modulation function.

3.2 Co-axial combination

The idea of imaging as convolution with field-variant kernels can be generalized further. In conventional convolution, the image, the object and the kernel have the same co-ordinate system, as in Eq. (3.2). A blurred two-dimensional image, for example, is the result of blurring a two-dimensional scene with a two-dimensional point spread function. If the image, the object and the kernel do not share the same co-ordinates, the imaging process can be denoted as a general mapping operation

$$I(\theta,d)_{\mathrm{rec};B} = \int_{\theta_0} I(\theta,d,\theta_0)_{\mathrm{PSF};B} L(\theta_0)_{\mathrm{sky}} \mathrm{d}\theta_0. \tag{3.5}$$

Again, a 'deconvolution' allows estimation of $L(\theta_0)$ from several $I(\theta,d)_{\mathrm{rec};B}$, with knowledge of the variant kernels $I(\theta,d,\theta_0)_{\mathrm{PSF};B}$. Although the domains of the recorded information are different from the domain of the sky, this operation will be referred to as deconvolution.

The famous stellar interferometer constructed by Michelson consisted of a 20 feet cantilever beam with a periscope system of mirrors on top of it, mounted on a 100 inch reflecting telescope. Hence, this interferometer combines the sky images of the individual apertures in the focal plane of the telescope. This type is the 'Michelson Stellar Interferometer' and is actually a 'Densified Pupil' imager. In Fig. 3.5, a co-axial Michelson interferometer is sketched, where the beams are combined via a beam splitter. In this type of interferometer, the beams are combined when collimated, before focusing on a detector. Therefore, this method is referred to as *pupil plane combination*. Sky images

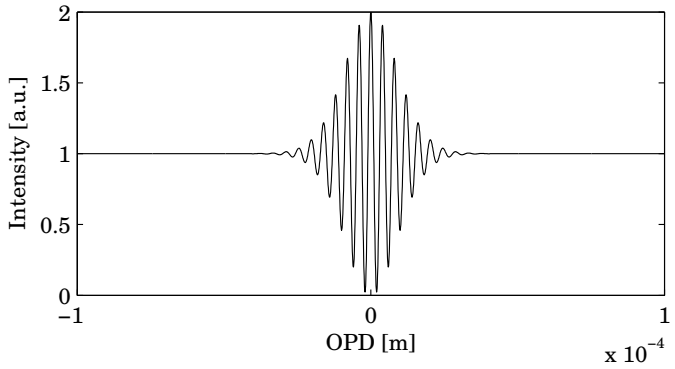

Figure 3.6: The bandwidth in the simulated experiments, 6 μm $\leq \lambda \leq$ 10 μm, results in a compact fringe pattern without side lobes, since a Gaussian amplitude envelope was applied to the spectrum.

are overlapped (when observed in focus) and stars appear without fringes across them, but rather they 'blink on and off' when the optical path length difference between interferometer arms is adjusted. Interesting work on wide-field performance of a co-axial interferometer is done on the Wide-Field Imaging Interferometry Testbed (WIIT) at the Goddard Space Flight Center (Leisawitz *et al.*, 2003).

3.2.1 Michelson interferometer

Co-axial beam combination is illustrated in Fig. 3.5. Since the exit baseline $B_0 = 0$, the interference part in the response is a function of the applied delay d and the external delay $B\theta_0$:

$$I(\theta, d) = 4D^2 \mathrm{sinc}^2 \left[\frac{D\pi}{M\lambda}(\theta - M\theta_0) \right] \cos^2 \left[\frac{\pi}{\lambda}(d - B\theta_0) \right]. \tag{3.6}$$

As discussed in Sect. 2.3.2, the large range of θ_0 (the Field-of-View) and the limited extent of the sinc-function pose the need to record the information with several detectors or pixels in a row.

As described in Section 2.3.3, Fig. 2.14, observing with a longer baseline results in a 'quicker movement' of the fringe packet in direction d, for a point source off-axis. This is the heart of interferometric imaging. Because of the different slopes of the lines through the origins of the sinc–cos response functions in (θ, d)-space and the fringe period λ remaining the same, the ensemble of point sources on the sky will produce a different sum of footprints, leading to different modulations or visibilities in the observed fringes. Cosines with equal period but different phases summed up, yield a cosine with still the same period, but with less modulation and another phase. This is the classical complex visibility $\mathcal{V}$ that is measured by the classical interferometer. The Zernike–Van Cittert theorem then states that this $\mathcal{V}$ is one value in the Fourier plane of the object to be reconstructed on the sky. However, in the treatment with P pixels, this would yield more than one complex visibility, $\mathcal{V}_{p=1\ldots P}$, but still only one Fourier-coordinate B/λ to assign them to. With the imaging description as given in Eq. (3.5), the detected information is treated in (θ, d)-space and can be visualized by a two-dimensional figure. To illustrate a wide-field, polychromatic observation, a spectral bandpass of Gaussian shape is chosen such

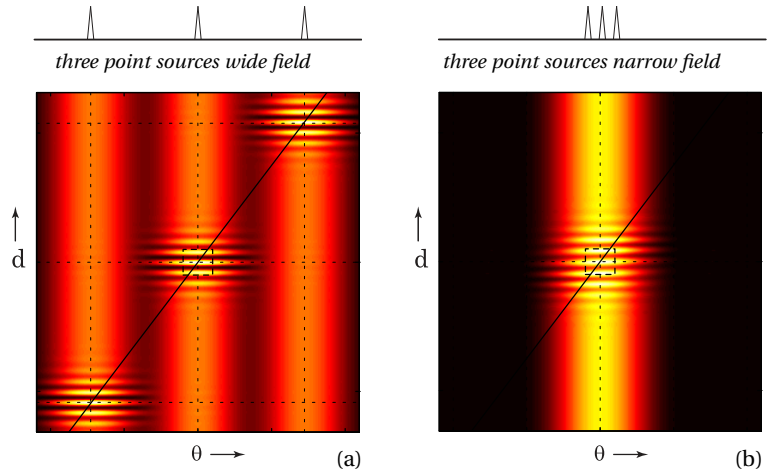

Figure 3.7: Measured intensities (color coded) in *detection space*, in θ-direction on the linear detector and at d-setting of the delay line. The outermost points of large sources (a) provide non-overlapping Airy patterns in θ-direction and no common delay-range at which all fringe packets produce fringes. For smaller sources (b), the information from all sources is superimposed by overlapping Airy profiles as well as communicating fringe packets. This results in baseline-dependent fringe contrast. The dashed boxes in the centers of both pictures indicate the valid regions for the application of the Zernike–Van Cittert theorem to predict the fringe contrast. In the wide-field case, a Fourier transform of the source function will not predict the fringe contrast correctly.

that a side-lobe-free fringe pattern arises as depicted in Fig. 3.6. Figure 3.7 shows the nature of the polychromatic detector response. Integration over the stellar source $L(\theta_0, \lambda)$ is, in the case of a collection of point sources the same as summing over the individual response functions (three in the example of Fig. 3.7). The indicated areas around the origins of the two plots have the approximate dimensions of half a diffraction pattern (in θ-direction) and a coherence length (in d-direction) and therefore span up one area to which the fringe prediction of the classical, quasi-monochromatic double slit theory applies. For a narrow-field, narrow-bandpass observation (conventional interferometry) all information about the source can be gathered by sampling this area, for several baselines B_k.

Since the observations are in general polychromatic, the coherence length or extent of the fringe packet is limited. Since fringes carry the information on high spatial frequencies in $L(\theta_0)$ and the fringe packets move (especially for the very long baselines) far away from $d = 0$, a long scan over d (many times the central wavelength) is necessary to collect all information. Alternatively, restricting the scan range to $-\lambda_c \leq d \leq \lambda_c$ implies that not all information on (the high spatial frequencies of) $L(\theta_0)$ is collected. A possible solution to reduce the scanning time while still measuring fringes over the full FOV is presented in the form of a Staircase-shaped mirror, as described in the literature (Montilla *et al.*, 2005).

3.2.2 Michelson with Staircase mirror

The detection space (for the linear array example) is stretched in two directions. The desired FOV governs the angular extent. The chosen width of the PSF then determines how

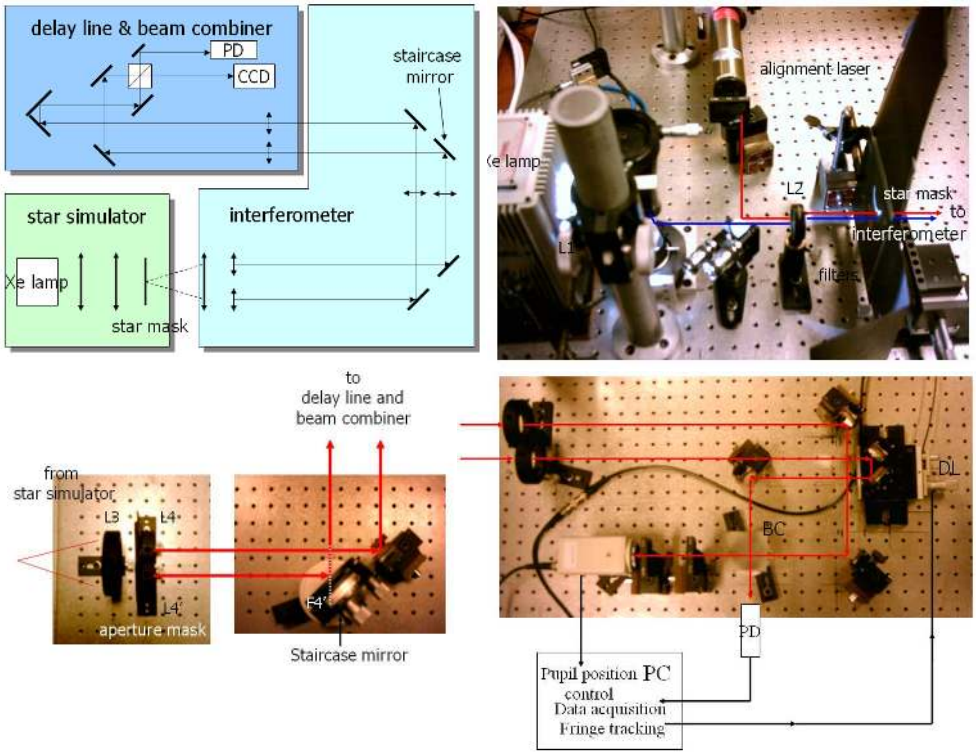

Figure 3.8: The Staircase testbed in the laboratories of Delft University of Technology. Illustration and photographs by courtesy of Iciar Montilla.

many pixels are needed to cover this FOV, roughly two pixels per diffraction-envelope-width. But in the delay direction, the needed scan length is depending not only on the FOV, but also on the baseline length. The longer the baseline (and for the required spatial resolution very long baselines are necessary), the further away will the central fringe be located, for the pixel at the corresponding edge of the FOV. And to sample all details via the fringes, requires then a very long scan with the delay line, in steps $\Delta d < \lambda_c/2$.

This problem can be overcome by installing a so called *Staircase mirror* (Montilla, 2004). This multi-faceted mirror is placed in an intermediate focus of one of the interferometer arms. This mirror compensates the field-dependent OPD $B\theta_0$. When step height and width are properly adjusted for central wavelength, PSF diameter and baseline length, the OPD is compensated in such a way that only one OPD scan in d through the fringe packet is needed. In other words, all point sources on the sky carry fringe information on the detector. None of them will be out of the coherence length. For every baseline length B, a different mirror is needed. When the step height is not adjusted, there will still be a partial compensation, so still the needed OPD scanning time will be shorter. Note that it is not true that all point sources on the sky have their zero OPD at the same setting. Still, the central fringe position for a star is a function (sawtooth-shaped) of its direction θ_0. The cosine-factor of the co-axial point source response

$$I(\theta, d) = 4D^2 \mathrm{sinc}^2\left[\frac{D\pi}{M\lambda}(\theta - M\theta_0)\right] \cos^2\left[\frac{\pi}{\lambda}(d - B\theta_0)\right], \tag{3.7}$$

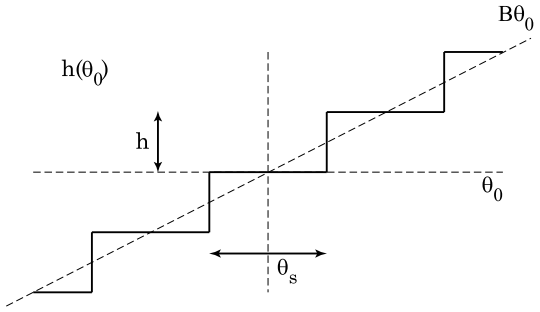

Figure 3.9: The staircase function $h(\theta_0)$, as described in the text.

is altered to

$$\cos\left[\frac{\pi}{\lambda}(d - B\theta_0 + h(\theta_0))\right], \tag{3.8}$$

with $h(\theta_0)$ the staircase function, see Fig. 3.9. For a certain step height h_0 and step width θ_s, the staircase function is given by

$$\begin{aligned} h(\theta_0) &= \sum_{n=-\infty}^{+\infty} n h_0 \,\mathrm{rect}\left[\frac{\theta_0 - n\theta_s}{\theta_s}\right] \\ &= \sum_{n=-\infty}^{+\infty} n h_0 \left[\mathrm{H}\left\{\frac{\theta_0 - (n-\frac{1}{2})\theta_s}{\theta_s}\right\} - \mathrm{H}\left\{\frac{\theta_0 - (n+\frac{1}{2})\theta_s}{\theta_s}\right\}\right], \end{aligned} \tag{3.9}$$

with $n \in \mathbb{Z}$. Here, the Heaviside step function $\mathrm{H}(x)$ is used, given as

$$\mathrm{H}(x) = \begin{cases} 0 & x < 0 \\ 1/2 & x = 0 \\ 1 & x > 0. \end{cases} \tag{3.10}$$

The step width θ_s and step height h have to correspond and need to be altered for changing baseline length B according to $h_0 = B\theta_s$ or alternatively $\theta_s = h_0/B$, to equalize the external OPD over the complete FOV. The example shows a staircase of five steps with constant width and variable height.

For long baselines in the order of 100m, the step height necessary to compensate the external OPD to a length comparable to the coherence length, might reach millimeters. For such step heights, the diffraction pattern in the intermediate focus experiences a dramatic discontinuity. A Fourier analysis of the electromagnetic field in the focus around such a discontinuity is treated in App. B. For step heights in the order of one or several wavelengths, a simple calculation shows that the diffraction pattern of a point source imaged via an intermediate focus on the edge of a step still resembles the Airy function (or sinc-function in the one dimensional case).

In Figs. 3.8 and B.1, a working prototype of the discussed type of interferometer is illustrated. The measurements showed that for these baselines, information from all over the FOV could be measured with a relatively short delay line stroke. The experimental set-up was not designed to perform imaging; only a very limited set of baseline lengths was sampled.

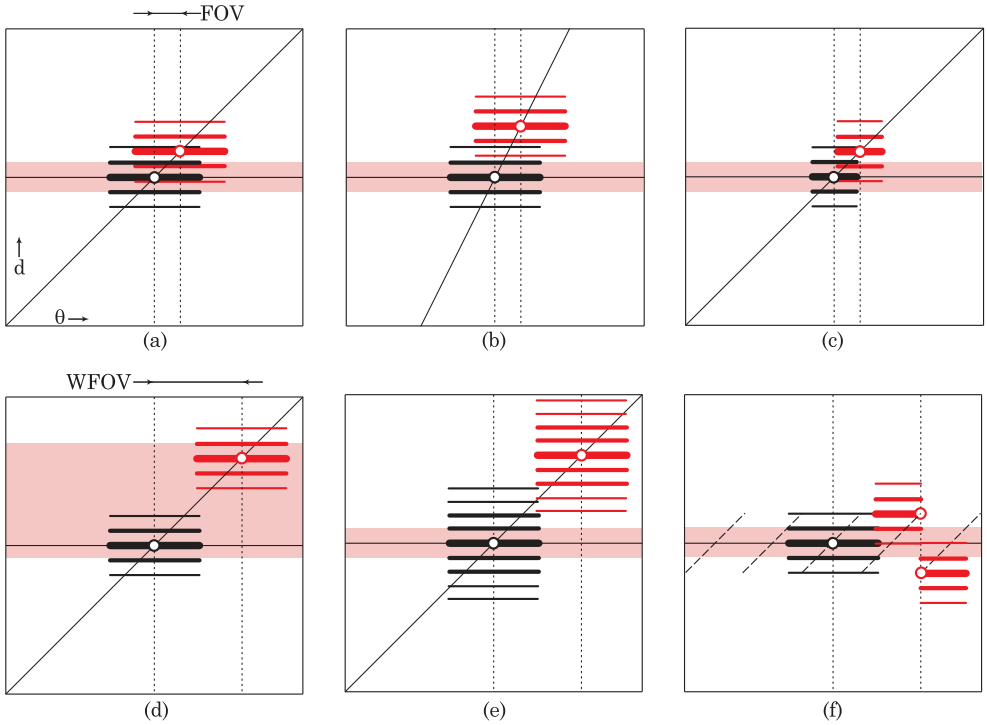

Figure 3.10: Diagrams for different imaging situations. Two point-like stars are imaged, producing two intensity footprints in (θ, d) or detector space. The dashed lines indicate the angular positions of the two stars. The diagonal line indicates the *origin* locations for fringe packets linked to a sky direction, where θ_0 is the origin for the envelope and $B\theta_0$ the origin for the fringe packet. The steepness hence relates to baseline length. The shaded areas indicate the slab in (θ, d)-space that is sampled as the linear detector is read-out at various settings of the delay d. Further details are given in the text.

3.3 Field, resolution and observation time

To be able to obtain information on the spatial spectral content of the observed stellar source, fringes will have to be measured at a desired baseline length B and with a central wavelength λ_c. The diagrams in Figure 3.10 clarify in what ways these necessary fringes may or may not appear, depending on other parameters concerning the interferometer array, such as field-of-view, telescope diameter D and scanning range. Each sketch shows the detection of two point sources with a separation equal to the field-of-view (FOV). Although the responses are drawn for a co-axial interferometer, the accompanying text is also applicable to image-plane interferometers. The sketches illustrate the following situations:

a In the reference situation, the sources in the Field-of-View (FOV) interact in the detection space. Their separation and the Airy-width causes the patterns to coincide in θ-direction. All point sources in between do so likewise. The baseline gives the reference steepness of the diagonal line.

b If now the baseline is extended with respect to situation (a), all patterns get a dif-

ferent relative offset $B\theta_0$ and another complex visibility can be observed. However, for very long baselines and a short packet length (large bandpass), the interaction will diminish and eventually be lost, as indicated by the minor overlap of the patterns. Point source responses from the edges of the large object do not overlap anymore with each other in the detection space. Hence, the coherence length l_{coh} limits the interferometric resolution (the maximum useful baseline B_{max}) if the scan over d is limited to the traditional $-\frac{1}{2}\lambda_c < d < \frac{1}{2}\lambda_c$.

c The size of the interferometrically coherent region on the sky is closely related to the dish diameter D of the telescopes. Increasing these will narrow the Airy profile. Compared to case (a), doubling the diameters imposes halving either the FOV or the maximum baseline, should the portion of overlap or the modulation of the final fringe signal remain the same. Therefore, an increase of the dish diameter D also limits the maximum resolution.

d The loss of overlap can also be the result of extending the FOV. The baseline is the same again as in case (a), but the FOV is three times larger. Overlap is lost in both θ- and d-direction. Multiple detectors and a long scan range are necessary.

e Reducing the bandpass reduces the necessary delay scan length required to obtain interacting fringed intensity signals and hence information for spatial resolution. A narrow bandpass implies a long coherence length, but limits the photon flux.

f A staircase-shaped mirror in an intermediate focus exhibits apparent discontinuities in the detection domain. The location of the fringe packet center as a function of point source location (dashed line) will be a sawtooth function. As a consequence, the fringes and hence the information for the spatial frequency related to this B-value, remain centered around 'zero OPD'. With only a short delay scan, all information can be gathered.

As can be seen, the diameter D, coherence length l_{coh}, the FOV and the resolution via B_{max} all interact. The scan length over d and the detector pixel size in direction θ have to be chosen such that all fringe information is covered, with sufficient modulation.

3.4 Quantitative comparison

In Chapter 1, the observational targets for the Darwin imaging array have been mentioned and detailed specifications of the requirements to enable their imaging with sufficient spatial and spectral resolution have been derived. A short list of these specifications is given again in Table 3.1. In the previous sections, four types of imaging arrays have been presented. In the next chapter, numerical simulations will show the detector responses for all these interferometers and the reconstruction of the luminosity distribution on the sky that can be estimated out of these signals. To be able to check if the resolution requirements are met, a *figure of merit* shall be applied to the results and a number of features shall be checked by inspection.

Table 3.1: Darwin imaging requirements

Objective	**Target Requirement**
Spectral Range	5 – 30 μm
Spatial Resolution	0.001"
Maximum Baseline	2000 m
Spectral Resolution	$R = 1000$
Path length Control	10 nm
Sensitivity	40 nJy
Dynamic Range	1000

1 Jy (Jansky) = $10^{-26} W m^{-2} Hz^{-1}$

The reconstructed intensity distribution on the sky can be compared with the known distribution, since in this case of numerical simulation, first a forward calculation is performed to derive the detection signals. These are then altered (quantization by photon count statistics) before the inversion process is started. The estimate of the sky should exhibit:

1. **Maximum spatial frequency**. The theory described how spatial frequencies relate to the baseline or separation of collecting telescopes. Since the simulations are polychromatic and the detection is quantized in both θ and d direction, it should be checked if these discrete signals still provide the spatial content to the inversion. Inspection of a Fourier analysis of both the chosen source function, $L(\theta_0)$, and the reconstructed one, $\hat{L}(\theta_0)$, will show which range of spatial frequencies is covered.

2. **Constant FOV**. It is known that for an increasing baseline length, the FOV narrows down for a fixed scanning length over d. As a result, a certain spatial frequency might indeed be present in the reconstruction, but details of that spatial frequency will only show up in the central region of the FOV. Moreover, the FOV is covered by a number of pixels in focus. It should be checked that in all regions of the reconstructed luminosity distribution (spanning several Airy-diameters) the coverage of spatial frequencies is according to the chosen range of B-values and the spectral bandpass. For the cases of Densified Pupil and the Staircase method, this check is of particular interest, since, respectively, fringes are encoded in both θ- and d-direction, or physical discontinuities are present in the system. The correct coverage is easily observed in the reconstructions $\hat{L}(\theta_0)$.

3. **Observation time**. The photon flux from the stellar object is 'binned' into a certain number of pixels using one or more snapshots. The collection of pixels and delay positions is referred to as the 'bins' over which the photons are distributed. Given the magnitude of the object, the needed observation time is not only a function of this amount of bins, but also of the numerical quantization and regularization of the inversion process.

In the simulations, the two-element array shall be 'fed' with a number of photons P. For a specific source, this amount of photons can be related to the observation time. Therefore, repeating the simulations with a decreasing number of photons means either a shorter observation, or the observation of a weaker source.

After the simulation process (details in the next Chapter) the estimate of the luminosity distribution can be compared with the known luminosity distribution. For N resolution elements on the sky, the normalized error in the estimate or the difference norm ϵ is calculated:

$$\epsilon = \frac{1}{N}\sqrt{\sum_i |s_i - \hat{s}_i|^2}. \tag{3.11}$$

Where s_i is the intensity level of one resolution element in the source and $\hat{s}_i$ is the corresponding element in the estimate. For the simulations, a non-existing stellar source is taken. The source luminosity function $L(\theta_0)$ is of unit scale; a variable and realistic photon flux is realized by adjusting the discretization of the measurement signals, rather than adjusting the source function. Therefore, the source function can be normalized so that it has a mean value of 1 and the estimate will also have an approximate mean value of 1. If then the comparison of an estimate to the original according to Eq. (3.11) yields an $\epsilon = 0.01$, this means that the dynamic range in the reconstruction is 1:100.

Dynamic range

The prime point of comparison of the estimation results, will be the dynamic range. It should be noted however, that a somewhat alternative definition of dynamic range is used. A formal definition would be the peak value $S_{\max}$ of a signal S, divided by the background level $S_{\min}$ of the signal:

$$D = \frac{S_{\max}}{S_{\min}}. \tag{3.12}$$

However, the notion of background level, is not adequate for interferometric imaging. In the reconstruction process, the amount of background can already be estimated with single-dish imaging, and therefore the background will not provide information as to how narrow the features are, that are reconstructed by the interferometer. Nor would it directly provide information on whether steep edges in the image are reconstructed. In other words, the 'background' is the incoherent image of the sky, comprising a direction-dependent magnitude, disqualifying the use of a single value $S_{\min}$ in the judgment of the dynamic range of an interferometric reconstruction. Considering the proposed error figure ϵ, the re-definition of dynamic range to

$$D' = \frac{1}{\epsilon}, \tag{3.13}$$

is valid. For a too poorly estimated peak value $S_{\max}$ or too high background level $S_{\min}$—for example, when only the envelope of the single-dish resolution is in the estimate—the error ϵ will be large and the dynamic range D' as well as D low. Note that ϵ can only be used since the original image is known.

Another reason to support the use of $1/\epsilon$ as measure for dynamic range is the following. The dynamic range is the ratio of the intensity resolution in the image, compared to the maximum value. Since the power in the original luminosity function $L(\theta_0)$ is normalized to 1, the amplitude in the Fourier spectrum $\mathscr{F}[L(\theta_0)](k)$ for $k = 0$ is 1. And since $L(\theta_0)$ is positive, all other values in $\mathscr{F}[L(\theta_0)](k)$ are smaller. And indeed, a low resolution version of $L(\theta_0)$ will show a rough envelope function resembling $L(\theta_0)$, with a periodic cosine-like oscillation around that envelope. The amplitude of that periodic function is related to the largest Fourier amplitude that was left out. Leaving out higher spatial frequencies either because a limited $B_{\max}$ is taken or because too much filtering is needed

in case of a photon-starved observation, results in a higher value of ϵ. And indeed, following the second definition of dynamic range, short baseline observations or observations with a lot of (photon-)noise in it, will result in a low dynamic range $1/\epsilon$.

Frequency content

Since the imaging process involves the regularized inversion of a convolution process together with an integration over pixels, it is clear that the resulting estimate of the sky is a *filtered* result. When the measurements are noisy, the regularization process will limit the participation of solution mode functions in the reconstruction to those of lower spatial frequency (Hansen, 1998) as described in Chapter 4. The maximum spatial frequency (expressed in cycles over the full FOV) present in the estimate of the intensity distribution on the sky $\hat{L}(\theta_0)$ is therefore not necessarily that frequency corresponding to the maximum baseline length and minimum wavelength as in $u \approx B_{\max}/\lambda_{\min}$. The Fourier spectrum of the estimate, in which a clear cut-off frequency can be observed, will be shown in several cases. The spatial frequencies will be expressed as baseline length B equivalent, at observational wavelength λ_c.

Imaging and spectrometry

With the number of photons P, the dynamic range $(1/\epsilon)$ and inspection of the spatial frequency coverage, the analysis can be made as to whether the proposed imaging arrays are able to meet the imaging requirements regarding spatial resolution. The spectral resolution is not yet considered. In the simulations, no dispersive element was incorporated, to spread the spectral content over more than one channel. This results in measured interferograms that incorporate the signals integrated over all wavelengths. Theoretically, a Fourier analysis of these interferograms could provide spectral information. However, a straightforward example will show the difficulties in this process, related to the integral over λ which produces an extra entanglement of information in the detected signals. Should the beam combination always be pairwise, even in the case of a three or more element array, dispersion in the direction orthogonal to that of the spatial detail, is a more robust way to measure the correlated spectra from a source. Then, the spatial reconstruction of a source can be done per wavelength channel. Inspecting

$$I(\theta, d)_L = \int_{\theta_0} 4D^2 L(\theta_0) \mathrm{sinc}^2 \left[\frac{D\pi(\theta - \theta_0)}{M\lambda} \right] \cos^2 \left[\pi/\lambda (d + B_0\theta - B\theta_0) \right] \mathrm{d}\theta_0, \tag{3.14}$$

it shows that the spatial deconvolution problem is fully decoupled from the spectral reconstruction if the wavelength λ is taken as a variable rather than as a constant. In Sec. 5.4, examples of this decoupling are given. However, since the collectors have finite sizes, the spatial dimensions of the diffraction pattern play a role in the spectral resolution. After dispersion, the collected signal in this direction should be deconvolved by a wavelength dependent kernel being the diffraction pattern. The full treatment of diffraction effects in spectrometry are outside the scope of this thesis.

Chapter 4

Ill-posed discrete inverse problems

The following sections will describe in detail the formulation of an interferometric imaging equation, relating observations to an observed source function. Starting with examples from the literature of sophisticated deconvolution algorithms—advanced deblurring of Hubble images with field-variant PSFs and image reconstruction from multiple observations, as performed at the Large Binocular Telescope—a simple general formulation of these problems is given. The formulation is far from being numerically efficient, but does allow regularized inversion, so that meaningful reconstructions can be made. Moreover, this formulation allows an extension of the concept of convolution, in the sense that the coordinate systems of source function and observation are allowed to be different, which is necessary to express the co-axial interferometric imaging process in the same formulation. Then, with the general imaging process formulated as matrix–vector multiplication, the inversion can be analyzed by means of Singular Value Decomposition. Besides giving insight into the interferometric imaging process, this decomposition is also essential in order to regularize the inversion, since straightforward inversion will not lead to meaningful image reconstructions.

4.1 Imaging as linear system of equations

Deconvolution

As stated in Chapter 2, the problem of imaging extended or multiple sources in classical terms, is the assignment of complex visibility data to the Fourier transform-plane of an image. In the general formulation of the imaging process in an interferometer, the intensity measurement is a sum of weighted responses to an ensemble unit amplitude point sources. A linear system of equations results, relating elementary point sources to their corresponding intensity detector responses. For 'true' imagers—by homothesis or monolithic telescopes—this linear system of equations resembles a convolution matrix. Hence, the inverse solution resembles a deconvolution process. For imagers that need modulation—because of the pupil plane combination—the linear system represents a transfer matrix from sky distribution to a measurement in 'detector space', where this space not only extends over the linear detector coordinate θ, but also in OPD direction

d. This can be regarded as a multivariate convolution in an extra dimension. Analogously, a two-dimensional luminosity distribution on the sky $L(\theta_0, \phi_0)$ will be convolved into three-dimensional data.

Image reconstruction for the Large Binocular Telescope

The reconstruction of an extended source was studied for the case of the Large Binocular Telescope (Bertero and Boccacci, 2000), a homothetic optical interferometric array of two telescopes. Although the two primary mirrors are fixed on a common mount, the baseline configuration is not constant. Earth rotation allows the LBT to sample the sky from different rotation angles, so that the spatial frequencies of the source or the (u, v)-plane can be sampled in more than one direction. This provides a different PSF or convolution kernel as a function of the rotation angle. In general, a homothetic array will be able to sample the sky in a number of observations, where for each observation the kernel can be estimated or even recorded. The observation of the sky can be denoted as a convolution of the true intensity distribution on the sky with this kernel.

Since a homothetic array acts as a masked monolithic telescope, the convolution kernel is—in the absence of aberrations—field-invariant. Misalignment or misplacement of a single aperture, or other aberrations over the *synthetic aperture* will give rise to a field-dependent PSF, complicating the deconvolution. Reconstruction with variant kernels is possible (Nagy and O'Leary, 1998) but for small variations of the PSF over the field, the standard deconvolution can be applied, be it that only a (small) part of the Field-of-View can be deconvolved with this (incorrect) invariant kernel, as suggested for Densified pupil imaging (Labeyrie, 1976; Tallon & Tallon-Bosc, 1992).

An efficient deconvolution scheme for the homothetic LBT is presented as the Ordered Subsets Expectation Maximization (OS-EM) algorithm (Bertero and Boccacci, 2000). This iterative method is stable and converges rapidly. The *de*-convolution problem is posed as a fairly straightforward double convolution calculation. Based on a Fast Fourier Transform (FFT), convolution can be performed quickly. This example illustrates that for the case of imaging with field-invariant convolution kernels, that yet are different per baseline configuration and hence yield different observations of a scene, efficient iterative methods exist to process all recorded data jointly, in order to produce a single high-definition reconstruction of the stellar source. Incorporation of a de-convolution algorithm for field-dependent kernels (Nagy and O'Leary, 1998) is possible, but outside the scope of this research. The result would be a general deconvolution algorithm, treating the data jointly and allowing both field- and baseline dependent PSFs. A less efficient, but easily implemented linear version of such an algorithm however, is derived in the following section.

General deconvolution

The reconstruction of an extended source can be considered as a deconvolution problem. As pointed out, the convolution kernel may even be variant. In that case, reconstruction is still possible, but a more general approach is needed. Although dedicated algorithms exist for image reconstruction with variant kernels, a reconstruction approach is developed that is not necessarily linked to image reconstruction. Deconvolution is typically an *ill-posed linear inverse problem*. To solve this type of problems, several strategies exist. These begin with the formulation of the problem

$$\mathbf{b} = \mathbf{A}\mathbf{x} + \mathbf{n}, \tag{4.1}$$

where the recorded data **b** is a result of the matrix multiplication of transfer matrix **A** with the sought function **x**. The recording process and the photon statistics 'add' noise **n** to it. The transfer matrix can now be considered as the convolving function, that may contain variant PSFs, variant amplitude response and even the presence of 'dead pixels'.

Solution estimates of this linear system of equations can be obtained in many different ways (Hansen, 1992) based either on Singular Value Decomposition (applicable to discrete Tikhonov regularization) or on iterative convergence, as is the case with Conjugate Gradients (CG). The goal of all of these methods is to dampen the devastating oscillatory behavior of the high spatial frequency components of the solution. The nature of ill-posed inverse problems causes even the slightest presence of noise in the measurement to completely blow up the solution. Taking the singular value decomposition of a large matrix—the number of elements in **A** will be the number of recorded pixels, times the number of resolution elements on the sky to recover, times the number of observations times the number of baseline configurations—is numerically a costly process. For such large systems, halted iteration of Conjugate Gradients (referred to as Partial CG) is more efficient. No actual matrix inversion has to be calculated, nor is a decomposition like SVD necessary. The reason for successful reconstruction lies in the fact that with CG, low order spatial structure of the sought solution appears more quickly in the estimate of the solution than the high order spatial modes. For an excellent description of the mathematics of CG and a proof of convergence, the reader is referred to (Shewchuk, 1994).

For problems with smaller transfer matrices and for illustrative purposes of the regularized inversion, the SVD-based regularization methods provide quick and satisfactory results, as will be shown in Sec. 4.2. In the preceding sections, two aspects in image reconstruction were treated. Dealing with multiple observations of the same source, as well as dealing with variant convolution kernels can be accommodated. Moreover, insight is given into the formulation of such a multiple-configuration observation as a straightforward matrix-vector multiplication. To complete the formulation of the forward imaging problem for all interferometric imagers, the final step is to realize that the detected data and the original observed function do not necessarily need to have the same coordinates. This is the case for co-axial interferometers; their imaging treatment results in essentially the same problem formulation: a convolution for multiple observations with a field-variant kernel.

General deconvolution algorithm

Homothetic arrays provide reconstructions of the sky after *true* deconvolution, that is convolution with a single kernel function. Misaligned or aberrated arrays can be represented by a linear system as described above, where multiple kernels are contained in a transfer matrix. From here, it is a small step to co-axial interferometers, where just as well a deconvolution approach can be used in order to reconstruct the luminosity distribution on the sky.

In the case of co-axial beam combination, the information from the high spatial frequencies is not present in the image plane itself, but in sets of image planes. Sequential recordings of these pixels (in general only a few large pixels) for various settings of added delay, provide a recorded data vector **b** that is a result of the sky distribution **x**. The transfer matrix **A** is different, because it does not necessarily relate image locations to object locations (as for image deconvolution). When the co-axial imaging process is described

as a linear system of equations, the same regularized inversion techniques can be applied and the recorded data sets are actually deconvolved to yield an estimate of the sky.

By processing all possible imaging interferometers as a linear system of equations, they can be compared efficiently and fairly. The traditional processing of (u, v)-data with algorithms such as CLEAN or MEM can be overcome, which provides flexibility in the simulation environment. Quick simulations of reconstruction with various interferometer types and baseline configuration are possible for the same modeled sky, where the characteristics of the retrieved sky are not depending on interferometer-bound (and possibly optimized) solution algorithms. Hence, the comparison of the interferometers is purely based on the nature or efficiency of the interferometric signals from each interferometer. Although the detection by all interferometers (forward problem) can be expressed by a matrix–vector multiplication, the direct inversion of this multiplication does not provide meaningful solutions. The following section will discuss this problem and ways to overcome it.

4.2 Analysis of ill-posed problems

A deconvolution problem or a decomposition of data onto basis functions can be performed by inverting a linear system of equations. The two mentioned problems of image deblurring and tomographic imaging, as well as many other linear problems, do not allow the naive inversion of this linear system to provide a solution. The reason for this is that the problem is considered to be *ill-posed*. The basis functions resemble each other a lot and are far from being orthogonal. When the system is inverted, small deviations in the data from an exact result of the forward problem (like measurement noise) will cause the solution of the inverse system to explode. The inverse basis functions are combined with very high amplitude to produce a source function that, multiplied with the transfer matrix, produces the noisy data exactly. This effect is illustrated in Fig. 4.1.

The solution exists and is even unique. But because of the very high amplitudes, it is useless. To obtain useful solutions of the inverse problem, *regularization* is needed. In general, regularization techniques modify the inverse problem, so that a well-posed or well-conditioned problem arises, that provides a good estimate to the sought solution of the original inverse problem. For more rigorous background material on this topic, reference is made to the work of Tikhonov and Goncharsky (Tikhonov and Goncharsky, 1977) or Hansen (Hansen, 1998).

Considering a stellar source to be a collection of mutually incoherent point sources, imaging them is numerically performed by adding point source intensity responses. A matrix vector multiplication then performs the transfer of any source into an intensity measurement. As stated, to invert this process, analysis of the discrete transfer matrix is necessary. A very good treatment of this analysis and the resulting solution of the inverse problem is given by Visser (Visser, 2004), on whose text the following paragraphs are based.

Singular Value Decomposition

A particularly useful numerical tool for the analysis of ill-conditioned problems is the Singular Value Decomposition (SVD) since it reveals all the difficulties associated with the ill-conditioning of matrix $\mathbf{A}$, e.g. see (Tikhonov and Goncharsky, 1977; Hansen, 1994). Considering the rectangular transfer matrix $\mathbf{A} \in \mathbb{R}^{m \times n}$, the SVD of this matrix is written

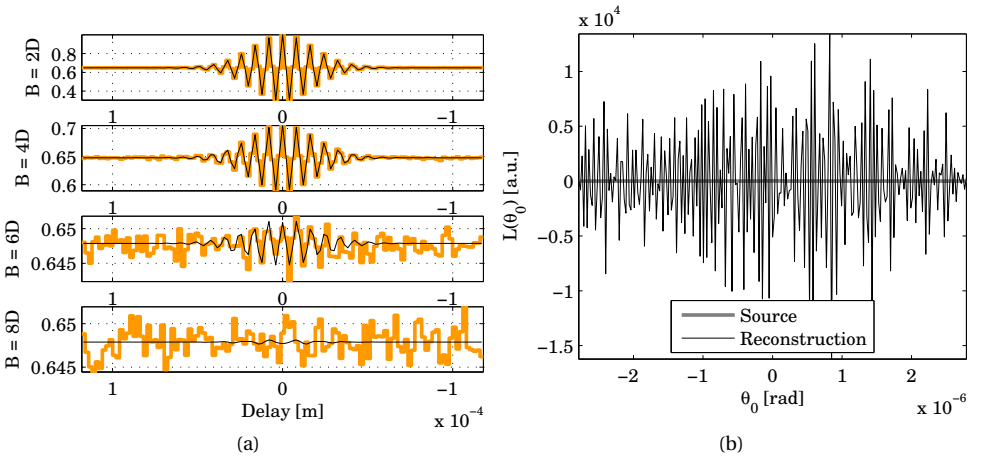

Figure 4.1: Naive inversion of interferometric data. Panel (a) shows a re-organized measurement vector $\mathbf{b}$, resembling intensity interferograms recorded at four different baseline lengths, obtained as $\mathbf{b} = \mathbf{A} \cdot \mathbf{x}$, where $\mathbf{x}$ is a source function $L(\theta_0)$. The results are then photon-quantized. Panel (b) then shows the naive reconstruction $\hat{\mathbf{x}} = (\mathbf{A}^{\mathrm{T}}\mathbf{A})^{-1}\mathbf{A}^{\mathrm{T}} \cdot \mathbf{b}$, where the 'pseudo inverse' or Moore–Penrose inverse is used since $\mathbf{A}$ is not square. The result is an estimate $\hat{L}(\theta_0)$ of very high magnitude (10^4 instead of 1), with a large number of sign changes.

as

$$\mathbf{A} = \mathbf{U} \cdot \mathbf{S} \cdot \mathbf{V}^{\mathrm{T}} = \sum_i \mathbf{u}_i \sigma_i \mathbf{v}_i^{\mathrm{T}}. \tag{4.2}$$

In the case of an overdetermined system ($m > n$), matrix $\mathbf{U}$ is of dimensions $m \times n$ and $\mathbf{V}$ is of $n \times n$. For an underdetermined system ($m < n$), $\mathbf{U}$ is of dimensions $m \times m$ and $\mathbf{V}$ of $n \times m$. In both cases $\mathbf{U}$ and $\mathbf{V}$ are unitary matrices—$\mathbf{U}^{\mathrm{T}} \cdot \mathbf{U} = \mathbf{I}_m$ and $\mathbf{V}^{\mathrm{T}} \cdot \mathbf{V} = \mathbf{I}_n$—with their columns representing the left and right singular vectors $\mathbf{u}_i$ and $\mathbf{v}_i$, respectively:

$$\mathbf{U} = \left[\mathbf{u}_1\ \mathbf{u}_2\ \cdots\ \mathbf{u}_{\min(m,n)}\right] \text{ and } \mathbf{V} = \left[\mathbf{v}_1\ \mathbf{v}_2\ \cdots\ \mathbf{v}_{\min(m,n)}\right]. \tag{4.3}$$

The nonnegative and real singular values σ_i are collected on the diagonal of matrix $\mathbf{S} = \mathrm{diag}\left(\sigma_1\ \sigma_2\ \cdots\ \sigma_{\min(m,n)}\right)$ in descending order such that $\sigma_1 \geq \sigma_2 \geq \cdots \geq \sigma_{\min(m,n)} \geq 0$.

The condition number of $\mathbf{A}$ equals the ratio of the largest and smallest singular value $\sigma_1/\sigma_{\min(m,n)}$. This ratio is a measure for the sensitivity of the solution to perturbation errors in matrix $\mathbf{A}$ or the right-hand side $\mathbf{b}$. It has to be remarked that the SVD presented in Eq. (4.2) is a so-called 'economy-sized' type of decomposition, i.e. the singular values and vectors associated with the null-space of matrix $\mathbf{A}$ are intentionally left out of consideration.

In connection with discrete ill-posed problems, three characteristic features of the SVD of $\mathbf{A}$ are often found (Hansen, 1990; Hansen, 1994; Hansen, 1998; Visser, 2001):

1. The singular values σ_i decay gradually to zero with no particular gap in the spectrum.

2. The condition number of $\mathbf{A}$ is large.

3. The left and right singular vectors $\mathbf{u}_i$ and $\mathbf{v}_i$ tend to have more sign changes in their elements as index i increases. In other words, for the lower values of σ_i the singular vectors become more oscillatory.

These characteristics are confirmed by the decomposition of the imaging transfer matrix, e.g. the multiple baseline homothetic interferometer transfer matrix. Figure 4.2 clearly illustrates the gradual decay of the singular values σ_i. Moreover, the condition number spans several orders of magnitude.

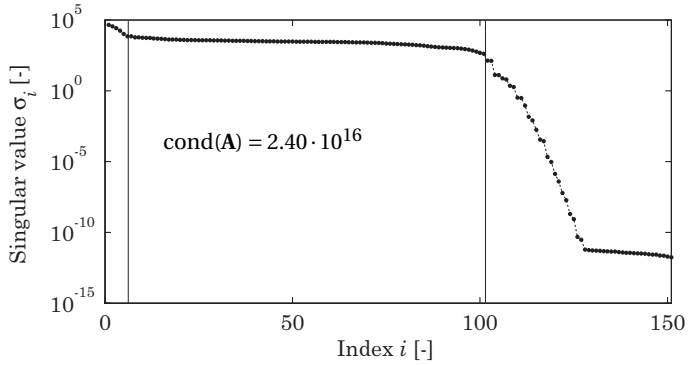

Figure 4.2: Singular value spectrum of an 1592×151 image transfer matrix **A**, as in Equation (4.1).

In Fig. 4.3 it is confirmed that the left and right-hand singular vectors indeed contain more oscillations as the index of the singular value increases. In the case of an interferometric transfer matrix, the modes can be separated into three regimes, based on their index i:

- For indices $1 \leq i \leq n_{\text{PSFs}}$, where n_{PSFs} is the number of incoherent PSFs fitting in the field-of-view, the modes relate to the low-resolution or incoherent image of the sky.
- The modes for indices $n_{\text{PSFs}} < i < i_B$, where the major spatial frequency of the mode with index i_B relates to the maximum baseline length $B_{\max}$, are the modes related to the interferometric character of the array.
- The region of indices $i > i_B$ contains modes of very high spatial frequency, which do not physically relate to the source nor the measurement, since these spatial frequencies are not sampled. This occurs when the discretization step size ($\theta_0^{(2)} - \theta_0^{(1)}$) is smaller than the smallest spatial period that is sampled, $\lambda_{\min}/B_{\max}$.

Clearly, the latter set of modes (related to the smallest singular values σ_i) has to be banned in all cases from the construction of a solution to the inverse problem.

The SVD also gives important insight into another aspect of ill-conditioned problems, namely the smoothing effect. This is typically associated with integral kernels encountered in many physical problems (Hansen, 1994; Hansen, 1998). For example, consider the mathematical mapping $\mathbf{b} = \mathbf{A} \cdot \mathbf{x}$ of an arbitrary vector $\mathbf{x}$. Application of the SVD yields

$$\mathbf{b} = \mathbf{U} \cdot \mathbf{S} \cdot \mathbf{V}^{\mathrm{T}} \cdot \mathbf{x}, \text{ or alternatively, } \mathbf{b} = \sum_i \sigma_i \left(\mathbf{v}_i^{\mathrm{T}} \cdot \mathbf{x} \right) \mathbf{u}_i. \tag{4.4}$$

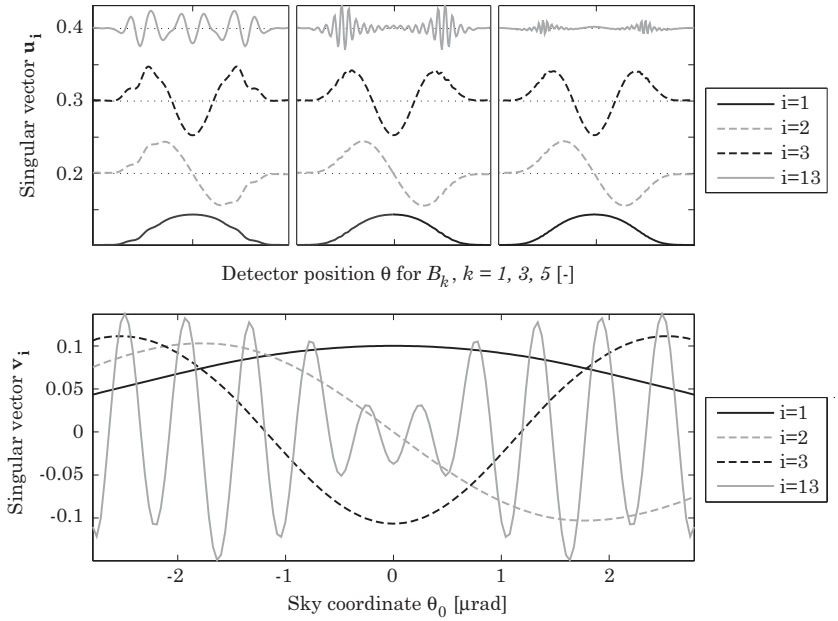

Figure 4.3: Singular vectors show more oscillations for higher index i. Vectors $\mathbf{u}_i$ can be interpreted as *measurement modes* whereas vectors $\mathbf{v}_i$ represent *source modes*. The vectors $\mathbf{u}_i$ are plotted with off-sets, both in the horizontal and vertical direction, and only for three baselines B_k, where $k = 1,3,5$.

The product $\mathbf{v}_i^{\mathrm{T}} \cdot \mathbf{x}$ can be interpreted as a measure for the spatial matching (or participation factor) between singular vector $\mathbf{v}_i$ and vector $\mathbf{x}$. With this knowledge and recalling that the singular vectors $\mathbf{u}_i$ and $\mathbf{v}_i$ become more oscillatory as σ_i decreases, it is obvious that the multiplication with σ_i leads to more damping of the high-frequency components of $\mathbf{x}$ and less damping of the low-frequency components in the map $\mathbf{A}\cdot\mathbf{x}$. As a consequence, in forward problems the solution $\mathbf{b}$ is generally smoother than the prescribed vector $\mathbf{x}$.

In contrast, the inverse problem (containing $1/\sigma_i$) will show the opposite effect, amplifying the high-frequency oscillations in the right-hand side $\mathbf{b}$. Owing to the smoothing characteristics of the forward problem, noise often has a relatively strong contribution to the high-frequency oscillations in $\mathbf{b}$. Therefore, especially the noisy components are subjected to a large amplification in the inverse process.

Concluding, the forward operation of mapping input vector $\mathbf{x}$ onto output vector $\mathbf{b}$ has a smoothing effect on $\mathbf{x}$, whereas the opposite operation tends to amplify oscillations in vector $\mathbf{b}$. Hence, if a solution of $\mathbf{x}$ is required with a limited L_2-norm, then not all distributions $\mathbf{b}$ form a valid right-hand side. In fact, vector $\mathbf{b}$ must be sufficiently smooth to 'survive' the inversion back to a physically meaningful $\mathbf{x}$. The mathematical formulation of this smoothness criterion on $\mathbf{b}$, given a certain kernel or transfer matrix, is known as the *Discrete Picard condition* (Hansen, 1990; Hansen, 1998).

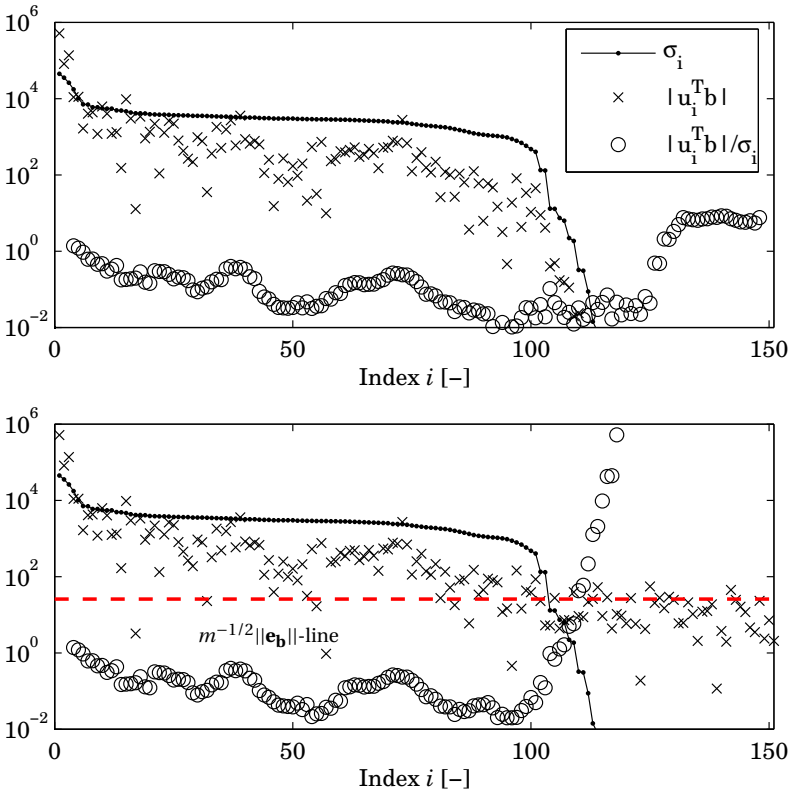

Figure 4.4: Visualization of the discrete Picard condition for an interferometric transfer matrix. **Top panel:** The problem satisfies the criterion as the exact Fourier coefficients (×) decay faster than the singular values (·). **Bottom panel:** With noise present, the Fourier coefficients $\left|\mathbf{u}_i^T \cdot \mathbf{b}\right|$ level off at $m^{-1/2}||\mathbf{e_b}||$.

Discrete Picard condition

Throughout this chapter the errors in the given problem $\mathbf{A} \cdot \mathbf{x} = \mathbf{b}$ are restricted to the right-hand side $\mathbf{b}$ and hence the assumption is made that the transfer matrix forms an accurate description of the actual physical system. An amount of noise is added to the data vector

$$\mathbf{b} = \bar{\mathbf{b}} + \mathbf{e_b}, \text{ with } \bar{\mathbf{b}} = \mathbf{A} \cdot \bar{\mathbf{x}}, \tag{4.5}$$

where $\bar{\mathbf{b}}$ represents the exact unperturbed measurement data, $\bar{\mathbf{x}}$ is the corresponding exact solution and vector $\mathbf{e_b}$ represents the errors in the data.

According to Hansen (Hansen, 1990), a regularized solution $\mathbf{x}_{\text{reg}}$ that approximates the exact solution $\bar{\mathbf{x}}$ is obtained if the corresponding exact right-hand side $\bar{\mathbf{b}}$ satisfies the *discrete Picard condition*:

> The unperturbed right-hand side $\bar{\mathbf{b}}$ in a discrete ill-posed problem satisfies the discrete Picard condition if the exact Fourier coefficients $\left|\mathbf{u}_i^T \cdot \bar{\mathbf{b}}\right|$ on the average decay faster toward zero than the singular values σ_i. Fulfillment of

this condition ensures that the exact, unknown, solution $\bar{\mathbf{x}}$ can be approximated by a nearby regularized solution $\mathbf{x}_{\text{reg}}$.

In practice, the errors in the right-hand side arise from many sources, e.g. measurement, rounding and approximation errors and in the case of light also the quantized nature of the arrival of photons. Consequently, these errors typically tend to have components in each left singular vector $\mathbf{u}_i$ or measurement mode. As explained by Hansen (Hansen, 1990), if the elements of $\mathbf{e_b}$ are unbiased and uncorrelated, then the expected values $\mathscr{E}$ of the Fourier coefficients of $\mathbf{e_b}$ satisfy

$$\mathscr{E}\left(\left|\mathbf{u}_i^{\mathrm{T}} \cdot \mathbf{e_b}\right|\right) = m^{-\frac{1}{2}} ||\mathbf{e_b}||, \; i = 1, \ldots, \min(m,n). \tag{4.6}$$

For this reason the perturbed Fourier coefficients $\left|\mathbf{u}_i^{\mathrm{T}} \cdot \mathbf{b}\right|$ level off at $m^{-\frac{1}{2}}||\mathbf{e_b}||$ approximately, even if the unperturbed right-hand side $\bar{\mathbf{b}}$ satisfies the discrete Picard condition, because these Fourier coefficients are dominated by $\left|\mathbf{u}_i^{\mathrm{T}} \cdot \mathbf{e_b}\right|$ for large i. This is illustrated in Fig. 4.4.

Naively solving the inverse problem results in constructing the least squares solution. With the SVD as defined in Eq. (4.2) this solution can be written as

$$\mathbf{x}_{\text{LS}} = \sum_i \frac{\mathbf{u}_i^{\mathrm{T}} \cdot \mathbf{b}}{\sigma_i} \mathbf{v}_i, \tag{4.7}$$

where the factors $\mathbf{u}_i^{\mathrm{T}} \cdot \mathbf{b}/\sigma_i$ represent the contribution of each singular vector $\mathbf{v}_i$ (source mode) in the least squares solution $\mathbf{x}_{\text{LS}}$. If now the Fourier components $\left|\mathbf{u}_i^{\mathrm{T}} \cdot \mathbf{b}\right|$ are leveled off at a noise floor, they cannot decay as fast as the singular values σ_i. The direct consequence is that the solution $\mathbf{x}_{\text{LS}}$ is dominated by terms in the sum corresponding to the smallest singular values σ_i; thus, the shape of the solution is mainly determined by the source mode shapes $\mathbf{v}_i$ associated with large i. Since these mode shapes have a highly oscillatory nature, the solution appears to be completely random. Apart from the many oscillations, the magnitude of the solution $\mathbf{x}_{\text{LS}}$ usually ends up being extremely large owing to the division by the very small singular values. This knowledge clarifies that the purpose of regularization is to dampen or filter out the contributions to the solution corresponding to the small singular values.

4.3 Regularization

Truncated Singular Value Decomposition

Once it is known that the ill-behavior is related to the smallest singular values σ_i, the most obvious cure is to simply truncate the number of terms in the solution $\mathbf{x}_k$:

$$\mathbf{x}_k = \sum_{i=1}^{k} \frac{\mathbf{u}_i^{\mathrm{T}} \cdot \mathbf{b}}{\sigma_i} \mathbf{v}_i, \text{ with } k \leq \min(m,n). \tag{4.8}$$

This truncation effectively eliminates the influence of all singular vectors $\mathbf{v}_i$ associated with singular values smaller than σ_k. Essentially, the TSVD approach replaces the ill-conditioned transfer matrix $\mathbf{A}$ with a new well-conditioned, but rank deficient, matrix $\mathbf{A}_k$ (Hansen, 1998).

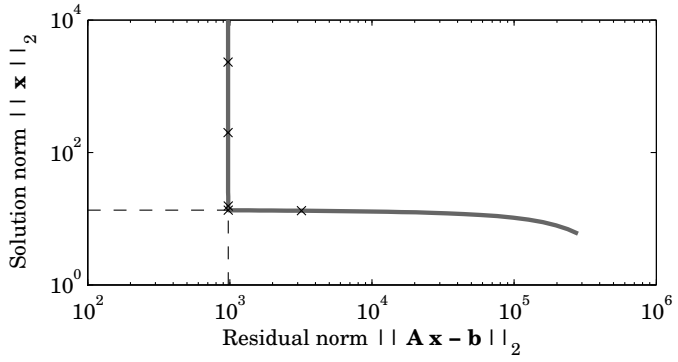

Figure 4.5: The 'L-curve' is a method to blindly find the optimum regularization parameter Λ. The norms $\|\mathbf{A}\cdot\mathbf{x}_\Lambda - \mathbf{b}\|$ and $\|\mathbf{x}_\Lambda\|$ are plotted for a range of Λ-values. The corner is found as the minimum radius of curvature in a spline-fit through the calculated points.

Tikhonov regularization

Tikhonov regularization (Tikhonov and Goncharsky, 1977) is probably the most popular and well developed method to handle discrete ill-posed problems. It differs from the TSVD approach in the fact that the initial ill-conditioned problem is solved simultaneously with a side constraint imposed on certain properties of the sought solution (Hansen, 1994). These constraints are usually associated with smoothness properties of the solution since ignoring contributions related to small singular values leads to a smoother solution with a reasonable L_2-norm. In discrete problems, the problem of Tikhonov regularization takes the form

$$\min_{\mathbf{x}} \left\{ ||\mathbf{A}\cdot\mathbf{x} - \mathbf{b}||^2 + \Lambda^2 ||\mathbf{L}\cdot\mathbf{x}||^2 \right\}, \tag{4.9}$$

where $\mathbf{L}$ represents the so-called regularization matrix. For a discussion of choosing the smoothing operator $\mathbf{L}$, the reader is referred to the work by Visser (Visser, 2004) on acoustical transfer matrices.

The most simple form of Eq. (4.9) is obtained with $\mathbf{L} = \mathbf{I}$. The Tikhonov regularized solution can in combination with the SVD be written as

$$\mathbf{x}_\Lambda = \sum_i \frac{\mathbf{u}_i^{\mathrm{T}} \cdot \mathbf{b}\sigma_i}{\sigma_i^2 + \Lambda^2} \mathbf{v}_i. \tag{4.10}$$

The regularization parameter Λ is chosen to lie between the largest and the smallest singular values. Like the TSVD approach, the Tikhonov method acts as a low-pass filter in the singular value spectrum, be it that TSVD manifestates an abrupt cut-off, whereas the filter spectrum in the Tikhonov case shows a gradual decline. Regularization of a linear inverse problem now comes down to finding the regularization parameter Λ, so that the norms

$$\|\mathbf{A}\cdot\mathbf{x}_\Lambda - \mathbf{b}\| \text{ and } \|\mathbf{x}_\Lambda\|, \tag{4.11}$$

respectively the data misfit-norm and the solution norm, are small. Figure 4.5 plots these two norms against each other, for a range of values of Λ. The result is a plot that clearly has an L-shape, as is generally the case for ill-posed discrete inverse problems (Hansen,

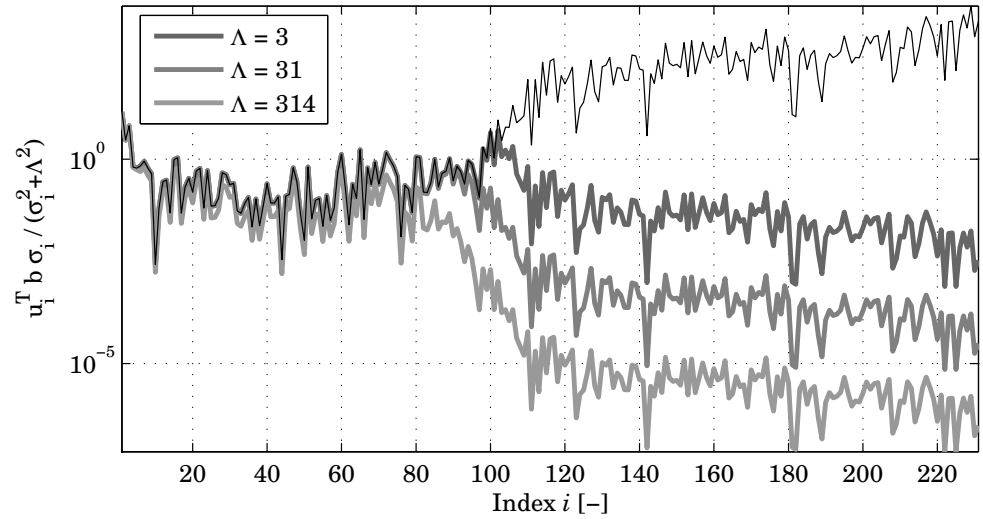

Figure 4.6: A plot of the mode participation, expressed as $\mathbf{u}_i^T\mathbf{b}/\sigma_i$, for a mode with index i. The thin line (no regularization, $\Lambda = 0$) shows that indeed the participation of noise-sensitive higher modes is strong. The thick lines show the regularized mode participation for $\Lambda = \Lambda_{\text{opt}} \cdot (\frac{1}{10}, 1, 10)$.

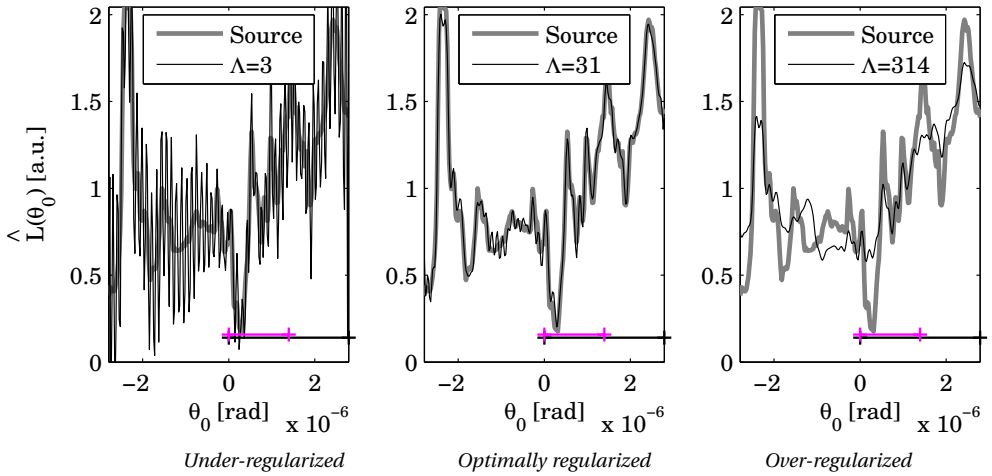

Figure 4.7: The estimates $\hat{L}(\theta_0)$ for $\Lambda = \Lambda_{\text{opt}} \cdot (\frac{1}{10}, 1, 10)$. In the figure, the size of the detector pixels in angular measure is indicated (short horizontal line), as well as the approximate size of the single-dish-diffraction envelope (long horizontal line).

1992). In the corner, the sum of the two norms is smallest, meaning that the corresponding Λ minimizes the expression in Eq. (4.9).

With Λ found, a solution can be calculated with Eq. (4.10). The participation of the solution modes $\mathbf{v}_i$ can now be controlled. Figure 4.6 shows the participation strength $\mathbf{u}_i^{\mathrm{T}} \cdot \mathbf{b}\sigma_i/(\sigma_i^2 + \Lambda^2)$ for three values of Λ, corresponding to an under-regularized solution, an optimally regularized solution and an over-regularized solution. In Fig. 4.7, the corresponding regularized solutions are plotted. Respectively, these show an estimate with

amplification of noise (under-regularization), an optimal estimate and an estimate, unable to recover sharp edges ('over-smoothing' due to over-regularization).

With the regularization tools in place, optimal estimates can automatically be obtained from photon-starved or otherwise degraded interferometric measurements. The transfer of stellar information through any of the four presented interferometers into interferometric signals can be described and stored in a single transfer matrix **A**. For various sources $L(\theta_0)$ and changing observation times, each interferometer will produce simulated measurements, from which optimal reconstructions $\hat{L}(\theta_0)$ are produced. The next Chapter will present detailed results of these simulations.

Chapter 5

Comparison of imaging interferometers

In this chapter, the four beam combination schemes and detector configurations for interferometric imaging, that have been discussed in the previous chapters, will be compared. The working principles as explained in Chapters 2 and 3 will be simulated. For every array, the same observation is simulated: the same source is observed with the same set of baseline lengths, for the same total observation time. The same image reconstruction algorithm is used for all four interferometers, so that this comparison is not relying on the strengths of optimized or better developed algorithms for one interferometer type. After a discussion on the implementation of noise in the simulations in Sec. 5.1, the simulation process is detailed in Sec. 5.2 for the two classical types, having perfect detectors. This illustrates that detection signals of very different nature can produce the same image with the same reconstruction algorithm. In Section 5.3, two other methods are included in the comparison, together with the introduction of realistic readnoise for observations with a CCD camera.

5.1 Photon-starved regime

Optical interferometers observe weak stellar sources and are therefore said to operate in the photon-starved regime. To adequately simulate low-light level observations, a noise model considering the statistics of photon arrival is a necessity. Moreover, since the detected data are the start of an inversion process, these data should represent realistic noisy recordings since the inversion and hence the final image formation shall be limited by the noise level in the recordings. Therefore, the noisy read-out process of an infrared detector array is also simulated.

The analytical expressions for the intensity detector response, derived in Chapter 2, predict the 'image' that the detector array will observe. However, this pattern will only be observed for very bright sources, when unlimited amounts of photons are available. The response of a weak source, such as the astronomical objects of interest, is better expressed by the arrival of photons from the object, at a certain location and at certain time intervals. Figure 5.1 illustrates this for a few arrival events. The analytical intensity distribution $I(\theta, d)$ is now seen as a *likelihood distribution* over space and time, where

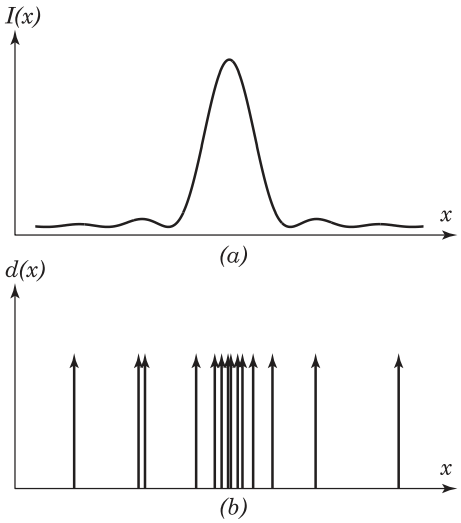

Figure 5.1: Classical and detected images: *(a)* classical image intensity $I(x)$; *(b)* detected image $d(x)$. From: *Statistical Optics* (Goodman, 1985).

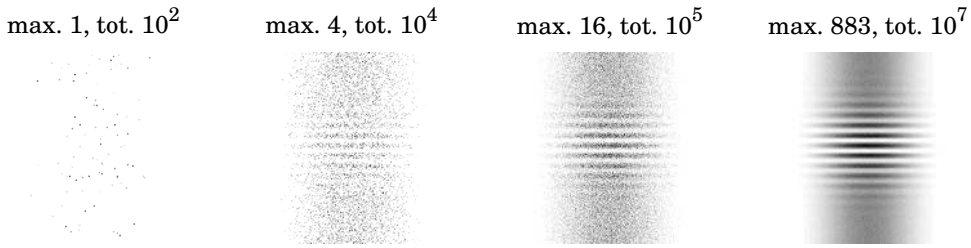

Figure 5.2: A polychromatic fringe pattern $I(\theta, d)$ out of a co-axial two-aperture interferometer. The images from left to right show observations of the theoretically predicted fringe pattern, moving from a photon-starved to a photon-rich regime. The maximum amount of photons per bin is indicated (max.) as well as the provided total amount of photons (tot.). These examples exhibit zero detector noise.

time is in this case the applied delay d. Time-dependency stems from the shot-noise, which is the arrival probability of a photon. This probability follows Poisson statistics[1], so that the probability P of a certain integer number k of unit rate Poisson random events occurring in a given interval of time t is

$$P_t(k) = e^{-\lambda t} \frac{(\lambda t)^k}{k!}, \tag{5.1}$$

where λ is a constant, defined as the average time between events (Papoulis, 1991), which is a measure for the photon flux. The analytical intensity response defines the average fluxes in all bins ('tiles' in (θ, d)-space), being pixels and delay settings. For each

[1]The statistical behaviour is only Poissonian, if the observation time t_{obs} is larger than the coherence time, $t_{\text{obs}} > t_c$ where t_c is defined as l_{coh}/c_0. The integration time for a stellar observation will be at least in the order of seconds, whereas the coherence time is in the order of femtoseconds.

bin, with its average flux, the number of photons per readout (after an integration time t_{int}) is then discretized, in such a way that the total number of photons is a specific desired amount N_{tot}, that can be chosen to match the integration time t_{int} and the magnitude m_v of the stellar object. The simulated amount of photons per bin (pixel and delay) is then returned, based on the calculated average amount, by an implementation of the Poisson statistics, as described in *Numerical Recipes* (Press *et al.*, 1989). A few examples are depicted in Fig. 5.2.

Thermal radiation of other origin than the stellar object, for example warm telescope optics, cause the presence of background counts, which are also Poisson distributed. Readout noise (the electronics register non-existing photons) further contributes to the degradation of the acquired images. This noise is characterized as a Gaussian random process. Note that the quantum efficiency of the detectors makes that not all photons are transferred to electrons for measurement. The image data acquired by a CCD camera can be expressed as (Snyder *et al.*, 1995)

$$r(j) = n_{\text{obj}}(j) + n_0(j) + g(j),\ j = 1,2,\ldots,J, \tag{5.2}$$

where $r(j)$ are the data acquired by a readout of pixel j of the CCD camera array, $n_{\text{obj}}(j)$ is the number of object-dependent photoelectrons, $n_0(j)$ is the number of background electrons, $g(j)$ is readout noise, and J is the number of pixels in the CCD camera array. Since the radiation from the object and the background are indistinguishable and follow the same statistics, there is no need to account for this noise in the simulations, other than taking a source $L(\theta_0)$ that incorporates a certain background level. For the readout noise, an actual camera should be considered, in order to arrive at a sensible mean value for the amount of electrons (photon arrival events can also be expressed in electrons) added to the detected count, and a proper standard deviation.

As an example, the IRAC camera for the Spitzer Space Telescope is considered (Fazio *et al.*, 2004; Hora *et al.*, 2000). The measured total read noise can be taken to have a mean $\mu = 15$ electrons (e^-) and a variance $\sigma^2 = 8\ e^-$. Note that these values are depending on gain setting and numerous device-dependent parameters. The mean value is usually subtracted from the data, which may result in negative values or counts in the detected signals.

It should be noted that in interferometry, 'background' signal is also generated by the source itself. In a polychromatic situation, the 'incoherent' tails of two fringe packets may cause the summed intensity pattern to have a large non-modulating component. For the detector signal, the modulating part holds the information. The background hence contains 'non-information', but the classical definition of background would be 'information from elsewhere than the source'.

5.2 Comparison for perfect detectors

In this study, only the two classical beam combination schemes are chosen. Co-axial combination is the most common type (Shao and Staelin, 1977) whereas the homothetic combination type (Angel *et al.*, 1998) is often referred to as the only one being capable of covering a wide field-of-view. The two modeled arrays are addressed as 'Multipixel Michelson' and 'Fizeau'. The collection and combination schemes are depicted in Fig. 5.3 for the case that there is no beam compression.

To illustrate the principles used here in the simulation and analysis more easily, only a two-element interferometer is considered. This means that the high angular resolution

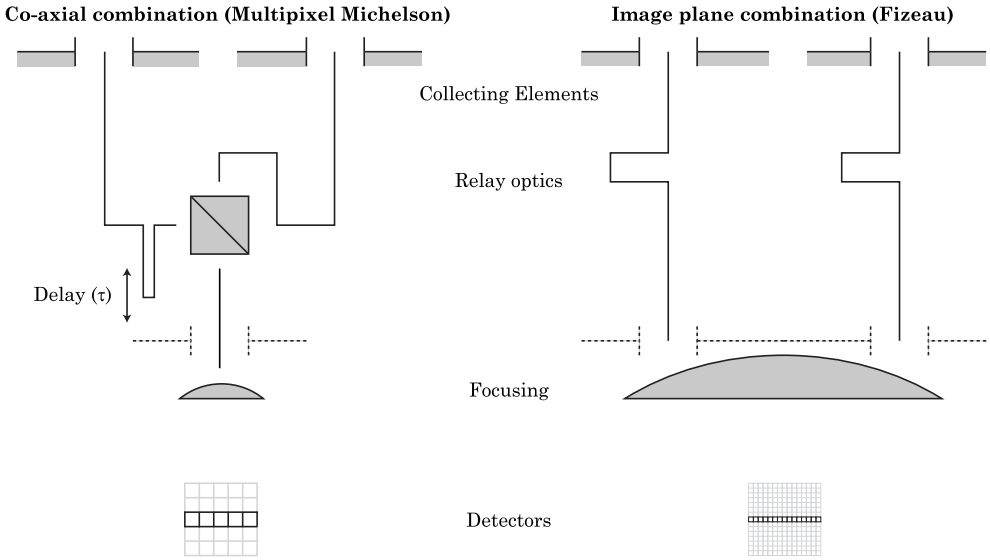

Figure 5.3: Two types of beam combination for optical aperture synthesis: co-axial combination for 'Multipixel Michelson' and image plane combination 'Fizeau'. The necessary number of pixels in the detector is indicated schematically.

is only attained in one direction. Therefore, all simulations are one dimensional. The detector is a line-detector; the source is a *linear* luminosity distribution on the sky. The source that is used as an example in the simulation, is depicted in Fig. 5.4. This is the young galaxy UGC00597, as observed by the Hubble Space Telescope. The dimensions of the object are chosen to be ~2 PSFs and the detector array to cover ~3 PSFs. The dish diameter $D = 3.5$ m and a central wavelength $\lambda_c = 10\mu$m result in an angular PSF diameter of 7 μrad. The cross-section in the figure indicates the linear luminosity function that is actually used in the simulation. The PSF size is indicated and the narrowest feature in the source is about 1/16th of this diameter. Therefore, the sampled baseline lengths will be limited to $16D$. The number of resolution elements in the simulated source is 231, with a spacing that is not necessarily resolvable by the synthetic aperture. Other specifications of the simulation parameters for both arrays are listed in Table 5.1. The divisions by 4 indicate that a fringe is sampled in respectively 4 delay bins or 4 detector pixels.

Table 5.1: Measurement settings for simulations

Case	Pixels	Pixel Size	OPD Range	OPD Step
Michelson	6 (3 PSFs)	$\simeq$ PSF/2	$2B_{\max}\theta_{\max}$	$\lambda_c/4$
Fizeau	235 (3 PSFs)	$PSF\frac{D}{B_{\max}}/4$	—	—

The simulated telescope array is considered to be consisting of two free-flying telescopes of ESA's Darwin mission. The beam combiner for the nulling task is replaced by

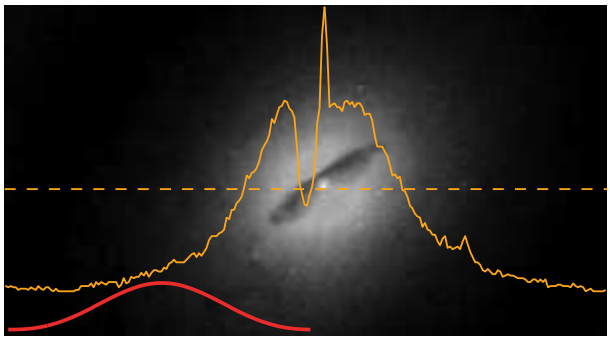

Figure 5.4: The young galaxy UGC00597 (Hubble Space Telescope image). The dashed line indicates the position of the slice of the image of which the pixel values were used as linear luminosity distribution $L(\theta_0)$. The thick line represents this function. The angular dimension of this source was set to be twice the diffraction-limited spot size of a single telescope (indicated with a thick line), the resolution limit without interference.

the simulated beam combiner. The alignment requirements for nulling in the Darwin mission provide a co-phased array with all metrology necessary to fulfill the needs for image overlap and fringe stability to a degree that is far beyond the needs for imaging. Therefore, no fringe shifts are assumed in this simulation and diffraction limited PSFs are assumed for all beams. Given the Darwin hardware, a number of interesting targets for imaging has been acquired. This led (see Chapter 1) to the imaging requirements listed in table 5.2.

Table 5.2: Darwin imaging requirements

Requirement	**Specifications**
Flux	1 μJy per hour
Bandwidth	4 … 28 μm
Field-of-View	3 arcsec (= 14.5 μrad)
Resolution	1 mas (= 4.9 nrad)
Dynamic range	1 : 100
Spectral Resolution	200 bands

1 Jy (Jansky) = $10^{-26} W m^{-2} Hz^{-1}$

The complete wavelength range will be covered in a few channels, typically half octaves. For the simulation, the range is $\lambda = 8 \ldots 12$ microns. This range has no astrophysical reason, it is just taken as a broad-band range and the spectrum is shaped by a Gaussian envelope. In the current Darwin design, the telescope primaries have a diameter $D = 3.5$ meter. This yields a PSF with an angular diameter on the sky of $d_{\text{Airy}} = 2.44\lambda_c / D = 7$ μrad, so the desired FOV is as large as two PSFs.

As discussed before, to model the detector response of such a source for the co-axial type, the 'traditional' fringe modulation prediction according to the restricted quasi-monochromatic theory of partial coherence (Born and Wolf, 1980) as applicable to radio interferometry could not be used. This theory assumes a narrow bandwidth, a stellar object

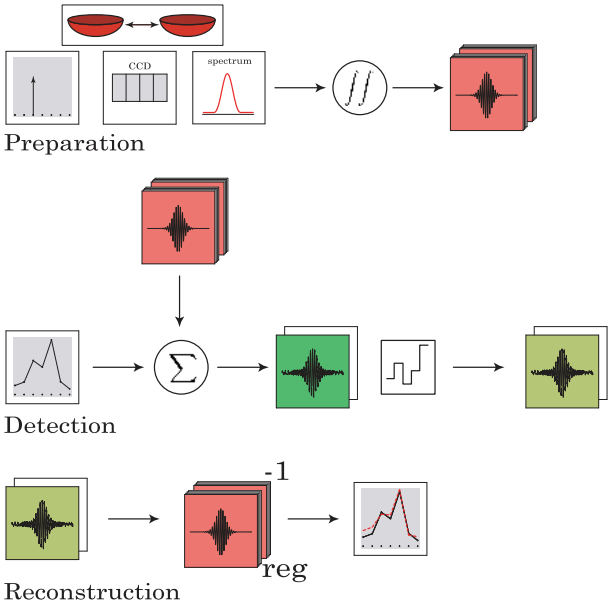

Figure 5.5: Flowcharts of the stages in the simulation process: Preparation, Detection and Reconstruction. The **Preparation** phase is the calculation of the response of the interferometer, based on the type of beam combination, the baseline configurations and the locations of source points and detector pixels. The output is a transfer matrix. With this matrix, the **Detection** can be performed, consisting of summing the weighted point source response functions and applying a discretization to the sum. Here, photon statistics and detector noise are applied and one signal per baseline configuration results. Finally, the **Reconstruction** takes the measured data and the transfer matrix. Without knowledge of the source, an optimal reconstruction of the sky is produced by multiplication of the noisy measurement with a regularized inverse of the transfer matrix.

no larger than the single-dish PSF and point-like collecting elements in stead of telescopes with a certain diameter. These assumptions are not applicable to the intended observation. The FOV larger than a PSF and the coherence length of only a few times the central wavelength, require the response function approach. The simulation process, based on response functions collected in a transfer matrix, is illustrated in Fig. 5.5.

5.2.1 Shot-noise limited detection

Recent developments in detector technology have led to CCDs for low light levels that can be assumed to provide shot noise limited read-out signals (Mackay *et al.*, 2001). Perfect quantum efficiency is assumed and there is no thermal or detector noise. To simulate shot noise limited interferometer responses, the theoretical intensities $I_{jk}(d)$ and $I_k(\hat{\theta})$ are treated as temporal and spatial *probability distributions* (Goodman, 1985). The photons will arrive with Poisson-distributed interval times and will be spatially distributed as well. The realization of the photon statistics is implemented according to the *Rejection Method* (Press *et al.*, 1989) that will iteratively create a measurement vector with the theoretical intensity as distribution and Poisson statistics as input. The observation time of the weak source is expressed as a total number of received photons, yielding 10^8 as an amount for high SNR observations. The detected signals with 10^8 photons are dis-

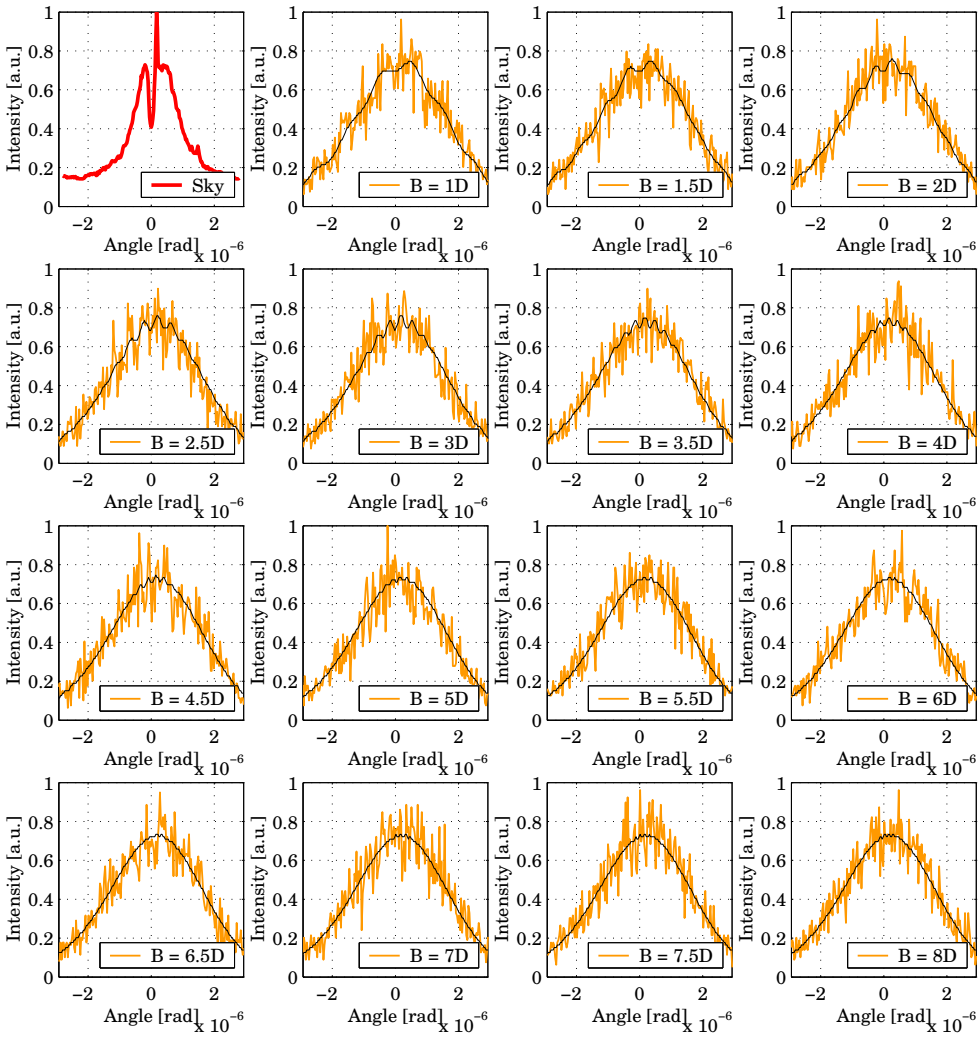

Figure 5.6: Tabular display of all **Fizeau** convolution results $I_k(\theta)$, the recorded intensities (photon counts) per pixel for each baseline length. The number of pixels is 256. The baseline lengths are $B = D \cdot [1, \ldots 8]$ in steps of $D/2$. For these sketches, the number of photons was 10^5, to illustrate the characteristics of the detector signals. The measurements are all normalized to one value, whereas the function on the sky is normalized to itself. The modulation amplitude as compared to the envelope is about 8% at best, since the source is partially resolved.

played in Figs. 5.6 and 5.7. To give more detail on the bin-integration and quantization process, Fig. 5.8 was included as well. Here, the theoretical intensity is plotted over the 'recorded' photon counts (also expressed as intensity) for the co-axial case.

5.2.2 Comparison of shot-noise limited classical beam combiners

It should be noted that both sets of intensity data resemble each other a lot. Compared to the short period of the fringes, the average signals in both the Michelson and the Fizeau

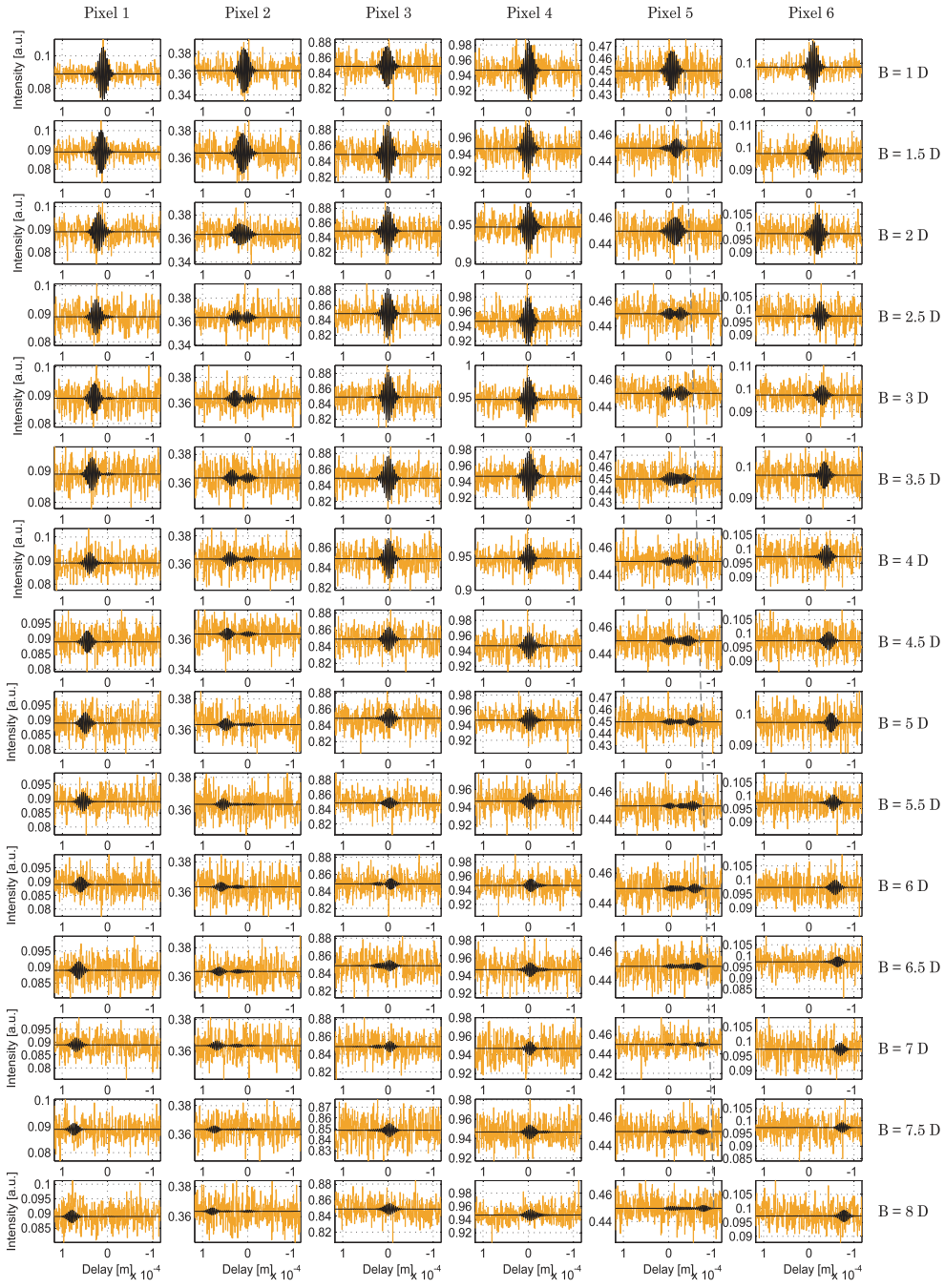

Figure 5.7: Tabular display of all **Michelson** $I_{jk}(d)$, the recorded intensities (photon counts) per pixel for each baseline length. The number of pixels is 6, the number of delay steps is 117. The baseline lengths are $B = D \cdot [1, \ldots 8]$ in steps of $D/2$. The fringes are sampled with 6 samples per λ_c and the total scan range ensures the 'coverage' of fringe packets for the longest baseline configuration on the outermost detectors. Observe the envelope lengthening for growing B, as indicated with the dashed line in the column for Pixel 5.

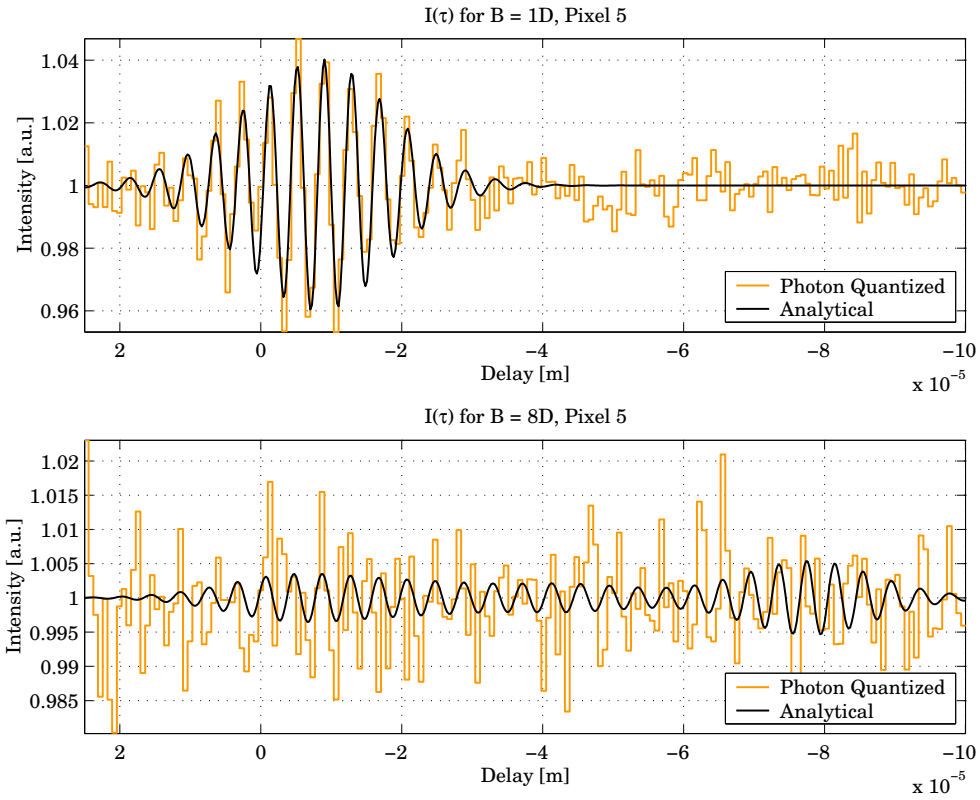

Figure 5.8: Detailed plot of two $I_{jk}(d)$, the recorded intensities (photon counts) per delay bin, for pixel $j = 5$ and baselines $k = 1, 15$, or $B = 1D$ and $B = 8D$, respectively, cf. Fig. 5.7. The period in each fringe packet is λ_c. Three effects appear very clearly from these plots. Firstly, the phase of the fringes with respect to the envelope changes, which is in accordance with experiences from narrow field imaging. Secondly, the length of the fringe packet changes with baseline length. Finally, the shape of the envelope changes. To generate an image of the sky from these data, the three mentioned features must be included in the inversion process. A joint deconvolution of all collected intensity traces does just this. The modulation $1.04 - 0.96$ as compared to the average normalized signal 1 is again about 8% at best, as for the Fizeau case (Fig. 5.6).

case, can be assumed to be constant, even for the long-period-envelope in the Fizeau case. Hence, both of these signals represent a strong background signal with a small amplitude modulation on it. The difference is only that the modulation is either in d- or θ-direction. As a result, the expected performance for inversion will be quite the same. For low light levels, the number of available photons per pixel or per delay bin goes down and this limits the reconstruction.

The number of pixels for homothesis is related to the desired ultimate resolution. The number of bins for co-axial combination is *just as well* related to the ultimate resolution. In the first case, the spatial period of the fringes gets smaller for larger baselines and these fringes should remain resolvable. For the other case, the fringe period is a constant, but the central location of the fringe packet and the extent of it grow for larger baselines and hence more bins are needed to sample it.

Without a compensation scheme (Montilla *et al.*, 2005) for the baseline length-dependent external path length difference, the 'simple' co-axial type will have a poor SNR for long baselines, just as the homothetic type. The homothetic type will have the same high number of bins (pixels) for the long as well as for the short baselines, whereas the co-axial type is allowed to have less bins for the shorter baselines. So for the photons per bin treatment of the SNR, the homothetic type has a constant value, whereas the co-axial type can have a decreasing value for growing baselines, but will end up in a SNR just as bad. Treating the SNR as the amount of modulation on top of the background signal, both types display the same decrease of SNR for growing baselines. The long baselines give the content of highest resolution in the sought image, but for both schemes, this SNR is low.

To compare the reconstruction possibilities at low light levels, the regularization routines (for blind imaging; the source is unknown) are slightly assisted in finding the optimal filtering parameter. This is done to be able to present the best possible reconstruction. It should be noted however that the optimum found by the algorithms hardly differed from the tuned one. With the proper value for the regularization parameter Λ, a few reconstructions can be produced for $\overline{\Lambda} = \Lambda \cdot [1/5,\ 1,\ 5]$. In this way, the effects of over- and under-regularization can be seen, showing up as too noisy or too smooth solutions, both resulting in a bad fit. For the reconstructions, the fit to the known object function can be given as a value ϵ. The non-normalized L^2-norm for a vector is used, given as

$$\epsilon = \frac{1}{N}\sqrt{\sum_i \left|I_i - \hat{I}_i\right|^2}, \tag{5.3}$$

where ϵ is the fit error, and I_i and $\hat{I}_i$ are the pixel intensity in the object function and the reconstruction, respectively. Some results are presented in Fig. 5.9. Note that ϵ will never reach zero—even for unlimited amounts of photons—since not all baseline lengths are sampled.

The photon counts and reconstruction quality for decreasing light levels (shorter integration times or weaker sources) are listed in Table 5.3. Note that the number of resolution elements is 231, so an $\epsilon \simeq 231$ indicates a fit where all point intensities are recovered with an average error of 1, compared to the simulated average signal level of 100, which compares to a dynamic range of 1/100.

Table 5.3: Blind imaging performance with shot noise limited detection. Simulated source: UGC00597.

Photons	ϵ_{opt} **Fizeau**	ϵ_{opt} **Michelson**	min., max. **Photons/bin Fiz**	min., max. **Photons/bin Mich**
10^8	42.6	71.7	1344, 59964	981, 13294
10^7	72.0	141.2	134, 5996	98, 1329
10^6	162.0	233.0	13, 600	10, 133
10^5	255.4	370.9	1, 60	1, 13

As predicted, the performance is nearly equal. The homothetic setup performs a bit better (reconstruction remains good down to 10^6 photons) but it should be noted that

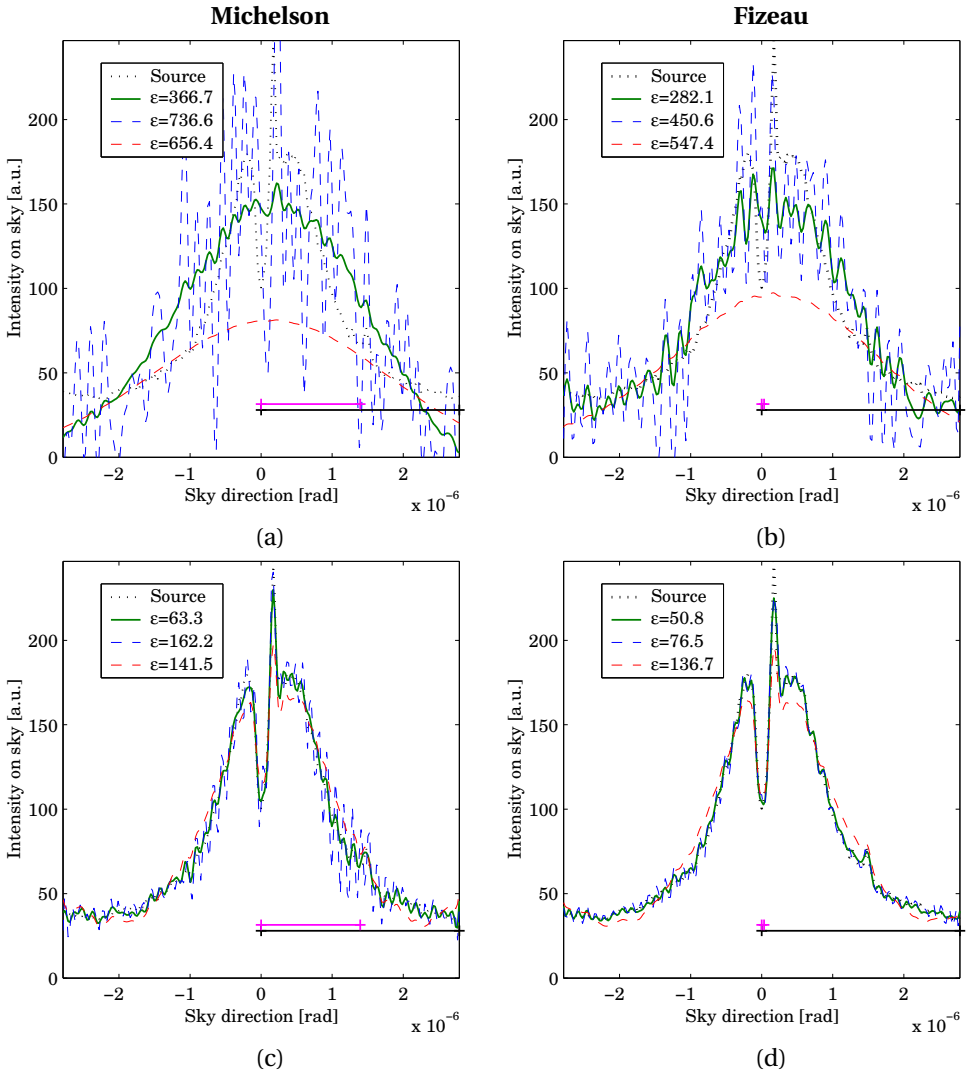

Figure 5.9: **Top row**: best blind reconstructions (continuous lines) of $L(\theta_0)$ for the 'Michelson' and the 'Fizeau' cases when 10^5 photons in total were collected. The dashed lines indicate under- and over-regularized solutions (noisy and smooth). **Bottom row**: same as top row, but now for 10^8 photons available. The ϵ-values are the L^2-norms of the differences with the now known original image; values below 231 indicate roughly a dynamic range of 1 : 100. Since the noise is different in every simulated detection–reconstruction run, the ϵ-values are not exactly equal to those displayed in Table 5.3. The horizontal lines in each plot indicate the detector pixel size and the diameter of the Airy disc, projected on the sky.

the performance of the co-axial type could be greatly improved if the scanning range—and with it the number of bins—was reduced. A solution exists in the form of a Staircase Mirror. Another way to increase the performance is to limit the background presence relative to the modulated signal, since the fringes carry the high spatial frequency information. This could naturally be done by limiting the bandpass, but that will also limit the number of photons.

The homothetic setup performs well in this simulation, but the realization of the hardware needed to produce a scalable and reconfigurable array of entrance and exit pupils is complicated (d'Arcio, 1999). However, solutions exist (Van der Avoort *et al.*, 2004b) for providing enough image and fringe stability to allow the assumption of a field-invariant convolution kernel. Should the kernel be field-*variant* in a known way, then imaging can still be performed, be it that the interferometric FOV is not as large as the single telescope FOV. The interferometric FOV can however be extended then by changing the delay, so that both spatial and temporal fringe encoding is used and interferometry can be done with only a few pixels and a few steps in delay. This is what is done in Densified pupil imaging.

Without detector noise, both the Michelson and the Fizeau approach are able to return a wide field-of-view where fine features of the luminosity function $L(\theta_0)$ can be recovered. Moreover, there is no difference in observation time necessary to reconstruct with a certain quality. In the next section, detector noise will be included. Moreover, two alternative beam combiners are added. Both the Staircase mirror approach as an alternative to the Michelson co-axial interferometer and the Densified pupil approach as an alternative to image plane interferometry will be subjected to the same simulated observation.

5.3 Comparison for real detectors

In the following simulations, detector noise is introduced. The previous examples made clear that, principally, the detector signals for spatially or temporally encoded fringes can be used for wide-field source reconstruction. Moreover, the presence of photon-noise showed that the number of pixels versus the number of delay steps pose a comparable limit to the reconstruction quality for a given total number of photons. With the introduction of detector noise, the dynamic range in the detector signals is lowered and hence the nature of the signal will start to play a role in the resulting fitness of detector signals. Pupil densification was 'invented' to improve the signal to noise ratio in detection signals. The Staircase Michelson solution has the goal to limit the observation time by partially equalizing the external OPD, at the cost of signal contrast.

After the comparison of the basic types, pupil versus image plane combination, the two other methods (see Fig. 5.10) presented in Chapter 3 are now subjected to the same simulation. The weaknesses and advantages of the Densified Pupil solution as compared to the homothetic interferometer have been addressed in Chapter 3. The same holds for the Staircase solution as compared to the Michelson Stellar interferometer. In short, these comparisons are as follows:

The hardware for the **Staircase**-solution is more complex than that of a classical **Michelson** interferometer. It does facilitate much shorter scans of OPD, but the key feature of the optics—a staircase-shaped mirror in intermediate focus per arm—is required to change shape with time (step width) and baseline length (step height). Active mirrors that can perform this task and maintain their optical accuracy do not yet exist.

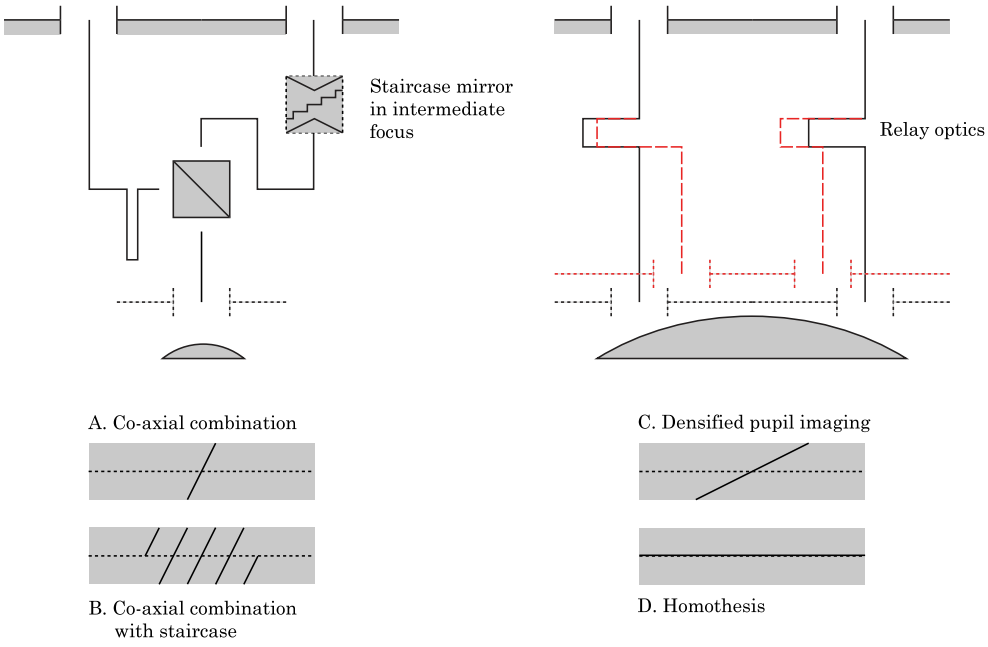

Figure 5.10: The four possible beam combination schemes, Michelson, Fizeau, Densified and Staircase. For clarity, beam compression is not applied, so $M = 1$. The diagrams of the focal planes indicate the 'movement' of the central fringe with respect to the center of the diffraction envelope. Hence, these four diagrams indicate the instantaneous FOV of the four methods.

5.3.1 Parameters

For the simulation runs with four methods, the discretizations of the (θ, d)-observation space are given in Table 5.4.

Table 5.4: Measurement settings for all simulations. B_0 in the case of Densified beam combination, is the fixed exit baseline length. The Pixel range spans 3 PSFs, in all cases, whereas the object $L(\theta_0)$ spans 2 PSFs.

Case	Pixels	Pixel Size	OPD Range	Size	Steps	Bins
Michelson	6	$\simeq$ PSF/2	$2B_{\max}\theta_{\max}$	$\lambda_c/4$	234	1404
Fizeau	235	$p_\theta(B_{\max})/4$	—	—	1	235
Densified	31	$p_\theta(B_0)/4$	$-l_{\text{coh}} \ldots + l_{\text{coh}}$	l_{coh}	3	93
Staircase	6	$\simeq$ PSF/2	$-\frac{3}{2}l_{\text{coh}} \ldots + \frac{3}{2}l_{\text{coh}}$	$\lambda_c/4$	25	150

The number of bins—photons arrive in (θ, d)-space with the calculated fringe pattern $I(\theta, d)$ as likelihood distribution—are now respectively 1404, 235, 93 and 150 bins. These are the minimum number of bins to guarantee for all methods the coverage of the full FOV in all spatial frequencies up to the maximum sampled frequency. The fringe sampling for the co-axial methods is according to the *ABCD*-method (Shao and Staelin, 1977).

The fringes in the image plane also have to be sampled with four pixels per period. For both the densified as well as the homothetic mode, the angular fringe period is derived from the earlier presented general expression for $I(\theta, d)$, and is calculated as

$$p_\theta(B_0) = \left(\frac{\lambda_c}{B_0}\right), \tag{5.4}$$

where for the homothetic case $B_0 = B$. For all methods, the fringe sampling is now adjusted to four samples per fringe, either in d-direction or in θ-direction. The exit baseline B_0 for Densified is fixed to $B_0 = 2D$. The maximum exit baseline for Homothesis is $B_0 = B = 8D$, so that the required number of pixels in focus is indeed reduced by a factor of 4.

For full densification ($B_0 = D$) the fringe period is $p_\theta(D) = \lambda_c/D$, which is close to the radius of the diffraction limited envelope. Although recombination at this separation is feasible and the detection of an entrance baseline-dependent signal is possible, this ultimate combination baseline was not chosen for these simulations.

Hardware is also the limiting factor for the first of the image-plane combined schemes, **Homothesis**. The beam combination scheme implies extra degrees of freedom to control. Hence, complicated metrology and active actuation are needed. However, clever solutions to reduce the degrees of freedom to easily controllable ones do exist (Van der Avoort *et al.*, 2004b). Next, the detector resolution poses a resolution limit to not only the recorded data, but as well to the final reconstructed image. The software needed to process data, taken in the form of snapshots, into a reconstruction of the sky is simple. For the case of iterative (see the Ordered Subsets Expectation Maximization algorithm developed for LBT, described in Sec. 4.1) FFT based deconvolution (Bertero and Boccacci, 2000), such software is also fast. **Densified** Pupil Imaging reduces the hardware requirements—fringe stability, number of detectors and size of detectors—greatly, but the interferometric field-of-view gets proportionally smaller as the exit baseline B_0 tends to co-axial combination. Multiple observations have to be made, where intentional OPDs in the order of the coherence length are applied in the arms. If enough observations are made, the full FOV is recoverable. The data has to be processed jointly. However, the number of detector pixels necessary is much lower than for Homothesis, since the fringe encoding is spatially, but the fringes have a fixed and long period. For an exit baseline $B_0 = 2D$, the fringe period on the detector will be $1/4^{\text{th}}$ of the diffraction envelope. Therefore, the total number of 'bins' can be less. Since there are less detector pixels, the flux per pixel will be higher, resulting in a more favorable signal-to-noise ratio.

5.3.2 Results

Optical aperture synthesis imaging of UGC00597

The overall comparison of all interferometers, with respect to signal strengths or modulation depths, background or incoherent radiation levels and necessary pixels or delay positions, is given in Fig. 5.11. As discussed, the dynamical range is related to the indicated error ϵ. For a dynamical range of $1/\epsilon = 100$, Fig. 5.11(a) shows the efficiency of each array or beam combination method. The lower the amount of photons per bin needed to achieve this dynamical range, the better, since, apparently, the beam combination method provides a fringe signal with larger information content. The read-noise level was set at $\sigma^2 = 8$ counts per pixel, conform the Spitzer-IRAC specifications. Amounts of photons reaching a detector pixel below this level can not be considered useful, for any

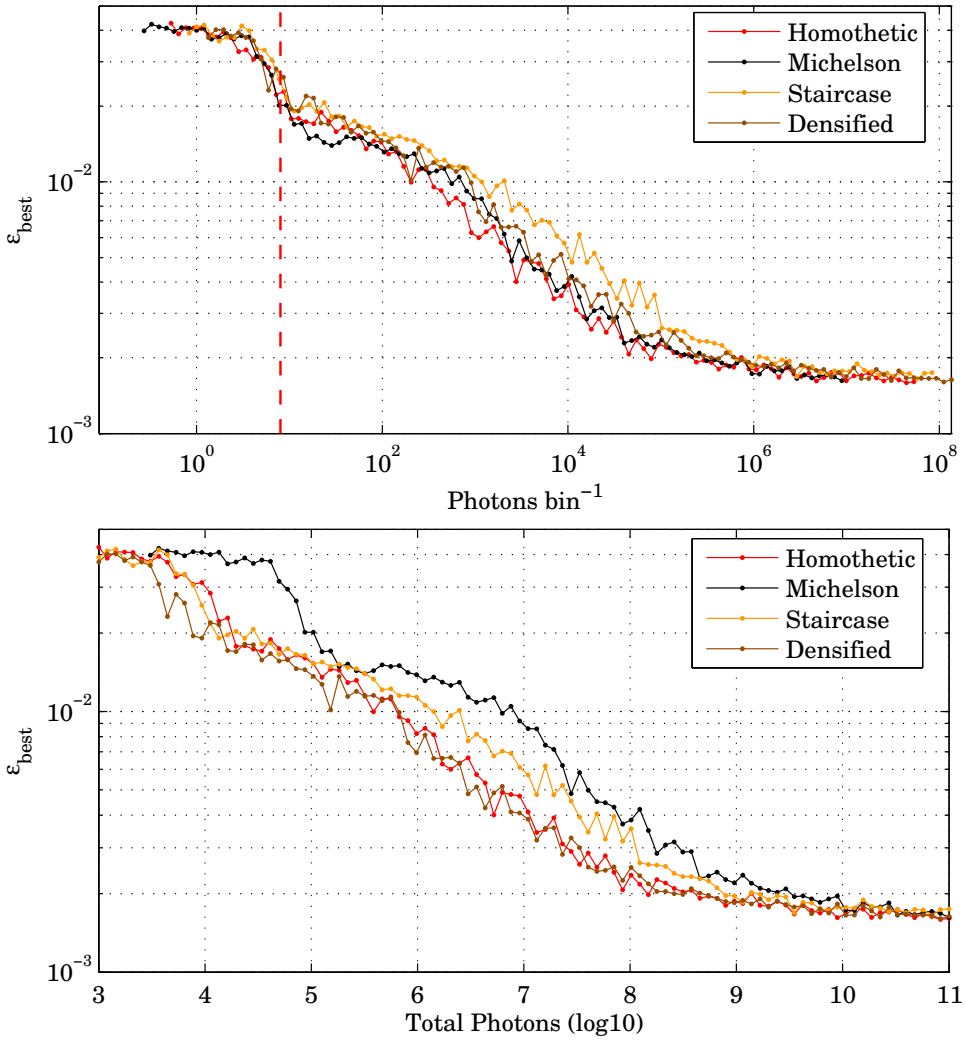

Figure 5.11: The reconstruction quality ϵ versus the number of photons per bin (top panel) and versus the total number of photons (bottom panel). Note that the number of 'bins' (pixels and delay settings) is different for each method. The total amount of photons is for each method equally spread over the baseline configurations, which are also the same for all methods. The reconstructed source is UGC00597.

shape of detection signal. It is only above this level that differences start to show up. The error figure ϵ for very low numbers of photons per bin (the range 8–100) is already agreeable. This is because the stellar object resembles the shape and size of the diffraction pattern of a single telescope. Since all methods provide at least a few detectors in a row, this very rough envelope can already quickly be recovered. And because of the match in shapes, this already leads to a fit of $\epsilon \approx 0.015$.

Table 5.5: Needed number of Photons per bin to reach $1/\epsilon = 100$

Method	**Photons bin^{-1}**
Homothetic	$2.5 \cdot 10^2$
Michelson	$6.3 \cdot 10^2$
Densified	$7.9 \cdot 10^2$
Staircase	$1.3 \cdot 10^3$

From Table 5.5 it is clear that the two 'classical' methods, Michelson and Homothetic, are most and nearly equally efficient. Densified performs slightly worse, since in the data taking, the recordings with non-zero delay settings provide fringe-less information for the largest part of the sky. Hence, a great number of photons is not contributing to reconstruction of high spatial frequencies. The efficiency for Densification could be improved by omitting the observations at non-zero delay settings for the short baselines. Apparently, the Staircase method is the least efficient. Although fringe packets are present throughout the measured signals, there is either redundancy in the information or less modulation, since a large number of photons per bin is needed to reconstruct the sky to the level of $\epsilon = 0.01$. Appendix B deals with the details of the measured Staircase signals. The fringe envelope of the point source interference response signal can be regarded as having a fringe envelope with two maxima instead of one[2]. Therefore, the responses do not uniquely link a source to a measurement. For example, a single point source falling near the edge of a stair, can produce the same response as two separated weaker point sources[3]. Despite the slight inefficiency, it can still be observed that the Staircase solution is an improvement with respect to the Michelson method, on the account of the total observation time needed. The number of bins can be drastically lower. The next tables (Table 5.6a,b) compare the methods on the aspect of total number of photons (or observation time) needed to reach the reconstruction quality $\epsilon = 0.01$ (a) and the best reconstruction (or smallest value of ϵ) achievable with a fixed number of photons (b).

Table 5.6: Observation time needed to reach $1/\epsilon = 100$ (a) and the reconstruction error ϵ for a fixed observation time (time expressed in total received amount of photons) of 10^7 photons (b)

Method	**Photons**
Homothetic	$10^{5.7}$
Densified	$10^{5.7}$
Staircase	$10^{6.2}$
Michelson	$10^{6.8}$

(a)

Method	**Error ϵ**	**Dyn.R. $1/\epsilon$**
Densified	$10^{-2.4}$	250
Homothetic	$10^{-2.4}$	250
Staircase	$10^{-2.2}$	167
Michelson	$10^{-2.0}$	111

(b)

In both tables, the two image-plane combination methods perform best. This means that the inefficiency of the post-processing in the case of Densification is compensated by the reduced number of bins needed. Moreover, it is clear that both co-axial types

[2]As measured experimentally (Montilla *et al.*, 2005), and studied in more detail in App. B.2.

[3]See App. B.4 for a more detailed study of this effect.

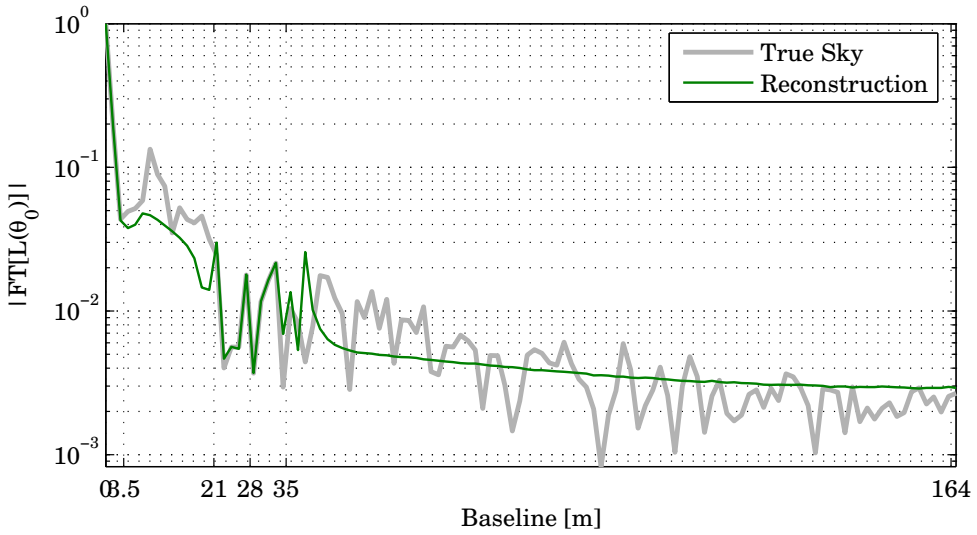

Figure 5.12: Spatial frequency analysis of the reconstruction in Fig. 5.13 clearly shows the presence of spatial frequencies within the single aperture radius and around the chosen heart-to-heart separation of 28m. The optical bandpass is 6 to 10 μm, resulting in a range of spatial frequencies present. These frequencies are expressed equivalently to the baseline for λ_c.

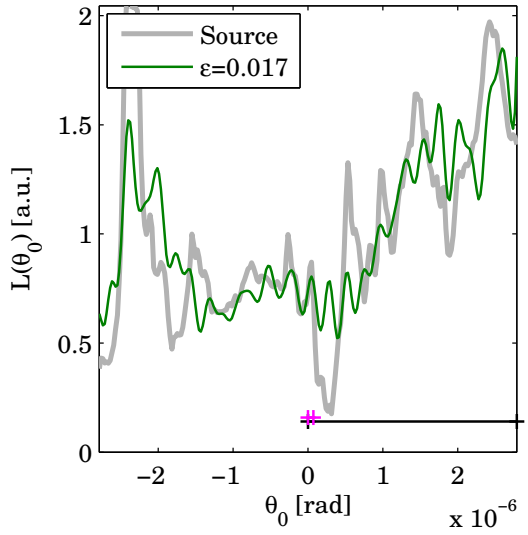

Figure 5.13: This diagram shows the original $L(\theta_0)$ and the reconstruction $\hat{L}(\theta_0)$ for the optimal filter parameter Λ. The *measurement* data only contains a single polychromatic observation for the baseline B = 28m. The optical bandpass is 6 to 10 μm, resulting in a range of spatial frequencies present. Due to multiple detectors, also the single-dish spatial frequencies are covered, resulting in the low-frequent envelope function. The high-frequent components are generally phased (steep rising edges) with the (for reconstruction unknown) source.

need either more time, or produce worse images given the same time, than the image-plane types. The dynamic range in the produced images is—for the same amount of 10^7 photons—nearly twice as large for the image plane methods. Recall that the number of bins is minimal in all cases.

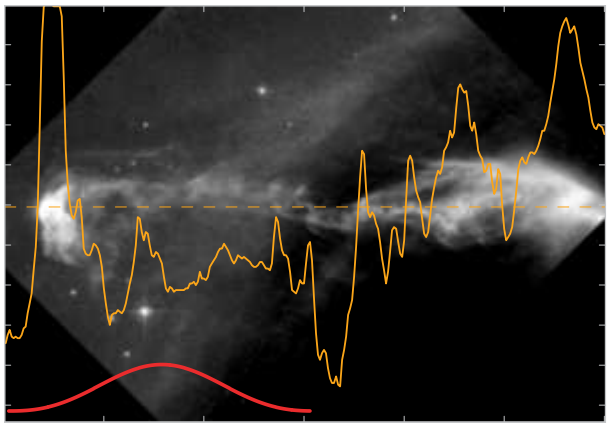

Figure 5.14: The object HH47 (New Technology Telescope image). The dashed line indicates the position of the slice of the image of which the pixel values were used again as the linear luminosity distribution $L(\theta_0)$. The thick line represents this function. Again, the diffraction limited spot size of a single telescope is indicated in red.

Spatial frequencies in the solution

From both reconstruction plots (Fig. 5.11), it can be seen that ϵ never reaches zero. This is because of the limited maximum baseline length. A spatial frequency analysis of a typical reconstruction result can clarify this. Figure 5.12 shows the FFT of the source function $L(\theta_0)$ and the FFT of the best possible reconstruction $\hat{L}(\theta_0)$ when only one observation with $B = 8 \cdot D = 28$m is used as measurement data. The beam combiner simulated here is the Densified Pupil. A very large amount of photons is available. The spatial frequency co-ordinate in the figure is expressed in equivalent baseline length at a wavelength of 10 μm. Because of the polychromatic detection signal, a range of spatial frequencies around B/λ_c is covered. The very short baselines are also covered, since the detector has multiple pixels and the single-dish diffraction envelope is larger than a single pixel. The limit in reconstruction quality can be explained by the amplitudes (presence) of the non-covered spatial frequencies. Accordingly, the reconstruction $\hat{L}(\theta_0)$ contains only a few harmonic functions. For illustration, the reconstruction with only $B = 28$m is presented in Fig. 5.13. It is noteworthy to see that the limited set of harmonic functions is approximately lined up with the original function, while this is a blind reconstruction from the measured data only. The steep edges of the source nearly co-align with the edges in the reconstruction.

Optical aperture synthesis imaging of HH47

The source UGC00597 could nicely be recovered by all beam combination methods. However, the steep edges and hence high spatial frequencies are predominantly present in the central region, close to on-axis observation angles. Even a reconstruction within only the central PSF could probably create a nice match to the source. Therefore, all simulations are repeated again with a different source, depicted in Fig. 5.14. The Herbig–Haro object HH47 is showing two jets out of an obscured stellar core. An image cross-section shows large contrasts, steep edges and features far out of the central region.

In Fig. 5.15, the results of a large number of simulations are displayed again, once as

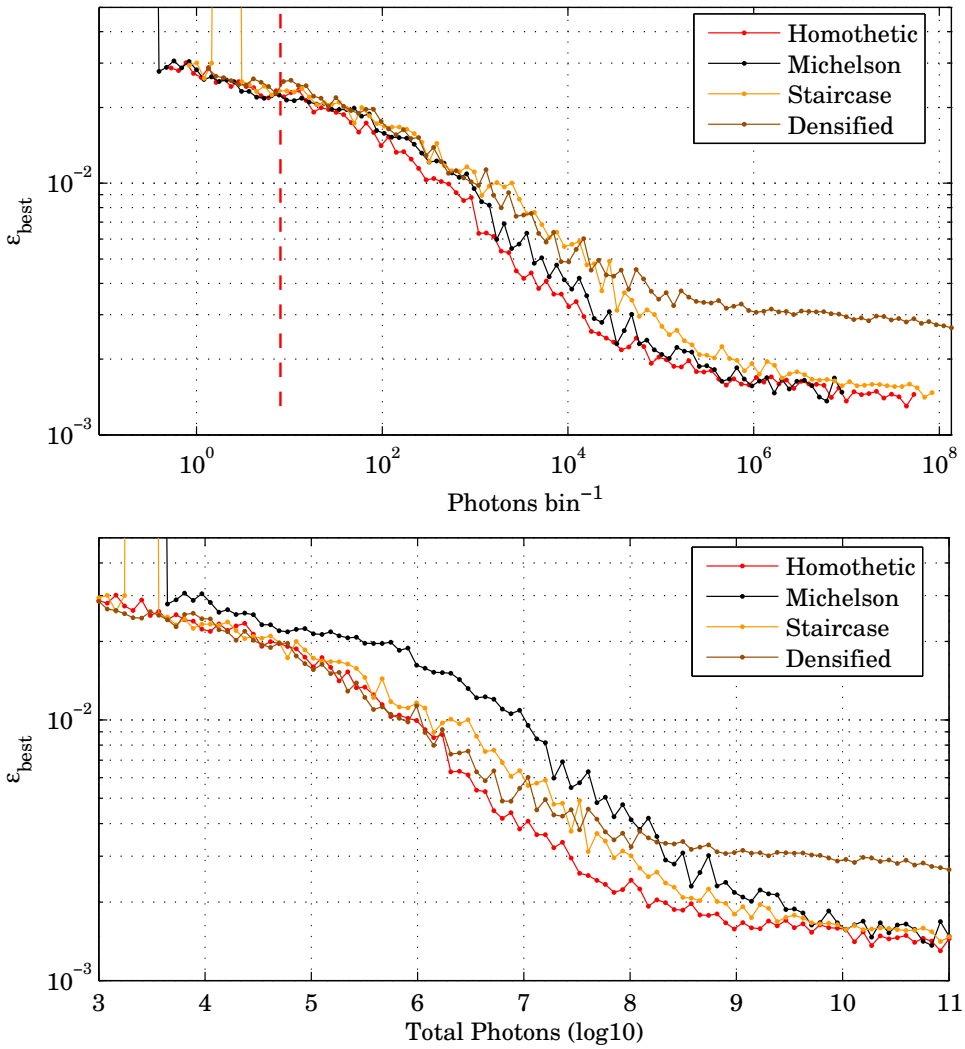

Figure 5.15: For reconstruction of the source HH47, the reconstruction quality ϵ versus the number of photons per bin (top panel) and versus the total number of photons (bottom panel) are plotted. With the steep edges and hence high spatial frequencies at the outer regions of the FOV, the Densified solution shows limited reconstruction quality. This is due to the chosen coverage of the higher spatial frequencies, as detailed in Fig. 5.16.

the reconstruction error ϵ at best regularization versus the number of photons per bin that the interferometer received, and once as the reconstruction error ϵ versus the total amount of photons received. The curves in both plots resemble the ones found in the simulated observations of UGC00597, except for two differences.

Firstly, the jump in reconstruction quality around 8 received photons per bin is absent. This level corresponds to the simulated read-out noise per pixel and hence per bin. The ϵ-levels for more than 8 photons per bin, are equal in the UGC00597 and the HH47 cases. Apparently, the 'random' reconstructions $\hat{L}(\theta_0)$ for recordings, drowning in

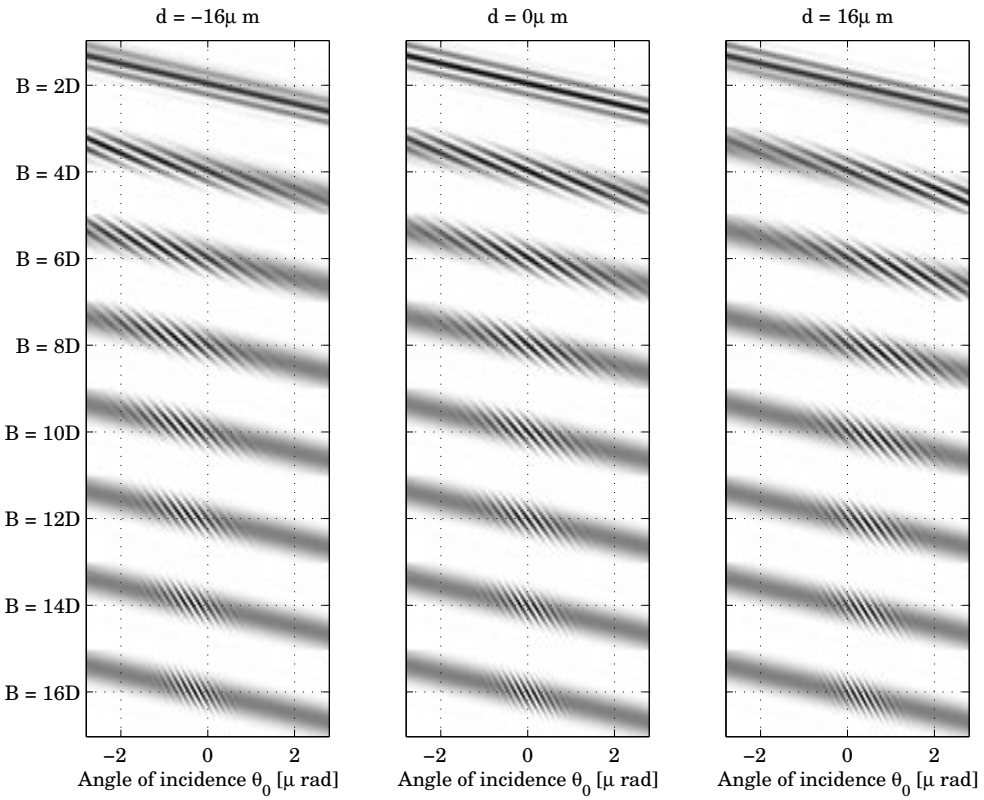

Figure 5.16: Visualization of the contents of the transfer matrix in the case of Densified pupil imaging. For a fixed recombination baseline $B_0 = 2D$, point source intensity response functions are calculated for entrance baseline lengths $B = (2 \ldots 16)D$ in steps of $2D$. The detector intensity is displayed as a (vertical) column of pixels for a certain angle of incidence θ_0. This pixel column is given per baseline length. For the indicated $B = 2D = B_0$, the beam combiner is homothetic, resulting in a field independent convolution kernel. For all other baselines, the fringe pattern—with fixed fringe period—moves out of the diffraction envelope, for incidence angles off-axis. For the longest baselines, fringes are lost toward the edges of the FOV. In these regions, the highest spatial frequencies cannot be reconstructed.

read-out noise, match slightly better to the original $L(\theta_0)$ in the case of HH47, as compared to UGC00597. However, reconstructions with $\epsilon_{\text{best}} = 2 \cdot 10^{-2}$, obtained just above the read-noise level, are still far from being useful.

The second and more important difference between Figs. 5.11 and 5.15 is the curve for Densified pupil imaging. In the case of UGC00597, where a wide field was imaged, but the really narrow features were mainly present on-axis, the Densified-method proved to be superior, in both imaging efficiency as well as imaging speed. But in the case of HH47, the Densified-lines do not approach the level $\epsilon_{\text{best}} = 10^{-3}$, whereas the other three do. This under performance is related to the nature of the function $L(\theta_0)$ in the case of HH47. In the function, steep edges are present near the boundary of the FOV. This means that high spatial frequencies are present, in regions far off-axis. The Densified method is known to have a FOV that narrows down for larger baselines. With the additional delay

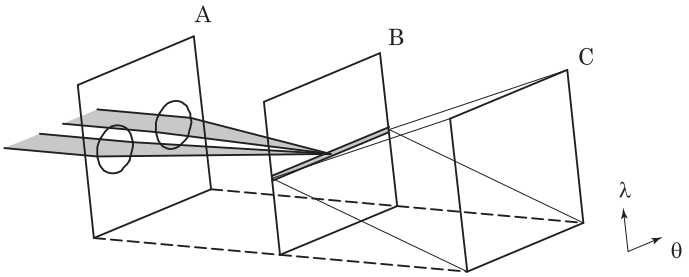

Figure 5.17: Illustration of the detection principle when the polychromatic fringe pattern is not detected on a line detector, but detected after dispersion. Right after the slit in plane B, a dispersive element (not drawn) adds a wavelength dependent angle to the field, causing an intensity pattern in plane C as a function of θ and λ.

settings, presented in Table 5.4, this FOV-narrowing is apparently compensated correctly for the source UGC00597, but not for HH47. Figure 5.16 illustrates this effect. The diagrams show the contents of the interferometric transfer matrix, in case of Densified pupil imaging. The regions for which only incoherent information is received, are identified by the lack of intensity modulation. The diagrams then show, that the ultimate imaging resolution, obtained at telescope separation $B = 16D$, is, due to the delay settings $d = (-16, 0, +16)$ μm, achieved only in the region of the source, for which the angle of incidence is $-1\mu\text{rad} < \theta_0 < +1\mu\text{rad}$. This region is large enough to cover the high spatial frequency content of UGC00597, but is too limited to represent HH47 with a solid range of spatial frequencies in all regions of the source. More delay settings are required.

5.4 Spectral capabilities

The discussion of imaging capabilities only considered the task of obtaining a (monochromatic) luminosity function $\hat{L}(\theta_0)$ out of polychromatic observations. To perform *spectroscopy* at this high angular resolution, one would rather perform this image reconstruction in a number of very narrow bands. To derive spectra from the fringed data makes it very hard to obtain spectra at the high angular resolution, since the number of pixels is low and an extra convolution process in the detection would have to be inverted. Therefore, pairwise beam combination[4] with dispersed detection, through a dispersive element placed perpendicular to the orientation of B_0 will be necessary to arrive at a beam combiner for the high spatial, high spectral resolution imaging task. See Fig. 5.17 for an illustration of this detection principle. Then, measurement signals can be recorded with which image reconstruction, finding $\hat{L}(\theta_0)$, can be performed for narrow wavelength bands. With a set of reconstruction images per band m available,

$$\mathbf{L}_m = \hat{L}(\theta_0; \lambda_c^{(m)}), \tag{5.5}$$

a spectrum $S(m)$ can be returned for a desired angle θ_0. Of the presented four beam combination schemes, a version including a dispersive element can be designed. Whether the beams are combined co-axially or in focus, the response signals $I_{jk}(d)$ or $I_k(\theta, d)$ can

[4]The examples presented in this thesis have not shown beam combination for three or more beams—although *all* methods allow this.

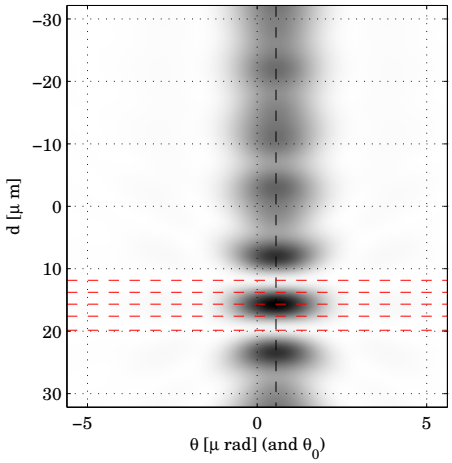

Figure 5.18: Detected fringe signal $I_{jk}(\theta,d)$ in focus, for co-axial combination $B_0 = 0$. The spatial intensity pattern (recorded with a line detector) is a function of delay d. For one specific d, the spatial pattern can be dispersed, so that the line detector signal is separated with respect to wavelength. This is done for the 5 indicated values of d.

be generated as presented, spreading the wavelength dependent information over any range from 0 (no dispersion; as presented) to what the dimensions of the CCD detector allow.

To illustrate this dispersion for a case where $B_0 = 0$ and one where $B_0 < B$, Eq. (2.26) is recalled,

$$I(\theta,d) = 4D^2\text{sinc}^2\left[D\pi(\theta - M\theta_0)/M\lambda\right]\cos^2\left[\pi(d + B_0\theta - B\theta_0)/\lambda\right]. \tag{5.6}$$

For simplicity, $M = 1$ so only uncompressed beams are combined. The intensity $I(\theta,d) = |A'(\theta,d)|^2$ is in fact also a function of λ, resulting in $I(\theta,d,\lambda)$. When the focused signal on the line detector would be dispersed, a two-dimensional signal as function of θ and λ can be measured. These data slabs can be recorded for any d, so that in principle an intensity data 'cube' can be measured. Figures 5.18 and 5.19 provide an example for a single point source, for the co-axial case $B_0 = 0$. Figure 5.20 does the same for the case the combination baseline length is $B_0 = 3D$ while the telescope separation is taken $B = 8D$.

The examples showed the dispersed detection of a single point source from direction θ_0. Since the intensity responses of all point sources can be summed, this detection principle can be used to observe a general source $L(\theta_0)$. The detected information in (θ,d,λ)-space can be used to generate narrow banded $I_{jk}(\theta,d)$ or $I_k(\theta)$ polychromatic intensity signals, with which—as simulated and discussed—aperture synthesis can be performed and an estimate of the source in that narrow band can be obtained.

5.5 Singular value analysis

The simulations in this chapter have shown the imaging result after the full simulation cycle of generating response functions, summing them to a measured intensity signal, 'noisyfying' that signal to represent low light levels and imperfect detection and, finally,

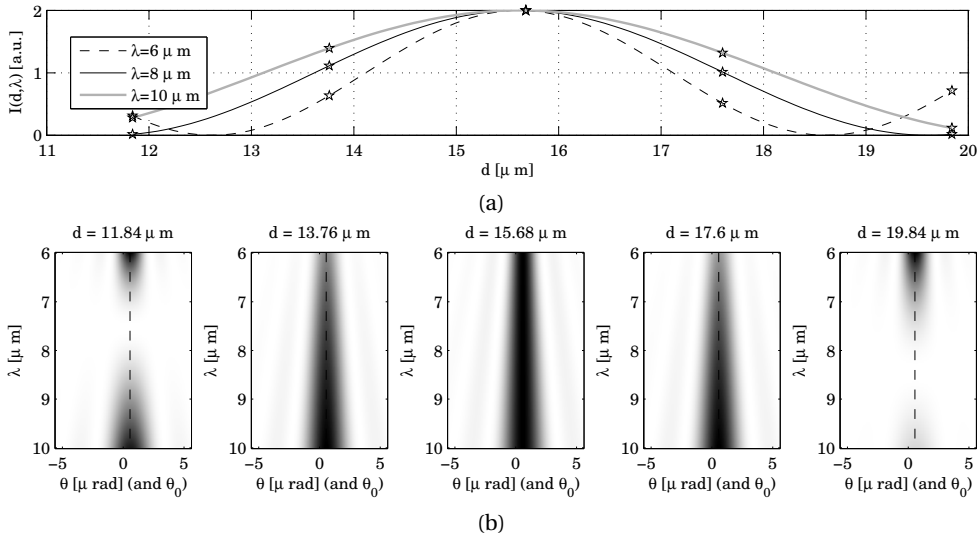

Figure 5.19: For 5 values of delay d, the co-axial polychromatic focal field is dispersed. This results in 5 detector signals, $I(\theta,\lambda;d)$, shown in panel (b). With these two-dimensional data, provided there is enough signal, aperture synthesis can be performed in very narrow wavelength bands. For three wavelengths, the intensity as a function of applied delay d is plotted in panel (a). The stars indicated the sample positions in panel (b). For the central value $d = 15.68$ μm, all wavelengths are at zero ODP, since the point source is placed at $\theta_0 = 0.56$ μrad and with a baseline $B = 28$m, the zero OPD delay is $B\theta_0 = 15.68$ μm.

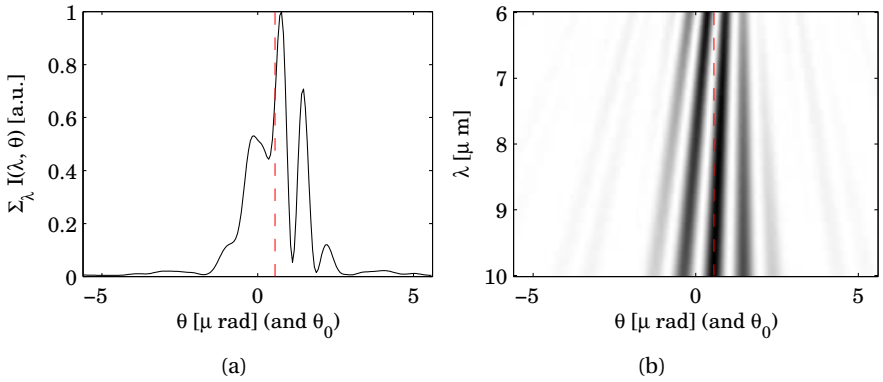

Figure 5.20: Line detector detection and dispersed detection of a point response function with spatially encoded fringes, see respectively panels (a) and (b). Again, $D = 3.5$ m, $B = 28$ m, $\theta_0 = 0.56$ μrad. Now, $B_0 = 3D = 10.5$m. Again, the spectrally dispersed data provides narrow-banded spatial intensity data, with which aperture synthesis per band can be performed.

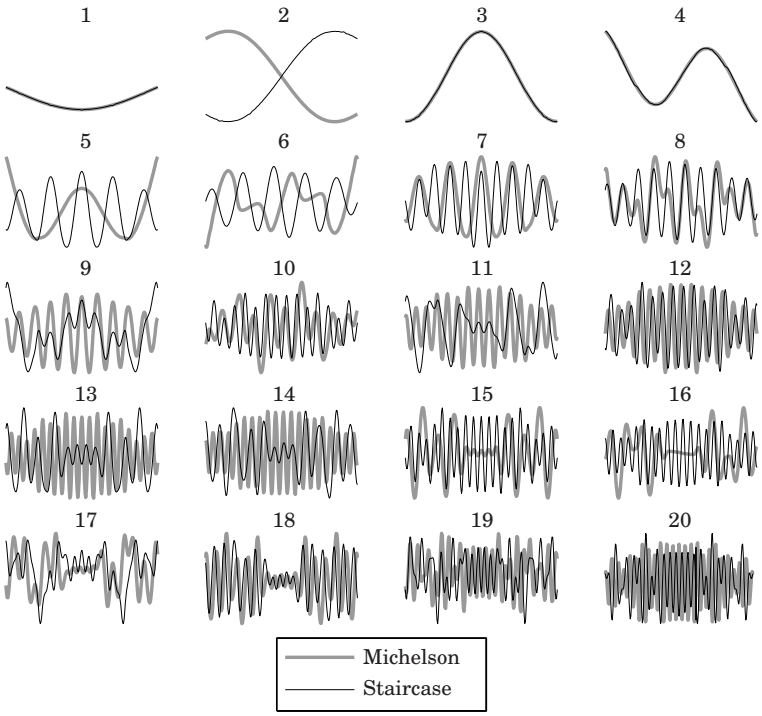

Figure 5.21: Comparison of the first 20 solution modes $\mathbf{v}_i$ for the Michelson and the Staircase method. Generally, the modes are a sum of several harmonics. Note the occurrence of symmetrical and anti-symmetrical modes, e.g. in the Staircase modes 5 and 6.

estimating an image out of these signals. Based on these estimations, a comparison of the imaging performance of four interferometers was made. In this section, these findings are compared with information on the interferometers that was already available after the generation of the response functions and transfer matrices. With these transfer matrices available, a plot can be made of the singular values related to the four interferometers and the chosen array parameters, such as delay settings and pixel dimensions.

The regularization process is described in detail in Sec. 4.3. Out of a measurement vector $\mathbf{b}$, an estimate of the source $\hat{L}(\theta_0)$, represented by vector $\mathbf{x}_\Lambda$, is given according to

$$\mathbf{x}_\Lambda = \sum_{i=1}^{n} \frac{\mathbf{u}_i^T \mathbf{b} \sigma_i}{\sigma_i^2 + \Lambda^2} \mathbf{v}_i, \tag{5.7}$$

where Λ is the regularization parameter, $\mathbf{u}_i$ and $\mathbf{v}_i$ are the measurement- and the solution modes, respectively, and σ_i are the singular values. This decomposition of the solution of the inverse problem is a direct result of the Singular Value Decomposition of the transfer matrix, based on point source responses. Based on the fact that the mode vectors $\mathbf{u}_i$ and $\mathbf{v}_i$ are unitary, Eq. (5.7) makes clear that the constant Λ and the values of σ_i, balance the participation of solution modes $\mathbf{v}_i$ in the estimate $\mathbf{x}_\Lambda$. The solution modes are ordered by the SVD with respect to spatial frequency content, from low to high, as depicted in Figs. 5.21 and 5.22. From a signal theory point-of-view, a good imager would be susceptible to all spatial frequencies with nearly equal amplitude. Examples are the

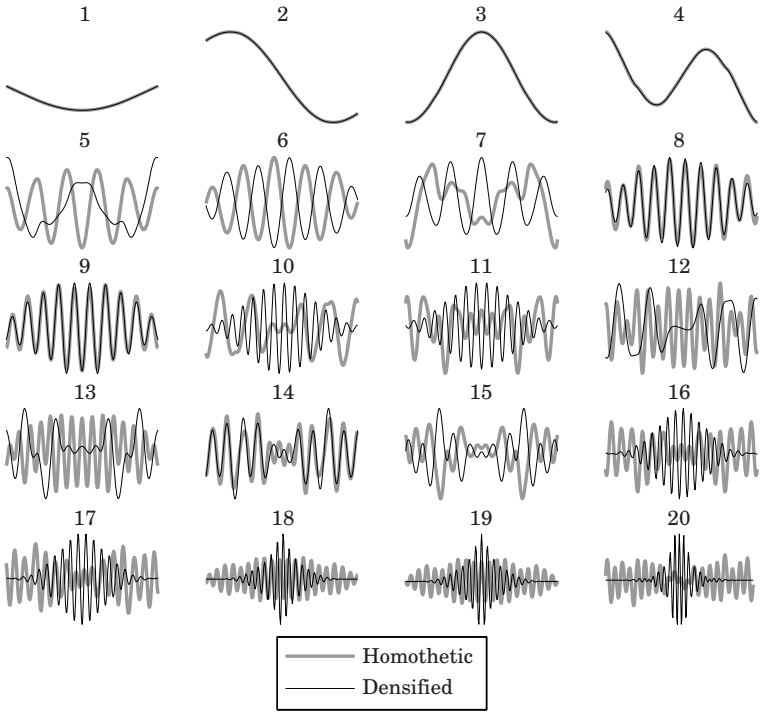

Figure 5.22: Comparison of the first 20 solution modes $\mathbf{v}_i$ for the Homothetic and the Densified method. Note how the FOV narrows down in the Densified case, as the spatial frequency increases.

flat frequency response of professional loudspeakers or the gradually decreasing Modulation Transfer Function (MTF) of a microscope in coherent imaging mode. In other words, it would be good if the singular values associated with the solution modes show a slow decline and a small ratio between the largest and the smallest participating singular value.

The plot in Fig. 5.23 shows the normalized singular values for the four beam combiners. This singular value plot can be separated into three regimes, based on the index i:

- **Incoherent regime:** For indices $1 \leq i \leq n_{\text{PSFs}}$, where n_{PSFs} is the number of incoherent PSFs fitting in the field-of-view, the modes relate to the low-resolution or incoherent image of the sky.
- **Interferometric regime:** The modes for $n_{\text{PSFs}} < i < i_B$, where the major spatial frequency of the mode with index i_B relates to the maximum baseline length B_{max}, are the modes related to the interferometric character of the array.
- **Unsampled regime:** The region $i > i_B$ contains modes of very high spatial frequency, which do not physically relate to the source nor the measurement, since these spatial frequencies are not sampled.

As stated, a good imager would demonstrate a slow decline in the singular values and a small ratio of the largest (in all cases normalized to one) and the smallest singular value.

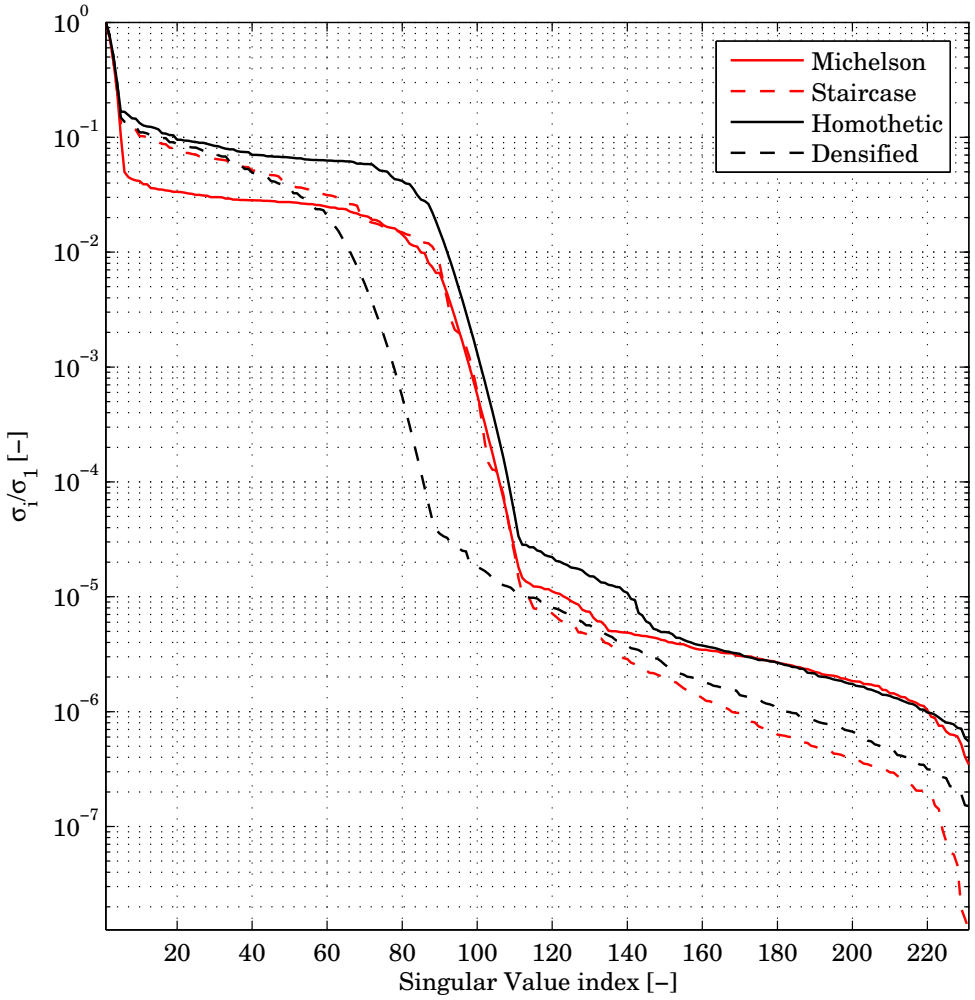

Figure 5.23: The normalized singular values σ_i/σ_1 for the four interferometry methods. A flat line upto the cut-off induced by the maximum baseline $B_{\max}$ (around $i = 100$) indicates a proper transfer of all spatial frequencies. See text for details.

Therefore, the limited condition number

$$C_i = \frac{1}{\sigma_i} \tag{5.8}$$

can be defined, should the plot be limited to index i. In terms of a flat frequency response, the Homothetic and the Michelson beam combiners perform well. The height difference between these two curves relates to the responsiveness of the very low order modes. Apparently for Michelson, the very low frequent nature of the source (imaged on the six large pixels) is relatively much stronger represented than the fine structure of the source. Like the Homothetic response, there is a large drop over the first few values. This can be related to the fact that the low-frequent response is present in every measurement at baseline length B_k. But the levels of the second regimes differ between the

Michelson and Homothetic lines. This is due to the nature of the measurement signals. A typical Michelson signal shows an extended incoherent signal (related to low spatial frequencies) of length $(d_{\max} - d_{\min}) \gg l_{\text{coh}}$ within which a relatively very short fringe packet of length l_{coh} is present. In the homothetic case—with field invariant point response functions—the high-frequent information is present all over the signal.

Compared to the relatively flat interferometric frequency response of the Homothetic and Michelson beam combiners, the beam combiners Staircase and Densified show steeper declines for the singular values in the interferometric regime. The curve for Densified is not even reaching the spatial frequencies related to the maximum baseline $B_{\max}$. This was noticed before in the reconstruction of the source HH47, where the transients at the edges of the FOV were not reconstructed. The singular value plot nicely shows how the Densified FOV narrows down for higher spatial frequencies, which is also visible in the $\mathbf{v}_i$ in Fig. 5.22. Clearly, more steps d are necessary for the Densified simulation to present a proper frequency transfer—which was not done for illustrative purposes.

The Staircase transfer is slowly degrading up to the frequency limit related to $B_{\max}$. This means that the higher spatial frequencies are relatively more susceptible to loss of signal strength induced by the staircase mirror. A possible source for this inefficiency is treated in Sec. B.4, namely that the 'folding' of the fringe signal destroys the unique relation between source $L(\theta_0)$ and measurement $I_{jk}(d)$. Apparently, this effect is growing worse for increasing baseline lengths.

5.6 Wavefront filtering

The interferometers under consideration are intended to operate in space. It should be noted however, that operation of these interferometers on the ground requires several adjustments of the optical systems, changing possibly the outcome of the comparison. The use of optical fibers for wavefront filtering, makes the interferometer inherently coaxial and therefore, it can be concluded that a fiber-equipped interferometer acts as an optical correlator, equivalent to a radio interferometer (Coudé du Foresto, 1993; Tallon & Tallon-Bosc, 1994). This prohibits the use of fibers for spatial wavefront filtering on image-plane interferometers. However, for earth-based stellar interferometry, wavefront filtering is essential (Saha, 2002; Keen *et al.*, 2001; Buscher *et al.*, 1995).

5.7 Conclusions

In this Chapter and in Appendix C,[5] four beam combiners have been compared in performing the same imaging tasks. The major point of comparison has been the image quality versus the time needed to acquire it. The ability to cover a wide field-of-view is a property of all methods. The study only considered pairwise beam combination and one-dimensional images. Although the measurement signals are of very different nature, the encoded information of the source can be sampled by a focal plane array, at one or more positions of a delay line in one of the two interferometer arms.

[5] In Appendix C, the four methods are simulated again. In this case, a very wide FOV of 11 PSFs is taken, that is fully covered by all four methods. A solid range of spatial frequencies is covered, for all angles of incidence θ_0. Baseline lengths up to 112 m are taken, in order to approach the desired resolution for the Darwin imaging mission.

The simulations show that the image plane combiners, Homothesis and Densified, image faster than co-axial imagers for relatively narrow FOVs. For a wide FOV, Densified imaging loses its advantages rapidly. Homothesis is then the most efficient and fasted imaging method. For the co-axial methods, Michelson and Staircase, it can be stated that the Michelson method is as efficient as Homothesis, but that it is less apt for wide FOVs, resulting in long observation times, since essentially multiple directions have to be imaged sequentially. Trading off for efficiency, the Staircase method cancels the need for sequential imaging with Michelson. Hence, the Staircase method gains imaging speed and is nearly as fast as Homothesis. Besides image quality and speed, the hardware required to build and operate a specific type of beam combiner can also be compared. This results in Table 5.7.

Table 5.7: Comparison of four beam combination methods. The 'Imaging efficiency' and 'Imaging speed' are based on the quantitative numerical simulations in this Chapter. The 'Robustness' is of qualitative nature.

Description	**Homothesis**	**Densified**	**Michelson**	**Staircase**
Imaging efficiency	⋆	∘	⋆	∘
Imaging speed	⋆⋆⋆	⋆⋆	⋆	⋆⋆
Robustness[a]	∘∘	⋆	⋆	∘∘

Legend: ⋆ = positive, ∘ = negative.

[a]The amount of moving surfaces needed for operation of the beam combiner is inversely proportional to the robustness of the beam combiner.

The conclusions drawn from this Table can be sorted with respect to the desired FOV for an observation. For narrow-field—or single-PSF—interferometry, a Michelson beam combiner is the optimal solution. A high imaging efficiency is realized with a very simple and robust beam combiner. For a FOV that is larger, comparable to the UGC00597-case, a Densified beam combiner provides the solution that still has a robust beam combiner and performs fast imaging. For very wide FOVs, the beam combiner needs to be more complicated. With the remark that the Homothetic imager performed better than the Staircase imager in all cases, with respect to both efficiency and speed, one of the two will have to be chosen. The technical difficulties to overcome are summarized in the following list:

- A homothetic imager with fixed beam compression needs a complicated and accurate opto-mechanical solution to position and point the beams in the exit pupil plane.
- A homothetic imager with variable beam compression can be equipped with a much simpler, fixed and robust beam combiner. However, variable beam compressors (in all beams) or zooming optics that consist of reflecting surfaces at variable separation, require stringent control of the degrees of freedom of these surfaces, since not only beam position and pointing have to be controlled, but also the phase aberrations on the exiting beams.

- A Staircase imager would principally need a staircase-shaped mirror, of which the stair height h_0 is actuatable while keeping all stair-facets parallel. This problem requires a mechatronical solution comparable to Adaptive Optics, with the difference that the staircase mirror is an element to be placed in the focal plane.
- Without an actuatable mirror, a Staircase imager can still operate with a (large) set of staircase mirrors available, each with a stair height optimized for one specific baseline length. In the case that the number of baseline lengths requires too many mirrors available, a limited set of mirrors can be used, so that for some baseline lengths, staircase mirrors with sub-optimal stair height h_0 can be used. The presence of a set of mirrors is not enough. A mechanical system is required, that can—like an optical filter-wheel—switch between the staircase mirrors in the focal plane. This switching would need tightly toleranced positioning accuracy.

With this list of mechanical difficulties and the performed study on the interferometric signals out of which images have to be produced, the comparison of techniques for interferometric wide-field stellar imaging is complete. A wide FOV requires a complicated beam combiner of Homothesis-type or Staircase-type, which have, for each of the four options, mechanical difficulties to overcome. Further research can prove the feasibility of these options and quantify the tolerances or opto-mechanical requirements for proper operation.

Chapter 6

Experiments on homothesis

In this chapter, a practical implementation of *homothesis* is demonstrated. The stability and alignment requirements to maintain homothesis, are validated in an experimental set-up. In the optical set-up, artificial stars are observed by artificial telescopes and the collected polychromatic light is coherently combined. The crucial part for the success of a homothetic observation lies in the accuracy with which the 'placing' can be made 'identical', that is the accuracy of placement of the relayed pupils. Less crucial—but nonetheless also scrutinized in literature (ESO, 1995)—is the detector. Critics of homothesis have always condemned the relaying step, because of its too strict tolerances and the detection for being too noisy, since the light is spread over a large amount of pixels.

This chapter will deal with the specific opto-mechanical tolerances that are required to ensure proper pupil relaying. In Sec. 6.1, the VLTI geometry is used as a model for these difficulties. Section 6.1.2 then details the solutions that the experimental set-up by the Dutch institute TNO TPD offers. Experiments with this homothetic beam combiner are clarified in Sec. 6.2.3 and the results are discussed in Sec. 6.3. The chapter is concluded in Sec. 6.5.

6.1 Design of a homothetic array

6.1.1 The Very Large Telescope Interferometer

In the early 90's of the previous century, a nearly complete study was presented concerning the Homothetic imaging mode of the VLTI (ESO, 1995). During planning and building of the site on top of Cerro Paranal, even an extra 'pit' was generated in the concrete basement below the future optical switchyard. The pit was meant to house the beam combiner for the homothesis. Detailed sketches for this beam combiner—a Cassegrain type telescope with movable inlets for collimated parallel beams from the delay lines—have been made. Yet, the beam combiner was never realized and the pit remained empty.

When an input pupil configuration of variable dimensions has to be relayed to an exact but scaled copy, and the delivery of beams is in a plane, it seems logical to direct these beams with mirrors to directions perpendicular to this delivery plane, as sketched in Fig. 6.1. Placing the mirrors at the desired locations yields parallel beams with a controllable configuration that allows a scaled copy of the input pupils. However, the mirror placement has to be a tilt-free translational placement in two directions. Mechanically,

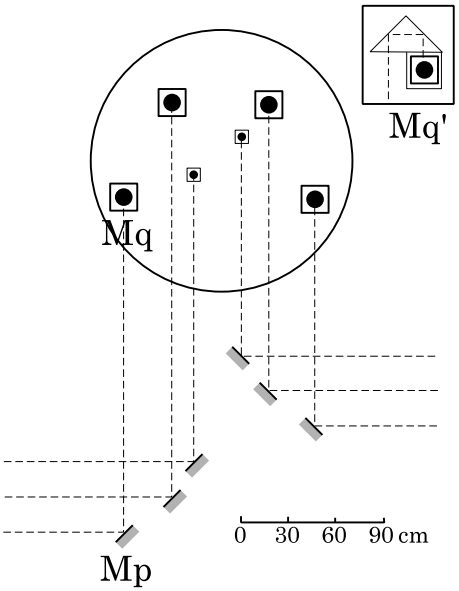

Figure 6.1: *"Possible configuration of the on-axis light beams or pupil images at the entrance of the beam combining telescope. The four large dark circles are the beams of the 8 m telescopes, the small ones those of the auxiliary telescopes. The beam/pupil images are positioned by linear movement of the flat mirrors M_p, which send the light horizontally into the beam combining laboratory, and by movements of the flat mirrors M_q which transfer the light downward into the beam combining telescope. M_q is replaced by M'_q in case it is desirable to rotate the image and/or pupil over 180^o (as is the case when combining telescopes located on opposite sides of the interferometer tunnel)."* From: J.Optics (Paris), 1991 (Beckers, 1991)

this is hard to realize.

6.1.2 The Delft Testbed for Interferometry

In order to image with a synthetic aperture, the homothetic conditions should be met. These can be described as: making sure that from input to exit pupils the system behaves as a regular imaging system. Otherwise, violation of the 'Golden Rules' (Traub, 1986) would disqualify the system for performing proper imaging and would lead to either a reduced field-of-view or poorly reconstructed images.

For a certain magnification or beam compression factor M, the wavefront of an off-axis point source at θ_0 produces beams of diameter D passing through the input pupils, separated by a center-to-center distance B. Compared to the exit pupils, the relations

$$\begin{aligned} B_0 &= B/M \\ \theta'_0 &= M\theta_0 \\ \frac{B_0}{D_0} &= \frac{B}{D}, \end{aligned} \tag{6.1}$$

should be maintained. These relationships provide that the spatial information from the imaged object, related to this B and D, is preserved, and that internal optical path length differences remain zero for all angles of incidence θ_0 at which the sky is observed. Consequently, there is a field-dependent OPD when the exit baseline length B_0 is not set properly. Controlling this length to have no field-dependent OPD effects is a key issue.

DTI has a magnification of $M = 1$. The next section will detail the tolerances needed for homothetic performance over the field-of-view of DTI. For an interferometer like VLTI, the magnification is $M_{\mathrm{VLTI}} = 800$. There, for proper homothetic performance, the exit pupils need to be positioned with tolerances of $1/M$ times the tolerances required for the $M = 1$ case (d'Arcio, 1999). However, the practical field-of-view of interest for such an

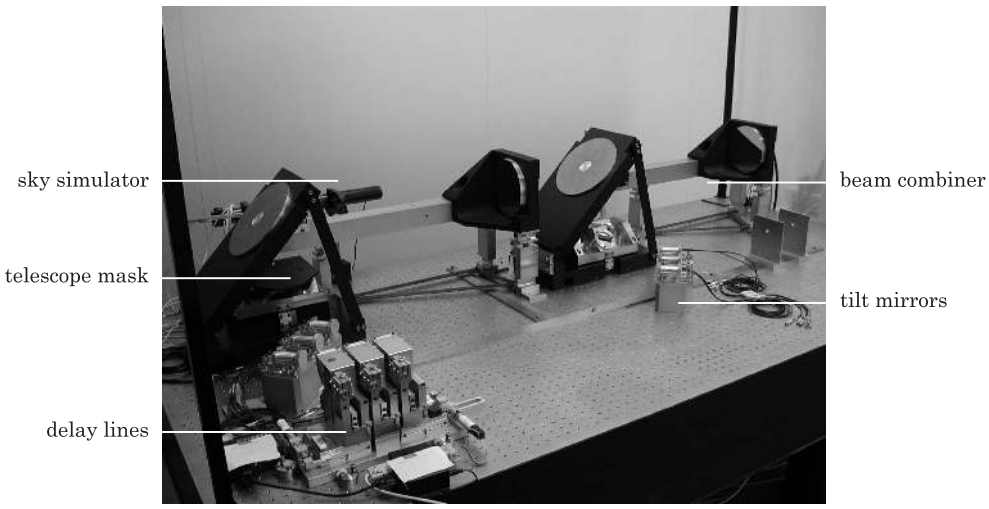

Figure 6.2: The experimental set-up for homothetic mapping DTI, the Delft Testbed for Interferometry (Van Brug *et al.*, 2002), in the labs of TNO-TPD in Delft, the Netherlands. Systems for telescope movement and sky rotation are not shown in this picture.

interferometer is much smaller than that of the DTI. DTI offers a FOV of 800 times that of the VLTI, if imaging aberrations can be neglected.

When a smaller field-of-view is accepted, so that fringes 'drift' off-center for off-axis stars, the absolute mapping condition in Eqs. (6.1) can be relaxed. Experimentally, one can determine to what extent the mapping can be relaxed and at what tolerance the exit pupils need to be positioned. From the formed image of the stars on the CCD, the mapping quality can be derived and position feedback to the pupil locations is possible. After discussion of the measurement algorithms and the actuation strategy, one experiment is performed. The goal of this experiment is to demonstrate the measurement of fringe phase on all stars in the FOV and to steer the beam combiner in such a way that the differences between these phases are less than the limit for cophasing.

6.1.3 Tolerances

Various authors have discussed the strenuous task of aligning an optical array of telescopes with combined focus (Meinel, 1970; Traub, 1986; Beckers, 1990; d'Arcio, 1999). Within the VLTI context, an extensive study was presented by Beckers. The study derives tolerances for the degrees of freedom that have to be restricted per beam: pupil rotation, magnification, pointing, path length and translation. As will be discussed, path length and translation are restrictions related purely to interferometry. The other three are obvious, considering the image on the camera that is provided by each beam. Every single beam offers a low-resolution image of stars or stellar objects on the sky. Multiple beams deliver multiple images of the sky, that should therefore not be rotated, magnified or displaced (displacement in focus is a tilt of the beam) with respect to each other. Therefore, the diffraction envelopes of point sources at the edges of the FOV should coincide with a tolerance of the size of a fraction of the diffraction envelope. The effect of having

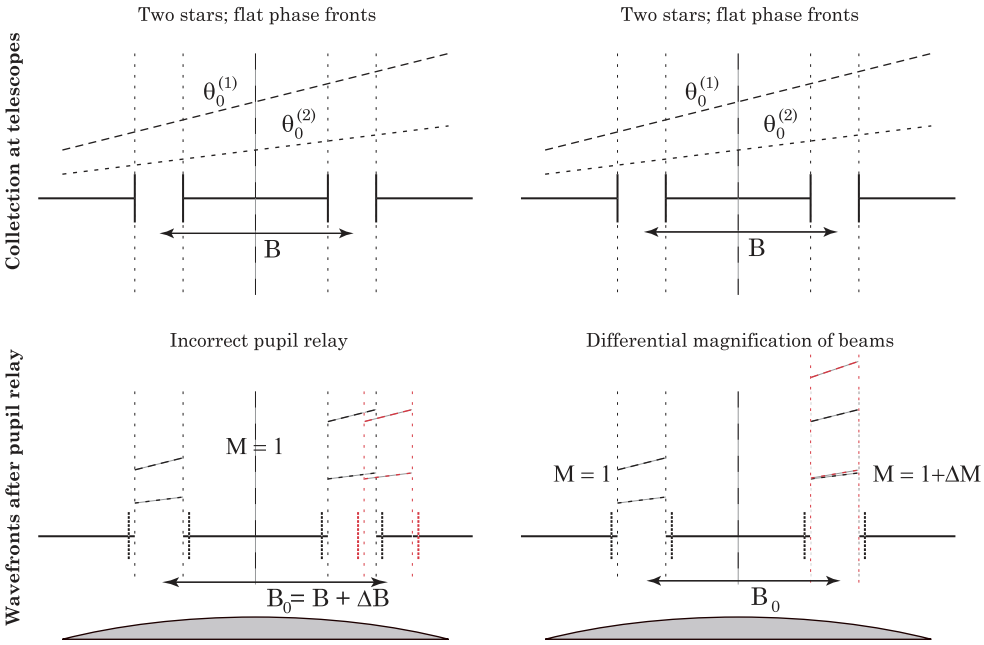

Figure 6.3: Illustrations of two mapping errors, beam translation (left) and differential magnification (right). The phase fronts for two stars, at $\theta_0^{(1)}$ and $\theta_0^{(2)}$ before collection are indicated, as well as the partial wavefronts in the beams just before entering the beam combiner. The **translated exit pupil** causes a field-dependent OPD, since the partial wavefronts in the righthandside beam for $\theta_0^{(1)}$ and $\theta_0^{(2)}$ have an extra difference with their respectively correct wavefronts. For the **differential magnification**, there is an extra tilt between the partial wavefronts, causing non-overlapping images of the sky. Moreover, the path length error is field-dependent again.

differential translation or path lengths of the beams, is illustrated in Fig. 6.3.

In 2002, the Delft-based organization of TNO, TPD, built a demonstrator for homothesis, called DTI, equipped with a different approach for pupil placement. For this set-up, the tolerancing study as done by Beckers, is repeated. The image overlap is allowed to be $1/10^{\text{th}}$ of a diffraction envelope size. This will not lead to very strict tolerances on the alignment. The amount of path length differences and variations (δP) across the field-of-view that can be allowed, determine more strictly the tolerancing of the pupil configuration parameters. Beckers considers three cases for δP:

1. A cophased field-of-view in which $\delta P << 1$ wavelength. In this case the white light fringe stays with a star[1] image, to within a fraction of a fringe, when the star is moved across the field-of-view.

2. A highly coherent field-of-view in which $\delta P <$ a few wavelengths. In this case, all stars in the field-of-view have fringes, but the fringe-phase of a star depends on its location on the sky.

3. A poorly coherent field-of-view in which $\delta P <$ many wavelengths. In this case

[1] In this study, stars are considered to be point sources. In the lab, the stars have a finite size, but are much smaller than the PSF. Wide-field stellar objects, much larger than a PSF, are not considered.

Table 6.1: Required tolerances for the testbed DTI to perform homothetic mapping up to a cophased condition, defined as $1/20^{th}$ fringe movement. The table is equivalent to that in *"Factors affecting wide field-of-view operation"* (Beckers, 1990). [A] *Field overlap: 10% of Airy diameter mismatch allowed.*

Criterion at field $\theta_{0,\max}$ is 20 μrad	Cophased FOV $\delta P < 0.1$ μm	DTI Criterion	Should match to
$\theta_0^{(1)}$ *terms*			
Fractional baseline $\Delta B/B$	$\mathbf{1.67 \cdot 10^{-4}}$	Exit baseline B_0	**10 cm** $\pm$**16.7** μ**m**
Fractional magnification $\Delta M/M$	$1.67 \cdot 10^{-4}$	Magnification M	$1 \pm 1.67 \cdot 10^{-4}$
$\theta_0^{(2)}$ *terms*			
Transverse exit pupil placement [μm]	$\mathbf{5 \cdot 10^4}$	Pupil Piston	0 ± 25 nm
Fractional magnification $\Delta M/M$	$5 \cdot 10^{-1}$	(M less severe)	—
Image matching[A]		$d\theta_0 = 6.1$ μrad	
Fractional magnification $\Delta M/M$	$8 \cdot 10^{-4}$	Pupil tilt	$\mathbf{0 \pm 6.1}$ μ**rad**
Pupil rotation [degrees]	0.045	(M less severe)	—
Pupil rotation			
ϕ_{max} [degrees]	**.002**	Pupil rotation	.23 deg or 4 mrad
$\delta\phi$ [degrees]	**.001**		
δP_{tot} [μm]	0.22	Fringe movement	1/4 fringe

*Numbers in **bold** are critical tolerances.*

fringes may be visible on a star in the field-of-view, but might have moved off for another star.

Ad 1. The fraction by which the fringe is allowed to move depends on the application. For astrometry, a more accurate fringe phase is needed than for imaging. For the DTI, the fraction is chosen to be 1/20, so that over the FOV, the central fringe is centered on a star and is not moving more than $1/20^{\text{th}}$ of a fringe width off-center.
Ad 2. After construction and coarse alignment of the beam combiner and relay optics by hand, the highly coherent FOV is already achieved. The optical alignment and mechanical construction lead to fringes on all stars in the field-of-view, be it clearly not centered on each star.

Beckers then constructs the following equation for the internal path difference Ω for off-axis rays in the VLTI:

$$\Omega(\theta_0) \approx d - \Sigma \cdot \left(1 - \frac{M^2\theta_0^2}{2} \cdot \frac{M^4\theta_0^4}{24}\right) - B_0\left(M\theta_0 - \frac{M^3\theta_0^3}{6}\right), \tag{6.2}$$

resulting from series expansion for small values of θ_0. The term Σ results from off-zenith observations, causing a field-dependent external delay that has to be compensated with delay d in the delay lines. DTI observes near zenith with all telescopes in one plane, eliminating the occurence of length Σ.

The tolerances following from the set of Beckers' equations—where all sources of unwanted field dependent OPDs (or δP) are summed—are listed in Table 6.1. The indications in bold refer to critical tolerances, based on knowledge of the relay optics. For

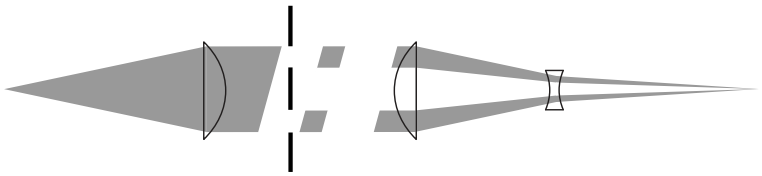

Figure 6.4: Sketch of an in-line version of the DTI set-up. Light from a point source is collimated, after which it encounters an aperture mask. Beams are then relayed independently from each other, with magnification $M = 1$. Then, the collimated beams are focused by a parabolic–hyperbolic mirror pair, indicated by positive and negative lenses, respectively. This combination was chosen to increase the effective focal length.

VLTI and DTI, the bold indications occur at different positions, since different hardware is used. Matching the baseline length $B_0 = B$ remains critical, but DTI's 3 μrad tilting mirrors with a separation of 1 meter give a high enough accuracy, even for the shorter baselines. The transverse exit pupil placement was found critical for VLTI,[2] but is not critical for DTI: both input and exit pupils do not have freedom to move out-of-plane and the path lengths can be controlled easily to be differing less than $\lambda_c/20 = 25$ nm. Pupil rotation as mentioned for VLTI is also not critical because the symmetric lay-out of the relay trains prevents pupil rotation to occur in the amount as specified for DTI. However, another source for image mismatching is pupil tilt. Since the DTI exit pupil placement system consists of tilting mirrors, it is necessary to monitor the occurrence of unwanted tilts. Both tilting mirrors have an angular accuracy of 3 μrad and the combined tilting of both (for pupil translation) is calibrated with a direct feedback on tilt, as will be described in Sec. 6.2.2.

6.1.4 Detector

The 1995 VLTI documentation speaks of several observational modes. One detector array should execute three tasks, being fringe tracking, imaging and spectrometry. This means that every single pixel should incorporate energy resolution, while keeping the individual detectors small enough to be able to detect fringes. For VLTI, the detector is not specified further. By using an array of fibers, the information in the focal plane could be transported for dispersed detection elsewhere. Therefore, the three observational modes seem possible. For DTI, an optical CCD camera was used as focal plane intensity detector. For the demonstrator, imaging and spectrometry are left out. Fringe tracking however, can be demonstrated with the intensity images the camera provides.

6.2 Measurement and actuation

As discussed before, the pupil relay and beam combination are toleranced with respect to beam rotation, pointing and magnification for sky overlap. Moreover, pupil positions and optical path lengths are toleranced to ensure a cophased FOV. The unknowns here, are the positions of every star i on the sky $\theta_0^{(i)}$, the baseline lengths B and B_0 (only relative

[2]For a general off-zenith observation at the site of VLTI, the telescopes are not in one plane, resulting in differential path lengths. The path lengths are equalized in the long delay lines, but after beam compression. This causes differential diffraction effects for each beam.

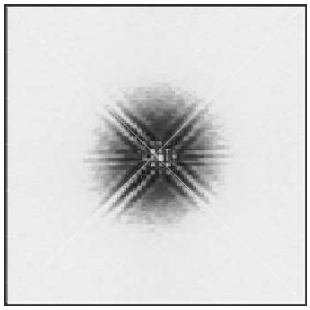

(a) Sub-image of a single star

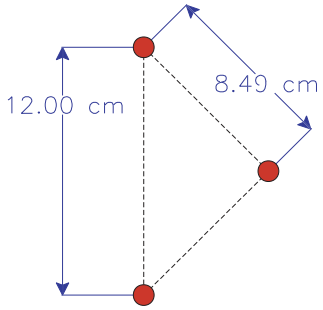

(b) DTI telescope configuration

Figure 6.5: Typical image of a point source, imaged through the DTI system: (a) an Airy envelope and fringe packets across it, perpendicular to the three baseline directions (b).

coordinates of pupils have to be considered) and the delay d_j per beam j. The knowns are listed in Table 6.2.

Table 6.2: Specifications of DTI.

Specification	**Value**
Beam diameter	$D = 1$ cm
Magnification	$M = 1$
Focal length	$f = 5$ m
Central wavelength	$\lambda_c = 500$ nm
Pixel size	pix = 7.5 μm

The only data available for arriving at $B_0 = B$ and $d_{j'} - d_j = 0$, are images from the camera. The algorithm for deriving the fringe phases is based on analysis of the Fourier space of a two dimensional image from the CCD camera. For clarity, the procedures in the algorithm will be explained by a one-dimensional example. This one-dimensional example can be regarded as a cross-section through a two-dimensional star image in the direction of any of the baselines.

6.2.1 Measuring star and fringe packet

The CCD-camera provides an image of the sky containing three stars, all resembling Figure 6.5a. The origin of the diffraction envelope of a star is measured in meter, as $x_1 = f \cdot \theta_0$. The coarse location x_0 is easily detected and a small sub-image $I(x)$ for $-d_{\text{Airy}} < (x - x_1) < d_{\text{Airy}}$ can be cut out around this location. The Fourier transform of such a sub-image allows to look at the spatial frequency content of the sub-image.

A star with fringes on it (see Fig. 6.6) is regarded to be a superposition of information in two different spatial frequency regimes. The star envelope is relatively large with respect to the size of the sub-image and yields information in the low spatial frequency band. The fringe pattern in the envelope consists of narrow lines and is hence related to higher spatial frequencies. The Fourier spectrum of the data is given in Fig. 6.7. The amplitude part clearly shows the presence of the envelope in the low spatial frequencies

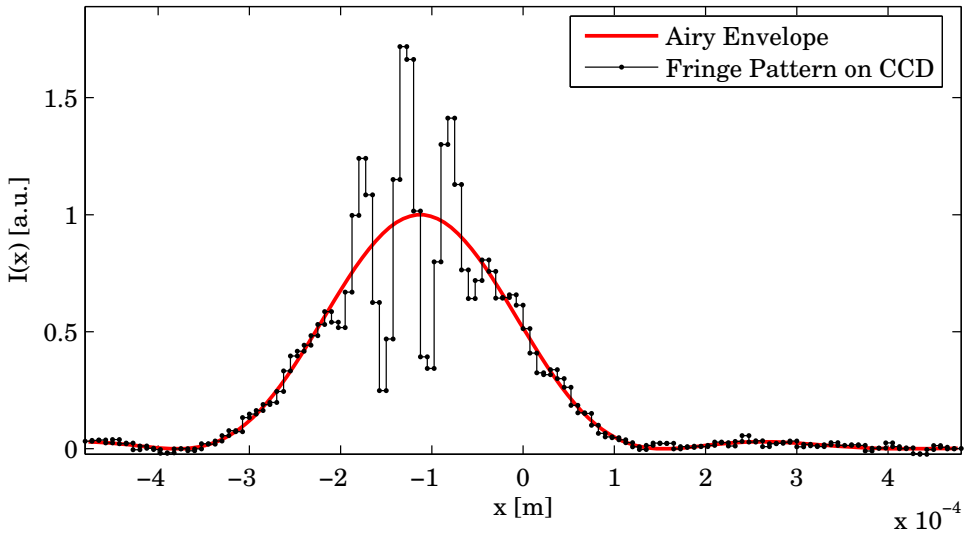

Figure 6.6: This dataset represents an Airy envelope with a packet of interference fringes in it. The envelope is not centered in the dataset (representing an unknown *exact* location of the star) and the fringe packet is not centered in the envelope, representing a non-zero OPD.

(in the center) and the fringes at some higher frequencies (on two sides of the center). In the definition of the Fourier transform,

$$\mathscr{F}[f(x)](k) = \int_{-\infty}^{\infty} f(x) e^{-2\pi i k x} \mathrm{d}x, \tag{6.3}$$

shifting a function $f(x)$ to $f(x-x_0)$ yields an addition of a phase contribution linear with wavenumber k and proportional to the shift x_0. Using $u = x - x_0$, this phase addition appears in

$$\begin{aligned} \int_{-\infty}^{\infty} f(u) e^{-2\pi i k u} \mathrm{d}u &= \int_{-\infty}^{\infty} f(x-x_0) e^{-2\pi i k (x-x_0)} \mathrm{d}(x-x_0) \\ &= e^{2\pi i k x_0} \int_{-\infty}^{\infty} f(x-x_0) e^{-2\pi i k x} \mathrm{d}x, \end{aligned} \tag{6.4}$$

where $\mathrm{d}(x-x_0) = \mathrm{d}x$ since x_0 is a constant. The result of Eq. (6.4) is referred to as the *shifting theorem*. It is the basis for both envelope position determination as well as fringe phase estimation. The Fourier amplitude spectrum and phase spectrum are defined as

$$\begin{aligned} F(k) &= |\mathscr{F}[f(x)](k)| \\ \Phi(k) &= \arg\{\mathscr{F}[f(x)](k)\}. \end{aligned} \tag{6.5}$$

The Fourier amplitudes of the shifted function $F(k)$ are used to identify the regions of interest and the Fourier phases $\Phi(k)$ in these regions provide the amount of shift. If the steepness

$$\alpha = \left.\frac{\mathrm{d}\Phi(k)}{\mathrm{d}k}\right|_{k=0} \tag{6.6}$$

of the central lobe's phase function is measured, the linear contribution in the *total* Fourier-phase function (after unwrapping) can be subtracted, according to

$$\Phi_2(k) = \Phi(k) - \alpha k, \tag{6.7}$$

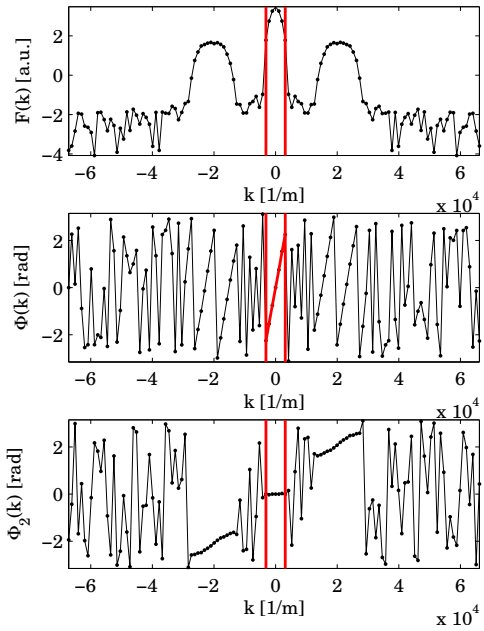

Figure 6.7: The representation of the dataset in Fig. 6.6 in Fourier amplitude and phase. **Top**: the amplitude part on a logarithmic scale. **Middle**: the phase information, wrapped between minus and plus π. The fitted line $\phi = 7.2 \cdot 10^{-4} k$ is indicated. **Bottom**: the processed phase information. The typical values for the spatial frequencies of the envelope and the fringe packet correspond to the wavenumbers $\pm k_d = 1.9 \cdot 10^3$ and $\pm k_f = 2.0 \cdot 10^4$ m^{-1}.

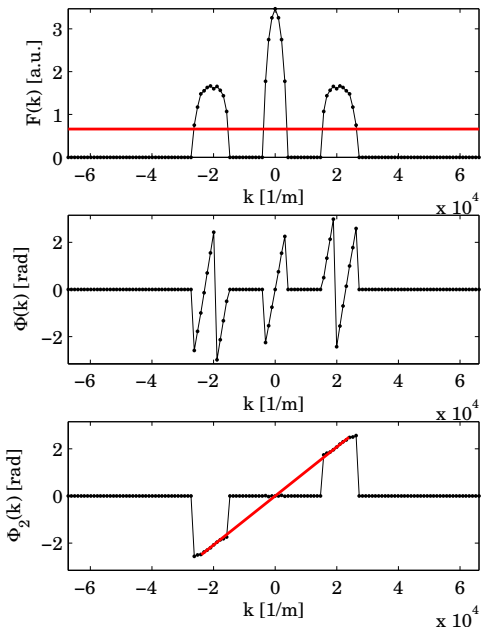

Figure 6.8: Thresholding the Fourier amplitude data clarifies the twofold slope retrieval. **Top**: the amplitude graph identifies a central lobe (containing the presence of the envelope) and two periferic lobes (for the presence of the fringe packet). **Middle**: the phase trend (present everywhere, but measured in the central lobe region) that is to be removed. **Bottom**: fitting a line through the phase information of the packet-lobes yields a measure for the packet position. The fitted line $\phi = 1.0 \cdot 10^{-4} k$ is indicated.

making the 'shift' of the function $I(x)$ undone. Comparing the multiplication with the phase factor $\exp[2\pi i k x_0]$ in Eq. (6.4) with the addition of $-\alpha k$ in Eq. (6.7), it can be deduced that the shift $x_0 = 2\pi\alpha$. This measure for how far the envelope was out of the center, together with the coarse cut-out location x_1, yields an accurate sub-pixel resolution position of the star as

$$x_2 = x_1 - 2\pi \left. \frac{\mathrm{d}\Phi(k)}{\mathrm{d}k} \right|_{k=0}. \tag{6.8}$$

The algorithm breaks down when the steepness is that high, that phase unwrapping in the central region is necessary. In practice, this occurs when the envelope is close to falling outside the boundaries of the sub-image, when the detected value of x_1 is too far out of range. Taking 128 pixels squared for a sub-image and having a diffraction envelope of approximately 50 pixels, the coarse position estimation should be accurate up to 78 pixels, which is easily achievable.

Figure 6.8 shows what happens in the regions of interest, using a threshold on the Fourier-amplitude graph in Fig. 6.7 to identify the spatial frequency regions where actual

information is present. The spatial frequencies of interest in Figs. 6.7 and 6.8 can be found around k_d, the wavenumber of the diffraction envelope, and k_f, the wavenumber of the fringe packet, given by

$$\begin{aligned} k_d &= \frac{2\pi D}{2.44\lambda_c f} \\ k_f &= \frac{2\pi B_0}{\lambda_c f}. \end{aligned} \tag{6.9}$$

After removing the linear slope in $\Phi(k)$, resulting in the Fourier-phases $\Phi_2(k)$, the remaining phase-slopes in the sidelobes around k_f provide likewise the information on how far the fringe packet is off-center, assuming a symmetric fringe packet. Again, the shift property of the Fourier transform is applied, this time to the function representing the fringe packet.

Whereas the total function was centered by fitting a line through the central phases $\Phi(k)$, for $-k_d < k < k_d$, the retrieval of the fringe phase (or packet position) is a result of a least squares fit through the peripheric phases $\Phi(k)$, for $|(k - k_f)| < k_d$. Both fitting functions are a straight line, so $\phi = a \cdot k + b$ with $b \simeq 0$. The outcome for b can be used to check the fit, since the line has to pass through zero. For steep lines (a packet far away from the center), phase unwrapping is necessary, starting from the origin. The algorithm breaks down at steepness values that make the unwrapping unreliable. This will occur when the packet is nearly off the envelope, so when the optical system is getting close to not being *coherenced*. 'Rough coherencing' should therefore be performed before this algorithm for fine coherencing can be used. The resolution of measuring the fringe shift by this principle can become very high by taking more than one measurement. This allows *cophasing* up to the level that fringes are being detected at $1/20^{th}$ of a fringe-distance off-center.

Measurements

To obtain information on the mechanical stability of the DTI set-up, a long term measurement was performed, logging the directions of nine beams running through DTI. Figure 6.9 shows the focused image of these nine beams. It is obtained by observing three white-light point sources through three apertures. The images of the sky are intentionally not overlapped. In the resulting image, the centroids of the spots are identified and logged.

This position logging resulted in the data represented in Fig. 6.10. Overnight, the passive opto-mechanical construction, placed in an unconditioned room, maintains a pointing accuracy of typically 8 μrad. Both the short-term pointing errors and the OPD behavior—after correct alignment so that fringes appear on the stars—were not measured. However, visual inspection of the CCD-feed (of which a still is depicted in Fig. 6.11) showed fringes at a fixed position, with a constant visibility value.

In the fringe-phase accuracy measurements, the fringe phase on each star with index i is expressed as a piston p_i. Through several measurements $p_i^{(j)}$, with $j = 1, 2, \ldots, J$, a straight line is fit, according to

$$\hat{p}_i^{(j)} = \alpha_i p_{\text{in},i}^{(j)} + p_{0,i}, \tag{6.10}$$

where $p_{\text{in},i}^{(j)}$ and $p_{0,i}$ are the applied pistons (OPD) and the OPD off-set, respectively. For

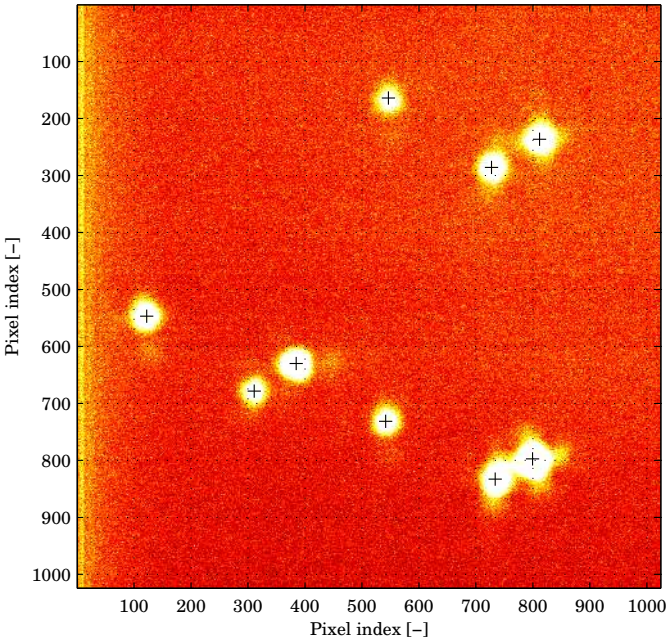

Figure 6.9: Camera view of DTI during the stability measurement. Three stars are imaged via three independent beams, generating nine spots in focus. The centroids of these spots are identified and logged.

the resulting misfit, the standard deviation is taken to be the square root of the bias-corrected variance, and is given as

$$\sigma_{N-1} = \sqrt{\frac{1}{N}\sum_{i=1}^{N}\left(p_i - \hat{p}_i\right)}. \tag{6.11}$$

The measurement, as well as the fit and the standard deviation, are presented in Fig. 6.12. From this Figure, it can be concluded that the fringe phase on each star, expressed as OPD in meters, can be measured with an accuracy of approximately 10 nm.

6.2.2 Actuation of beam relay

As mentioned, wrong baseline lengths $B_0 + \Delta B$ in the exit pupil configuration show up as field-dependent OPD effects, $\delta P = \Delta B \cdot \theta_0$. The location of the optical axis on the camera is unknown and the axis might even be projected outside the CCD. Therefore, only relative coordinates of the stars $\theta_0^{(2)} - \theta_0^{(1)}$ can be measured with the procedure described in Sec. 6.2.1. With this relative coordinate known, the measured OPDs on all stars are the sum of the true OPD between to beams plus the field-dependent OPD effect,

$$\delta P_{12} = (d_2 - d_1) + \Delta B(\theta_0^{(2)} - \theta_0^{(1)}). \tag{6.12}$$

This requires that a baseline has to be set to at least two values of ΔB, for which then the fringe positions on the stars are measured, before distinction can be made between the

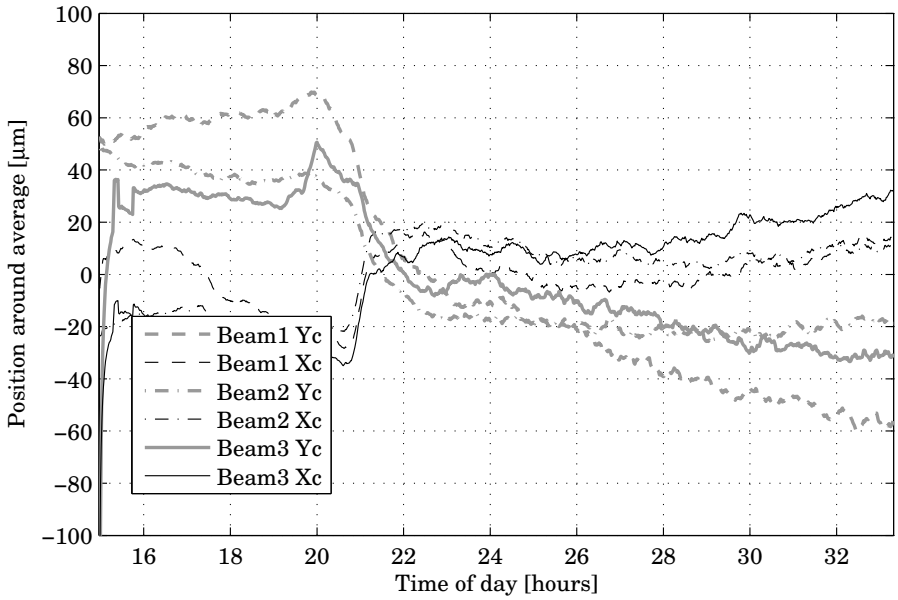

Figure 6.10: Stability of DTI. The graph shows the filtered time trace of the centroid locations of one star, as imaged via three beams. As a function of time, the coordinates on the CCD register the angular stability of DTI. The measurement started at 15h in the afternoon and ran until 9h in the morning. After the air circulation in the adjacent laboratory was shut down at 21h in the evening, the set-up drifts are typically 40 μm. This yields a long-term pointing drift of 8 μrad. The short-term effects due to vibrations were not properly measured.

unknown OPD $(d_2 - d_1)$ and the unknown baseline-error-OPD $\Delta B(\theta_0^{(2)} - \theta_0^{(1)})$. The location of the optical axis can be found by extrapolation of the obtained data. Additionally, since exit pupil displacement in the DTI is performed by a periscope system, at least four measurements on at least two different stars are needed. The following experiment will clarify this.

Pupil positioning

To reach homothesis $B_0 = B$, the tilt mirrors need to place and point each beam (exit pupil) to the proper position and direction. It is required that this can be done automatically and for changing B. For correct homothetic mapping[3], stars over the total field should look the same, so that the PSF is field-independent.

Periscope

The exit pupils are placed with a so-called *periscope* system of mirrors, as depicted in Fig. 6.13. By controlling the orientation of the two mirrors, one can influence the outgoing light in three manners. The direction of the wavefront normal can be changed (by tilting either of the mirrors), the optical path length through this subsystem can be

[3]Mapping is the process of arriving at and maintaining $B_0 = B$.

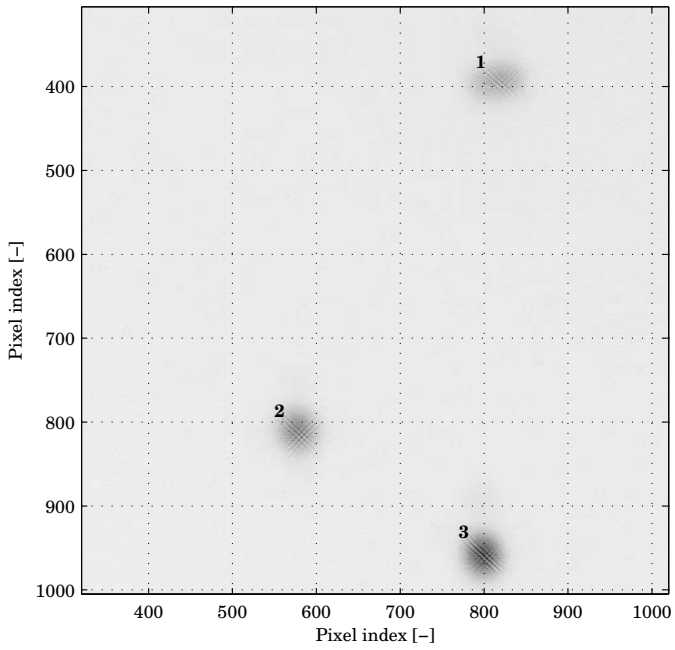

Figure 6.11: Camera image of DTI, when the three images of the sky are overlapped and the optical path lengths of the three beams are equalized. The three stars (white-light point sources) in the FOV display fringes in three directions.

changed (by pistoning either of both mirrors) and the location of the *virtual* exit pupil position can be changed by tilting both mirrors over exactly the same angle.

These six degrees of freedom, namely two orientations of the exit beam, two positions of the exit beam and two pistons of the mirrors, have to be controlled by six mounted actuators. The actuators are piezo elements with nanometer positioning accuracy over a 30μm range. A linearized system is valid for the small angles that are envisaged, so a system of equations can be constructed that relates the effect of every single actuator to the six degrees of freedom. The six degrees of freedom are not all directly measurable. However, very good estimates of them can be made. Most important is the strict control of the direction of the light exiting the periscope. If any combined piezo movement in the periscope results in a tip or tilt of the outgoing beam with respect to the common plane of incidence, the star field overlap with the star fields in the other beams is lost. This important degree of freedom, tilt of the exit beam, is directly measurable on the camera, since a tilt will result in displacement of the stars related to one beam.

The to be calibrated 6×6 matrix $\mathbf{C}$, relating the 6 piezos to the 6 degrees of freedom, will then look like

$$\mathbf{C} \cdot \mathbf{p} \quad = \quad \mathbf{b}$$

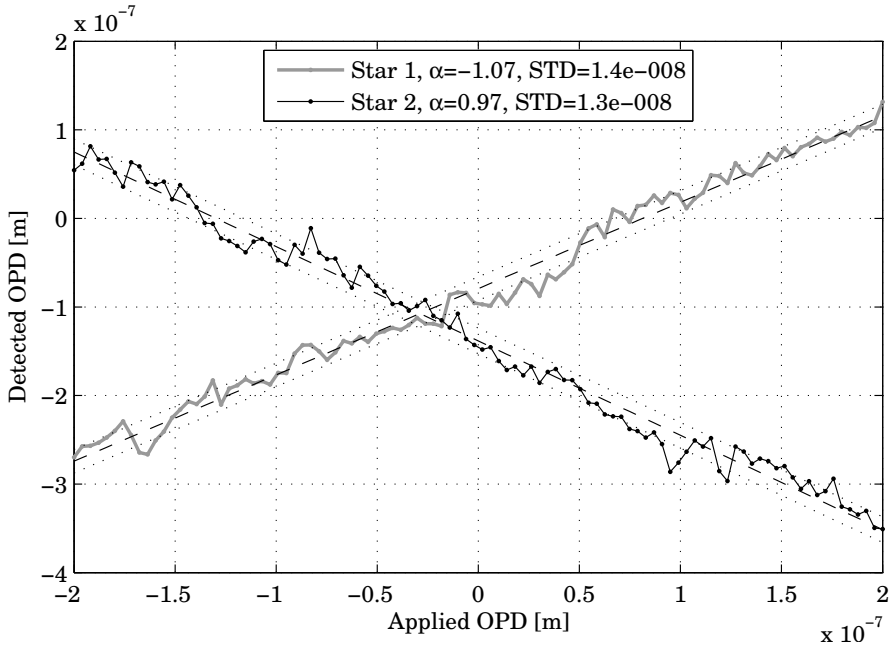

Figure 6.12: Accuracy of fringe phase estimation. With the calibrated control matrix **C**, see Eq. (6.13), pure piston without tilts can be applied to a beam, resulting in a shift of the fringe packet in focus. This shift can be measured by the FT-based detection algorithm. The graphs show a slight linear error (the slopes should have been $\alpha_{1,2} = \pm 1$) and a standard deviation in the OPD estimate with $\sigma_{N-1,\mathrm{OPD}} \approx 15$ nm.

$$\begin{bmatrix} a_1 & \cdots & a_6 \\ & \ddots & \\ a_{31} & \cdots & a_{36} \end{bmatrix} \begin{pmatrix} l_1 \\ \vdots \\ l_6 \end{pmatrix} = \begin{pmatrix} \text{Tilt} \\ \text{Tip} \\ T_x \\ T_y \\ \text{Piston A} \\ \text{Piston B} \end{pmatrix}, \tag{6.13}$$

where l_i is the length of piezo element i, ranging from 0 to 30 μm, a_j are 36 unknowns and T_x and T_y are beam translations in directions x and y, respectively. If 36 measurements would be performed, where all l_i take on random values and the measurement vector could be obtained, the unknowns could be derived. However, as mentioned, the observables are partly only observable *indirectly*.

This problem is solved in the following way. Firstly, the piston movement per mirror is taken to be the average of the lengths of the three piezos attached to it, so PistonA = $1/3(l_1 + l_2 + l_3)$. Secondly, the idea of putting random values on the piezos is abandoned. For all measurements, all piezos are first set to a central stretch of $l_i = 15$ μm. Then only one piezo is set to another length $l_{i'} = 15 + \Delta l$, making sure that the resulting tilt[4] does not shift the spot off the detector area. In this way, knowing which mirror is moving, the tilt can be accounted for in constructing the measurement vector **p** separately for

[4]A change of any l_i results in a combined tip and tilt for the corresponding beam, since the actuators are mounted at 120^o angles.

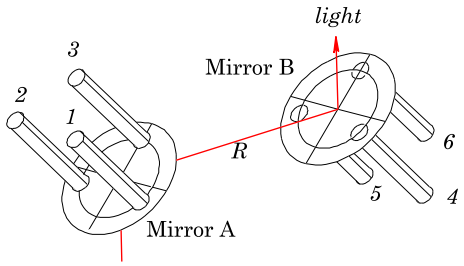

Figure 6.13: Sketch showing the *periscope* system for controlling the location of the exit pupil and the pointing direction its normal. The two mirrors A and B are actuated by six piezo-electric actuators, mounted on the backside of the mirrors. Such a periscope is in place for each moving telescope; in the case of DTI this leads to two periscopes. The third beam is relayed by fixed mirrors.

movements of mirror A (piezos 1,2 and 3) or mirror B (piezos 4,5 and 6):

$$\mathbf{b}(l_i)_{i=1,2,3} = \begin{pmatrix} \Delta x \\ \Delta y \\ \Delta x \cdot R \\ \Delta y \cdot R \\ \frac{1}{3}(l_1+l_2+l_3) \\ 15 \end{pmatrix}, \quad \mathbf{b}(l_i)_{i=4,5,6} = \begin{pmatrix} \Delta x \\ \Delta x \\ 0 \\ 0 \\ 15 \\ \frac{1}{3}(l_4+l_5+l_6) \end{pmatrix}. \tag{6.14}$$

In these expressions Δx and Δy are the shifts of one focused spot on the camera and R is the distance between mirrors A and B. A tilt is thus expressed as a lateral shift, measured in units of pixels. Tilting mirror A results not only in a measurable tilt of the beam, but also in a displacement of the exit location, depending on mirror separation distance R. These measurements do not require fringes on the stars.

6.2.3 Validation

Tilting the periscope mirrors A and B, induces a *parallel translation* of the exit beam. It also induces a quadratic dependence of the optical path length, with respect to the tilting angles of both mirrors. This quadratic behavior of the OPD of one moving beam with respect to one or more static beams was used as reference for both the FFT-based measurement algorithm and the **C**-matrix actuation equation.

Assuming that mirrors A and B pivot around a fixed coordinate, the lateral position Δx of a beam exiting the periscope and the change of path length Δl with both mirrors at an angle α (see Fig. 6.14), are

$$\Delta x = R\sin(2\alpha),\ \Delta l = R[1-\cos(2\alpha)]. \tag{6.15}$$

Limited series expansion of these expressions yields

$$\Delta x(\alpha) = R(2\alpha),\ \Delta l(\alpha) = R(2\alpha^2). \tag{6.16}$$

This change of path length Δl results in an OPD with the other beams. As a result, fringes will shift position. At the same time, star overlap has to be maintained, since a pure beam translation is free of tilt and focuses the beam on the same focal plane location. For

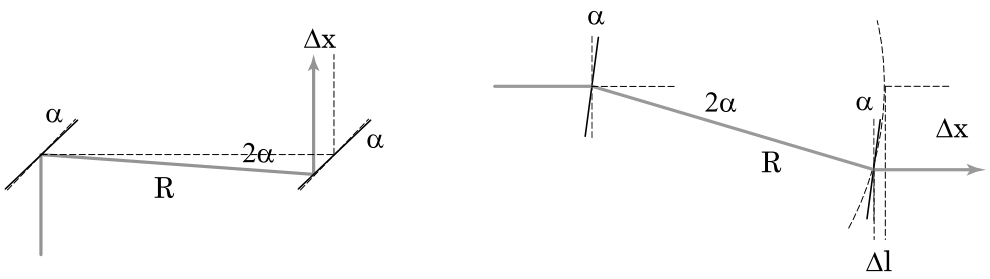

Figure 6.14: The periscope mirrors at an angle of 45^o degrees plus α are separated by a distance R. For small angles and the assumption that the mirrors pivot around a constant point, this model yields the displacement Δx and the change in path length Δl of the exiting beam as a function of α.

the experiment, the fringe phases ϕ_1 and ϕ_2 in one baseline direction are measured on two stars at directions $\theta_0^{(1)}$ and $\theta_0^{(2)}$. Then, the length of this baseline is either stretched or shortened by an amount ΔB at the exit pupil plane, by making use of the periscope system. The extra δP for a star with an off-axis angle θ_0 with respect to the projected baseline is:

$$\delta P = \Delta B \sin\theta_0, \tag{6.17}$$

which is, for small angles, linear with respect to ΔB as well as to star position on the sky. Note also that a general OPD effect in the optical train results in a fringe shift that is equal for all stars. The OPD effect of the DTI exit pupil placement method—the quadratic function $\Delta l(\alpha) \simeq \delta P(\Delta B)$—will therefore show up equally in all stars.

If both the piezo-calibration and the fringe-sensing algorithms are correctly implemented, the quadratic ODP dependence should be measurable and can be fit to the expected curve, based solely on the separation R of the tilting mirrors—neglecting the pivot point of the mirrors. The measured results and fitting process are depicted in Fig. 6.15. The residuals (Fig. 6.16) can be explained as results from slight mis-alignment in the beam combiner. This is a parabolic-hyperbolic mirror pair, which is known for its aberration sensitivity for small displacements of the mirrors. These aberrations will introduce small pupil-position dependent OPD effects that are not accounted for. To obtain an estimate of this OPD-landscape, a method for in-situ aberration retrieval—necessary, since aberration measurements on the two parabolae and the hyperbolic mirror do not include alignment errors—was devised, based on a Hartmann-type measurement (Malacara, 1992). When DTI is built up, the full aperture of the beam combiner is unavailable for measurements. Only the $D = 1$ cm beams are available. The method described in Sec. 6.4 can obtain an OPD landscape of the beam combiner, for a small area around a beam. Without compensation for this OPD-landscape, the found standard deviation in the measurement of δP can be used to predict the obtained interferometric FOV.

6.3 Obtained interferometric Field-of-View

With the results presented in Figs. 6.15 and 6.16, the obtained interferometric FOV can be calculated. After correction for the periscope-induced delay effect, a straight line can

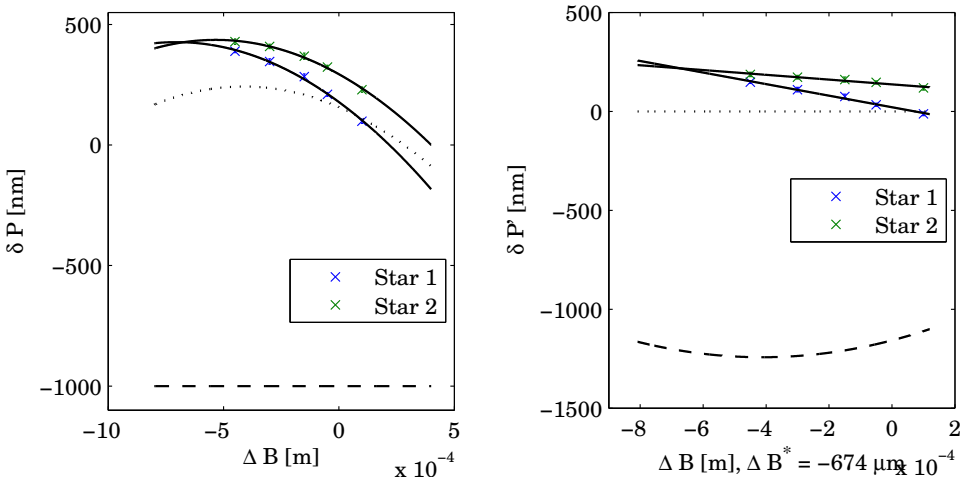

(a) Fit through measured data

(b) Data corrected with parabola

Figure 6.15: The measured OPD effect $\delta P(\Delta B)$ of making a baseline shorter or longer is corrected for the parabolic OPD effect of the *periscope*. Panel (a) shows the measured $\delta P(\Delta B)$. The data are fit to a parabolic function (the same for both series) plus a linear part. In panel (b), this linear part clearly shows up, because the parabola is subtracted. Homothetic conditions are met at the intersection of these lines: at this baseline length, the fringe phases in the stars are equal and can be set to zero by adjusting the delay d.

be fit through the measured $p_i(\Delta B)$ data, resulting in $\hat{p}_i(\Delta B)$, equivalently to the expression in Eq. (6.10). The steepnesses of the lines indicate, that the stars #1 and #2 have a separation $|\theta_0^{(2)} - \theta_0^{(1)}|$ on the sky of 193 μrad, perpendicular to the projected baseline direction. The absolute differential optical path length $|p_2 - p_1|$ is therefore measured at a separation smaller than the FOV. The found standard deviation on these measurements is at best 5 nm. After adding this standard deviation as an error η to the fit through the differences, a guaranteed FOV can be found. Therefore,

$$\mathrm{FOV}(\Delta B) = \frac{|\theta_0^{(2)} - \theta_0^{(1)}| \cdot \frac{\lambda}{20}}{|\hat{p}_2(\Delta B) - \hat{p}_1(\Delta B)| + \eta}, \tag{6.18}$$

in which the cophased field-of-view (or interferometric FOV) is stated to be the region on the sky for which the OPD or $|\hat{p}_2(\Delta B) - \hat{p}_1(\Delta B)| + \eta < \lambda/20$. The measurement error η therefore narrows down the guaranteed cophased FOV. Figure 6.17(b) shows three obtained FOVs, as the exit baseline length B_0 is scanned (from an arbitrary origin) and approaches the entrance baseline length B. For the case $\eta = 0$ nm, the FOV is larger than the FOV of the camera in the range $-692 < \Delta B < -656$ μm, which is in accordance with the baseline length tolerance derived from Beckers' calculation, given as 10 cm $\pm$ 16.7 μm. However, η is not zero in practice. Due to noise sensitivity the algorithm provides estimates with $\eta = 15$ nm (see the piston measurement in Fig. 6.12) but even after averaging, other error sources cause a remaining $\eta = 5$ nm (see the residuals in Fig. 6.16). As a result, the co-phasing of the full FOV can *not* be guaranteed to be at least $\lambda/20$. Although DTI is equipped with a pupil positioning system that can easily meet the 10 cm $\pm$ 16.7 μm requirement, no proof can be given that the desired FOV of 1.5 mrad is achieved.

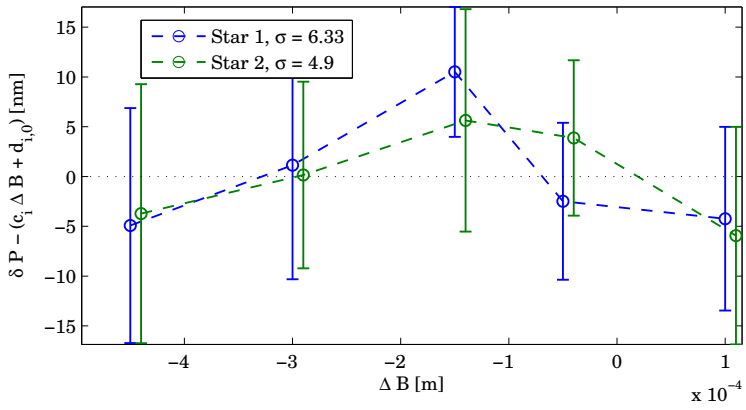

Figure 6.16: The deviation from the fit shown in figure 6.15b is depicted here. The σ of the fit is around 5 nm, being $\lambda/100$. The error bars correspond to averaging 16 times per baseline setting. This figure shows that OPD effects in the nanometer regime can be detected, where micrometer disturbances are present, without placing the set-up in a conditioned room.

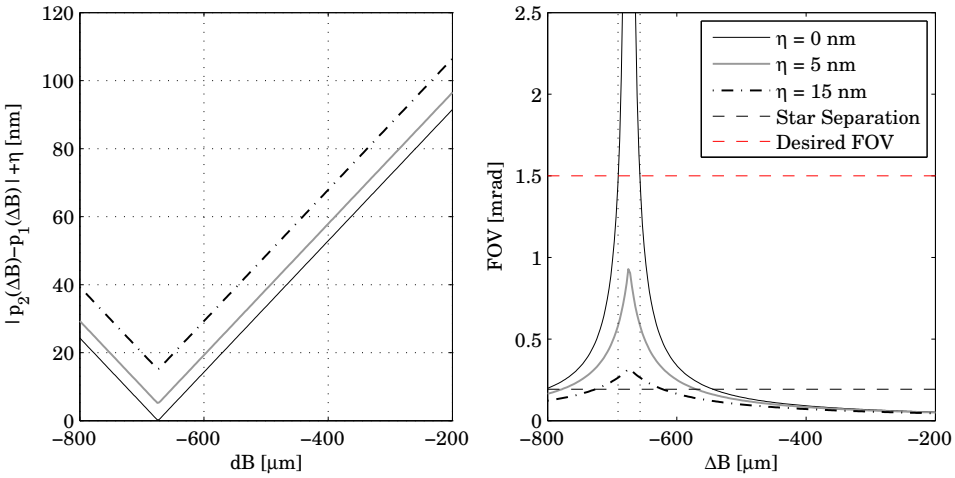

Figure 6.17: Two stars on the sky at $\theta_0^{(1)}$ and $\theta_0^{(2)}$, have a fringe phase translated to piston $p_i(\Delta B)$ in meters. A measurement error η is added to a fit through these p_i, resulting in panel (a), $|\hat{p}_2(\Delta B) - \hat{p}_1(\Delta B)| + \eta$. With this difference, the interferometric FOV(ΔB) can be calculated, panel (b). See text for details.

Repeating the calculation with $\eta = 2.5$ nm results in a co-phased 1.5 mrad FOV with a 10 cm $\pm$ 4 μm tolerance.

Both the algorithm that estimates the central fringe position relative to the star envelope *and* the origins of remaining OPD variations across the field have to be improved. The latter—causing residuals in the expected linear OPD behavior—is an effect that can be compensated for, once known. For the algorithm, a more sophisticated estimator has to be developed, especially when weaker stars have to be used as references for co-phasing.

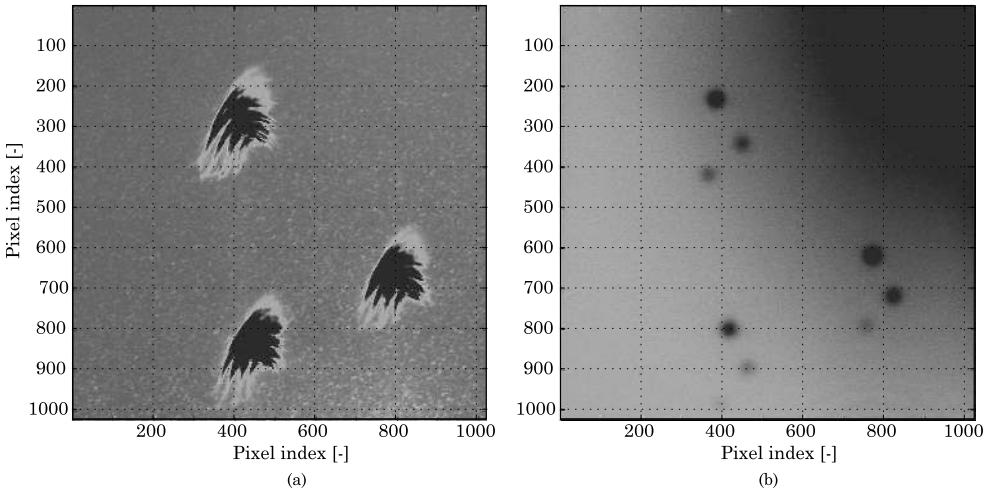

Figure 6.18: **(a)** Image of three stars in best focus, as observed by the full synthetic aperture without telescope mask. The full area of the beam combiner (synthetic aperture) was *not* intended to approach the diffraction limit. **(b)** Three stars, as imaged through three telescopes on the DTI. If the images of the sky are intentionally placed side-by-side, it is clear that the images of the sky are not exactly the same. This makes it impossible to overlap corresponding stars from different beams.

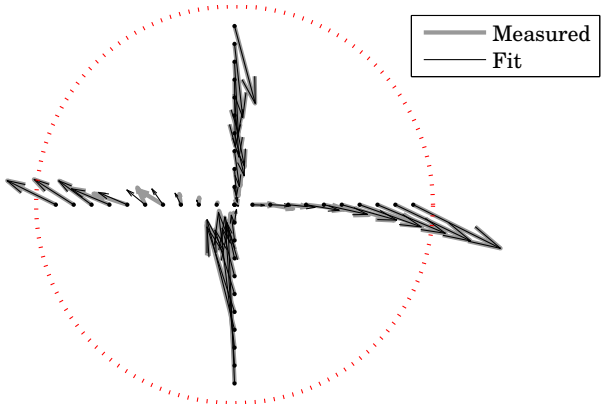

Figure 6.19: This diagram indicates the measurement locations of the aperture in the synthetic pupil. For each position of the aperture, the displacement of the focus on the camera is measured. This displacement is indicated in the plot, originating from the aperture location (although the focus remains close to the origin) with arrows having a scaled length, of arbitrary units.

6.4 In-situ aberration retrieval

The images of the sky as 'seen' through the three telescopes are not exactly the same. Figures 6.18(a,b) show a three-star sky, imaged through DTI once with and once without a three-telescope aperture mask. Although differential pupil rotation is eliminated, it is impossible to obtain exact overlap of the sky images from each beam. In other words, three images of one star can be made to overlap, but this will result in a non-overlap of

the three images of another star in the sky. This might be due to differential deformation of the images of the sky, which can be expected if the beam combination optics show aberrations. Aberrations include production inaccuracies on the various curved surfaces as well as alignment errors of these surfaces with respect to each other. The locations of the three apertures make that completely different parts of the curved surfaces of the beam combiner elements are addressed. Moreover, the relatively long path that has to be traveled from the entrance pupil to the beam combiner optics (≃2 meter) makes that essentially all of the nine beams present (three telescopes looking at three stars each) hit a slightly different part of the beam combiner. An aberration on one of the surfaces or generally on the beam combiner will then add a different tilt to each beam. These beam and star dependent extra tilts cause improper image overlap at the camera. Figure 6.19 shows a measurement of this beam location-dependent tilt effect. But moreover, location-dependent added OPD can be expected as well, resulting in OPD changes as a function of the location of a beam in front of the beam combiner. Knowledge of such a 'beam combiner induced OPD landscape' is essential to be able to automatically align a set-up such as DTI to homothesis. A situation might occur, in which the phases of the fringes on stars in the FOV cannot be equalized to a degree comparable to the detection accuracy.

Production accuracy

The production accuracy of the curved beam combiner surfaces was chosen such, that a 1 cm beam footprint would experience small enough aberrations, to reach a nearly diffraction-limited spot in focus. To no extent it was desirable to produce the full synthetic aperture of the beam combiner to operate near the diffraction limit. The synthetic aperture has a diameter in the order of 10 cm, a beam is 1 cm in diameter. The desirable diameter of a near-to-aberration-free virtual surface through the beam combiner lies in between these values. For proper image overlap, the footprint of the full FOV on the beam combiner should be nearly aberration-free.

A tilt of a wavefront causes a shift in focus. For an overlap of two beams, encountering two different areas of the beam combiner, the differential tilt for them to be overlapped better than a tenth of an Airy diameter, is then $\lambda/10D$, since a phase shift of 2π over the beam diameter induces a tilt as large as the angular Airy diameter. For an image of the sky, where the stars at the edges are overlapped just as well as the central stars, the same rule of thumb has to be applied to the footprint of the FOV on the beam combiner. The optical path length from the entrance pupil plane to the virtual plane of the single-lens beam combiner, is roughly[5] 2 m. This yields a footprint diameter of $FOV \cdot 2 = 2$ mm. Around the three exit pupil positions, there should hence be areas of approximately 1.5 times the beam diameter, where the OPD landscape has a Peak-to-Valley height of less than a tenth of the central wavelength. Only then, the full FOV, as imaged through three apertures, can be overlapped.

The next section will demonstrate how the beam combiner-induced tilts are measured and how a virtual OPD landscape is calculated from these data. Knowing the added OPD as a function of the position in the synthetic aperture, differential fringe phases per star can be compensated for.

[5]The beam combiner is illustrated as a single-lens imaging system. However, in practice, the beam combiner is a Cassegrain-telescope, consisting of a parabolic and a hyperbolic surface, separated by a certain distance. The distance of 2 m is the best case estimate for the distance from entrance apertures to the beam combiner, since this is the distance at which the first surface—the parabola—is encountered.

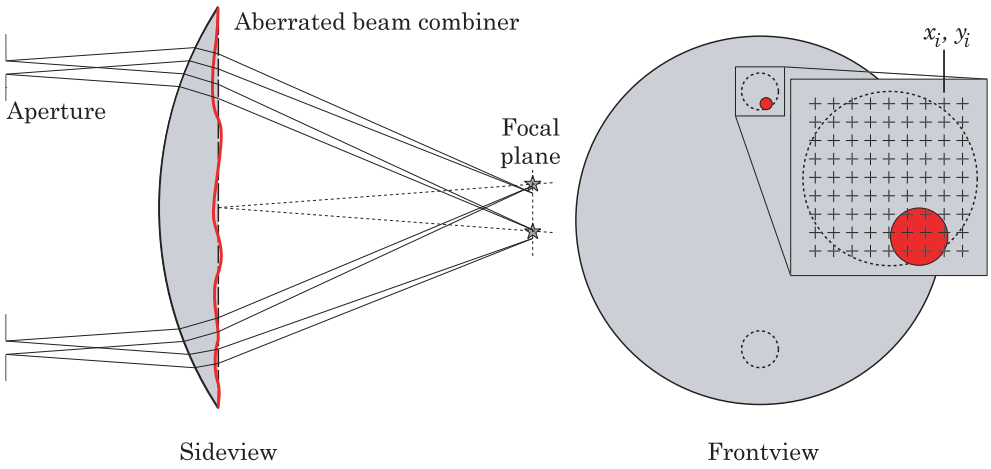

Figure 6.20: Sketches illustrating the in-situ measurement of beam combiner aberrations. The **side view** shows how two stars, from directions $\theta_0^{(1)}$ and $\theta_0^{(2)}$, are imaged via two apertures. An aberration-free beam combiner would focus these stars twice, on top of each other, with interference fringes. The sketch shows how in stead of two focused stars, *four* spots are visible in focus. This is due to the aberrations, indicated schematically at the back of the lens. The **front view** illustrates how one beam can be translated (without additional tilt) to a position (x_i, y_i). The aberration profile in the area around this location will cause a slight but measurable displacement in focus. For the measurement of these displacements, only one beam at a time is passing through the beam combiner.

The pupil function $P(r,\vartheta) = 1 \cdot \exp[i\Phi]$ represents a uniform amplitude part and an unknown phase departure $\Phi(r,\vartheta)$. Based on the Zernike polynomials Z_n^m, any complex pupil function can be expressed as the sum of several of these functions. The amplitude (transmission through the pupil) is assumed to be constant and of unit magnitude. The phase function can be expressed as

$$\Phi(r,\vartheta) = \sum_{n,m} \alpha_{nm} Z_n^m(r,\vartheta), \tag{6.19}$$

where α_{nm} is a constant for the participation factor of that polynomial. The sought 'added OPD landscape' can now be approximated by

$$P'(r,\vartheta) = \frac{\lambda_c}{2\pi} \arg[P(r,\vartheta)]\,. \tag{6.20}$$

Since the deviations are expected to be very small as compared to the dimensions of the pupil, there holds $e^{ix} \approx 1 + ix$ and the sought landscape is, apart from a constant, very well approximated by the sum in Eq. (6.19).

This landscape will be sampled at discrete locations rather than over the full coordinate range. Moreover, rather than measuring 'heights' or the phase profile, only the surface normal vectors can be measured. Similar to the famous Hartmann screen test, e.g. as described in (Malacara, 1992), the focus locations of various sub beams within the aperture are analyzed. However, in stead of a drilled screen, only one beam was used and repositioned sequentially. Both the Hartman test and this one rely on the fact that an aberration-free optical system focuses parallel beams on the same location and has

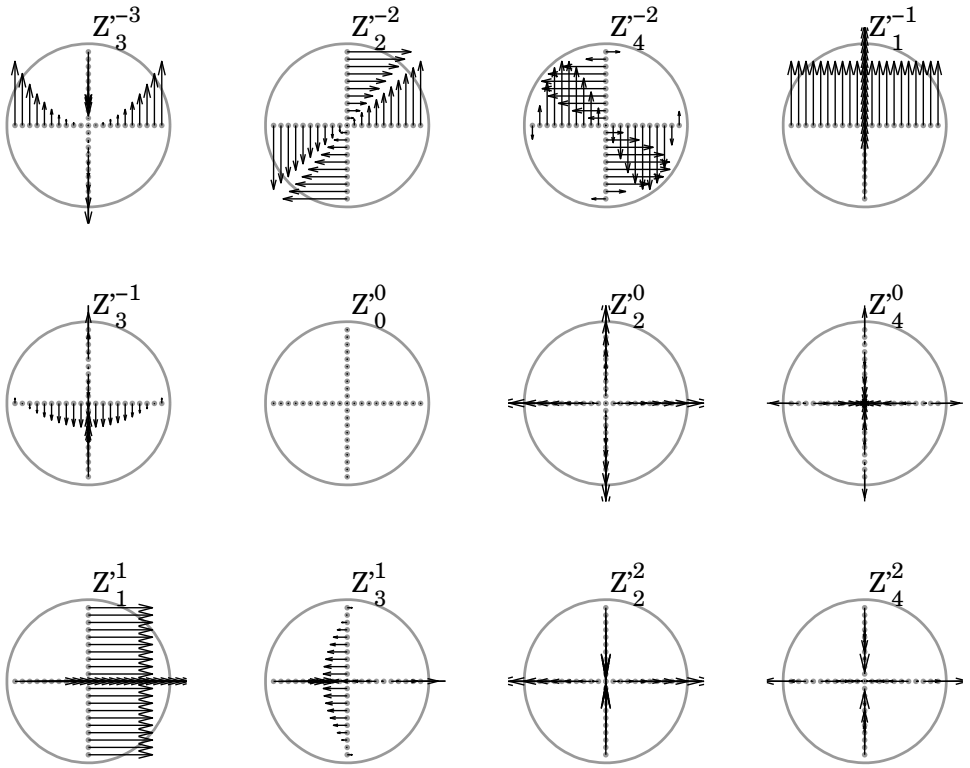

Figure 6.21: Illustration of the decomposition modes, corresponding to the x- and y-derivatives of the Zernike functions, evaluated at the measurement locations. The circle represents the area of the full synthetic aperture.

a linear relationship between off-axis angle of the collimated beam and the off-axis location in focus. Deviations from this location, depending on the area of the pupil that was used, are due to aberrations. The spot dislocation hence leads to a measure for the deviation of the surface normal and the normal vector can be rotated by $\pi/2$ to give the surface tangential vector, corresponding to the derivatives of the 'landscape'. Figure 6.19 shows this measurement of dislocations. Unlike the Hartmann- or alternative tests, the method based on Zernike derivatives does not require a regular sampling grid. Extrapolation from probe locations to the full aperture is easy using the Zernike functions and is allowed as long as the Zernike derivatives, evaluated at the probe locations, form a near orthogonal basis, like the full Zernike functions. Naturally, very localized defects on an optical surface can only be reconstructed when the area of this defect is probed.

The derivatives to be measured in x and y-direction, are introduced in the expression as

$$\frac{\partial P'}{\partial x} = \frac{\partial \Phi}{\partial x} = \sum_{n,m} \alpha_n^m \frac{Z_n^m(r,\vartheta)}{\partial x}. \tag{6.21}$$

Analytically, the derivatives of the Zernike functions would have to be calculated. Numerically, this is realized by a few extra evaluations of the Zernike functions at minimally separated locations, from which the Euler derivative can be calculated. The polar coor-

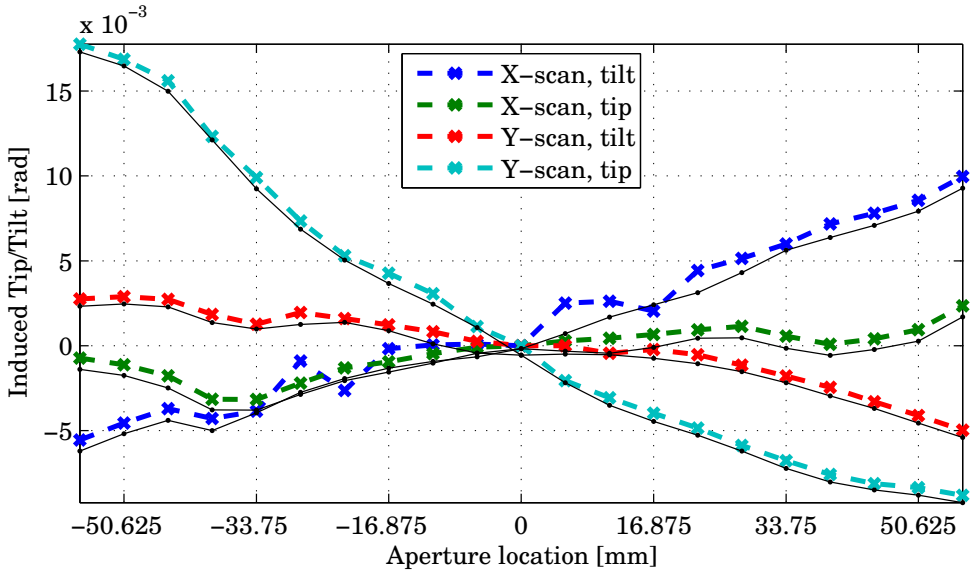

Figure 6.22: When the measured tips and tilts are plotted as a function of aperture position, the fit using the Zernike mode decomposition can be observed to nicely match the data and provide a smoothened set of tips and tilts.

dinates are transformed according to $x = r\cos\vartheta$ and $y = r\sin\vartheta$. Still only considering the x-derivative, this yields, at a location (x_i, y_i), the expression

$$\begin{aligned} \left.\frac{\partial\Phi}{\partial x}\right|_{x_i,y_i} &= \sum_{n,m} \alpha_n^m \frac{Z_n^m(x_i,y_i)}{\partial x} \\ &= \sum_{n,m} \alpha_n^m \frac{Z_n^m(x_i+\Delta x,y_i) - Z_n^m(x_i,y_i)}{\Delta x}, \end{aligned} \tag{6.22}$$

where Δx is very small. The same expression can be given for the y-direction. The coefficients α that are sought are the same for the expressions in x and y directions. Therefore, the linear system of equations that is constructed, consists of two parts.

$$\begin{pmatrix} \frac{\partial\Phi}{\partial x}|_{x_1,y_1} \\ \vdots \\ \frac{\partial\Phi}{\partial y}|_{x_1,y_1} \\ \vdots \end{pmatrix} = \begin{bmatrix} \frac{\partial Z_0^0(x_1,y_1)}{\partial x} & \frac{\partial Z_2^0(x_1,y_1)}{\partial x} & \cdots \\ \vdots & \vdots & \\ \frac{\partial Z_0^0(x_1,y_1)}{\partial y} & \frac{\partial Z_2^0(x_1,y_1)}{\partial y} & \cdots \\ \vdots & \vdots & \end{bmatrix} \begin{pmatrix} \alpha_{00} \\ \alpha_{20} \\ \alpha_{11} \\ \alpha_{31} \\ \vdots \end{pmatrix} \tag{6.23}$$

The derivatives are a linear combination of the derivatives of the Zernike functions. This expression can be denoted as

$$\mathbf{d} = \mathbf{Z}\cdot\boldsymbol{\alpha}. \tag{6.24}$$

A few examples of these Zernike derivatives are presented in Fig. 6.21. The Zernike participation coefficients α_n^m can be found after a regularized inversion $\boldsymbol{\alpha} = \mathbf{Z}_{\text{reg}}^{-1}\cdot\mathbf{d}$. With the coefficients found, the pupil function or the OPD profile can be constructed as the

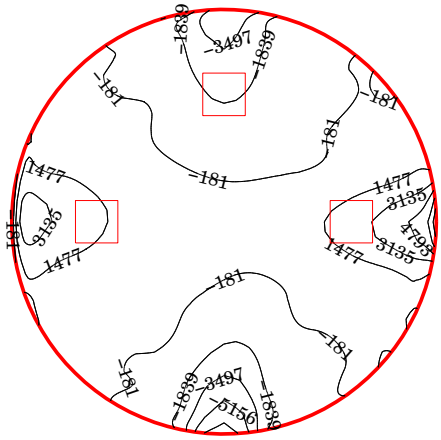

Figure 6.23: The resulting OPD landscape (heights in nm) over the strongly astigmatic synthetic aperture, matching the measured tips and tilts, projected on a unit circle. The Peak-to-Valley distance is 14 μm. The squares indicate the exit aperture locations of DTI.

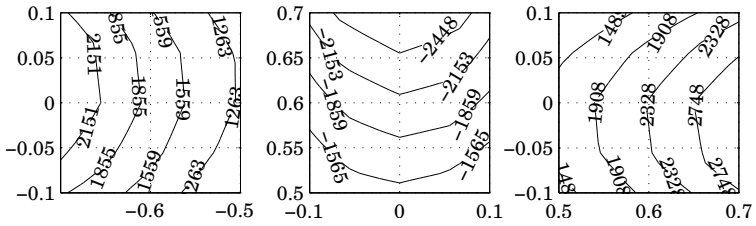

Figure 6.24: Enlargements of three regions of Fig. 6.23. See text for details.

sum of regular Zernike functions, as in Eq. (6.19). This allows for evaluation of the locally added OPD at other locations than the probe locations. Moreover, the sample locations do not necessarily have to be located in a grid, unlike for conventional integration (Malacara, 1992). Since the expected aberrations are assumed to be smooth, the Zernike expansion even allows for extrapolation outside the scanned area. In addition, the components for defocus (Z_2^0) and tip and tilt ($Z_1^{\pm 1}$) can be removed, since these aberrations are not effectively present as aberrations of the beam combiner. Including them would falsely aggravate the Peak-to-Valley height difference in the OPD landscape.

In Fig. 6.22, the result of the fitting operation is illustrated. As in Fig. 6.19, both the tip and tilt measurements are plotted, for both the horizontal and the vertical set of probe locations. The fit with Zernike derivatives produces an adequate representation of the noisy measurement. With the participation factors α_n^m known, the virtual OPD landscape can be composed. The result is depicted in Fig. 6.23. The beam combiner is found to be strongly astigmatic, which is qualitatively in accordance with the full-aperture PSFs as imaged in Fig. 6.18(a), where—going through best focus—clearly a horizontal and vertical orientation of the foci before and after best focus, respectively, could be observed. Quantitatively, the OPD landscape shows deviations in the order of microns, where the Peak-to-Valley range is 15 μm. Over areas of the diameter of the FOV-footprint, deviations in the order of 1000 nm can be expected, which would—considering a wavelength

of $\lambda_c = 500$ nm—cause stars at the edges of the FOV to be possibly mis-overlapped with their images from other beams by an amount of two Airy diameters. During the experiments, such severe mis-matches were never encountered. The square areas in Fig. 6.23 are enlarged and plotted in Fig. 6.24. These contour plots basically demonstrate mainly a tip or tilt over the area, which can be accounted for by re-pointing the three beams. But the other features, indicated by the fact that the lines are curved, cannot be compensated for and will cause distortion of the image of the sky, that is different for the three images delivered by the three telescopes.

6.5 Conclusions

In this Chapter, an experimental set-up and a number of different experiments have been described. Unlike in the preceding Chapters, image reconstruction was not the main issue in these experiments. The set-up DTI offers only a single (although not rigid) baseline configuration, which provides far too little information to reconstruct an image. However, a number of conclusions can be drawn from the performed experiments.

Mechanically, DTI performs outstanding. Without feedback loops to control beam pointing or piston movements, the pupil relay optics are stable enough to provide an image of the sky where all stars in the FOV are visible as diffraction envelopes with clearly visible fringe patterns on them.

The interferometric FOV, for which the imaging array can be considered to provide a field-invariant interferometric PSF, is as large as the FOV of the detector. However, this statement is largely depending on the measurement accuracy of a fringe packet position with respect to its envelope. The Fourier transform-based algorithm for this task provides enough accuracy, be it that DTI is operating in a photon-rich regime.

To properly measure the relative position of a fringe packet with respect to a diffraction envelope, the diffraction envelope needs to be well-defined. The single-telescope images of the sky need to be overlapped perfectly, in order to find the correct centroid of a star. This is impossible with DTI. Aberrations in the beam combiner induce distortions in the single-telescope images that are different per image. It should be noted however, that a slight mis-overlap of images of a star does not shift the resulting fringes noticeably. But the fact that field-dependent distortions occur, means that there exists field-dependent optical path lengths, causing fringes to shift directly. Erroneous measurements of fringe phases will be the result.

Chapter 7

Aberration retrieval

7.1 Introduction

Aberrations play an important role in any optical imaging system. Constant monitoring of them is required. For complicated optical projection systems as encountered in lithography, long-term drifts or deformations might occur, degrading the performance of the lithographic imager. For optical systems in astronomy, short-term changes of the aberrations are induced by the changing atmosphere and the dynamics of the support structure and housing of the telescope. In the special case of interferometry, an improper placement, pointing or co-phasing of one of the apertures in the array, can be considered as a strongly localized aberration of the synthetic and sparsely filled aperture.

Although several methods exist for aberration retrieval, (Farrar *et al.*, 2000; Zach *et al.*, 2001), a new approach was developed, based on the analysis of the intensity point-spread function at multiple values of defocus. For low to moderate numerical aperture optical systems, the Extended Nijboer–Zernike (ENZ) formalism was developed (Janssen, 2002; Braat *et al.*, 2002; Dirksen *et al.*, 2003; Janssen *et al.*, 2004). With ENZ, the intensity PSF in the focal region can be described, given a de-focus parameter, the numerical aperture and an (aberrated) pupil function. The heart of the method lies in the fact that analogous to the series expansion of the pupil function in Zernike functions, the focal electric field can also be represented by a series of focal field functions. Moreover, it is shown that with knowledge of the intensities rather than the electric fields at various planes around focus, decomposition of the intensity data into contribution factors of the elementary focal field functions becomes possible. These contribution factors then deliver the Zernike coefficients of the aberrated pupil function (Van der Avoort *et al.*, 2005a).

Although developed for aberration retrieval in lithography, the ENZ formalism for aberration retrieval was applied to interferometry. After presenting the theory in Sec. 7.2, its use for retrieving aberrations on the beam combiner of an optical imaging array are investigated. Moreover, an analogue description and retrieval experiment will be given for retrieval of alignment and co-phasing errors of a sparse aperture. The following description of the ENZ formalism is a shortened version of the description in (Van der Avoort *et al.*, 2005a), in which also proofs, limits and enhancements of the theory are discussed.

7.2 High-accuracy general aberration retrieval

The ENZ theory for low to moderate numerical aperture optical systems can perform aberration retrieval for two cases, being pure-phase aberrations and general aberrations, including transmission differences over the pupil. Clearly, the second case includes the first, yet they will be described separately. The theory for phase-only is much simpler and describes the basis of the retrieval process.

Zernike representation and retrieval for pure-phase aberrations

A pure-phase aberration in the pupil function P in normalized coordinates is written as

$$P(\rho,\vartheta) = \exp\left[i\,\Phi(\rho,\vartheta)\right], \qquad 0 \le \rho \le 1, \;\; 0 \le \vartheta \le 2\pi, \tag{7.1}$$

with Φ the real-valued aberration phase. This Φ is thought to be expanded as a Zernike series

$$\Phi = \sum_{n,m} \alpha_n^m \, Z_n^m, \tag{7.2}$$

with real α_n^m and Zernike functions Z_n^m given as

$$Z_n^m(\rho,\vartheta) = R_n^m(\rho) \left\{ \begin{array}{l} \cos m\vartheta \\ \sin m\vartheta \end{array} \right. , \qquad 0 \le \rho \le 1, \;\; 0 \le \vartheta \le 2\pi, \tag{7.3}$$

with R_n^m the Zernike polynomials in standard convention (Born and Wolf, 1980), Sec. 9.2 and App. VII. The summation in Eq. (7.2) is over all integer $n, m \ge 0$ with $n - m \ge 0$ and even. The usual symmetry assumption on Φ: $\Phi(\rho,-\vartheta) = \Phi(\rho,\vartheta)$, is made, so that only the cosine-option in the right-hand side of Eq. (7.3) needs to be considered[1]. The α's in the expansion in Eq. (7.2) carry physical significance: α_2^0 represents defocus, α_1^1 represents tilt, α_2^2 represents astigmatism, α_4^0 represents spherical aberration, α_3^1 represents coma, etc.[2] The complex amplitude at normalized defocus parameter f of the point-spread function is denoted by U and follows from Fourier optics as

$$\begin{aligned} U(x,y;f) \equiv U(r,\varphi;f) \;&= \\ &= \frac{1}{\pi} \iint\limits_{\nu^2+\mu^2 \le 1} \exp\left[i f(\nu^2+\mu^2) + i\,\Phi(\nu,\mu)\right] \exp\left[2\pi i \nu x + 2\pi i \mu y\right] \mathrm{d}\nu \mathrm{d}\mu \;= \\ &= \frac{1}{\pi} \int_0^1 \int_0^{2\pi} \exp\left[i f \rho^2\right] \exp\left[i\,\Phi(\rho,\vartheta)\right] \exp\left[2\pi i \rho r \cos(\vartheta-\varphi)\right] \rho \,\mathrm{d}\rho \mathrm{d}\vartheta \,. \end{aligned} \tag{7.4}$$

Note the use here of Cartesian coordinates ν, μ and polar coordinates in the exit pupil $[(\nu,\mu) = (\rho\cos\vartheta, \rho\sin\vartheta)]$, and Cartesian coordinates x, y and polar coordinates in the focal planes $[(x,y) = (r\cos\varphi, r\sin\varphi)]$. The relationship between normalized image coordinates (x,y) and defocus parameter f on one hand and the image coordinates (X,Y,Z) in the lateral and axial direction is given by

$$x = X\,\frac{2\pi NA}{\lambda}, \qquad y = Y\,\frac{2\pi NA}{\lambda}, \qquad f = \frac{\pi NA^2}{\lambda}\,Z, \tag{7.5}$$

[1] The general case can be treated by working with two sets of α-coefficients, one for the cosine- and one for the sine-functions in Eq. (7.3).

[2] Also see (Born and Wolf, 1980), Sec. 9.2 for this matter.

with NA the numerical aperture of the lens and λ the wavelength of the used light. In all this, it is assumed that NA is sufficiently small, say $NA \leq 0.60$, so that certain approximations are permitted; in particular, the third formula in Eq. (7.5) follows from linearizing the true focal quantity $2\pi Z\lambda^{-1}(1-(1-NA^2)^{1/2})$ as $\pi NA^2 Z\lambda^{-1}$.

Under the assumption that Φ is sufficiently small, $\exp[i\Phi]$ may be linearized, and inserting Eqs. (7.2)–(7.3), this results in

$$\exp[i\,\Phi(\rho,\vartheta)] \approx 1 + i\,\Phi(\rho,\vartheta) = 1 + i\sum_{n,m}\alpha_n^m\,R_n^m(\rho)\cos m\vartheta\;. \tag{7.6}$$

Using that for integer m

$$\int_0^{2\pi}\exp[iz\cos(\vartheta-\varphi)]\exp(im\vartheta)\,d\vartheta = 2\pi i^m\exp(im\varphi)\,J_m(z)\;, \tag{7.7}$$

with J_m the Bessel function of the first kind and of order m, the integration over ϑ in the integral in Eq. (7.4) can be carried out term-by-term by inserting the right-hand side expression in Eq. (7.6). There results

$$U(r,\varphi;f) \approx 2V_0^0(r,f) + 2i\sum_{n,m} i^m\,\alpha_n^m\,V_n^m(r,f)\cos m\varphi\;, \tag{7.8}$$

where

$$V_n^m(r,f) = \int_0^1 \rho\,e^{if\rho^2}\,R_n^m(\rho)\,J_m(2\pi r\rho)\,\mathrm{d}\rho\;. \tag{7.9}$$

In (Janssen, 2002) and (Janssen *et al.*, 2004), series representations for the integrals in Eq. (7.9) are presented. The representation in (Janssen, 2002) is a generalization of Lommel's representation of the aberration-free point-spread function, see (Born and Wolf, 1980), Subsec. 8.8.1, and reads

$$V_n^m(r,f) = e^{if}\sum_{l=0}^{\infty}\left(\frac{-if}{\pi r}\right)^l\sum_{j=0}^{p}u_{lj}\,\frac{J_{m+l+2j+1}(2\pi r)}{2\pi r}\;, \tag{7.10}$$

where

$$u_{lj} = (-1)^p\,\frac{(m+l+2j+1)}{q+l+j+1}\binom{m+j+l}{l}\binom{j+l}{l}\binom{l}{p-j}\Big/\binom{q+l+j}{l}\;, \tag{7.11}$$

for $l = 0,1,\ldots$ and $j = 0,1,\ldots,p$, and where $p = \frac{1}{2}(n-m)$, $q = \frac{1}{2}(n+m)$. This representation can be used for values of $|f|$ as large as 10π, where as a rule of thumb some $3|f|$ terms in the infinite series over l at the right-hand side of (7.10) are required, see (Braat *et al.*, 2002), App. B. The series representation of V_n^m given in (Janssen *et al.*, 2004) is somewhat more complicated, involving both spherical Bessel functions and Bessel functions of the first kind and integer order, but has the advantage that it can be used for any value of f (and r).

The term $2V_0^0$ at the right-hand side of Eq. (7.8) corresponds to the aberration-free pupil function $P \equiv 1$. For relatively small aberrations, this term dominates the totality of all other terms. Accordingly, the intensity point-spread function $I = |U|^2$ is written as

$$I(r,\varphi;f) = 4|V_0^0(r,f)|^2 - 8\sum_{n,m}\alpha_n^m\mathrm{Im}[i^m V_n^m(r,f)V_0^{0*}(r,f)]\cos m\varphi + C(r,\varphi;f), \tag{7.12}$$

where

$$C(r,\varphi;f) = 4 \sum_{n_1,m_1;n_2,m_2} \alpha_{n_1}^{m_1} \alpha_{n_2}^{m_2} \mathrm{Re}[i^{m_1-m_2} V_{n_1}^{m_1}(r,f) V_{n_2}^{m_2 *}(r,f)] \cos m_1\varphi \cos m_2\varphi \quad (7.13)$$

comprises all second order cross-terms.

Equation (7.12) shows how one can compute the intensities in the focal planes from the Zernike coefficients α of the pure-phase aberration Φ (assumed that the $\exp[i\Phi]$ may be linearized). The inverse problem, in which the α's are computed from the intensity I is, in principle, awkward due to the C-term at the right hand side of Eq. (7.12) involving the α's quadratically. In Sec. 7.2 a strategy is presented for handling Eq. (7.12) in which the C-term disappears altogether from the formulas, leaving a set of linear systems in α (decoupled per azimuthal order m) that can easily be solved. Thus, within this procedure, it is permitted to delete C.

The procedure detailed in this Section to compute α's from intensities I forms the basis for the aberration retrieval algorithm related to the ENZ formalism. Thus the assumption is made to have available recorded intensity functions I_{meas}. The subscript "meas" serves here to distinguish from the "theoretical" intensity I in Eq. (7.12); no truly measured data are available. Applying the procedure of Sec. 7.2, with I at the left-hand side of (7.12) replaced by I_{meas}, results in finding α's that are considered to describe the pupil function that gave rise to the recorded I_{meas}.

Inversion process

The retrieval procedure derives the Zernike coefficients α_n^m of the aberration phase

$$\Phi(\rho,\vartheta) = \sum_{n,m} \alpha_n^m R_n^m(\rho) \cos m\vartheta \quad (7.14)$$

occurring in the pupil function $P = \exp[i\Phi]$ from the intensity $I = |U|^2$ in the focal region.

The pupil $\exp[i\Phi]$ is linearized as in Eq. (7.6) so that the approximation Eq. (7.8) of U results. Measurements I_{meas} of the intensity I in the $(r,\varphi;f)$-space are considered to be available, and α_n^m are intended to be estimated by adopting a best-fit approach in Eq. (7.13). A convenient decoupling in subproblems per m occurs by multiplying Eq. (7.13) by $\cos m\varphi$ and integrating over $\varphi \in [0,2\pi]$. Thus the functions Ψ_{meas}^m are introduced for $m = 0,1,...$ by

$$\Psi_{\mathrm{meas}}^m(r,f) = \frac{1}{2\pi} \int_0^{2\pi} I_{\mathrm{meas}}(r,\varphi;f) \cos m\varphi \, \mathrm{d}\varphi \quad (7.15)$$

and

$$\Psi_n^m(r,f) = -8\varepsilon_m^{-1} \mathrm{Im}[i^m V_n^m(r,f) V_0^{0*}(r,f)] \,, \quad (7.16)$$

where $\varepsilon_0 = 1$, $\varepsilon_1 = \varepsilon_2 = ... = 2$ (Neumann's symbol). The Ψ_{meas}^m in Eq. (7.15) are obtained from the measured data by a Fourier analysis in which only the cosine part matters because of the symmetry assumption. Equation (7.16) is restricted to integer $n, m \geq 0$ with $n - m \geq 0$ and even; all V_n^m are analytically available in accordance with (7.10)– (7.11). With these notations, one can write Eq. (7.12) under deletion of the term C in Eq. (7.13) as

$$\Psi_{\mathrm{meas}}^m(r,f) \approx 4\delta_{mo} |V_0^0(r,f)|^2 + \sum_n \alpha_n^m \Psi_n^m(r,f) \,, \quad (7.17)$$

where $m = 0, 1, ...$ and where Kronecker's delta δ_{mo} is used.

Being decoupled per $m = 0, 1, ...$, the α_n^m, $n = m, m+2, ...$ are chosen, such that in Eq. (7.17) the match between the left-hand side data and the (approximate) theoretical expression at the right-hand side is optimized. For this, the inner product for functions $\Psi(r, f)$ and $\chi(r, f)$ is introduced as

$$(\Psi, \chi) = \int_0^\infty \int_{-\infty}^{\infty} \Psi(r, f)\, \chi^*(r, f)\, r\, \mathrm{d}r\mathrm{d}f \,. \tag{7.18}$$

Before proceeding, it is noted that

$$(|V_0^0|^2, \Psi_{n'}^0) = 0 \,, \quad \text{for all } n' \,. \tag{7.19}$$

This follows from the more general fact, see Eq. (7.9), that for all m, n

$$V_n^m(r, -f) = V_n^{m*}(r, f) \,, \tag{7.20}$$

so that $|V_0^0|^2$ is even in f while all $\Psi_{n'}^0$ are odd in f. Taking inner products in Eq. (7.17) yields for $m = 0, 1, ...$

$$\sum_n \alpha_n^m (\Psi_n^m, \Psi_{n'}^m) \approx (\Psi_{\text{meas}}^m, \Psi_{n'}^m) \,, \tag{7.21}$$

in which n, n' are restricted to the range $m, m+2, ...$.

For $m = 0, 1, ...$ a vector of estimates $\hat{\boldsymbol{\alpha}}^m$ of $\boldsymbol{\alpha}^m = (\alpha_n^m)_{n=m,m+2,...}$ can now be obtained from Eq. (7.21) as follows. A Gram matrix $\boldsymbol{\Gamma}^m$ is defined by

$$\boldsymbol{\Gamma}^m = \left((\Psi_n^m, \Psi_{n'}^m)\right)_{n', n=m,m+2,...} \,, \tag{7.22}$$

and a right-hand side vector $\mathbf{r}^m$ by

$$\mathbf{r}^m = \left((\Psi_{\text{meas}}^m, \Psi_{n'}^m)\right)_{n'=m,m+2,...} \,, \tag{7.23}$$

and the estimate is then

$$\hat{\boldsymbol{\alpha}}^m = (\boldsymbol{\Gamma}^m)^{-1} \mathbf{r}^m \,, \tag{7.24}$$

where $(\boldsymbol{\Gamma}^m)^{-1}$ is the inverse of the Gram matrix $\boldsymbol{\Gamma}^m$ in Eq. (7.22). This completes the description of the estimation procedure.

It has been observed numerically, that the functions Ψ_n^m, $n = m, m+2, ...$, for fixed $m = 0, 1, ...$ are close to being orthogonal with respect to the inner product in Eq. (7.18). As a consequence, the Gram matrices in Eq. (7.22) are well-conditioned, and the inversions in Eq. (7.24) present no problems.

In a practical implementation of the method, the ranges in Eq. (7.21) for n, n' are finite, say $m, m+2, ..., m+2M$. The solution vector $\hat{\boldsymbol{\alpha}}^m(M)$ obtained by solving the truncated system has the property that

$$\left\| \Psi_{\text{meas}}^m - \sum_{n=m,m+2,...,m+2M} \eta_n^m \Psi_n^m \right\|^2 \tag{7.25}$$

is minimal for $\eta_n^m = \hat{\alpha}_n^m(M)$, $n = m, m+2, ..., m+2M$. Here $\| \; \|$ is the inner product norm corresponding to $(\,,\,)$ in Eq. (7.18).

Retrieval of general aberrations

The problem of retrieving the phase Φ of a pupil function $P = \exp[i\Phi]$ with a pure-phase aberration resulted in an algorithm that is surprisingly simple and easy to implement. However, its application range is restricted to pure-phase aberrations. In this section, a method for retrieving both amplitude $A > 0$ and phase Φ of a pupil function $P = A\exp[i\Phi]$ from the intensity point-spread function in the focal region will be derived.

The pupil function P is expanded into a Zernike cosine series

$$P = A\exp[i\Phi] = \sum_{n,m} \beta_n^m Z_n^m \; ; \qquad Z_n^m(\rho,\vartheta) = R_n^m(\rho)\cos m\vartheta \; , \tag{7.26}$$

where now the β_n^m are general complex numbers. In the often occurring case that $A \approx 1$, Φ small, one has that $\beta_0^0 \approx 1$ while all other β_n^m are small, and in that case the imaginary parts of the β_n^m describe Φ while the real parts of the β_n^m describe A. When $A \not\approx 1$ and/or Φ is not small, the physical significance of the β's is not straightforward anymore, but this diminishes in no way the efficiency of the representation of P by means of its complex Zernike coefficients.

Assume that β_0^0 is positive and relatively large compared to the other β_n^m's. For the point-spread function from Eq. (7.26) the exact representation is

$$U(r,\varphi\,;f) = 2\beta_0^0 V_0^0(r,f) + 2{\sum_{n,m}}' \beta_n^m i^m V_n^m(r,f)\cos m\varphi \; , \tag{7.27}$$

where the $'$ on the summation sign means to indicate that the term with $n = m = 0$ has been deleted. Expansion of $I = |U|^2$ results in

$$\begin{aligned} I \approx 4(\beta_0^0)^2|V_0^0|^2 \quad &+ \quad 8{\sum_{n,m}}' \beta_0^0 \mathrm{Re}(\beta_n^m)\,\mathrm{Re}[i^m V_n^m V_0^{0*}]\cos m\varphi \\ &- \quad 8{\sum_{n,m}}' \beta_0^0 \mathrm{Im}(\beta_n^m)\,\mathrm{Im}[i^m V_n^m V_0^{0*}]\cos m\varphi \; , \end{aligned} \tag{7.28}$$

with omission of the term

$$4{\sum_{n_1,n_2\,;\,n_2,m_2}}'' \mathrm{Re}[\beta_{n_1}^{m_1}\beta_{n_2}^{m_2*} i^{m_1-m_2} V_{n_1}^{m_1} V_{n_2}^{m_2*}]\cos m_1\varphi\cos m_2\varphi \; , \tag{7.29}$$

where the $''$ on the summation sign means to indicate that all terms with $n_1 = m_1 = 0$ or $n_2 = m_2 = 0$ have been deleted.

Then, as in the pure-phase case, the use of the functions Ψ_n^m in Eq. (7.16) appearing on the second line of Eq. (7.28), is extended with the functions

$$\chi_n^m(r,f) = 8\varepsilon_m^{-1}\,\mathrm{Re}[i^m V_n^m(r,f)\,V_0^{0*}(r,f)] \tag{7.30}$$

with ε_m Neumann's symbol as in Eq. (7.16). Furthermore, there is the same Ψ_{meas}^m as in Eq. (7.15). Then, upon multiplying the near-identity in (7.28) by $\cos m\varphi$ and integrating over $\varphi \in [0, 2\pi]$, there results

$$\Psi_{\mathrm{meas}}^0 \quad \approx \quad \tfrac{1}{2}(\beta_0^0)^2\chi_0^0 + {\sum_n}' \beta_0^0\,\mathrm{Re}(\beta_n^0)\,\chi_n^0 + {\sum_n}' \beta_0^0\,\mathrm{Im}(\beta_n^0)\,\Psi_n^0 \; , \tag{7.31}$$

$$\Psi_{\mathrm{meas}}^m \quad \approx \quad \sum_n \beta_0^0\,\mathrm{Re}(\beta_n^m)\,\chi_n^m + \sum_n \beta_0^0\,\mathrm{Im}(\beta_n^m)\,\Psi_n^m \; , \tag{7.32}$$

for $m = 0$ and $m = 1, 2, \ldots$, respectively.

As previously, the inner products are taken. Note that as a consequence of Eq. (7.20), for all $m = 0, 1, \ldots$, the products

$$(\chi_n^m, \Psi_{n'}^m) = 0 \,, \qquad \text{all } n, n' = m, m+2, \ldots \,. \tag{7.33}$$

Indeed, it follows from Eq. (7.20) that χ_n^m is even in f when m is even and odd in f when m is odd, whereas $\Psi_{n'}^m$ is odd in f when m is even and even in f when m is odd. Hence, by building for $m = 0, 1, \ldots$ linear systems as in Eq. (7.21) by taking inner products in the near-identities in Eqs. (7.31)–(7.32) with $\chi_{n'}^m$, $\Psi_{n'}^m$, a decoupling occurs according to

$$\left\{ \begin{array}{rcl} \frac{1}{2}(\beta_0^0)^2(\chi_0^0, \chi_{n'}^0) + {\sum_n}' \beta_0^0 \,\mathrm{Re}(\beta_n^0)(\chi_n^0, \chi_{n'}^0) & \approx & (\Psi_{\mathrm{meas}}^0, \chi_{n'}^0) \,, \\ {\sum_n}' \beta_0^0 \,\mathrm{Im}(\beta_n^0)(\Psi_n^0, \Psi_{n'}^0) & \approx & (\Psi_{\mathrm{meas}}^0, \Psi_{n'}^0) \end{array} \right. \tag{7.34}$$

for $m = 0$ where $n, n' = 0, 2, \ldots$, and

$$\left\{ \begin{array}{rcl} \sum_n \beta_0^0 \,\mathrm{Re}(\beta_n^m)(\chi_n^m, \chi_{n'}^m) & \approx & (\Psi_{\mathrm{meas}}^m, \chi_{n'}^m) \,, \\ \sum_n \beta_0^0 \,\mathrm{Im}(\beta_n^m)(\Psi_n^m, \Psi_{n'}^m) & \approx & (\Psi_{\mathrm{meas}}^m, \Psi_{n'}^m) \end{array} \right. \tag{7.35}$$

for $m = 1, 2, \ldots$ where $n, n' = m, m+2, \ldots$.

The procedure to estimate the β_n^m's is now as follows. The first system in Eq. (7.34) is solved, involving $(\beta_0^0)^2$, $\beta_0^0 \,\mathrm{Re}(\beta_n^0)$ linearly. This then gives β_0^0 (which was assumed to be positive) and subsequently $\mathrm{Re}(\beta_n^0)$, $n = 2, 4, \ldots$. Having found β_0^0, the second system in Eq. (7.34) can be solved, involving $\beta_0^0 \,\mathrm{Im}(\beta_n^0)$ linearly and the two systems in Eq. (7.35) involving $\beta_0^0 \,\mathrm{Re}(\beta_n^m)$ and $\beta_0^0 \,\mathrm{Im}(\beta_n^m)$, respectively, linearly for $m = 1, 2, \ldots$. Estimates $\hat{\beta}_n^m$ are obtained by replacing all $\approx$ in Eqs. (7.34)–(7.35) by $=$ and solving the linear systems.

Note that in the case of purely imaginary β_n^m, only the second lines in Eqs. (7.34)–(7.35) need to be considered (and also the first line in Eq. (7.34) with $n' = 0$ to find β_0^0). This then yields the pure-phase retrieval method.

As in the case of pure-phase retrieval, the systems are normally well-conditioned since either system $(\Psi_n^m)_{n=m,m+2,\ldots}$ and $(\chi_n^m)_{n=m,m+2,\ldots}$ is close to being orthogonal. Also, the finitization issues are similar to those in the pure-phase retrieval case.

However, the deletion of the small-cross-terms expression Eq. (7.29) from the theoretical intensity $I = |U|^2$ has a quite different effect on the linear systems in Eqs. (7.34)–(7.35) than that deletion of Eq. (7.13) had on the systems in Eq. (7.21). The reason for this is that the functions

$$\mathrm{Re}\,[\beta_{n_1}^{m_1} \beta_{n_2}^{m_2 *} \, i^{m_1 - m_2} \, V_{n_1}^{m_1} \, V_{n_2}^{m_2 *}] \tag{7.36}$$

are, in general, neither even nor odd in f since the β_n^m are general complex numbers.

A simple predictor-corrector approach, however, can in many cases completely eliminate the error incurred by deleting the term in Eq. (7.29). Here one constructs iteratively estimates $\hat{\beta}_n^m(k)$ of the β_n^m as follows. Let $\hat{\beta}_n^m(0) = \hat{\beta}_n^m$, where $\hat{\beta}_n^m$ are the estimates of β_n^m as found by applying the above procedure in which the $\approx$ in Eqs. (7.34)–(7.35) are replaced by $=$. Having available $\hat{\beta}_n^m(k)$ for some $k = 0, 1, \ldots$, the above procedure is applied for finding $\hat{\beta}_n^m$, however, with the measured I_{meas} replaced with $I_{\mathrm{meas}} - E(k)$ in which $E(k)$ is the term Eq. (7.29) with

$$\hat{\beta}_{n_1}^{m_1}(k)(\hat{\beta}_{n_2}^{m_2}(k))^* \quad \text{substituted for} \quad \beta_{n_1}^{m_1}(\beta_{n_2}^{m_2})^* \,. \tag{7.37}$$

Under normal conditions, this predictor-corrector procedure converges rapidly while even under not so favorable conditions (with β_0^0 not large or even rather small compared to some of the other β_n^m) convergence, be it slow, often takes place as well (Van der Avoort *et al.*, 2005a).

The computational scheme for the predictor-corrector approach requires handling the quantities $I_{\text{meas}} - E(k)$, $k = 0, 1, \ldots$, as if they were measured quantities. Thus, these $I - E(k)$ have to be multiplied by $\cos m\varphi$ and integrated over $\varphi \in [0, 2\pi]$, and, subsequently, inner products with the $\chi_{n'}^m$, $\Psi_{n'}^m$ have to be taken.

As an example, Table 7.1 and Fig. 7.1 show the final result of a general aberration retrieval and the convergence of the predictor–corrector approach. From intensity data, general aberration coefficients $\hat{\beta}_n^m$ are obtained, that after k iterations converge to the applied aberration coefficients β_n^m.

Table 7.1: Applied and retrieved (100 iterations) aberration coefficients.

n	**m**	Re(β)	Re($\hat{\beta}$)	Im(β)	Im($\hat{\beta}$)
0	0	0.6610	0.6611	0	0
2	0	-0.0303	-0.0312	0	-0.0000
4	0	-0.2875	-0.2869	0	0.0000
6	0	-0.5506	-0.5502	0	-0.0000
1	1	0	0.0000	-0.1007	-0.1006
3	1	0	-0.0000	1.7948	1.7924
5	1	0	-0.0000	-0.1867	-0.1858
2	2	-0.4872	-0.4857	0	0.0000
4	2	0.0852	0.0876	0	-0.0000
6	2	-0.6983	-0.6991	0	-0.0000
3	3	0	-0.0000	-0.1134	-0.1125
5	3	0	0.0000	-0.2385	-0.2376

It is also interesting to consider a case where some of the $|\beta_n^m|$ are allowed to be larger than β_0^0, see Table 7.1. These β_n^m are obtained as the quantities $\frac{1}{3}\beta_n^m(\alpha)$ resulting from Zernike mode expansion, Eqs. (7.38)–(7.45), of the comatic pupil function $\exp[i\alpha Z_3^1]$ with α as large as $2\sqrt{1.6}$ (twice the diffraction limit) and $n \le 6$, $m \le 3$. Evidently, for accurately representing $\exp[i\alpha Z_3^1]$ where α is this large, considerably more terms should be considered; however, the present intention is just to show that perfect reconstruction is possible with a non-dominant β_0^0-term, and taking $\exp[i\alpha Z_3^1]$ with large α is such a case. The 4$^{\text{th}}$ and 6$^{\text{th}}$ column show reconstruction results after 100 iterations. In Fig. 7.1, the reconstruction error curves $|\beta_n^m - \hat{\beta}_n^m(k)|$ are displayed for the n, m as in Table 7.1 that occur with $\beta_n^m \neq 0$. Indeed, convergence takes place, but at a very slow rate.

Zernike mode expansion

When $P(\rho, \vartheta)$ is a (symmetric) pupil function, its Zernike expansion coefficients β_n^m in

$$P(\rho, \vartheta) = \sum_{n,m} \beta_n^m R_n^m(\rho) \cos m\vartheta \tag{7.38}$$

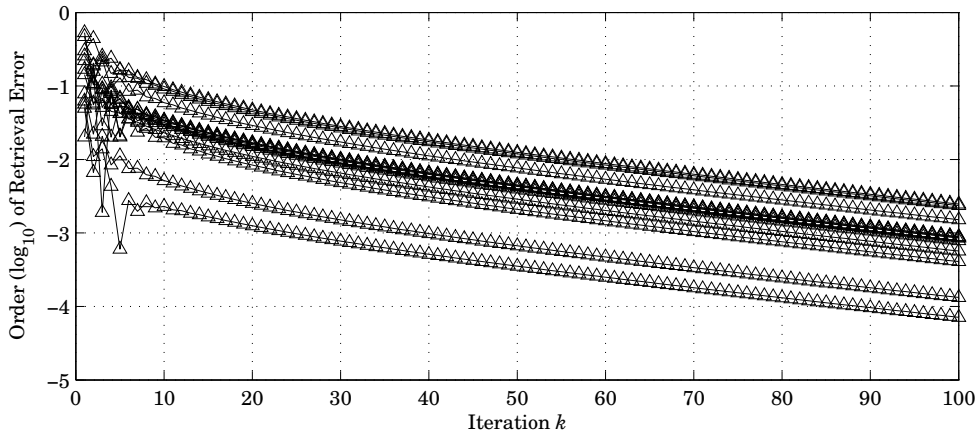

Figure 7.1: The absolute values of the reconstruction errors $|\beta_n^m - \hat{\beta}_n^m(k)|$ decrease slowly but steadily for the high value of $\alpha_3^1 = 2\sqrt{1.6}$, describing a comatic pupil beyond the diffraction limit. The largest error after 100 iterations (k) is below $10^{-2.5}$.

are given from orthogonality of the Zernike functions, see (Born and Wolf, 1980), formula (3) on p. 523, as

$$\beta_n^m = \frac{1}{\pi}\,(n+1)\,\varepsilon_m \int_0^1 \int_0^{2\pi} P(\rho,\vartheta)\,R_n^m(\rho)\cos m\vartheta\,\rho\,\mathrm{d}\rho\mathrm{d}\vartheta \tag{7.39}$$

with ε Neumann's symbol, $\varepsilon_0 = 1$, $\varepsilon_1 = \varepsilon_2 = \ldots = 2$. Next the Zernike expansion coefficients ${}_3^1\beta_n^m(\alpha)$ of $P(\rho,\vartheta) = \exp[i\,\alpha\,R_3^1(\rho)\cos\vartheta]$ shall be computed. The integral in Eq. (7.39) over ϑ can be done using Eq. (7.7), resulting in

$${}_3^1\beta_n^m(\alpha) = 2(n+1)\,\varepsilon_m\,i^m \int_0^1 R_n^m(\rho)\,J_m(\alpha\,R_3^1(\rho))\,\rho\,\mathrm{d}\rho\ . \tag{7.40}$$

Inserting the series expansion of J_m, see (Abramowitz and Stegun, 1970), formula 9.1.10 on p. 360, into the right-hand side integral in Eq. (7.40), there results

$${}_3^1\beta_n^m(\alpha) = 2(n+1)\,\varepsilon_m\,i^m \sum_{j=0}^{\infty} \frac{(-1)^j\,(\frac{1}{2}\,\alpha)^{m+2j}}{j!\,(j+m)!} \int_0^1 (R_3^1(\rho))^{m+2j}\,R_n^m(\rho)\,\rho\,\mathrm{d}\rho\ . \tag{7.41}$$

The remaining integrals can be evaluated by using that $R_3^1(\rho) = 3\rho^3 - 2\rho$, Newton's binomium, and the fact that, see (Braat *et al.*, 2003), formula (A2) on p. 2289,

$$\int_0^1 \rho^{m+2s}\,R_{m+2p}^m(\rho)\,\rho\,\mathrm{d}\rho = \tfrac{1}{2}\,(-1)^p\,\frac{(-s)_p}{(m+s+1)_{p+1}}\ , \tag{7.42}$$

where Pochhammer's symbol is used, defined as

$$(a)_0 = 1\,;\ \ (a)_k = a(a+1)\cdot\ldots\cdot(a+k-1)\ ,\qquad k = 1,2,\ldots\ . \tag{7.43}$$

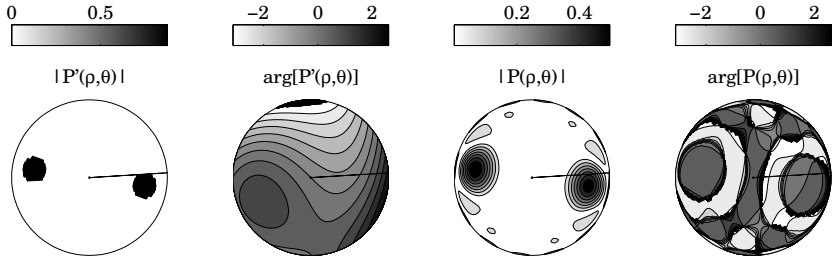

Figure 7.2: Of the aberrated sparse aperture $P'(\rho,\vartheta)$, the transmission profile is given as $|P'(\rho,\vartheta)|$, where the two-aperture mask is clearly visible. The phase profile $\arg[P'(\rho,\vartheta)]$ comprises tilt, coma and astigmatism of various magnitudes and at various angles (leftmost figures). This pupil function is approximated by the pupil function $P(\rho,\vartheta) = \sum_{n,m} \beta_n^m Z_n^m$, in which the Zernike polynomials with maximum indices $n_{\max} = m_{\max} = 9$ are taken into account (rightmost figures).

This yields

$$\int_0^1 (R_3^1(\rho))^{m+2j} R_{m+2p}^m(\rho)\,\rho\,\mathrm{d}\rho =$$

$$= \tfrac{1}{2}(-2)^{m+2j} \sum_{l=0}^{m+2j} \binom{m+2j}{l} \left(\frac{-3}{2}\right)^l \frac{(-j-l)_p (-1)^p}{(m+j+l+1)_{p+1}}\,, \tag{7.44}$$

and with some final rewriting this results in

$${}_1^3\beta_{m+2p}^m(\alpha) = (m+2p+1)\,\varepsilon_m \sum_{j=0}^{\infty} \frac{(-i\alpha)^{m+2j}}{j!(j+m)!} \cdot$$

$$\cdot \sum_{l=0}^{m+2j} \binom{m+2j}{l} \frac{(-1)^p (-j-l)_p}{(m+j+l+1)_{p+1}} \left(-\frac{3}{2}\right)^l . \tag{7.45}$$

7.3 Application to interferometry

Alignment of sub-apertures

The ENZ formalism is applicable to any optical imaging system. Especially the forward problem of obtaining the PSF, given an exit pupil function, can be illustrated for aperture synthesis. Using the ENZ formalism, the intensity PSF of a synthetic aperture can be calculated, after describing the synthetic aperture as a general pupil function, decomposed onto the Zernike basis. Then, the β_n^m-coefficients of the (large set of) Zernike functions are used in the summation of the V_n^m functions to calculate the electrical field. The squared modulus of this field results indeed in a fringed PSF, where the diameter of the envelope is related to the diameter of the individual apertures and the fringe period is related to the separation of these apertures.

Although a typical interferometer pupil function is easily transformed into a fringed focal field, see Fig. 7.3, the inversion of this process is not readily available using ENZ.

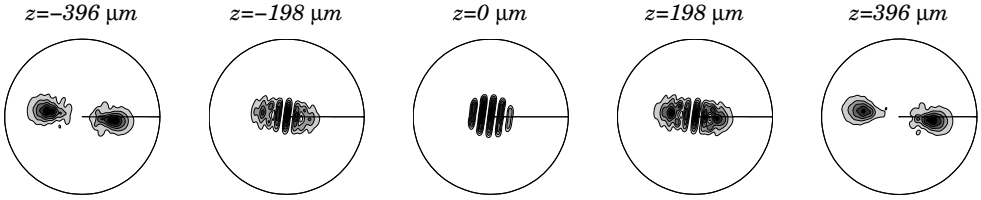

Figure 7.3: Through-focus intensity data, as obtained by illuminating the aberrated sparse aperture, described by the pupil function $P(\rho,\vartheta)$ of Fig. 7.2.

Table 7.2: The complex β_n^m-coefficients that construct the pupil function $P = \sum_{n,m} \beta_n^m Z_n^m$, for the pupil function P depicted in Fig. 7.2. Two sets of Zernike functions Z_n^m are taken, having either cosine-symmetry or sine-symmetry. Only the largest contributions are listed, which are all larger than β_0^0.

	$Z_n^m(\rho,\vartheta) = R_n^m(\rho)\cos m\vartheta$		$Z_n^m(\rho,\vartheta) = R_n^m(\rho)\sin m\vartheta$	
(n,m)	**Re**(β_n^m)	**Im**(β_n^m)	**Re**(β_n^m)	**Im**(β_n^m)
0,0	0.0275	0.0244	—	—
4,0	-0.0638	-0.0552	—	—
8,0	0.0500	0.0372	—	—
4,2	-0.0459	-0.0690	-0.0757	-0.0301
8,2	0.0398	0.0531	0.0622	0.0201
6,4	-0.0267	-0.1076	-0.1059	-0.0134
8,6	0.0093	-0.1131	-0.1057	0.0150

The decomposition of the sparse pupil function[3] resulted in a series of β_n^m-coefficients, see Tab. 7.2, where β_0^0 is no longer the largest, or nearly largest component. This results in the following breakdown of the retrieval process, including the predictor–corrector iterations. The initial guesses of all $\hat{\beta}_n^m(k=0)$ are very wrong. This has a too large effect on the cross-product correction term, that is added to the measured intensities, after which these altered intensities are used as a new measurement for the retrieval of the set $\hat{\beta}_n^m(1)$. The resulting intensity pattern is no longer significantly related to the physical imaging system under study, a beam combiner with a sparse pupil function. It should also be noted, that the representation of the sparse pupil function required a large number of Zernike modes and consequently the cross-product term involves are very large amount of innerproducts, which again qualifies the ENZ approach as accurate, but not optimized for speed. The retrieval process for the example with a strongly comatic pupil function already showed that the relatively large values of all β_n^m with respect to β_0^0 resulted in very slow convergence. For the case of the synthetic aperture, convergence is lost completely.

For correct retrieval of both the amplitude mask $|P'|$ and the phase profile, a different approach is required, in which the factor $1/\beta_0^0$ is not incorporated in the estimate of all β_n^m. Moreover, for an array of telescopes there is very accurate knowledge on $|P'|$. Including this a priori information will—as in any inverse problem—improve the estimate

[3]Evidently, the set of Zernike functions with $n_{\max} = m_{\max} = 9$ is too small to represent the aperture mask with steep edges. However, including more Zernike functions would not decrease the values of the β_n^m's for the low order functions. The example of the fact that β_0^0 is no longer governing the expansion, would remain the same.

of P'.

Higher order aberrations in sub apertures or beam combiner

As demonstrated, the ENZ formalism allows straightforward description of a focal field, given the series representation of a pupil function. In addition, several fields may be co-added, resulting an intensity pattern showing interference effects. Principally, this methodology is very promising for retrieving higher order aberrations—instead of only piston and tilt—in the individual apertures of an array of telescopes. This might provide information on the alignment of optical surfaces in each telescope and or in the beam compressor in each interferometer arm. However, the representation of a sparse pupil function requires a very large amount of coefficients, that have a large range in contribution amplitudes.

Studies have been done to represent a sparse aperture by a limited set of Zernike functions, by altering the Zernike functions to a function with a displaced origin. Even if a formalism for translated Zernike functions is available, the inverse operation, comparable to the ENZ predictor–corrector approach, has to be tailor-made, based on this set of translated functions. To develop such an analytic mathematical tool is a task too far out of the scope of this thesis.

Chapter 8

Chromatic multi-beam nulling

8.1 Introduction

To detect an Earth-like planet around a nearby star and to perform spectroscopy on its atmosphere, two difficulties have to be overcome. Firstly, a regular telescope would need a very high resolution to separate the planet from the star. Secondly, an immense dynamic range in detection is required, since the intensity contrast ratio between the bright star and the dim planet is 10^6 in the infrared regime and even higher for visible wavelengths. One solution to meet these two requirements is nulling interferometry. In short, this technique consists in two or more separated telescopes that deliver beams which are co-phased and combined with intentional phase shifts in such a way that *destructive* interference between the beams occurs for the starlight. Since the planet is at a small off-axis angle θ_0, its light is combined with an additional phase shift, e.g. $\theta_0 B/\lambda_c$, causing constructive interference of the planetary light. Because of the very high contrast ratio, the phases or relative optical path lengths of the beams have to be controlled down to the picometer level in order to prevent 'leakage' of the stellar light into the detected signal. The optical path length difference (OPD) or phase error $\epsilon(\lambda)$ is a function of wavelength, resulting not only from path length control, but also from the fact that a star has an angular dimension. Therefore, the nulling performance of an array of telescopes will improve if the choice of beam combination results in a destructive interference that is less dependent on $\epsilon(\lambda)$.

Such a beam combination strategy for N beams was found and an experimental set-up for three-beam nulling was built in the Optics Research Group (Mieremet and Braat, 2002; Mieremet and Braat, 2003). The promising theory that even allowed chromatic nulling—no optical elements for achromatic phase shifting were necessary—was to be proved in practice. Despite repeated efforts, the theoretical result was never attained. A small study was performed to analyze the origin of this failure. The theory and expected result will be explained, after which the issue of robustness of this theory will be detailed. Finally, in Section 8.6, a recommendation is stated for future multi-beam nulling experiments. The text of this Chapter is largely based on an earlier publication (Van der Avoort *et al.*, 2004a).

N	$\mathbf{f_1 \ldots f_N}$	$\boldsymbol{\phi_1 \ldots \phi_N}$
2	1 1	$0\ \pi$
3	1 2 1	$0\ \pi\ 2\pi$
4	1 3 3 1	$0\ \pi\ 2\pi\ 3\pi$
5	1 4 6 4 1	$0\ \pi\ 2\pi\ 3\pi\ 4\pi$
6	1 5 10 10 5 1	$0\ \pi\ 2\pi\ 3\pi\ 4\pi\ 5\pi$

Table 8.1: Overview of the values of f_i, ϕ_i for $N = 2,\ldots,6$ (for simplicity, the ϵ terms have been left out)

8.2 Role of amplitude and phase in a nulling experiment

Recently, an alternative family of nulling interferometers was found that was less sensitive to phase shift errors that are produced by the 'achromatic' phase shifters (Mieremet, 2003; Mieremet and Braat, 2002; Mieremet and Braat, 2003). As a consequence, the tight constraint of achromaticity of a few milliradians could be relaxed to such a level that delay lines are possible candidates to function as phase shifter for Darwin (Léger *et al.*, 1996). A small summary on this idea is given below.

In a nulling interferometer, each telescope provides a beam with a relative amplitude f and phase ϕ. After recombination of the beams of each telescope, the final transmittance of the star is expressed in terms of rejection. Even without any phase and amplitude noise, the achievable rejection strongly depends on the choice of f and ϕ. The following amplitude and phase distribution was proposed by Mieremet (Mieremet and Braat, 2003):

$$\begin{aligned} f_i &= \binom{N-1}{i-1} \\ \phi_i &= [i-1][\pi - \epsilon(\lambda)]. \end{aligned} \tag{8.1}$$

In this distribution, N represents the number of telescopes, $\epsilon(\lambda)$ the wavelength dependent phase shift error introduced by the phase shifter and i the index of the telescope. Note that $\epsilon(\lambda)$ does not represent noise, but a systematic phase shift error with respect to an achromatic phase shift. In Table 8.1 an overview of f and ϕ is shown for several values of N.

It can be derived that for this case the rejection ratio R is given by

$$R_N(\lambda_1, \lambda_2) \approx \binom{2N-2}{N-1} \langle \epsilon^{2(N-1)}(\lambda) \rangle^{-1}, \tag{8.2}$$

where the $\langle\rangle$ represent the average of the wavelength region $[\lambda_1, \lambda_2]$. The approximation sign has been used because higher order effects have been neglected.

The main result is that the influence of $\epsilon(\lambda)$ becomes much less for larger N, since $R_N \propto \langle \epsilon^{2(N-1)}(\lambda) \rangle^{-1}$, which implies that the achromaticity requirement is strongly reduced for increasing N. This is not the case for other nulling interferometers. For $N = 2$, a rejection ratio of 10^6 requires that ϵ must be of the order of milliradians. This level of achromaticity is mentioned in literature.

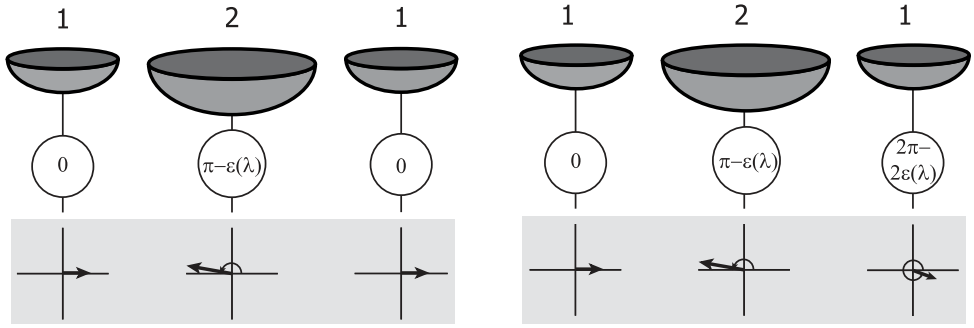

(a) DAC nulling interferometer (b) Optimized nulling interferometer

Figure 8.1: The advantage of applying more than only one chromatic phase shift of approximately π. When more beams get a shift, the residual in complex amplitude of the combined beams will be smaller. The sum of complex vectors of the DAC interferometer (a) clearly has a much larger vertical component left over as compared to the optimized configuration (b).

To understand why the influence $\epsilon(\lambda)$ becomes much less for larger N, an example is shown, comapring a $N = 3$ configuration to the Degenerate Angel Cross (Angel and Woolf, 1997) (DAC) nulling interferometer, see Fig. 8.1. Below each telescope, the complex representation of each beam is drawn. The state of the recombined beam can be obtained by adding the vectors. For the DAC nulling interferometer, the vertical component is far from perfectly 'nulled' and causes the DAC interferometer to have a $\langle\epsilon^2\rangle^{-1}$ dependence. If this is compared with the three-telescope configuration of example (b), it becomes clear that for that case the vertical component is much better nulled causing the $\langle\epsilon^4\rangle^{-1}$ dependence.

8.3 Experiments

8.3.1 The set-up

The goal of the experimental setup was to give a proof-of-principle. This would be achieved, when a higher rejection ratio was measured for the proposed configuration than for any other. A three telescope system is chosen, which is the most simple configuration to take benefit from the nulling approach. As can be deduced from the theory, such an experiment could even in the case of perfect performance not reach a nulling depth of 10^6, over the wavelength range of 500 to 650 nm. However, a depth of several thousands should be possible, whereas the combination of three beams with equal amplitude would yield a null of a few hundreds.

The Delft nulling set-up (see Fig. 8.2) can be divided in three stages: the star-simulator, the interferometer and the detection stage. The star simulator consists of a color-filtered Xe arc light source (LS), focused on a pinhole (PH). From here the light is collimated so that flat wavefronts emerge as starlight. This light is then not collected by separated telescopes, but branched off by means of two beam splitters (BS1, BS2) to produce three beams. Each of the beams is sent into another light path.

The nulling part is the heart of the set-up. Two of the three beams are directed onto retro-reflectors mounted on piezo translation stages serving as delay lines. In this way,

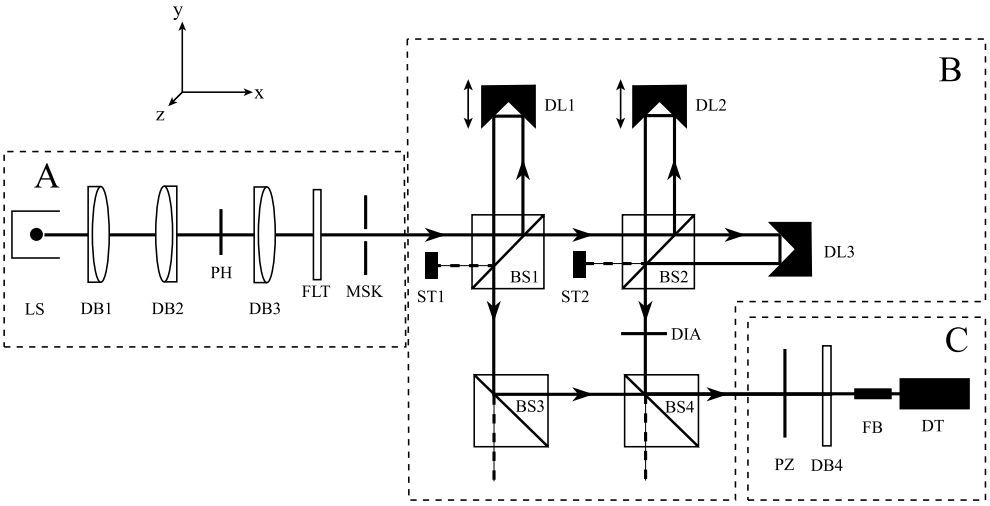

Figure 8.2: Schematic diagram of the previous delay-line-only nulling set-up. Region A is the star simulator. Region B is the actual interferometer and C is the detection stage

the optical path difference between all three beams can be controlled. The path of the third beam is used as a reference. The beams are recombined again by using beam splitters (BS2 and BS4). Between BS2 and BS4 a diaphragm (DIA) or a functionally similar component is placed to be able to control the amplitude of beams 2 and 3 with respect to beam 1.

The recombined beams have a common path and are directed to a matched system of achromatic lenses and a single-mode fiber. The single mode fiber acts as a modal and spatial filter (Tatulli and Chelli, 2004). The exiting power after the fiber is detected with a sensitive power meter.

The setup allows to investigate both different amplitude and phase distributions by changing the diaphragm and delay lines, respectively. Interferograms can now be recorded using the power meter and the known setpoints of the two delay lines. When both delay lines are used, a two dimensional 'interferogram' is produced, resembling a landscape with peaks and valleys aligned in some grid shape. This landscape represents the achieved null of the star as a function of different phase shift distributions. The deepest valley is the configuration that provides the best nulling performance.

8.3.2 Three-beam nulling

Experiments have been performed with combining three beams to perform nulling, both according to 'conventional' schemes (all amplitudes equal and hence OPDs needed of fractions of a wavelength) as well as with 'optimized' schemes. For the latter, amplitude matching involved more than adjusting a few percent by placing a knife-edge in the beams.

Obtaining the prescribed amplitude ratio of $2:1:1$ for the $N = 3$ case, which corresponds to a power ratio of $4:1:1$, is not trivial. Placing neutral density filters in the paths is not an option: the third beam would also need extra optical path and all elements inserted should have exactly the same thickness and quality, to prevent dispersion effects.

Alternatively, a knife-edge would have to be inserted far into the beam, causing its focus on the single-mode fiber to be displaced and hence have coupling losses, which are chromatic and would distort the spectral shape. As a possible solution, a diaphragm was tried. It gives diffraction effects, but the focal shape and central position are not altered and it provides a power tuning possibility.

Two sets of spectra have been intensively investigated. The first set is the equal amplitude distribution, while the second represents the amplitude distribution as given in Eq. (8.1). During the experiments, it was found that the three-beam nulling experiments with beams with equal amplitude could quite nicely match the expectations from simulations (see Table 8.2). But the much deeper nulls that should come with the optimized strategy were never measured. It was suspected that the method of power reduction (that had to keep the spectral shape the same) was ruining the measurement. Either the reduction method adjusted the spectral balances in the beam itself, or it adjusted the chromatic coupling efficiency into the detection fiber, where the actual nulling takes place.

Table 8.2: Expected and measured nulling ratios for the combination of three beams for a wavelength range of 500 to 650 nm. The given value is the ratio of maximum and minimum total intensity.

Power Balance	Theoretical null depth	Measured
1 : 1 : 1	275	188
4 : 1 : 1	3100	42

In order to analyze the problem of proper beam attenuation further, the individual beam spectra were measured. Because of low light levels, it was done by Fourier analysis of pairwise interferograms (an explanation of this procedure can be found in Sec. 8.4). Figure 8.3 shows the derived spectra for three beams in two different cases, having power balances of 1 : 1 : 1 and 4 : 1 : 1. Clearly, these balances are not constant nor exact over the wavelength range. Simulations that were used for the prediction of the null depth were adjusted to be able to process three different spectra. The results (see Fig. 8.4) show striking resemblance with what was measured: the deepest null measured in a two-delay-line scan was limited in the 1 : 1 : 1-case, but near to nothing in the 4 : 1 : 1-case. Experiments were repeated, where the power ratio of 4 : 1 : 1 was realized in many different ways (knife-edges, density filters, irises and metal wire gratings) but the expected gain in null-depth was never found.

8.4 Beam spectra out of three interferograms

It is essential that the spectra of the three beams in the experiment are very close. The power in each beam is rather low (typically 1 nW) and obtaining an accurate spectrum of the light emitting from the fiber is not feasible with general spectrometers, since the power, even in relatively wide wavelength bins, is in the order of picowatts. Another way was sought to obtain the spectra. This was achieved by performing an extended Fourier analysis of interferograms. The notion that three spectra are sought, and that interferograms can be measured successively, resulting from three different combinations of beams, led to the following procedure.

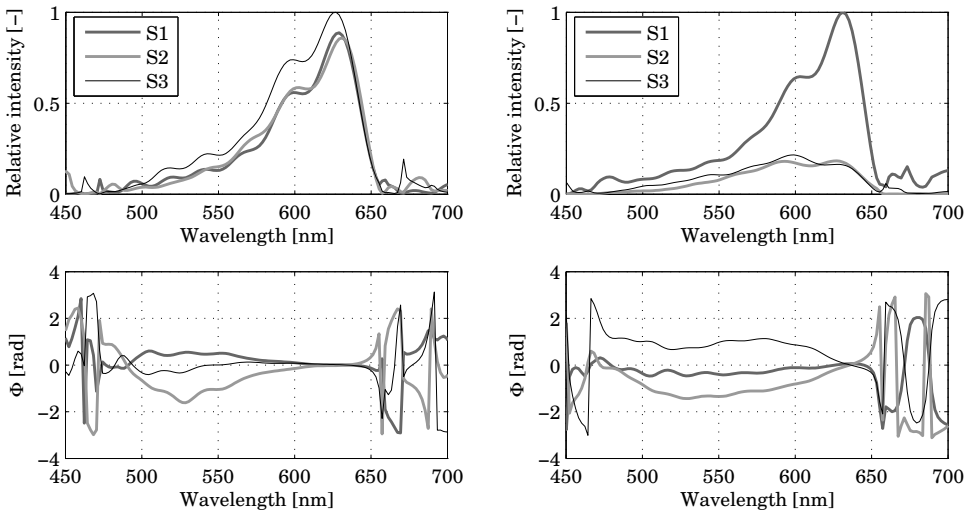

(a) Spectra with almost equal power

(b) Spectra with power ratio 4 : 1 : 1

Figure 8.3: The top panels show the measured spectra of each beam for the equal amplitude distribution (top left) and the optimized distribution (top right). The three beam Fourier technique delivers the complex spectra per beam. The phase spectra were brought together at 633 nm, where a laser interferogram provided the zero OPD for that wavelength. The derived complex spectra are for the case that the three beams have equal power (left-hand side) and for the case that two beams pass through an iris, to limit their power (right-hand side).

The spectrum of one beam of light in the nulling system can be expressed as $S_i(k)$ where k is the wave number, i is the index to beam 1, 2 or 3. An interferogram resulting from interference of beams i and j as a function of optical path length difference x is then

$$I_{ij}(x) = \frac{1}{2}\int_{-\infty}^{\infty}\left[S_i(k) + S_j(k) + 2\sqrt{S_i(k)S_j(k)}\,e^{ikx}\right]\mathrm{d}k \tag{8.3}$$

where $I_{ij}(x)$ is the recorded intensity. The Fourier transform $G(k)$ of this expression is written as

$$\begin{aligned} G_{ij}(k') &= \frac{1}{2}\int_{-\infty}^{\infty}\int_{-\infty}^{\infty}\left[S_i(k) + S_j(k) + 2\sqrt{S_i(k)S_j(k)}\,e^{ikx}\right]e^{-ik'x}\mathrm{d}k\mathrm{d}x \\ &= \frac{1}{2}\left(\int_{-\infty}^{\infty}\left[S_i(k) + S_j(k)\right]\mathrm{d}k\right)\delta(k') + \int_{-\infty}^{\infty}\sqrt{S_i(k)S_j(k)}\,\mathrm{d}k\,\delta(k-k') \\ &= \frac{1}{2}\left(\int_{-\infty}^{\infty}\left[S_i(k) + S_j(k)\right]\mathrm{d}k\right)\delta(k') + \sqrt{S_i(k')S_j(k')}. \end{aligned} \tag{8.4}$$

Equation (8.4) shows that the Fourier-transformed interferogram is the sum of the DC values of both signals and a square root term of the product of both, per wavenumber. Application to three measured interferograms now gives the three individual beam spectra:

$$\begin{aligned} G_{12}(k') &= (P_1 + P_2)_{k'=0} + \sqrt{S_1(k')S_2(k')}, \\ G_{13}(k') &= (P_1 + P_3)_{k'=0} + \sqrt{S_1(k')S_3(k')}, \\ G_{23}(k') &= (P_2 + P_3)_{k'=0} + \sqrt{S_2(k')S_3(k')}, \end{aligned} \tag{8.5}$$

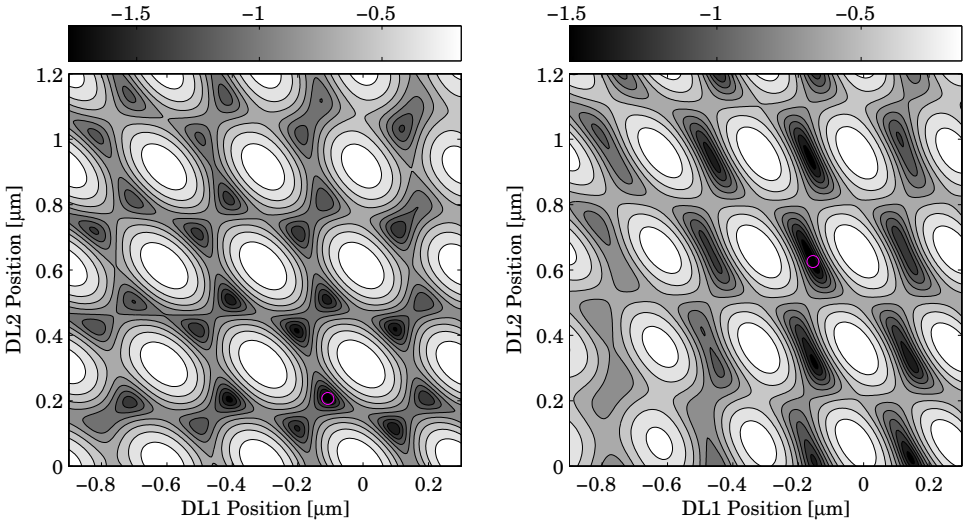

(a) 1 : 1 : 1-nulling (b) 4 : 1 : 1-nulling

Figure 8.4: Color-coded representation of the null-depth as a function of delay line-positions DL1 and DL2. The scales indicate the $\log_{10}$-value of the null-depth. With the spectra (as given in Fig. 8.3) obtained at the set-up, a three-beam nulling simulation is performed. Figure (a) shows a pattern as expected, with a null-depth that is worse than expected. (Depth is 188, whereas exactly equal spectra would provide a depth of 275.) Figure (b) shows a pattern of deteriorated 'islands', in which a null depth of only 42 is found, whereas a value over 3000 was calculated for spectra having the same envelope but a constant power ratio according to 4 : 1 : 1.

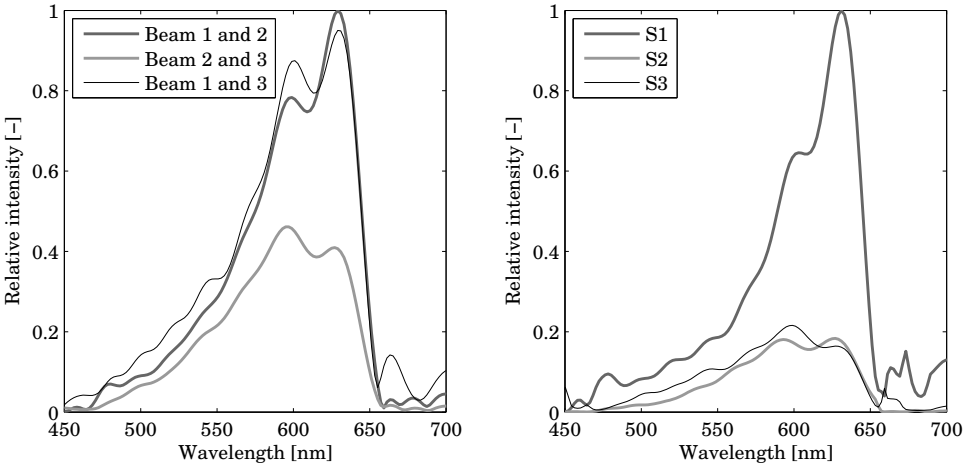

Figure 8.5: The spectra of the three individual beams (right panel) can be obtained from the Fourier transforms of three interferograms, obtained from pairwise combinations (left panel). The data for this example were taken when a diaphragm was placed in beams 2 and 3, in order to arrange an intensity balance of 4 : 1 : 1. Apparently, the spectra of these beams—as detected after the fiber—are non-uniformly attenuated.

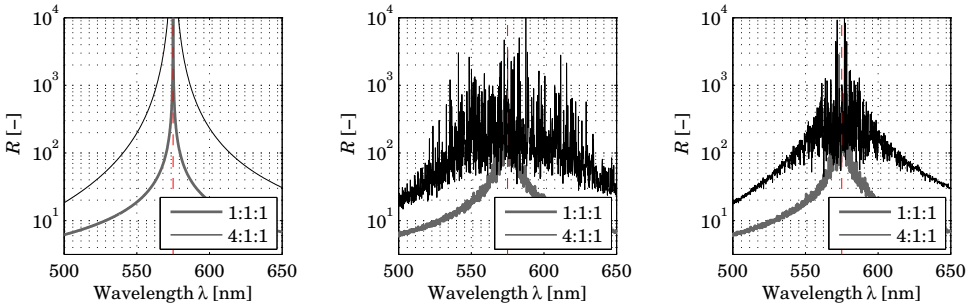

(a) Clean (b) Amplitude-noise (c) Phase-noise

Figure 8.6: The sensitivity to amplitude or phase deviations when combining three beams, is much higher for the case of a power ratio of $4:1:1$. In this simulation three beams having spectra with unity (for the second case a constant fraction of unity) amplitude over the wavelength range are combined. Figure (a) shows for both nulling configurations the achievable null depth with ideal spectra. Figures (b) and (c) respectively show what happens if white noise of amplitude 0.01 is put on the beam amplitudes or white noise of amplitude $0.01 \cdot 2\pi$ is put on the phases in the spectra. The dashed lines indicate the wavelength for which the delay lines are set to provide optimal phase shifts, $\lambda = 575$ nm.

where P_i is the total power in beam i, represented as the DC term of the transform. Rearranging these expressions yields e.g. the spectrum of beam 2:

$$\frac{\left[G_{12}(k') - (P_1 + P_2)\right]\left[G_{23}(k') - (P_2 + P_3)\right]}{\left[G_{13}(k') - (P_1 + P_3)\right]} = \frac{\sqrt{S_1(k')S_2(k')}\sqrt{S_2(k')S_3(k')}}{\sqrt{S_1(k')S_3(k')}} = S_2(k'). \quad (8.6)$$

Likewise, each element of $S_1(k')$ and $S_3(k')$ can be calculated per 'frequency' k'. See Fig. 8.5 for the results. The total power P_i for each beam i can simply be measured before recording an interferogram or can be obtained from the zeroth element of the Fourier transform of this interferogram. With three FTs available, the different total powers or DC terms per beam can be obtained from a linear system of equations.

8.5 Robustness

The investigation to ways of achromatically reducing the power present in two of the three beams led to the insight that it might not be the method of reduction that caused the lack of a deep null, but that the method itself simply was more vulnerable to mismatching amplitudes.

To verify this assumption, simulations with either amplitude or phase perturbations in the beams have been performed. The results of these simulations are shown in Fig. 8.6. In the left panel, the achievable rejection ratio as a function of wavelength is shown for the two distributions of interest in the case that no amplitude and phase noise are present. As a next step, an amplitude and phase noise of 1% are applied. The consequences of this are shown in the middle and right panel, respectively. Figure 8.6 clearly shows that the optimized nulling technique is much more vulnerable to mismatching amplitudes or phases. The constructed Delft nulling set-up was not designed to attain much better matching than $\sim 1\%$ in intensity, since the coatings on the beam splitters could not be applied at a tighter tolerance.

8.6 Recommendation

As demonstrated, configuring the differential amplitudes and phases in nulling interferometers (either without or with the aid of dispersive elements for phase shifting) according to Pascal's triangle will theoretically improve the destructive interference. However, the assumption of equal spectra per beam is too optimistic. The exact balance of amplitudes is needed for every single wavelength. Slight variations in coatings on mirrors or beam splitters will induce variational spectra and the recombination of these beams will result in moderate to weak nulling. Full control of spectra (both amplitude and phase) is a necessity in nulling, and the optimized theory relies even more on such control.

Since the coupling efficiency of a single mode fiber (used for wavefront filtering in many nulling experiments) is chromatic, and taking into account the spectral tolerances declared before, very tight pointing and positioning tolerances are posed on the fiber coupling as well.

The shape of the focus of a beam is depending on the cross section of the beam. Tuning the power of one beam with respect to another in a nulling set-up should therefore not be performed with a knife-edge, especially not when amplitude ratios according to Pascal's triangle are to be obtained. The cross section of the attenuated beam will be altered and hence the shape of the focus. The size of the focus is again wavelength-dependent, so even when coupling into a fiber for wavefront filtering, the knife edge will induce spectral differences and hence degrade nulling performance.

Full spectral tuning has been demonstrated (Weiner, 2000) for high power femtosecond pulses. To keep the pulse short, the phase spectrum of the pulse needs to be controlled. With the aid of dispersion and polarizing liquid crystal screens, this can be done. If spectral control is performed by choosing high-quality coatings or when possible a symmetric nulling set-up (Serabyn and Colavita, 2001), it should be possible to attain three (or more) beams of equal spectral shape from a source. For the optimized theory to work, it is required that these beams then get a different amplitude. Since a knife-edge can not be used because of the chromatic spot shape and a uniform gray filter would mean extra glass in the light path, other attenuation means have to be sought. This can be found in the area of metal wire gratings. When placed in a beam, multiple beams will exit at an angle with the central beam. The ratio between obstructed and unobstructed area in the grating will tune the attenuation in the central beam and the pitch of the grating will tune how far the first diffraction order will be focused next to the fiber. To a very high degree, the attenuation will be achromatic without altering the beam cross section or the optical path length. That makes a grating very suitable for a reflection-only set-up.

8.7 Measured spectra

As explained in the previous sections, the spectral mismatch of the three beams was identified as an origin for the disappointing nulling achievement of the set-up. The Fourier analysis of the recorded interferograms allowed to make an estimate of the spectra. A direct measurement of the spectra was difficult to obtain, due to the low power and the broad spectrum, over which this power is distributed. With an addition to the experimental set-up, realized years later, the relative power in the beams could be measured at certain selected wavelengths. For this goal, interference filters were used, with passbands of $\Delta\lambda \simeq 20$ nm, around the central wavelengths $\lambda = 500, 550, 600, 650$ nm. In addition, a continuous spectrum could be measured with a spectrometer, equipped with a

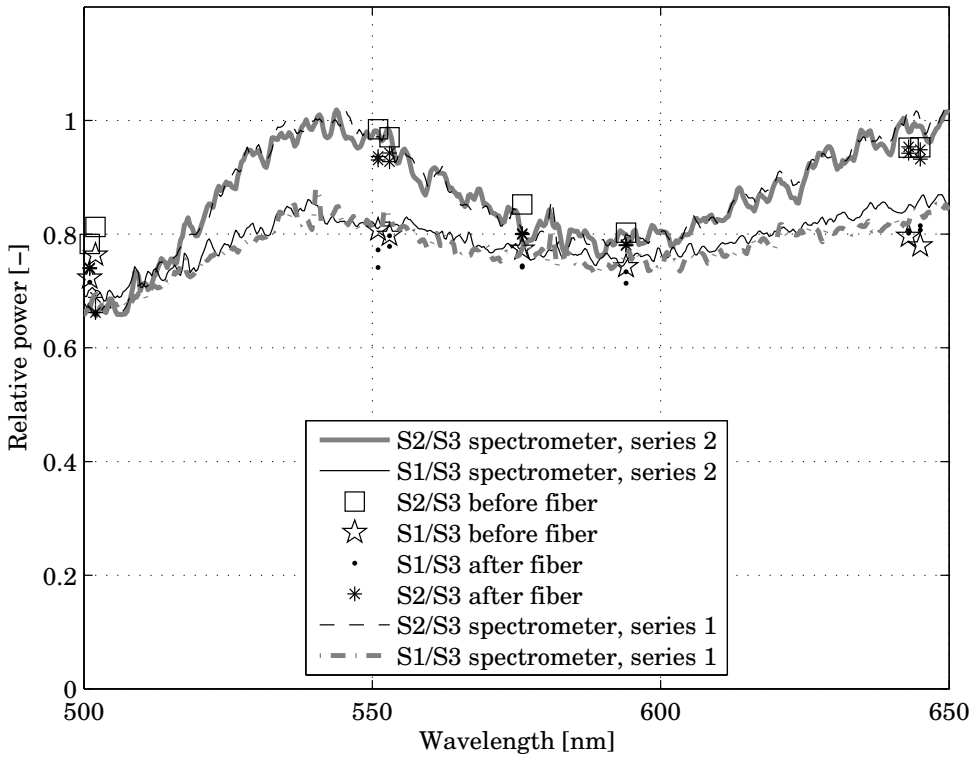

Figure 8.7: Direct measurements of beam spectra S_1, S_2 and S_3, expressed in intensity relative to spectrum S_3. See text for details. Diagram by courtesy of J. Spronck.

linear CCD-detector allowing long integration times. The fiber-fed spectrometer returns a noisy and—due to a large slit width—smoothened spectrum for each beam. To be able to compare the spectral measurements, the *relative* spectra were considered. With beam three taken as a flat reference $S_3(\lambda) \equiv 1$, the spectra $S_1(\lambda)/S_3(\lambda)$ and $S_2(\lambda)/S_3(\lambda)$ are plotted. In Figure 8.7, the continuous CCD-spectra are plotted, together with the relative intensities acquired with the interference filters.

The measurements with the interference filters and the CCD are in good accordance. The diagram shows power differences of 20% for certain wavelengths, while all beams pass through an equal number of coated BK7 elements in the set-up. The coupling of each beam into the single-mode fiber might give rise to spectral imbalances, but the measurements with the interference filters were performed both before and after this fiber. The measurements before the fiber, e.g. the □-series, show a non-flat spectral balance between two beams.

8.8 Conclusions

The studies of the transformed interferograms, as well as the directly measured spectral differences, lead to the conclusion that the three-beam nulling set-up suffers from spectral unbalance, even when no individual beam attenuation is applied. This causes

a worse nulling performance than predicted. The approach of chromatic nulling with optimized power balances suffers more from spectral unbalance than equal-amplitude multiple beam nulling.

Chapter 9

Conclusions and recommendations

The research described in this thesis treated various topics related to aperture synthesis. The main part covered synthesis imaging, but also nulling interferometry can be seen as a special kind of observation with a synthetic aperture. In addition, the influence of aberrations on imaging has been treated. For ultimate performance of synthetic apertures for the stated applications, knowledge of aberrations—of both the synthetic aperture or beam combiner as well as the individual apertures—is essential. Although nulling interferometry was the rationale for this research, it did not become its main topic. ESAs Darwin mission is primarily a nulling mission. This mission however, can valuably be extended with a wide-field imaging mode. In Chapter 1, the research objective was therefore defined as follows:

> The goal of this research can be summarized as a comparison of the performance of different types of stellar interferometers for the specific task of imaging an extended source and retrieving spectral information from that source within a limited observation time.

To perform this comparison, the path of numerical simulation of actual observations was chosen. More specifically, the imaging process in every interferometer under consideration was regarded as a multi-dimensional convolution operation. Regarding the optical systems and their consecutive responses in this convolution-oriented way, provided valuable insight in the nature and limitations of the stellar interferometers under consideration. Their performance in delivering high resolution spatial and spectral information on a stellar source could not only be simulated, but also predicted by analysis of the decomposition of the so-called optical transfer matrix. The conclusions and recommendations following from the research described in this Thesis are listed group wise, regarding the topics of aperture synthesis imaging, nulling interferometry and aberration retrieval. Since aperture synthesis imaging is the main subject, the conclusions and recommendations on this subject will be bulleted.

9.1 Conclusions

Aperture synthesis imaging

- The approach of modeling the response of interferometers as a superposition of intensity patterns showed two advantages. Firstly, physical insight is gained with respect to the theory of partial coherence. Secondly, this approach made possible that the image reconstruction capabilities of different interferometers could be compared easily for various parameter settings of either the modeled interferometer or the source under observation. The singular value decomposition of the obtained optical interferometric transfer matrices proved to be a valuable tool to predict the performance of a chosen beam combiner concept and to compare performances of several beam combiners, irrespective of the modeled stellar source.

- For the defined task of imaging a stellar source of several PSFs wide, with high angular and spectrometric resolution, given the array dimensions for the Darwin nulling mission under consideration, a Homothetic imager is best suited, even although the collected information is spread over many detector pixels. However, a co-axial Staircase imager approaches the superior qualities of Homothesis with respect to imaging efficiency and needed observation time. In practice, both solutions require delicate actuatable opto-mechanical systems to operate. For narrow fields or moderate resolution requirements, a Densified pupil imager offers a good solution regarding both the imaging speed and the practical issues as combiner robustness and detector dimensions.

- Regarding the co-axial Michelson imager and observing the polychromatic wide-field source fringe patterns it delivers, it can be stated that performing spectroscopy on this source by Fourier-analysis of recorded interferograms, will not lead to the desired spectroscopic resolution. The morphology of the source alone, whilst the spectrum is uniform for all parts of the source, is already providing a different spectrum for each pixel and each baseline length in the measurement data set. In the interferograms, it can be seen that the fringe packets have different envelope shapes and lengths. The co-axial Staircase imager is totally excluding the possibility of performing spectroscopy on recorded interferograms, because of the fringe-packet multiplexing. For both co-axial imagers, spectroscopy has to be performed by dispersion in the detection, after which synthesis imaging can be performed in narrow wavelength bands, resulting in a stellar luminosity distribution per wavelength band.

- Performing wide-field synthesis imaging with the Staircase mirror is possible. Although a discontinuous surface is present in the interferometer, the reconstructed field will be continuous. The multiplexing nature of this interferometer reduces observation time, but also reduces the efficiency of the imager. This is caused by the fact that multiplexing destroys the unique source–response relationship per array configuration.

Nulling interferometry

For multiple-beam nulling experiments, the Fourier analysis of pairwise-recorded interferograms can provide spectroscopic information on the individual beams, even if the

optical power in these beams is very low. Rough spectroscopic measurements confirmed the presence of spectral differences in the beams of the experimental three-beam nulling beam combiner. Nulling with optimized amplitude distribution in the interferometer beams, is more vulnerable to spectral mismatches than regular multiple-beam interferometry with equal amplitudes.

Aberration retrieval

For optical systems of moderate numerical aperture and in the absence of birefringence, the Extended Nijboer–Zernike aberration retrieval can provide very accurate and fast aberration measurements on both phase aberrations and transmission defects. The retrieval of aberrations is possible for amplitude and phase aberrations with a magnitude of two, indicating transmission variations over the pupil of 100% and optical path length variations of two wavelenghts. However, to reconstruct the amplitude and phase pupil of a synthetic, sparse aperture, many Zernike modes are necessary, with much larger amplitudes. Consequently, such a pupil cannot simply be reconstructed from recorded focal intensity data; the use of prior knowledge about the geometry of the synthetic aperture might alleviate the problem.

9.2 Recommendations

Aperture synthesis imaging

- Wide-field imaging always requires data of more than one fringe per observation. It should be noted that the working principle of a correlator, scanning only the central fringe, should be abandoned.
- For planning a wide-field imaging observation, more consideration than only that of u, v-plots is necessary, as these plots do not give information on the FOV of the observation. The analogy and difference between Fourier analysis and wavelet multi-scale analysis of a function, where the analogy is the organization of the information into a scale spectrum, but the difference is the localization property of the wavelet transform, should be applied to the analysis of the response of a stellar interferometer, regarding wide-field imaging. The simulations have shown, that one not only has to cover spatial frequencies by setting the proper baseline lengths, but also has to deal with field narrowing as a function of baseline length and coherence length, causing the presence of certain spatial frequencies in the solution to indeed be present, although not in the full field-of-view. Only by taking into account not only the baseline lengths, but also the coherence length, the delay scan length and the angular dimensions of the diffraction envelope, the coverage of spatial frequencies over the multiple-PSF wide field-of-view can be guaranteed.
- As clarified by the diagrams in Fig. 3.10 for a co-axial interferometer, the choices of spectral range, telescope diameter, resolution and FOV, all interact—as they do for an image plane interferometer. As a result, the imaging requirements for the Darwin imaging mission, cited in Chapter 1, need to be reviewed.
- The wave diffraction and propagation after the Staircase mirror have to be investigated further. As extensively investigated in the work by Montilla, the polychromatic point-source response of this interferometer is generally a double-enveloped

fringe packet. That these fringes can be used for imaging, was confirmed by the numerical simulations presented in this thesis. However, no experimental confirmation of this imaging capability exists. Therefore, an experiment has to be conducted, in which a range of baselines can be chosen and a well defined zero-OPD position is available. Only then, a set of multiplexed fringe data can be obtained, from which an image can be distilled. On a more fundamental level, the field response as calculated and the scattering behavior of a realistic staircase mirror with rounded-off edges should be measured.

- There will be no recommendation to perform the simulations presented here for two-dimensional stellar objects. Instead, it is recommended that the evolution of detector arrays with energy resolution is monitored. The simulations have shown, that a one-dimensional object produces two-dimensional data (when the use of delay is necessary), extendable to three if dispersion is applied. Consequently, two-dimensional objects would require four-dimensional data sets (when the use of delay is necessary), in order to perform synthesis imaging and spectroscopy. This can only be performed with a two-dimensional detector array that embeds energy resolution in each detector element.

- The beam combiner for homothesis is essentially an inverted telescope. In the DTI, the optical elements for beam positioning are nicely separated from those for sky tracking, but this leaves the beam combiner (the synthetic aperture) unavailable as a whole for alignment measurements. Therefore, it is advisable to implement an alignment strategy of the beam combiner itself, so that aberrations over the full synthetic aperture can be minimized.

- This thesis regarded all interferometers as optical imaging systems. The use of fibers for wavefront filtering, was not considered. Since a fiber-fed interferometer acts as a correlator, equivalent to the practice in radio interferometry, the conclusions of the performance comparison might change. For a space-based observation, wavefront filtering was not the primary concern. Should the course of this research be followed for a ground-based observation, the application of fibers should be included in the construction of the transfer matrices.

Nulling

The mayor hurdle in nulling interferometry at the time of the research, seemed to be the contrast ratio of 10^6. Nowadays, this requirement is slightly relaxed as nulling capabilities are sought in improved modulation schemes. Nonetheless, the recommendation is made that beam combiners for broad band nulling interferometry are kept as simple as possible, involving the least possible amount of optical surfaces. This, to reduce the occurrence of spectral differences. Ultimately, this would lead to a symmetrical beam combiner, in which all beams encounter the same optical elements. To achieve this, performing nulling interferometry with an odd number of three or more beams would then require a point-symmetric configuration of optical elements.

Aberration retrieval

Aberration retrieval on the pupil function of a sparse aperture is required mainly for the retrieval of the very low-order aberrations piston and tilt in the areas of the sub-

apertures. The phase-diversity method offers a solution for this retrieval problem, able of providing frequently updated information on the array configuration. The Extended Nijboer–Zernike analysis is in general capable of delivering much more aberration information with much higher accuracy. However, the speed is low, which disqualifies ENZ to be included in a feedback loop. Nonetheless, it is recommended that ENZ is used for aberration retrieval of the telescopes/beam compressors and the beam combining optics. These subsystems can be measured an corrected if necessary, on an incidental basis. Highly accurate knowledge of the field-dependent OPD behavior will then be available. In addition, an extension of the ENZ formalism for sparse apertures could be considered. Working with translated versions of the Zernike polynomials, a sparse aperture could be represented with much less polynomials. Then, possibly, a retrieval algorithm could provide aberration information per aperture, for as many aberrations as desired.

Nomenclature

General

The symbols that are used throughout this thesis are divided into three classifications: Roman, Greek and Mathematical. Additionally, a list of abbreviations has been included after the definition of the symbols.

The following typographic conventions are applied for the symbols. When a symbol represents a scalar, it is written in a normal mathematic font like a or ρ. In the case of a vector, two types are distinguished: a general purpose multi-dimensional data vector and a geometrical three-dimensional vector. The data vector is always symbolized with a bold character in lower case, e.g. $\mathbf{b}$, whereas the geometric vector $\vec{x}$ is written in a normal mathematic font with an arrow above the character. Symbols denoting a matrix or tensor are always written in bold uppercase, like $\mathbf{A}$ or $\mathbf{\Gamma}$.

In some rare cases, the same symbol is applied for different quantities. In these cases the context of the symbol explains its meaning. The arrangement of the list is as follows, first the symbol is written, then the description and finally the dimensions if applicable.

Roman

a	Radius of the sphere	[m]
A	Amplitude for general purpose	
A'	Electric field	[V/m = kg m/C s^2]
$\mathbf{A}$	Matrix for general purpose	
B	Baseline length, telescope separation	[m]
B_0	Beam separation before combination	[m]
B_k	Baseline length, index k	[m]
$\mathbf{b}$	Right-hand side vector with measured data	
C	Constant for general purpose	
$\mathbf{C}$	Control matrix for piezo actuation	[–]
c_0	Speed of light	[m/s]
D	Diameter of aperture	[m]
d	Delay or applied path length difference	[m]
$\mathbf{e_b}$	Right-hand side error vector, $\mathbf{b} = \bar{\mathbf{b}} + \mathbf{e_b}$	
f	Frequency ($= c_0/\lambda$)	[Hz]
h	Height of a Staircase step	[m]
I_k	Intensity for baseline B_k	[W/m^2]
I_{jk}	Intensity for pixel j and baseline B_k	[W/m^2]
J_n	Bessel function of the first kind and order n	[–]

k	Wave number ($=\omega/c_0$)	[1/m]
L	Luminosity distribution function	[W/rad]
l_i	Length of piezo i	[m]
l_c, l_{coh}	Coherence length	[m]
$\mathbf{L}$	Regularization matrix, set equal to $\mathbf{I}$	[–]
M	Magnification	
m	Index into measurement vector	
P	Field-dependent path length, expressed as difference δP	[m]
$\mathbf{p}$	Lengths of six periscope piezos	[m]
$S(\lambda)$	Intensity spectrum	[W/m]
$\mathcal{V}$	Visibility	[–]

Greek

β	Size of detector pixel	[rad]
β_{nm}	Participation factor of Zernike-mode Z_{nm}	
γ	Complex coherence	[–]
$\mathbf{\Gamma}$	Gram matrix	
ϵ	Normalized reconstruction error	[–]
ϵ_0	Electric permittivity of vacuum	[C^2 s^2/kg m^3]
λ	Wavelength	[m]
λ_c	Central wavelength	[m]
μ_0	Magnetic permeability in vacuum	[kg m/C^2]
ν	Frequency	[Hz]
σ_i	i^{th} singular value	
θ	Coordinate in detector plane	[rad]
θ_0	Coordinate in object plane	[rad]
ω	Angular frequency ($=2\pi f$)	[rad/s]
Ψ	Complex field disturbance	[kg m/C s^2]
Ψ_m	Integrated measurement of order m	[W]

Mathematical

$\cdot$	Inner product, first order contraction
$x!$	Factorial of x
$\mathbf{A}^{-1}$	Inverse of matrix $\mathbf{A}$
$\mathbf{x}^{\text{T}}$	Transpose of vector $\mathbf{x}$
$\lvert\mathbf{x}\rvert$	Absolute values of vector $\mathbf{x}$
$\lvert\lvert\mathbf{x}\rvert\rvert$	L_2-norm of vector $\mathbf{x}$
$\mathcal{E}(x)$	Expected value of x
$i=\sqrt{-1}$	Imaginary unit
$\mathbf{I}$	Identity matrix
Σ	Summation
cond($\mathbf{A}$)	Condition number of matrix $\mathbf{A}$
$()_p$	Pochhammer's symbol

$\left(\begin{array}{c} n \\ k \end{array} \right)$ Newton's binomium, k subsets out of a set of n items

Abbreviations

AU	Astronomical Unit
CCD	Charge Coupled Device
DAC	Degenerate Angel Cross
DOF	Degree(s) Of Freedom
DTI	Delft Testbed for Interferometry
ENZ	Extended Nijboer–Zernike
FFT	Fast Fourier Transform
FOV	Field-of-View
HD	Hennen–Debye Catalog
HH	Herbig–Haro
LBT	Large Binocular Telescope
MAOT	Multiple Aperture Optical Telescope
MEM	Maximum Entropy Method
MTF	Modulation Transfer Function
OPD	Optical Path length Difference
PSF	Point-Spread Function
SVD	Singular Value Decomposition
TSVD	Truncated Singular Value Decomposition
VLTI	Very Large Telescope Interferometer
WFOV	Wide field-of-view

Appendix A

The nature of the response signals

The following pages show the simulated measurements of the object HH47, for the four types of beam combination. The nature of these signals is very different. In all cases, the measured signal per baseline length setting k is given. Then, for the image-plane combiners Homothesis and Densified, the recorded intensity $I_k(\theta)$ as a function of detector location θ is given. For the co-axial types Staircase and Michelson, the intensities $I_{jk}(d)$ are given as a function of applied delay d. For each pixel with index j, such a trace or interferogram is given.

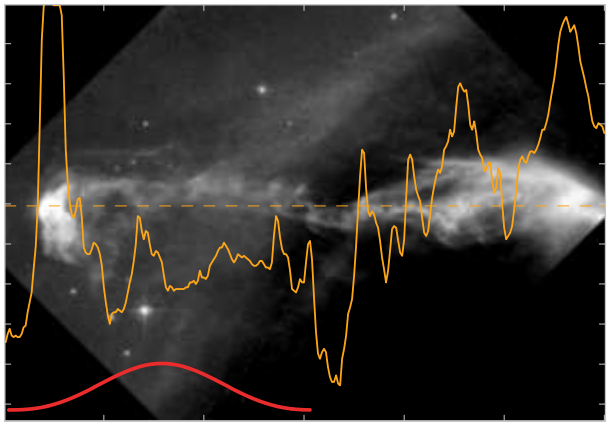

Figure A.1: The presented measurement data (Figs. A.2,A.3,A.4 and A.5) are all obtained from a simulated observation of the object HH47. In this figure, the dashed line indicates the position of the slice of the image of which the pixel values were used again as the linear luminosity distribution $L(\theta_0)$. The thick line represents this function. The diffraction limited spot size of a single telescope is indicated at the bottom.

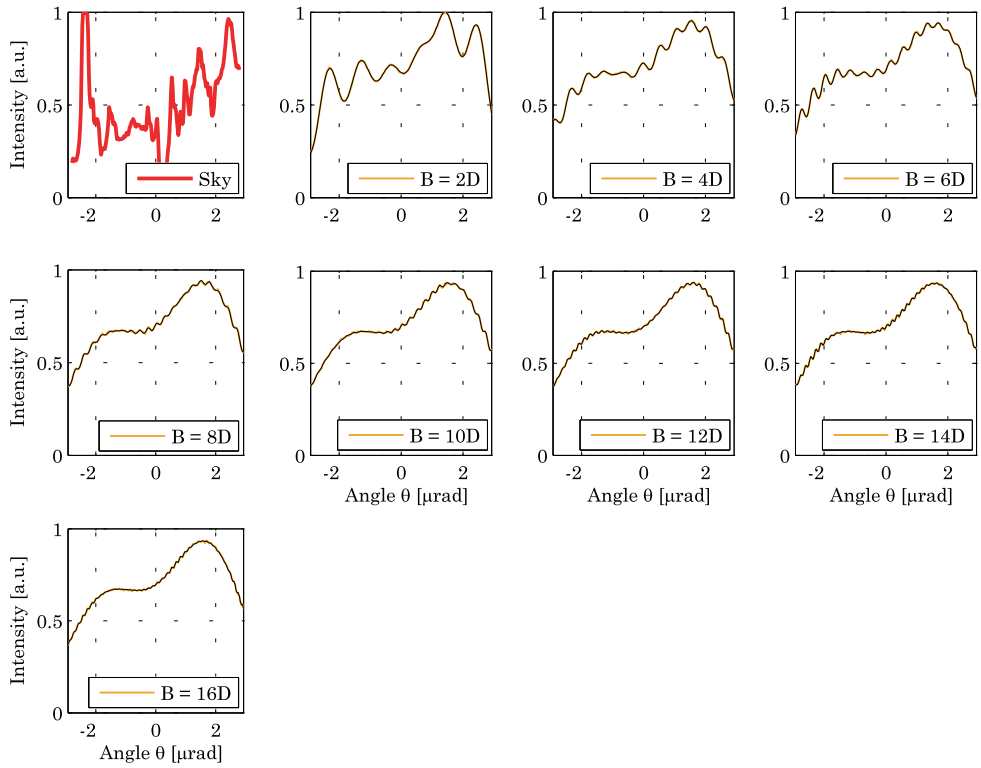

Figure A.2: Tabular display of all **Homothetic** simulated measurements $I_{jk}(\theta)$, the recorded intensities (photon counts) per bin for each baseline length. The number of pixels is 235. The baseline lengths are $B = D \cdot [2, \ldots 16]$ in steps of $2D$. For these sketches, the amount of photons was 10^8. The Homothetic measurements are characterized by the presence of fringes over the full FOV and a decrease of fringe period for an increasing baseline length.

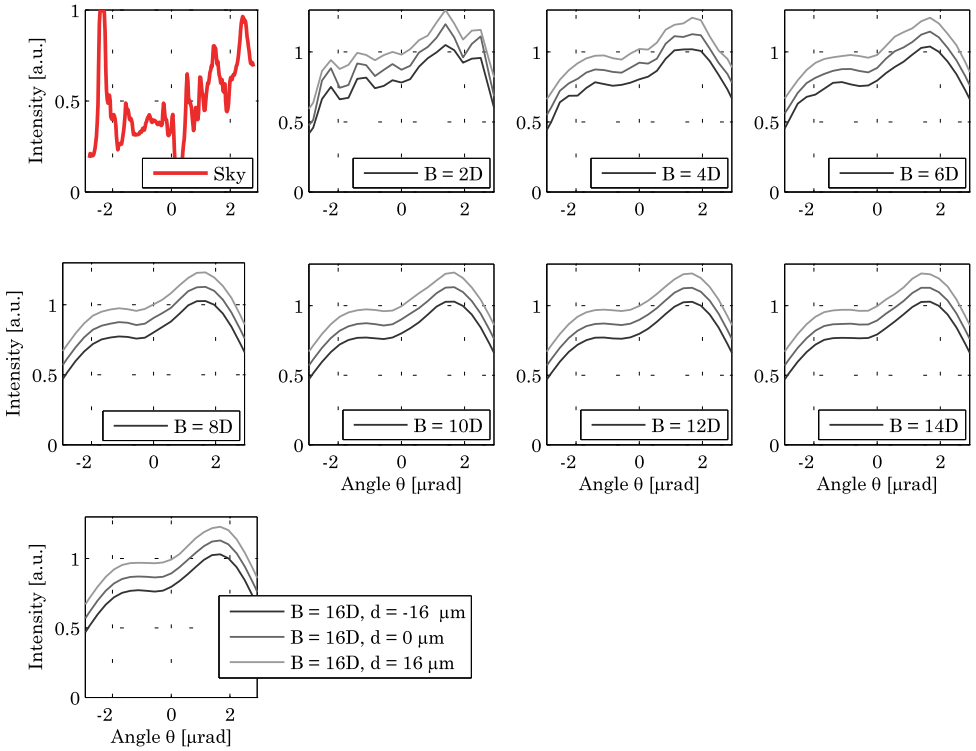

Figure A.3: Tabular display of all **Densified** simulated measurements $I_{jk}(\theta)$, the recorded intensities (photon counts) per bin for each baseline length. The number of pixels is 31. The baseline lengths are $B = D \cdot [2, \ldots 16]$ in steps of $2D$. For these sketches, the amount of photons was 10^8. The measurements per delay setting $d = -16, 0, +16$ μm, are plotted with an intentional off-set. The Densified measurements are characterized by the fact that multiple images per baseline are taken, that fringes are not present over the full FOV, especially for the longer baselines, and that the fringe period is equal in all gathered images.

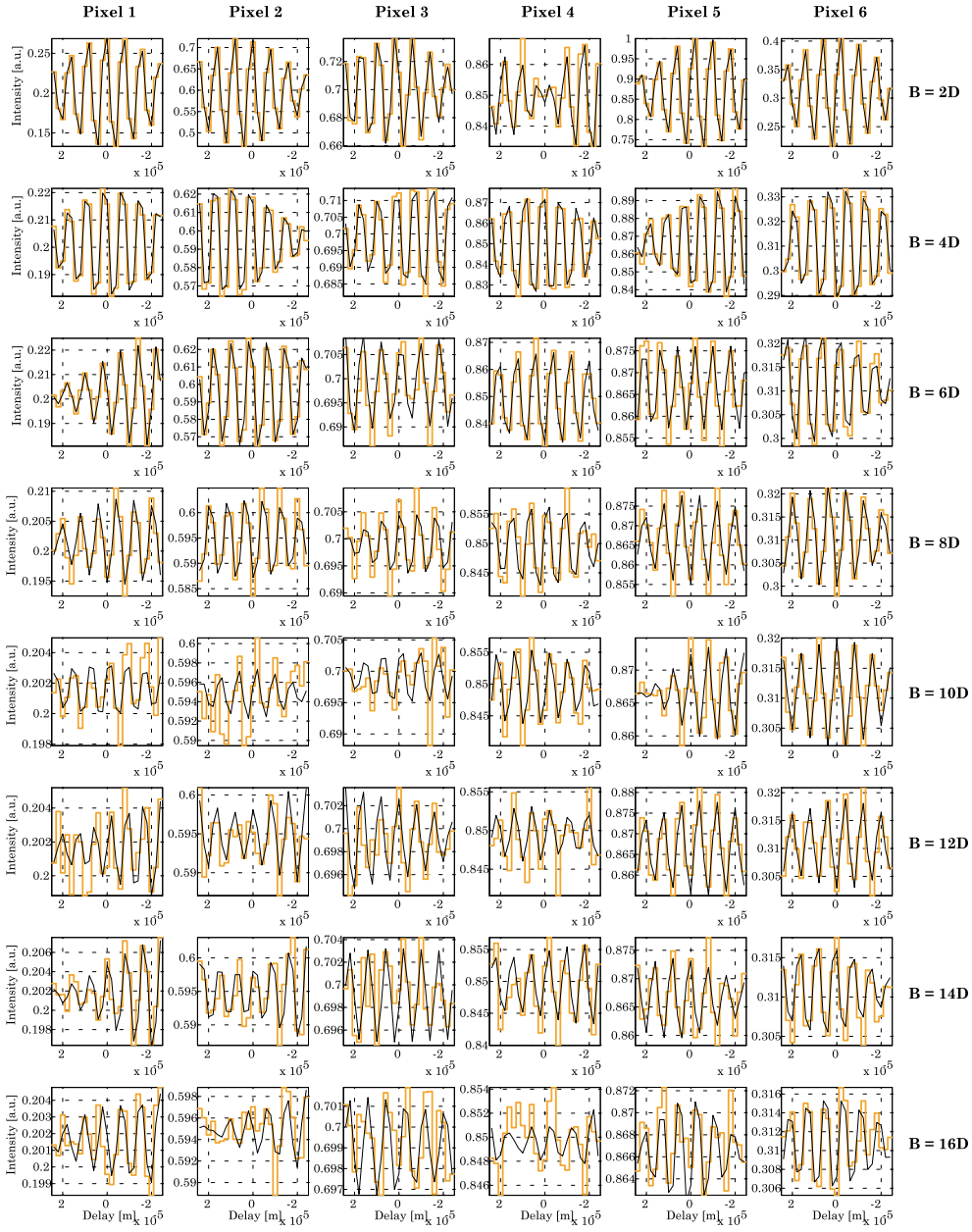

Figure A.4: The measurements for the **Staircase** simulation. The measurements $I_{jk}(d)$ are displayed as intensity traces, noise-free and photon-noise quantized, with a total of 10^8 photons. There is one trace for every pixel j and baseline setting k. There are 6 pixels and 25 d-positions. The FOV is focused on a staircase mirror having 6 facets, between which the height difference h_0 is optimized per B and then rounded to the nearest multiple of λ_c. The Staircase measurement signals are characterized by the fact that fringes are present in every measured signal, over the complete scanning range. The range is of the order of several wavelengths.

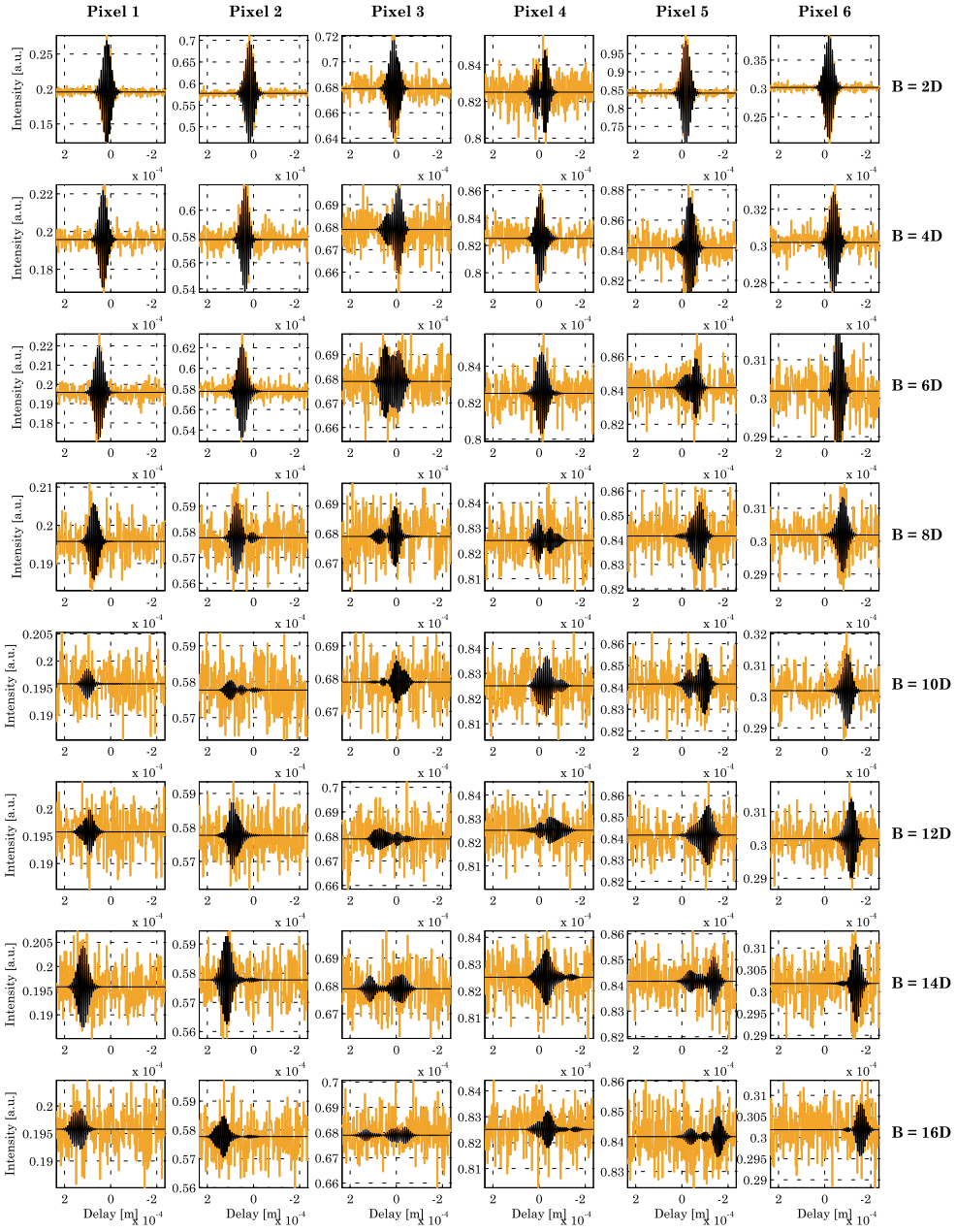

Figure A.5: The measurements for the **Michelson** simulation. Again, the measurements $I_{jk}(d)$ are displayed as intensity traces, noise-free and photon-noise quantized, with a total of 10^8 photons. There is one trace for every pixel j and baseline setting k. There are 6 pixels and 234 d-positions. The Michelson measurement signals are characterized by fringe packets that are present only on a fraction of the scanned signal. The length and shape of the fringe packet differ per pixel and baseline length.

Appendix B

Staircase response functions and imaging efficiency

The set of response functions $I_{jk}(d)$ for the Staircase beam combiner are, unlike the functions in all other cases, not simply obtainable by integrating the sinc–cos function over a certain wavelength range for every sky direction θ_0. In one ore more beams, there is a discontinuous surface placed in an intermediate focus. The extended source will be imaged over this surface, encountering one or more discontinuities. The electrical fields are diffracted, propagate further and are combined. A two-beam interferometer with a staircase mirror in one arm is depicted in Fig. B.1. To demonstrate the effects of the discontinuous surface on the response functions and the ensemble of response functions—the measured signal from the stellar source—three calculations of the intensity response can be made. These will be a naive calculation, a calculation based on Fourier optics and a calculation where propagation of the electrical field through the entire optical train is simulated.

B.1 Naive approximation

A two-element interferometer is considered. One arm of the interferometer (see Fig. B.2) is equipped with the staircase mirror, the other one is unaltered. A plane wave of unit amplitude in direction θ_0,

$$A(x) = \exp[-2\pi i x\theta_0/\lambda] \tag{B.1}$$

at z_0, for $|x| < D/2$, is focused in the plane z_1. The z-dependence has been omitted for the sake of simplicity. The aberration-free optics cause the focal field to be

$$A(\theta) = D\mathrm{sinc}[\pi(\theta-\theta_0)D/\lambda]. \tag{B.2}$$

For a focal length f, this expression gives the electric field A' at a location $A'(x') = A(x'/f)$. The staircase mirror is now naively considered as a pure phase mask. With a discontinuity placed at $x' = x_m$, the focal field receives a phase change ϕ_s given by

$$\phi_s = \begin{cases} 0 & \text{for } x' < x_m \\ 2\pi h/\lambda & \text{for } x' \geq x_m \end{cases}, \tag{B.3}$$

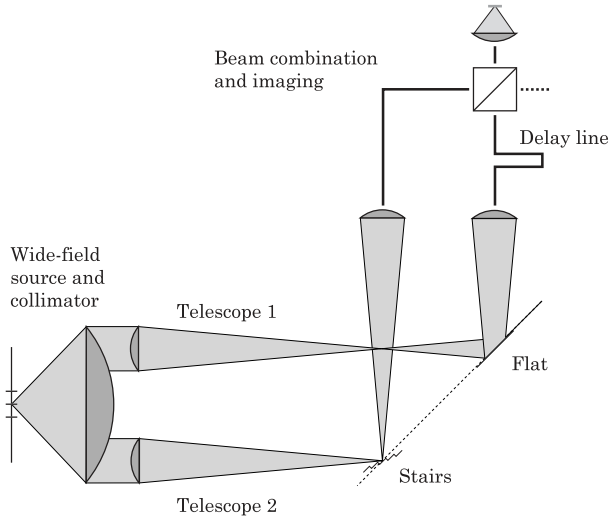

Figure B.1: The principles of the Staircase path length compensation have been tested in an experimental set-up, in which a several-PSFs-wide simulated sky was imaged with a two-element co-axial interferometer.

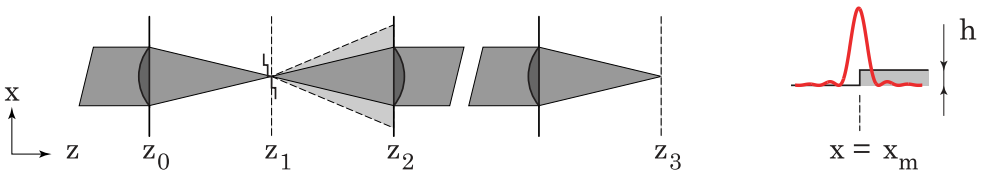

Figure B.2: Sketch accompanying the shallow step approximation. The staircase mirror is modeled as a phase mask, so that a part of the diffraction spot in focus receives an additional phase $\phi = 2\pi h/\lambda_c$.

so that the altered focal field is

$$A''(x') = 2D\text{sinc}[\frac{\pi(x'-x'_0)D}{f\lambda}]\exp[i\phi_s]. \tag{B.4}$$

The focal field of the other beam is now simply added to this focal field. A delay d is applied in the other beam, so that the summed focal field yields

$$A_{\text{tot}}(x',d) = 2D\text{sinc}[\frac{\pi(x'-x'_0)D}{f\lambda}]\exp[i\phi_s] + 2D\text{sinc}[\frac{\pi(x'-x'_0)D}{f\lambda}]\exp[2\pi id/\lambda]. \tag{B.5}$$

The intensity recorded is $I(x',d) = |A_{\text{tot}}|^2$, and this function can be calculated for a number of wavelengths. The summation of these functions yields a fringe pattern as before, consisting of a diffraction pattern as cross section and an enveloped cosine function for the fringes, be it that a sharp discontinuity is present. Since for the co-axial beam combiners the detector array is chosen to have pixel dimensions of roughly half the size of the diffraction envelope, the function $\int_\lambda I(x',d)$ can be integrated over the pixel dimensions. The sharp discontinuity is no longer visible and a fringe pattern with two regions

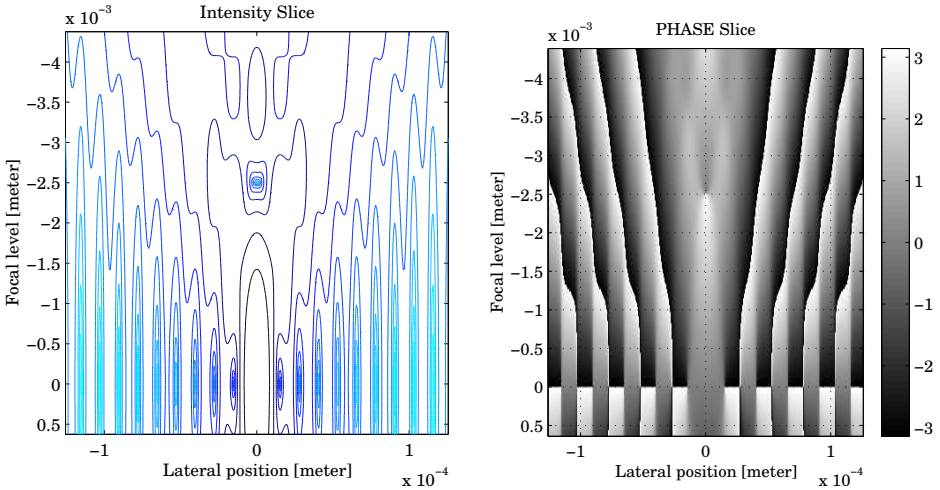

(a) (b)

Figure B.3: Logarithmic contour plot of the intensity in the focal region for low numerical aperture (a) and the phase of the electric field (b). Ranging up to a millimeter out-of-focus, the intensity is constant with respect to f and the phases do not change. Introducing a step at a defocus level of 3 microns will not cause any other effect than a phase jump. Note: the Airy diameter is 20 microns.

of maximum interference results. The distance between the centers of these two regions is, of course, the step height h. To prevent the halves of the double fringe packet to diminish the fringe contrast of the other, the step height should be chosen to be a multiple of the central wavelength: $h = N \cdot \lambda_c$.

B.2 Shallow-step approximation

For shallow steps, the approximation of treating the staircase mirror as a phase mask for the calculation of the electric field in focus, is valid. Figure B.3(b) shows the phase of a focal field at low numerical aperture. The phases near best focus $z = 0$ are nearly constant in the range $|z| < 10\lambda$. A partial phase addition, as demonstrated in the naive approach, is therefore a valid way to describe the electrical focal field just after the staircase mirror. However, when this altered field is propagated again, the field at the plane z_2 is radically different from the original field at z_0.

The field after re-collimation is the field that is combined with the plane waves in the other arm. The combined field is focused again, and if an analytical expression can be derived for this focal intensity, the response matrix can quickly be calculated. Figure B.4 shows two edge-adjusted fields. One was obtained by numerically propagating the expression in Eq. (B.4). The other one is mathematically derived. The first approach is as follows. For a pupil function $P = 1$ for $|x| < D/2$, the focal field can be expressed as

$$A(\theta) = \int_x P \cdot \exp[-i2\pi x\theta/\lambda]\mathrm{d}x. \tag{B.6}$$

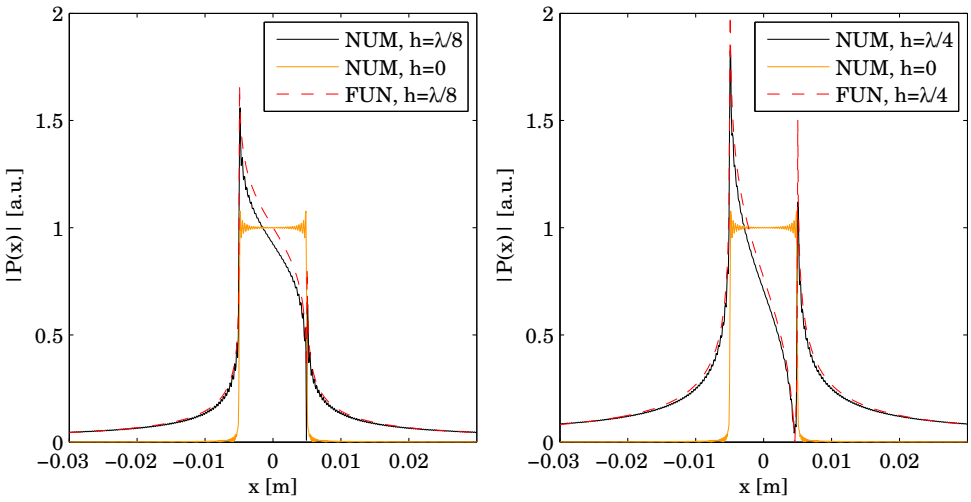

Figure B.4: Comparison of numerical (NUM) and analytical (FUN) methods to calculate the electrical field after re-collimation. The step height is taken $h = \lambda/8$ (left) and $h = \lambda/4$ (right), the angle of incidence is $\theta_0 = 0$ and the step edge is located at $\theta = 0$. Aperture diameter $D = 0.01$ m and the discretization X grid spans $6 \cdot D$ in 700 divisions.

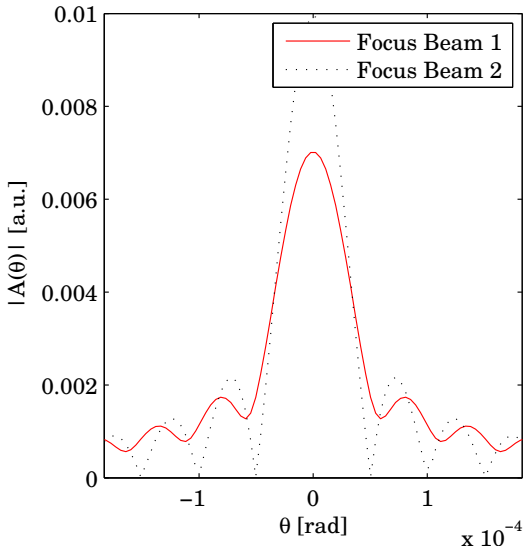

Figure B.5: The foci of two beams of equal diameter D. Beam 1 passed through the arm in which the step edge was present in an intermediate focus. Beam 2 passed through the other arm of the interferometer. The focal discretization grid Θ spans $50 \cdot r_{\text{Airy}}$ in 698 divisions.

The result is the sinc-function. Numerically, the integral is expressed as

$$A(\Theta) = \sum_X P \cdot \exp[-i2\pi X\Theta/\lambda] \cdot \Delta x. \tag{B.7}$$

Here, X and θ are a set of discrete values, where $X_j = j\Delta x$ and $\Theta_k = k\Delta\theta$ for indices $j = 1,2,\ldots,J$ and $k = 1,2,\ldots,K$. The re-collimated field is then expressed as:

$$\begin{aligned} P'(X) = &\sum_{\Theta_{k'}} A(\Theta)\exp[i2\pi X\Theta]\Delta\Theta + \\ &\sum_{\Theta_{k''}} A(\Theta)\exp[i2\pi(h+X\Theta)]\Delta\Theta, \end{aligned} \tag{B.8}$$

where k' and k'' indicate the first and second half of the range over Θ, that will encounter respectively the unraised and the raised part of the stair. This numerical Fourier analysis takes the series X,Θ with finite discretization and limited domains. This results in loss of spatial frequencies in the result, as can be observed for the two lines in Fig. B.4 with the 'NUM' label. Even with step height $h = 0$, the exact pupil function $P = 1$ is not recovered.

An analytical expression can be found by using the convolution theorem, which states that a convolution of functions is a multiplication of their Fourier transforms, and vice versa. Since the focal field and pupil field form a Fourier pair, the analytical pupil expression can be obtained by convolving the original pupil function (giving an unaberrated diffraction pattern in focus) with the Fourier transform of the staircase function. A simple staircase is taken, expressed as

$$S(\theta) = \mathrm{H}(-\theta) + \mathrm{H}(\theta)\exp[2\pi i h/\lambda]. \tag{B.9}$$

Here, the Heaviside step function $\mathrm{H}(x)$ is used, given as

$$\mathrm{H}(x) = \begin{cases} 0 & x < 0 \\ 1/2 & x = 0 \\ 1 & x > 0 \end{cases} \tag{B.10}$$

This step function has amplitude $|S(\theta)| = 1$ and a phase off-set for $\theta > 0$. The Fourier transform of this function is then

$$\mathscr{F}[S(\theta)](x) = \frac{i\lambda(\exp[2\pi i h/\lambda] - 1)}{2\sqrt{2}\pi^{3/2}x} + \frac{1}{2}\sqrt{\frac{\pi}{2}}\delta(x)(1 + \exp[2\pi i h/\lambda]), \tag{B.11}$$

where Dirac's delta function is used, which is the derivative of the Heaviside function:

$$\delta(x) = \frac{\mathrm{d}}{\mathrm{d}x}\mathrm{H}(x). \tag{B.12}$$

The function $\mathscr{F}[S(\theta)](x)$ is the pupil-plane equivalent of the staircase function in focus. However, it is acting as a convolution kernel. The original pupil function is expressed as

$$P(x) = -H\left(\frac{-D}{2} - x\right) + H\left(\frac{D}{2} - x\right). \tag{B.13}$$

Hence, the resulting pupil field is

$$\begin{aligned} P'(x) &= P(x) \otimes \mathscr{F}[S(\theta)](x) \\ &= \int_\xi P(x) \cdot \mathscr{F}[S(\theta)](x-\xi)\mathrm{d}\xi. \end{aligned} \tag{B.14}$$

Unfortunately, this expression has singularities for $|\xi| \to \infty$. However, it does turn out that the interesting central region $|\xi| < D$ is well approximated by limiting the integration over ξ to a large value, typically $|\xi| = 30$. The result is

$$\begin{aligned} &P'(\xi) = \\ &\frac{-1}{\sqrt{2}\pi^{3/2}}\Big[e^{i\pi h/\lambda}\left(\lambda\sin[h\pi/\lambda]\left[(-\log[60]+\log[D+2\xi]\right)\right. \\ &\mathrm{H}(60-D-2\xi)+\left(-i\pi+\log[1/60(-D+2\xi)]\right)\mathrm{H}(-60+D-2\xi)+ \\ &\left(\log[60]-\log[-D+2\xi]\right)\mathrm{H}(60+D-2\xi)+(\log[60]-\log[D+2\xi]) \\ &\mathrm{H}(-30-D/2-\xi)+i\pi\left(\mathrm{H}(D-2\xi)+\mathrm{H}(-30-D/2-\xi)-\right. \\ &\left.\left.\mathrm{H}(-D/2-\xi)\right)\right]+\pi\lambda\cos[h\pi/\lambda]\left[\mathrm{H}(-D/2+\xi)-\mathrm{H}(D/2+\xi)\right]\Big)\Big]. \end{aligned} \tag{B.15}$$

With the appearance of several step-functions $\mathrm{H}(x)$, an expression for variable staircase step height h, arbitrary aperture diameter $D \ll 30$ m and arbitrary wavelength λ is obtained. In Fig. B.4, the dashed line shows the accordance of this expression with the numerically derived expression, for the same D, h and λ. The analytical expression in Eq. (B.15) can be evaluated very quickly.

It turns out that an implementation of arbitrary step edge location, other than at $\theta = 0$, or equivalently, the response from an off-axis point source at $\theta_0 \neq 0$, is not yielding any tractable analytical expression, even after applying some approximation. The intermediate field, as derived in Eq. (B.15) would need to be calculated for any off-axis direction, but this is not possible analytically[1]. It needs to be available for a proper continuation of the calculation, since only the field for $|\xi| < D/2$ is propagated further.

The electrical field is cut-off by the lens at z_3. The displayed field is not consistent with the flat field from the other arm and therefore the modulation of the interference shall not be perfect. If now the electrical field at z_3 is focused and compared to the focus of the beam from the other arm (Fig. B.5), the resulting focal fields have different cross-section. The unaberrated focus of 'Beam 2' has the shape of the sinc-function. Any aberration on a pupil function widens the point spread function. Therefore, the focus of 'Beam 1', after passing the staircase and the second aperture stop, is wider. The modulation of the interference between these foci will not be one; perfect extinction after combination does not occur. Figure B.6 shows the effect of the step height h relative to the wavelength and the effect of the angle of incidence θ_0.

The numerical approach is lengthy, since fine discretization grids are necessary in both the pupil and the focal domain. However, it does allow angles of incidence θ_0 and more complex (multi faceted) staircases are easily implemented. A parametric expression for the final focal intensity, without calculating intermediate planes, was not obtained. For quick calculation of response functions, this would be favorable. However, in the framework of an observation, the calculation of response functions would be carried out off-line. The simulations in this thesis were performed with the naively calculated fringe functions. Figure B.7 shows that this approximation is, apart from a scale factor, valid for the integrated large pixel detector response.

[1] Introduction of either a general point source direction θ_0 in the pupil function $P(x)$ or a general step-edge location in $S(\theta)$, see respectively Eqs. (B.13) and (B.9), results in the occurrence of the Exponential Integral, defined as

$$E(x) = \int_1^\infty \frac{e^{-tx}}{t}\mathrm{d}t, \tag{B.16}$$

in the convolution expression of Eq. (B.14). The Exponential Integral is known to have no analytical solution. Therefore, only a numerically approximated expression for the general pupil field can be evaluated.

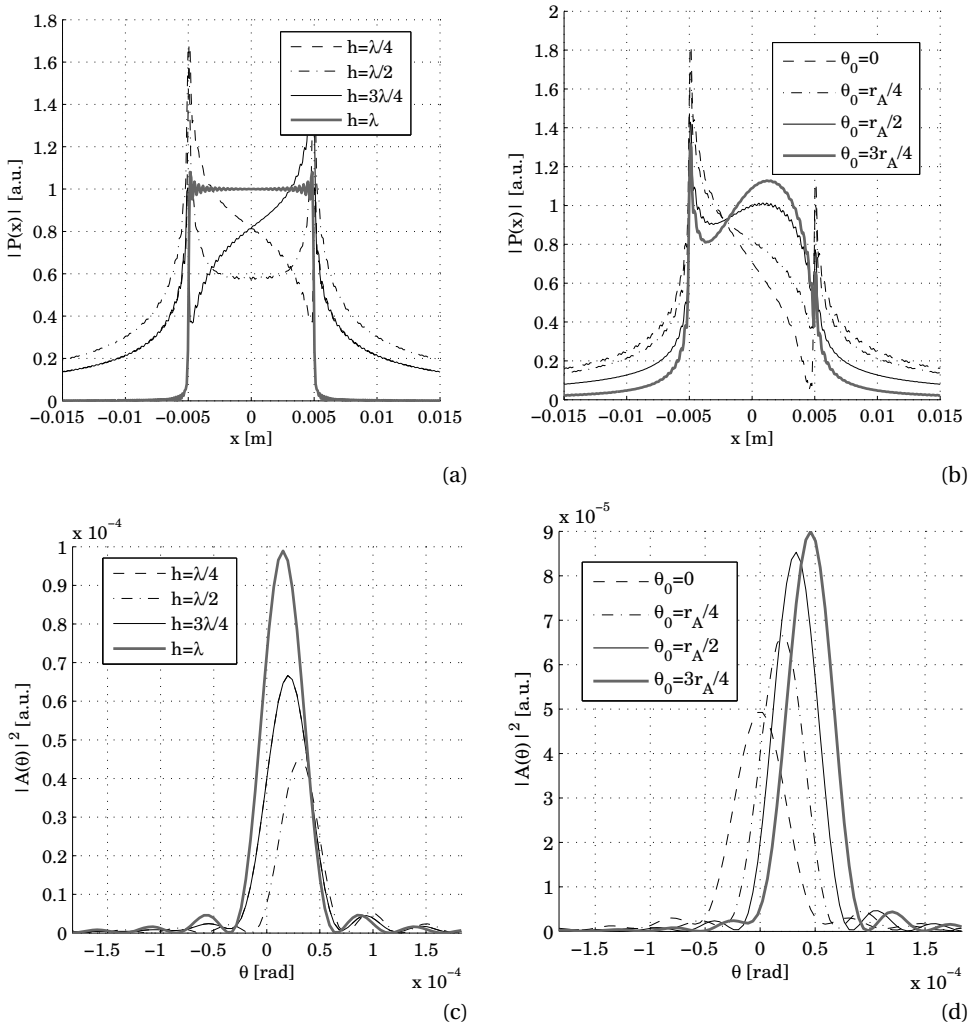

Figure B.6: Numerical evaluation of the pupil function $P(x)$ and the focus $A(\theta)$, when a beam in direction θ_0 is focused on a step with height h. For the focus, only $P(x)$ for $|x| < D/2$ is taken. The step height is relative to the wavelength λ. The incoming beam angle is relative to the Airy-radius r_A. Figures (a) and (c) respectively show the pupil and focal field for various h, while $\theta_0 = r_A/4$. Figures (b) and (d) respectively show the pupil and focal field for various θ_0, while $h = \lambda/4$.

B.3 Long baseline calculation

For very long baselines, the step height will be very large. For a FOV or $2\theta_0$ of 14 μrad and a baseline B of 200m, the external OPD is $\theta_0 B \approx 3$ mm, which means thousands of wavelengths or hundreds of coherence lengths. In order to equalize this field dependent OPD, either very tall steps are needed, or a large number of very narrow shallow steps is needed. In the first case, a shadowing effect and large diffraction effect from the step edges can be expected (see Fig. B.8) and for detection a delay scan of several times the coherence length is necessary. In the latter case, the Airy diffraction pattern in focus

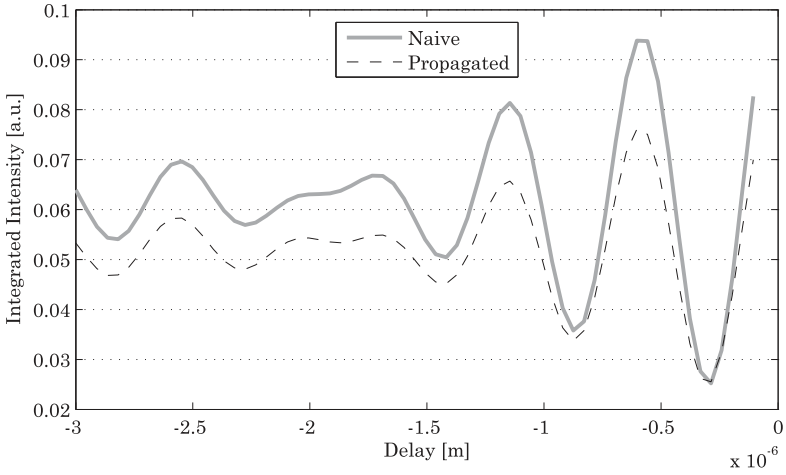

Figure B.7: The intensity response of polychromatic light on one single detector is obtained by integrating $I(\theta, d)$ over the θ-range corresponding to that detector. Due to the diffraction effects and the fact that the field outside $|\xi| < D/2$ is cut off in the calculation where the step edge is propagated, the resulting fringe contrast will be lower than the contrast predicted by the integration of the naively split-shifted fringe packet. The same holds for the mean flux, since light is lost after the re-collimation lens. However, the fringe functions are very alike. A correction factor applied to the naive but quick calculation provides an adequate intensity response.

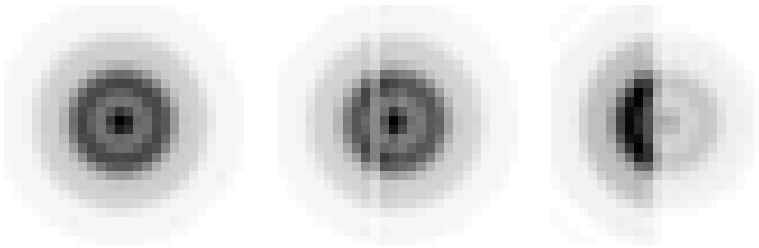

Figure B.8: Three near-focus intensity images of a beam without step edge $|A_2|^2$, with an edge present $|A_1|^2$ and the combined focus $|A_1 + A_2|^2$. The step height was taken 3 mm, which is 1000× higher than the step used in the simulation.

falls on a 'phase mask' that is fragmented to such a degree, that an analytical expression for the field after re-collimation is not available. The question rises whether that field will still have regions of small phase slope, so that interference with another beam still produces a periodic fringe pattern.

The alignment of the step edges is always perpendicular to the baseline orientation of the telescope pair. Therefore, the field after the staircase will show differences for the polarization components perpendicular to and parallel to the edge direction. A full vectorial analysis of the perpendicular and parallel components of the focal field is therefore advisable. However, again for shallow steps, the field summed from these field components will not differ much from the field derived with scalar diffraction theory.

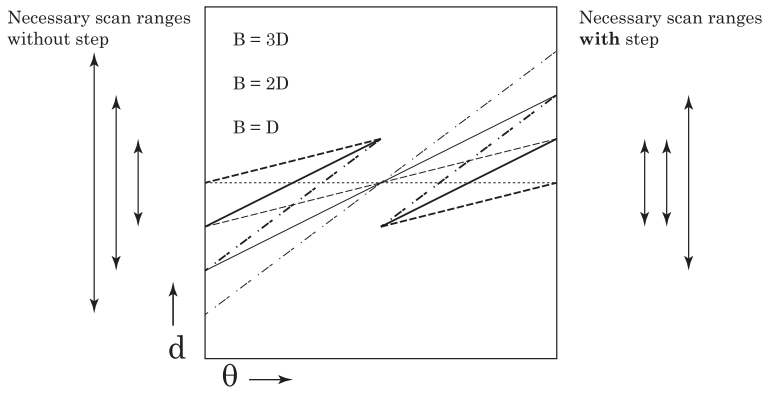

Figure B.9: The shape of the staircase has to be optimized for every needed baseline length and should hence be actuatable. If this is not possible, a set of mirrors with fixed dimensions could be placed in the intermediate focus. This illustration shows how one mirror, optimized for one baseline length, $B = 2D$, still reduces the total necessary scanning time for three different baseline lengths.

Sub-optimal step heights

For equalization of the external field-dependent path length differences, the heights of the steps h of the staircase have to be adjusted to every baseline length B_k. Only then, the necessary scan length $(d_{\max} - d_{\min})$ is minimal and constant for all baseline lengths. Actuating such a mirror however, requires micro-mechanic mirrors that have not yet been demonstrated. Unlike Adaptive Optics, the adjustable staircase mirror has to operate in focus rather than on a collimated wavefront. However, even without a fully adjustable staircase mirror, benefit of the path length compensation can be taken. Figure B.9 shows a diagram of envelope/fringe packet center locations in (θ, d)-space for three different baseline lenghts B. The necessary scan ranges with and without a staircase mirror present are indicated to the left and right hand side respectively, of the diagram. The staircase mirror under consideration has one height h for all three baseline lengths and is hence not optimized. Still, the total necessary scan range is reduced.

B.4 Inefficiency of staircase response functions

Besides the loss of light due to the presence of edges in focus, there is also a signal processing-related 'loss' connected to the Staircase method. As found in Chapter 5, the production of estimates $\hat{L}(\theta_0)$ is in the case of Staircase imaging slightly less efficient than in the case of Michelson imaging. Despite the fact that the Staircase compacts the fringed measurement signals, it needs more photons per bin to obtain an estimate of equal fit to the original. This inefficiency is again illustrated in Fig. B.10. The inefficiency can be explained by the nature of the fringed signal. In the case of Staircase imaging, there is no unique relation between the location and intensity of a point source on the sky and the resulting single-point response function.

Following the staircase-induced staggered line in (θ, d)-space for the origin location of the envelope and the fringes, one can think of situations where the *integrated* response signal in a pixel, as function of d, is the same, while a different $L(\theta_0)$ caused these re-

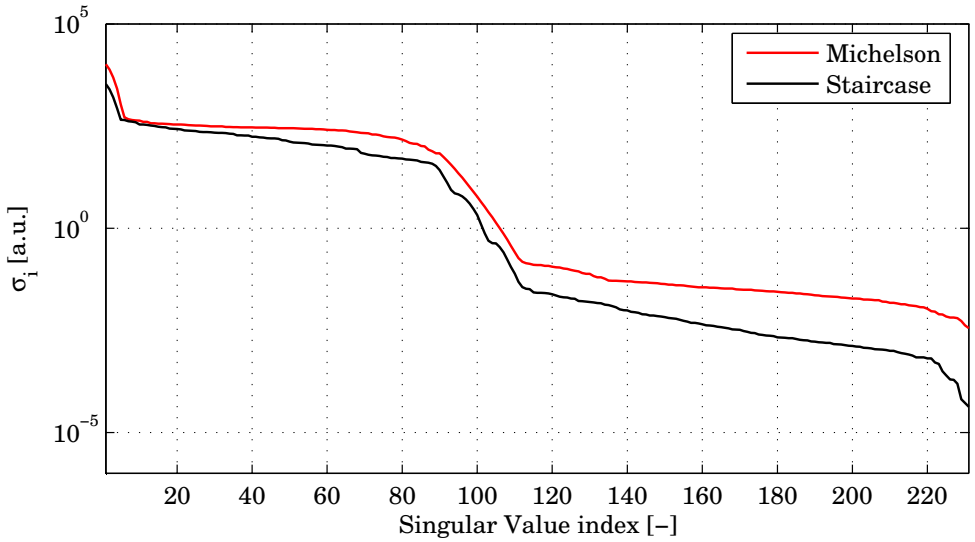

Figure B.10: Comparison of the singular values σ_i of the transfer matrices of the Michelson and the Staircase simulation. For a description of Singular Value Decomposition and the meaning of σ_i, see Sec. 4.3. The singular values of the Staircase are always lower than those of Michelson. Lower singular values mean higher noise amplification in the inversion and hence require more filtering in the reconstruction process. Apparently, the Staircase method is more sensitive to noise than the Michelson method.

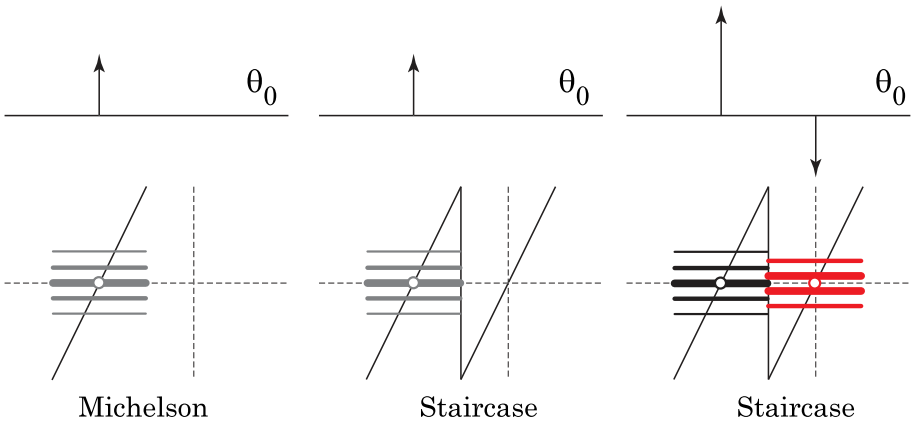

Figure B.11: Three elementary source functions $L(\theta_0)$ are depicted. The detector responses in (θ, d)-space are given, at a certain baseline B_k. The response in the Michelson case uniquely matches to the given source function. Since in the case of Staircase imaging the fringe data is compacted, the two sketched responses provide after integration over a pixel the same intensity signal $I_{jk}(d)$, but a totally different—yet allowed—source function $L(\theta_0)$.

sponses. Figure B.11 illustrates such a situation, based on the fact that *negative* contributions ($L(\theta_0) < 0$) to a response are, in principle, allowed. In the sketched situation, the combination of a large and positive response with a small and negative response yields the same measurement as the combination of a single, smaller, positive response. Due to the fact that different source functions $L(\theta_0)$ can lead to the same or nearly the same measurement, the Staircase method will need more information to be able to give a correct estimate of the sky. Therefore, given the same set of baseline lengths as the Michelson case, it will perform worse, as is indicated by the singular values in Fig. B.10, where the normalized singular values of the Staircase imager are lower than those of the Michelson imager and show a steeper drop-off, and is confirmed by the numerical simulations, presented in Sec. 5.3.2, where the plot of the reconstruction error versus the number of photons per bin (referred to as the imaging efficiency) shows that the Staircase imager needs more photons per bin (or less noise) to reconstruct an image as good as the Michelson imager.

Appendix C

Prediction for the Darwin array

A final set of simulations is performed in order to predict the imaging performance of the Darwin array. As for the other presented simulations, the array under consideration is a two-element configuration, generating a one-dimensional, high-resolution estimate of the luminosity distribution on the sky $\hat{L}(\theta_0)$. The simulations are performed at the ultimate values allowed by the software and the computer. Since a linear system of equations lies at the basis of the simulation process, large values of the FOV and ultimate angular resolution generate matrices that reach the storage capacity of the internal memory of the computer on which the simulations are run. For that reason, the following simulations do not reach the requirements for the Darwin imaging mission, listed earlier in this thesis; the achieved angular resolution is 71 nrad, whereas the requirement was 0.005" or 24 nrad.

C.1 Simulation parameters

The original source function or luminosity distribution $L(\theta_0)$ is again taken to be a cross-section of the object HH47. In Fig. C.1, the function $L(\theta_0)$ is depicted, together with the PSF of a single telescope. The source function is chosen to span approximately 11 PSFs. The magnification is again chosen to be $M = 1$. The detector array has the same angular span as the source function.

The telescope diameter is $D = 3.5$ m. The baseline lengths B at which snapshots are taken, are then given as

$$B_k = \begin{cases} 2D & k = 1 \\ 4(k-1)D & k = 2, 3, \ldots, 9. \end{cases} \tag{C.1}$$

The baseline length differences of $4D$ might seem large, but with an observational bandwidth for which 6 μm $\leq \lambda_c \leq$ 10 μm, this set of baselines leads to a spatial frequency coverage with no gaps up to the desired ultimate spatial frequency, expressed as angular wavenumber, given by

$$\frac{B_{\max}}{\lambda_c} = \frac{112}{8 \cdot 10^{-6}} = 1.4 \cdot 10^7 \, [\text{rad}^{-1}]. \tag{C.2}$$

The frequency coverage is illustrated in Fig. C.2. The 11 PSFs wide source function is discretized on a 333-points equidistant grid. This leaves 33 resolution elements per PSF,

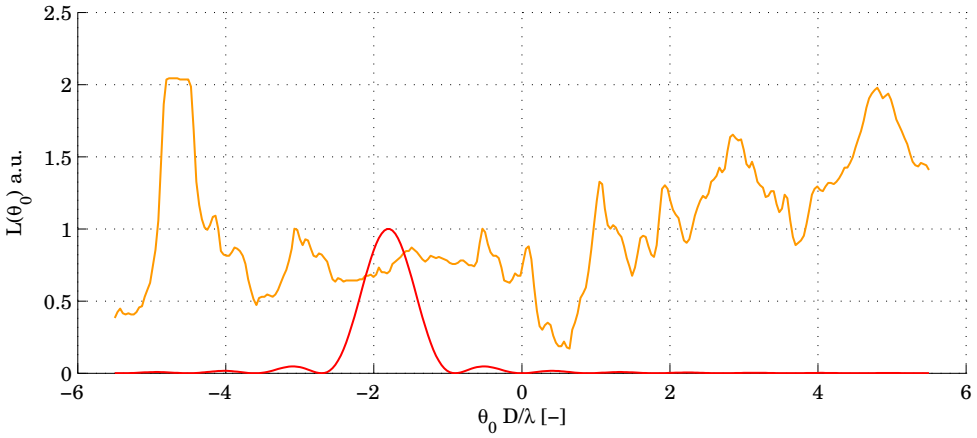

Figure C.1: The function $L(\theta_0)$ is a normalized cross-section through an image of the object HH47 (gray line). Its angular extent is chosen to span 11 incoherent PSFs; one single PSF is indicated with the black line.

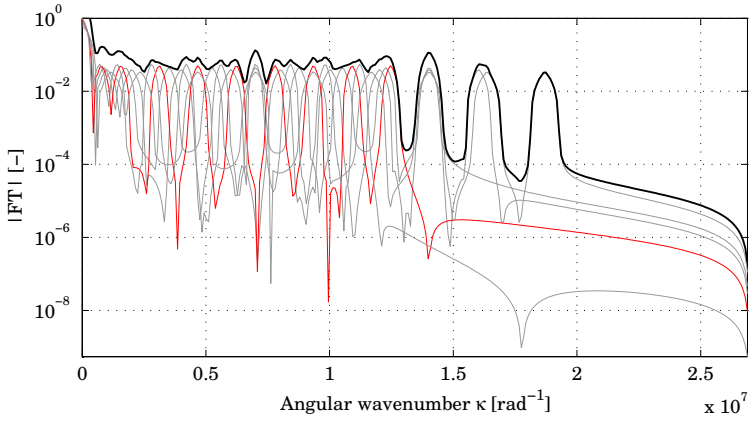

Figure C.2: To check the coverage of spatial frequencies, a homothetic PSF is calculated for the range of wavelengths under consideration and for all values B_k. The Fourier Transform (FT) of these PSFs is taken and the absolute values are plotted per wavelength. Per trace or wavelength, the spacing of peaks corresponding to the $4D$ gaps in baseline lengths can be observed. The FT of the sum of all PSFs is plotted as a thick black line, representing the spatial frequency coverage for the complete set of baseline lengths and wavelengths.

matching to the ratio $B_{\max}/D = 32$. Therefore, all features in the function $L(\theta_0)$ should be recoverable, leading to reconstruction error ϵ-values that are only limited by shot-noise.

Table C.1 provides a list of the detector discretization, needed for the four different imagers, in order to cover the FOV and reach the same spatial angular frequency coverage. For the methods other than Densified, the discretization is straightforward. The necessary range of delay steps for the Densified case to have coherent information from all regions of the sky, is derived from the modulation part of the intensity point-source

response for a general interferometer, given as, see Eq. (2.28),

$$\cos\left[\frac{\pi B_0}{\lambda}\left(\theta-\left[\frac{B}{B_0}\theta_0\right]+\frac{d}{B_0}\right)\right]=1,\ \text{ for } \theta_0=\theta_0^{(\max)}. \tag{C.3}$$

The expression of Eq. (C.3), states that a bright fringe is necessary at the boundary of the field-of-view. Since the observation is polychromatic, this requirement is reduced to finding the delay d, for which the *central* fringe appears in the center of the diffraction envelope. This center is located at $\theta=\theta_0^{(\max)}$. Equation (C.3) now reduces to

$$d=B_0\theta_0\left(1-\frac{B}{B_0}\right). \tag{C.4}$$

With the given FOV of 11 PSFs wide, a combination baseline length of B_0 = 7 m and a maximum collection baseline length of B = 112 m, Eq. (C.3) yields a maximum delay $d_{\max}$ = 1.5 mm, corresponding to $187\cdot\lambda_c$. The amount of steps to go through this delay-range is then chosen such that for every direction θ_0, the corresponding intensity PSF shows an envelope with clearly visible fringes. This amount is related to the coherence length and can be found by inspection of the calculated PSFs. Increasing the amount of steps leads eventually to a PSF with a central fringe in it, for every sky coordinate θ_0. A very large number of steps will then be necessary. Decreasing the amount of steps leads to regions of the sky for which the PSF hardly shows fringes, since only for the values of θ_0, matching to the delays d according to Eq. (C.4) the PSF will show a central fringe in the center of the PSF. The 11 PSFs wide sky is adequately covered with 36 steps of d, spanning the $-1.5\ldots+1.5$ mm range.

Table C.1: Measurement settings for the simulations. B_0 in the case of Densified beam combination, is the fixed exit baseline length. Both the pixel range and the function $L(\theta_0)$ span 11 PSFs, in all cases.

Case	Pixels	Pixel Size	OPD Range	Size	Steps	Bins
Michelson	20	$\simeq$ PSF/2	$2B_{\max}\theta_{\max}$	$\lambda_c/4$	1561	31220
Fizeau	1562	$p_\theta(B_{\max})/4$	—	—	1	1562
Densified	101	$p_\theta(B_0)/4$	$-187\lambda_c\ldots+187\lambda_c$	$10\lambda_c$	36	3636
Staircase	20	$\simeq$ PSF/2	$-\frac{3}{2}l_{\text{coh}}\ldots+\frac{3}{2}l_{\text{coh}}$	$\lambda_c/4$	25	500

For the Staircase method, the number of stairs was chosen to be equal to the number of pixels. The stair heights h_0 are optimized for each baseline length. As a result, all fringes are present within a very short d-range, as illustrated earlier by the sawtooth-shaped (θ,d)-space plot. The ultimate delay d at which the central fringe can be found, is a function of the stair width and the baseline length—and is in the h_0-optimized case equal to the stair-height.

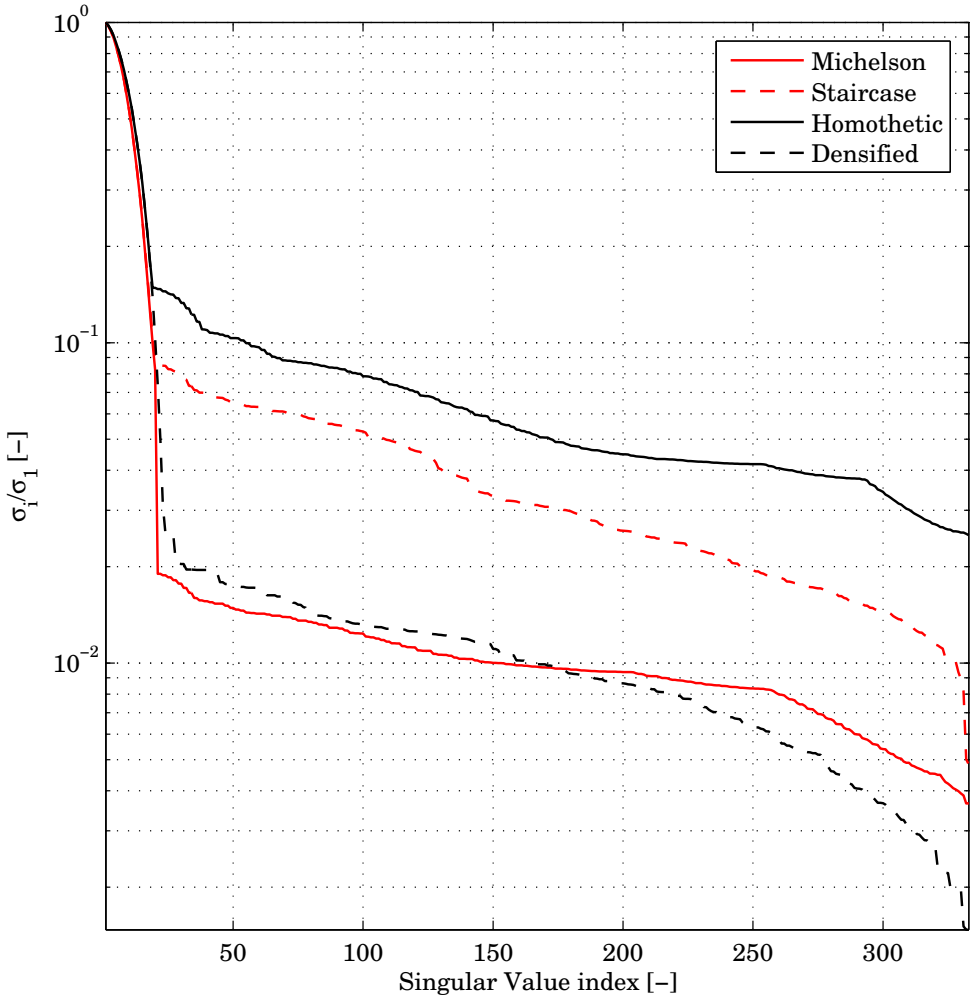

Figure C.3: The singular values σ_i are normalized with respect to the largest singular value σ_1. This allows comparison of the responsiveness of the imaging method with respect to spatial frequencies in the observed luminosity function $L(\theta_0)$. The graphs show an incoherent imaging regime, for indices $i \leq 20$, and a coherent imaging regime, for indices $20 < i \leq 333$. There is no unsampled regime, because of the very long baseline lengths.

C.2 Simulation results

Comparison of the transfer matrices

The transfer matrices for the four methods can be composed and analyzed with Singular Value Decomposition. The resulting series of singular values σ_i are plotted in Fig. C.3, where each series is normalized by its largest singular value, σ_1. Inspection of the plots provides the following information.

Up to index $i = 20$, the singular values drop heavily. Inspection of the singular vectors $\mathbf{v}_i$ for these indices learns that these modes correspond to the incoherent regime. With a

resolution, governed by telescope diameter D, the flux is addressed to the 11 PSFs wide sky. Apparently, a set of $\simeq 11 \cdot 2$ functions is sufficient for this task. The co-axial imagers have 20 pixels on the detector, but the image-plane methods have much more.

In the coherent regime, for which $20 < i \leq 333$, the average level of the slowly decreasing lines is a measure for the amount of coherent information in the detection signals. Homothesis and Staircase both have fringe information in all regions of every snapshot they record, whereas Densified and Michelson record large amounts of incoherent intensity data per snapshot. However, not only the average level is related to quality. The 'flatness' of the traces is a measure for the coverage of the field at all spatial frequencies. The flatness of Homothesis and Michelson is better than that of Staircase and Densified. Apparently, for a certain spatial frequency, not every direction θ_0 is represented with equal strength. In other words, these two non-classical methods have a field-variant response, changing with the spatial frequency. However, this does not mean that not all information of $L(\theta_0)$ cannot be restored. For the Staircase method, an analysis of the slight inefficiency is presented in Sec. B.4. For the Densified method, the reason for the slight inefficiency lies in the fact that only a limited set of values of d is taken per baseline configuration, and that the fringe packet moves out of the diffraction envelope.

The analysis of the transfer matrices by inspection of their singular values, can be done before starting simulation runs for each method. Facts such as complete coverage of field at all spatial frequencies, and a correct number of singular values related to the incoherent image, can be checked. The simulations can then be started with transfer matrices that match the desired imaging parameters, such as field and resolution. But even without simulations, the lines in Fig. C.3 already predict which imaging method will perform best. The method that demonstrates in its σ_i/σ_1-trace

- a limited drop of magnitude between the incoherent and the coherent regime,
- an as limited as possible decrease of magnitudes in the coherent regime, and
- a coherent regime continuing until index i, where i is equal to the number of resolution elements in the function $L(\theta_0)$,

is stated to be the best performing imaging method. The numerical simulations, incorporating detector-noise and shot-noise, should prove this statement.

Comparison of simulated observations

Figures C.4 and C.5 represent the results of 100 simulations. The four imaging methods are applied to the same source $L(\theta_0)$, from which an increasing number of photons is received. Figure C.4 displays the imaging efficiency, expressed as the reconstruction error ϵ, for the best reconstruction possible, versus the number of photons per bin. Detector noise is again 8 photons per bin. Above this amount of photons per bin, all imaging methods demonstrate a drop in reconstruction error. The methods Homothesis and Michelson—the two classical methods—have a comparable efficiency and perform better in terms of efficiency than the methods Densified and Staircase. The reasons for this lie in the large amount of incoherent information and the use of multiplexing, respectively.

Figure C.5 finally, shows the performance of the four imaging methods as a function of observation time. Whether the best reconstruction is sought for a given observation time, or the shortest observation time is sought provided a minimum reconstruction

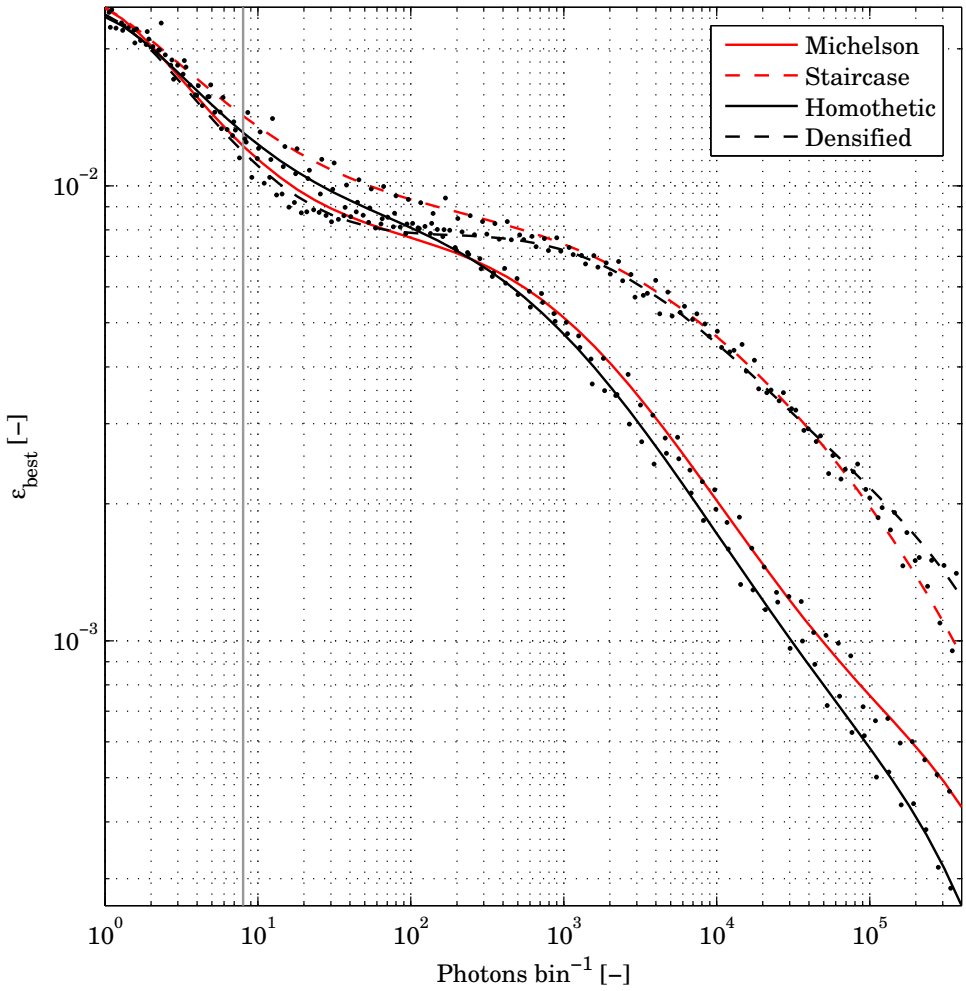

Figure C.4: The normalized reconstruction error ϵ is expressed as a function of the number of photons per bin. Above the indicated detector noise level of 8 photons per bin, the curves indicate the efficiency of the imaging methods. Polynomials are fit through the data, for displaying purposes only.

quality, the outcome will be the same. The best imaging method is Homothesis, followed by the Staircase method.

C.3 Conclusions

Homothesis is the superior imaging method for wide-field, high angular resolution images. Not surprisingly, it is this method that resembles most the ideal situation of a very large telescope with an aperture mask in front of it. However, the construction and operation of a homothetic imaging array are no trivial issues. The Staircase method achieves storage of high resolution information from the sky into a minimal number of detector

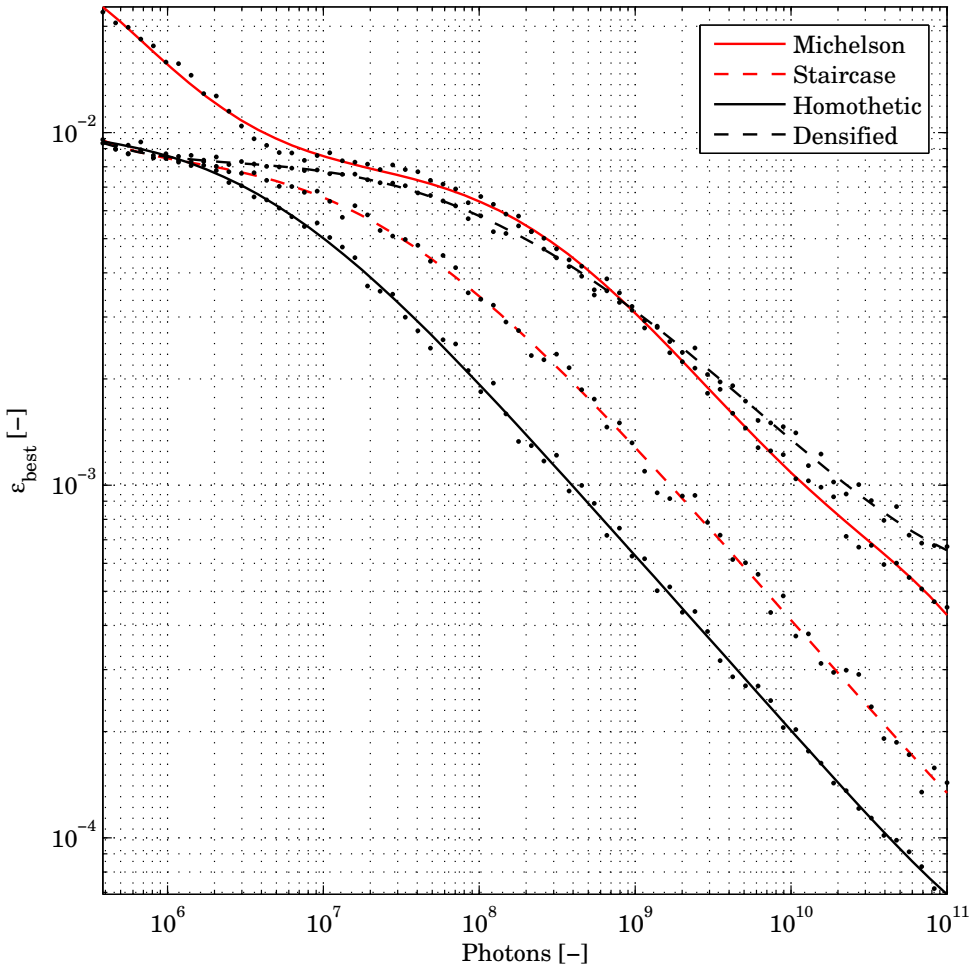

Figure C.5: The normalized reconstruction error ϵ versus the total amount of received photons for the complete observation of $L(\theta_0)$. Polynomials are fit through the data, for displaying purposes only.

bins—with only 500 bins, it has by far the smallest amount. Although the reconstruction process suffers slightly from this data-compaction by multiplexing, the Staircase method performs very well in the sense that it is fast, or, in other words, that it needs less photons to reconstruct an image than Michelson or Densified. As in the case of Homothesis, there are practical issues to overcome. A staircase-shaped mirror with 20 aligned facets can be produced. But then, either an actuatable version with tuneable stair-height has to be designed, or a system should be installed that can replace a rigid staircase mirror for each of the k observations with baseline lengths B_k.

Considering the merit of the analysis of the transfer matrices, the conclusion can be drawn that inspection of the singular values is a quick and accurate means to predict the imaging performance of an interferometer. The superiority of Homothesis, followed by the Staircase method, is in accordance with the final simulation results.

Bibliography

M. Abramowitz and I.A. Stegun, *Handbook of Mathematical Functions*, Dover, New York, 1970.

K.R. Anantharamaiah, T.J. Cornwell and R. Narayan, "Synthesis imaging of spatially coherent objects," in *Synthesis Imaging in Radio Astronomy* (Perley, Schwab and Bridle, editors) pp. 415–430, Astronomical Society of the Pacific, 1994.

J.R.P. Angel, J.M. Hill, P.A. Strittmatter, P. Salinari and G. Weigelt, "Interferometry with the large binocular telescope," *Astronomical Interferometry, SPIE* **3350**, pp. 881–889, 1998.

J. R. P. Angel and N. J. Woolf, "An imaging nulling interferometer to study extra-solar planets," *The Astrophysical Journal* **475**, pp. 373–377, 1997.

L.A. d'Arcio, *Selected aspects of wide-field stellar interferometry*. Ph.D. thesis, Delft University of Technology, November 1999.

L.A. d'Arcio *et al.*, "The imaging mode of the Infrared Space Interferometer IRSI-Darwin," *SPIE* **4838**, pp. 184–195, February 2002.

C. van der Avoort, A. Mieremet, S.F. Pereira and J.J.M. Braat, "Demonstration of nulling using delay line phase shifters," *SPIE New Frontiers in Stellar Interferometry* **5491**, pp. 816–823, October 2004.

C. van der Avoort, H. van Brug, J.W.A. den Herder, L.A. dŠArcio, R.S. Le Poole and J.J.M. Braat, "Experimental Validation of Homothetic Mapping," *SPIE New Frontiers in Stellar Interferometry* **5491**, pp. 1587–1598, October 2004.

C. van der Avoort, J.J.M. Braat, P. Dirksen and A.J.E.M. Janssen, "Aberration retrieval from the intensity point-spread function in the focal region using the extended Nijboer-ŰZernike approach," *Journal of Modern Optics* **52** Nr. 12, pp. 1695–1728(34), August 2005.

C. van der Avoort, J.W.A. den Herder and J.J.M. Braat, "Comparison of blind imaging performance of Fizeau and Michelson type arrays for a partially resolved object," *Proc. SPIE* Vol. **5905**, pp. 206–218, Techniques and Instrumentation for Detection of Exoplanets II; Daniel R. Coulter; Ed., August 2005.

J.E. Baldwin, M.G. Beckett, R.C. Boysen, D. Burns, D.F. Buscher, G.C. Cox, C.A. Haniff, C.D. Mackay, N.S. Nightingale, J. Rogers, P.A.G. Scheuer, T.R. Scott, P.G. Tuthill,

P.J. Warner, D.M.A. Wilson and R.W. Wilson, "The first images from an optical aperture synthesis array: mapping of Capella with COAST at two epochs," *Astronomy and Astrophysics* **306**, p. L13, February 1996.

J.E. Baldwin and C.A. Haniff, "The application of interferometry to optical astronomical imaging," *Phil. Trans. R. Soc. London.* A **360**, pp. 969–986.

J.M. Beckers, "The VLTI, part III: Factors affecting wide field-of-view operation," *Advanced Technology Optical Telescopes IV, SPIE* **1236**, pp. 379–389, 1990.

J.M. Beckers, "Interferometric imaging with the Very Large Telescope," *J.Optics (Paris)* **22**, no.2, pp. 73–83, 1991.

M.J. Beran and G.B. Parrent, *Theory of partial coherence*, Second edition, Society of Photo-optical Instrumentation Engineers, 1974.

M. Bertero and P. Boccacci, "Image restoration methods for the Large Binocular Telescope (LBT)," *Astron. & Astroph. Supplement Series* **147**, pp. 323–333, 2000.

R. van Boekel, M. Min, Ch. Leinert, L.B.F.M. Waters, A. Richichi, O. Chesneau, C. Dominik, W. Jaffe, A. Dutrey, U. Graser, Th. Henning, J. de Jong, R. Köhler, A. de Koter, B. Lopez, F. Malbet, S. Morel, F. Paresce, G. Perrin, Th. Preibisch, F. Przygodda, M. Schöller and M. Wittkowski, "The building blocks of planets within the 'terrestrial' region of protoplanetary disks," *Nature* **432**, pp. 479–482, November 2004.

M.A. Born and E. Wolf, *Principles of Optics*, Sixth edition, pp. 508–510, Pergamon Press, New York, 1980.

J.J.M. Braat, P. Dirksen and A.J.E.M. Janssen, *J. Opt. Soc. Am. A* **19**, p. 858, 2002.

J.J.M. Braat, P. Dirksen, A.J.E.M. Janssen and A.S. van de Nes, *J. Opt. Soc. Am. A* **20**, p. 2281, 2003.

R. Bracewell, "Detecting nonsolar planets by spinning infrared interferometer," *Nature* **274**, pp. 780–781, 1978.

H. van Brug, T. van den Dool, W. Gielesen, P. Giesen, B. Oostdijck, and L. d'Arcio, "Delft testbed interferometer — layout design and research goals," *Interferometry for Optical Astronomy II, SPIE* **4838**, pp. 425–429, August 2002.

D.F. Buscher, J.T. Armstrong, C.A. Hummel, A. Quirrenbach, D. Mozurkewich, K.J. Johnston, C.S. Denison, M.M. Colavita and M. Shao, "Interferometric seeing measurements on Mt. Wilson—power spectra and outer scales," *Appl. Opt.* **34**, pp. 1081–1096, 1995.

P.H. van Cittert, *Physica* (Amsterdam) **1**, p. 201, 1934.

V. Coudé du Foresto, S. Ridgway and J.-M. Mariotti, "Deriving object visibilities from interferograms obtained with a fiber stellar interferometer," *A&A Supplement series* **121**, pp. 379–392, February 1997.

T.J. Cornwell, 1994, "Wide field imaging III: mosaicing," *Synthesis Imaging in Radio Astronomy,* pp. 277–286.

P. Dirksen, J.J.M. Braat, A.J.E.M. Janssen and C. Juffermans, "Aberration retrieval using the extended Nijboer–Zernike approach," *J. Microlith. Microfab. Microsyst.* **2**, p. 61, 2003.

DARWIN The Infrared Space Interferometer Redbook, ESA-SCI(2000) **12**, July 2000.

Various authors, "VLTI for newcomers," ESO internal report, 1995.

N.R. Farrar, A.L. Smith, D. Busath, and D. Taitano, "In-situ measurement of lens aberrations," *Proc. SPIE* **4000**, p. 18, 2000.

G.G. Fazio , J.L. Hora, L.E. Allen, M.L.N. Ashby, P. Barmby, L.K. Deutsch, J.-S. Huang, S. Kleiner, M. Marengo, S.T. Megeath, G.J. Melnick, M.A. Pahre, B.M. Patten, J. Polizotti, H.A. Smith, R.S. Taylor, Z. Wang , S.P. Willner, W.F. Hoffmann, J.L. Pipher, W.J. Forrest, C.W. McMurty , C.R. McCreight, M.E. McKelvey, R.E. McMurray, D.G. Koch , S.H. Moseley, R.G. Arendt, J.E. Mentzell, C. T. Marx, P. Losch, P. Mayman, W. Eichhorn, D. Krebs, M. Jhabvala, D.Y. Gezari, D. J. Fixsen, J. Flores, K. Shakoorzadeh, R. Jungo , C. Hakun , L. Workman, G. Karpati, R. Kichak, R. Whitley, S. Mann , E.V. Tollestrup, P. Eisenhardt, D. Stern, V. Gorjian, B. Bhattacharya, S. Carey, B.O. Nelson, W.J. Glaccum, M. Lacy, P.J. Lowrance, S. Laine, W.T. Reach, J.A. Stauffer, J. A. Surace, G. Wilson, E. L. Wright, A. Hoffman, G. Domingo and M. Cohen, "The Infrared Array Camera (IRAC) For The Spitzer Space Telescope," *The Astrophysical Journal Supplement Series*, **154**, Issue 1, pp. 10–17, September 2004.

Fizeau *et al.*, "Prix Bordin," *Comptes Rendus Hebdomadaires des Séances de l'Académie des Sciences* **66**, pp. 932–934, 1868.

D. Geman and C. Yong, "Nonlinear image recovery with half-quadratic regularization," *IEEE Trans. on Image Proc.*, Vol. **4**, No. 7, July 1995.

M. Golay, "Point arrays having compact non-redundant autocorrelations," *J. Opt. Soc. Am.* **61**, pp. 272-Ű273, 1971.

J.W. Goodman, *Statistical Optics*, John Wiley & Sons, 1985.

P.C. Hansen, "The discrete Picard condition for discrete ill-posed problems," *BIT* **30**, pp. 658–672, 1990.

P.C. Hansen, "Analysis of discrete ill-posed problems by means of the L-curve," *SIAM Rev.*, vol. **34**, no. 4, pp. 561Ű-580, Dec. 1992

P.C. Hansen, "Regularization tools: A Matlab package for analysis and solution of discrete ill-posed problems," *Numerical Algorithms* **6**, pp. 1–35, 1994.

P.C. Hansen, "Rank-Deficient and Discrete Ill-Posed Problems: Numerical Aspects of Linear Inversion," *SIAM*, Philadelphia, 1998.

J.W. Hardy, "Adaptive Optics for Astronomical Telescopes," *Oxford University Press*, July 1998.

E. Hecht, *Optics*, Print Partners, 1995.

J.L. Hora, G.G. Fazio, S.P. Willner, M.L.N. Ashby, J. Huang, S.T. Megeath, J.R. Stauffer, E.V. Tollestrup, Z. Wang, W.J. Glaccum, J.L. Pipher, W.J. Forrest, C.R. McCreight, M.E. McKelvey, W.F. Hoffman, P. Eisenhardt, J.A. Surace, W.T. Reach, S.H. Moseley, R.G. Arendt, K.P. Stewart and F.D. Robinson, "Calibration and performance of the Infrared Array Camera (IRAC)," *SPIE* **4131**, pp. 13–25, 2000.

W. Jaffe, K. Meisenheimer, H.J.A. Röttgering, Ch. Leinert, A. Richichi, O. Chesneau, D. Fraix-Burnet, A. Glazenborg-Kluttig, G.-L. Granato, U. Graser, B. Heijligers, R. Köhler, F. Malbet, G.K. Miley, F. Paresce, J.-W. Pel, G. Perrin, F. Przygodda, M. Schöeller, H. Sol, L.B.F.M. Waters, G. Weigelt, J. Woillez and P.T. de Zeeuw, "The central dusty torus in the active nucleus of NGC 1068," *Nature* **429**, pp. 47–49, May 2004.

A.J.E.M. Janssen, "Extended Nijboer–Zernike approach for the computation of optical point-spread functions," *J. Opt. Soc. Am. A* **19**, pp. 849–857, 2002.

A.J.E.M. Janssen, J.J.M. Braat and P. Dirksen, "On the computation of the Nijboer–Zernike aberration integrals at arbitrary defocus," *J. Mod. Optics* **51**, pp. 687–703, 2004.

J.W. Keen, D.F. Buscher and P.J. Warner, "Numerical simulations of pinhole and single-mode fibre spatial filters for optical interferometers," *Mon. Not. R. Astron. Soc.* **326**, pp. 1381–1386, 2001.

A. Labeyrie, "High resolution techniques in optical astronomy," *Prog. Opt.* **14**, pp. 47–87, 1978.

A. Labeyrie, "Resolved imaging of extra-solar planets with future 10-100km optical interferometric arrays," *Astronomy and Astrophysics Supplement* **118** pp. 517–524, September 1996.

P.R. Lawson, *Selected papers on long baseline stellar interferometry*, SPIE Milestone Series 139, Bellingham, WA, 1997.

P.R. Lawson (editor), *Principles of long baseline stellar interferometry*, course notes from the 1999 Michelson Summer School.

A. Léger, J. Mariotti, B. Mennesson, M. Ollivier, J. Puget, D. Rouan, and J. Schneider, "Could we search for primitive life on extrasolar planets in the near future? — The DARWIN project," *Icarus* **123**, pp. 249–255, 1996.

D.T. Leisawitz, B.J. Frey, D.B. Leviton, A.J. Martino, W.L. Maynard, L.G. Mundy, S.A. Rinehart, S.H. Teng and X. Zhang, "Wide-field imaging interferometry testbed I: purpose, testbed design, data, and synthesis algorithms," *Interferometry in Space* **SPIE 4852**, Michael Shao ed., pp. 255–267, 2003.

D. Loreggia, D. Gardiol, M. Gai, M.G. Lattanzi and D. Busonero, "Fizeau interferometer for global astrometry in space," *Applied Optics* **43**, pp. 721–728, February 2004.

C.D. Mackay, R.N. Tubbs, R. Bell, D. Burt and I. Moody, "Sub-Electron Read Noise at MHz Pixel Rates," *SPIE* **4306**, pp. 289–298, January 2001.

D. Malacara, *Optical shop testing*, John Wiley & Sons, 1992.

Mayor, M. and D. Queloz, "A jupiter mass companion to a solar-type star," *Nature* **378**, pp. 355–359, 1995.

A. Meinel, "Aperture synthesis using independent telescopes," *Applied Optics* **9**, pp. 2501–2504, 1970.

A.B. Meinel and M.P. Meinel, "Large sparse-aperture space optical systems," *Optical Engineering* **41** Issue 8, pp. 1983–1994, August 2002.

M.R. Meyer, J.R. Najita, T.P. Greene and J. Bally, "Visiting a Place Where Stars are Born: Star and Planet Formation Research with the NGST," *Bulletin of the American Astronomical Society* **30**, p. 1298, December 1998.

A.A. Michelson, "On the application of interference methods to astronomical measurements," *London, Edinburgh and Dublin Philosophical Magazine and Journal of Science*, Series 5, **30**(182), pp. 1–21, July 1890.

A.A. Michelson and F.G. Pease, *Astrophysics Journal* **53**, p. 249, 1921.

A. L. Mieremet, *Nulling Interferometry for direct exo-planet detection.* Ph.D. thesis, Delft University of Technology, May 2003.

A. L. Mieremet and J. J. M. Braat, "Nulling interferometry without achromatic phase shifters," *Applied Optics* **41**(22), pp. 4697–4703, 2002.

A. L. Mieremet and J. J. M. Braat, "Deep nulling by means of multiple-beam recombination," *Applied Optics* **42**(10), pp. 1867–1875, 2003.

J.D. Monnier, "Optical interferometry in astronomy," *Rep. Prog. Phys.* **66** (2003) pp. 789–857

I. Montilla, *Michelson wide-field stellar interferometry.* Ph.D. thesis, Delft University of Technology, November 2004.

I. Montilla, S.F. Pereira and J.J.M. Braat, "Michelson wide-field stellar interferometry: principles and experimental verification," *Applied Optics*, vol. **44**, no. 3, pp. 328–336, 2005.

J.G. Nagy and D.P. O'Leary, "Restoring images degraded by spatially variant blur," *SIAM J.Sci.Comput.* Vol. **19**, No. 4, pp. 1063–1082, July 1998.

A. Papoulis, *Probability, Random Variables, and Stochastic Processes*, Third edition, McGraw–Hill, 1991.

F. Paresce, A. Richichi., A. Chelli and F. Delplancke (editors), *Proceedings of the ESO Workshop on The Power of Optical/IR Interferometry: Recent Scientific Results and 2nd Generation VLTI Instrumentation*, ESO, Garching, April 2005.

E. Pedretti, A. Labeyrie, L. Arnold, N. Thureau, O. Lardiere, A. Boccaletti and P. Riaud, "First images on the sky from a hyper telescope," *Astron. Astrophys. Suppl. Ser.* **147**, pp. 285–290, 2000.

R.A. Perley, "Wide field imaging II: imaging with non-coplanar arrays," in Perley, Schwab and Bridle (editors), *Synthesis Imaging in Radio Astronomy* pp. 259–275, 1994.

W.H. Press, B.P. Flannery, S.A. Teukolsky and W.T. Vetterling, *Numerical Recipes in Pascal*, Cambridge University Press, 1989.

A. Quirrenbach, V. Coudé du Foresto, G. Daigne, K.-H. Hofmann, R. Hofmann, M. Lattanzi, R. Osterbart, R. Le Poole, D. Queloz, F. Vakili, "PRIMA: Study for a Dual Beam Instrument for the VLT Interferometer," *SPIE*, vol. **3350**, 1998.

A. Quirrenbach, "Optical interferometry," *Ann. Rev. Astron. Astroph.* **39**, 2001.

H.J.A. Röttgering, L.A. d'Arcio, C. Eiroa, I. Labbé and G. Rudnick, "Astrophysical imaging with the Darwin IR Interferometer," *Towards other Earths: DARWIN/TPF and the Search for Extrasolar Terrestrial Planets* (ESA, Fridlund & Henning), pp. 299–308, October 2003.

G. Rousset, L.M. Mugnier, F. Cassaing and B. Sorrente, "Imaging with multi-aperture optical telescopes and an application," *C.R. Acad. Sci. Paris*, t. **2**, Série IV, pp. 17–25, January 2001.

S.K. Saha, "Modern optical astronomy: technology and impact of interferometry," *Rev. Mod. Phys.* **74**, 551, 2002.

M. Schöller, R. Wilhelm and B. Koehler, 2000, "Modeling the imaging process in optical stellar interferometers," *Astron. Astrophys. Suppl. Ser.* **144**, pp. 541–552.

S.K. Saha, "Modern optical astronomy: technology and impact of interferometry," *Reviews of Modern Physics* **74**, pp. 551–600, April 2002.

E. Serabyn and M. M. Colavita, "Fully symmetric nulling beam combiners," *Applied Optics* **40**, pp. 1668–1671, April 2001.

J. Shewchuk, "An introduction to the conjugate gradient method without the agonizing pain," Technical Report CMUCS-TR-94-125, Carnegie Mellon University, 1994.

M. Shao and D.H. Staelin, 1977, "Long-baseline optical interferometer for astronomy," *J.Opt.Soc.Am.* **67**, p. 81, 1977.

D.L. Snyder, C.W. Helstrom, A.D. Lanterman, M. Faisal and R.L. White, "Compensation for readout noise in CCD images," *J. Opt. Soc. Am. A*, **12**, No. 2, pp. 272–283, February 1995.

M. Stéphan, "Sur l'extrême petitesse du diamètre apparent des étoiles fixes," *Comptes Rendus Hebdomadaires des Séances de l'Académie des Sciences* **78**, pp. 1008–1012, 1874.

M. Tallon and I. Tallon-Bosc, "The object-image relationship in Michelson stellar interferometry," *Astronomy and Astrophysics* **253**, pp. 641–645, 1992.

M. Tallon and I. Tallon-Bosc, "Beam combination for wide field imaging," *Very High Angular Resolution Imaging*, Int. Astron. Union Symp. **158**, pp. 83-Ű90, 1994.

P. M. E. Tatulli and A. Chelli, "Single-mode versus multimode interferometry: a performance study," *Astronomy and Astrophysics* **418**, pp. 1179–1191, 2004.

A.R. Thompson, J.M. Moran and G.W. Swenson Jr., *Interferometry and Synthesis in Radio Astronomy*, Wiley–Interscience Publishers, New York, 1986.

A.N. Tikhonov and V.Y. Goncharsky, *Solutions of ill-posed problems*. Winston & Sons, Washington DC, 1977.

W. Traub, "Combining beams from separated telescopes," *Applied Optics* **25**, pp. 528–532, February 1986.

S.G. Turyshev, "Analytical modeling of the white-light fringe," *Applied Optics* **42**, pp. 71–90, 2003.

R. Visser, "Regularization in nearfield acoustic source identification," *Proceedings Eighth International Congress on Sound and Vibration*, pp. 1637–1644, Hong Kong, China, 2001.

R. Visser, *A boundary element approach to acoustic radiation and source identification,* Ph.D. Thesis, University of Twente, Enschede, The Netherlands, September 2004.

C.P. de Vries, J.W.A. den Herder, R.S. le Poole, A. Quirrenbach, H. Röttgering, R. Haaksman and S. Wolf, "Darwin imaging mode requirements," Internal Communication SRON-DARWIN-05-004

A.M. Weiner, "Femtosecond pulse shaping using spatial light modulators," *Rev. Sci. Inst.* **71**, p. 1929, 2000.

M. Young and P.D. Hale, "Off-axis illumination and its relation to partial coherence," *American Journal of Physics* **63**, Issue 12, pp. 1136–1141, December 1995.

F. Zach, C.Y. Lin and J.P. Kirk, "Aberration analysis using reconstructed aerial images of isolated contacts on attenuated phase-shifting masks," *Proc. SPIE* **4346**, p. 1362, 2001.

F. Zernike, *Physica* (Amsterdam) **5**, p. 785, 1938.

M.V. Zombeck, *Handbook of Astronomy and Astrophysics*, Second Edition, Cambridge, UK: Cambridge University Press, 1990.

Nawoord

Het proefschrift is geschreven, het werk is gedaan. Vier jaar geleden begon ik aan deze klus, zonder al te veel kennis over optiek noch astronomie. En nu ligt er dan een proefschrift over apertuursynthese! De enige voorkennis op dat specifieke onderwerp had ik opgedaan—maar dat realiseerde ik me pas later—in *De ontdekking van de hemel*. Het zoveel jaren later doorgronden van de principes achter deze astronomische waarneemtechniek was dan ook een fantastische *ontdekking* voor mezelf. Het doen van dit soort ontdekkingen en uiteindelijk *begrijpen* wat je eerst nog niet wist, was wat ik wilde toen ik begon—ik ben tevreden.

Minstens zoveel genoegen als uit het ontdekken kwam me toe uit de samenwerking met anderen en het onderwijs dat ik kon geven. Alle docenten en collega-promovendi met wie ik dit deed wil ik daarvoor dan ook bedanken. Een bijzondere samenwerking was er met Rudolf, Eddy, Bastiaan en Teun als het gaat om de DTI. Deze opstelling kreeg uiteindelijk geen hoofdrol in dit proefschrift, maar de vele uren rondom deze *mepper* hebben me—mede dankzij jullie—veel inzicht en plezier opgeleverd.

Twijfels zijn er vaak geweest, maar op zulke momenten kon ik steun vinden bij velen, niet in de laatste plaats bij mijn ouders. De voortgang en de inhoud van mijn werk baarden me nogal eens zorgen en het is te danken aan de goede begeleiding om me heen dat ik het proefschrift toch heb afgerond. Luigi en Jan-Willem, van jullie heb ik veel opgestoken, zowel op het gebied van astronomie en optica, als ook op het sociale vlak. Silvania en Joseph, dankzij jullie werd ik wegwijs in de optica en ging ik geloven in mijn eigen kunnen op dit gebied. Bedankt allemaal!

Voor de fijne sfeer in de Optica groep kan ik zonder uitzondering iedereen bedanken; het was echt heerlijk om hier zo'n vier jaar rond te lopen. Lucia, Yvonne, Roland, Marnix, Rob en ook Aad en Leen, jullie maakten (in veel gevallen letterlijk) de sfeer compleet en hadden gelukkig altijd tijd voor een praatje. Praatjes waren er ook in de kamer van onze concurrenten. De Kamercompetitie is bij mijn weten nog altijd onbeslist en Janne, Arthur: dat moesten we maar zo laten. 'Onze' leidt natuurlijk naar Oana, Wouter en Bas. Het kan aan het verdwenen uitzicht hebben gelegen dat het laatste jaar veel aandacht binnen bleef in plaats van naar buiten vloog. Hoe dan ook, in onze kamer was altijd wat te doen!

Tenslotte gaan mijn gedachten uit naar het water van Zuid-Holland en de bossen rond Utrecht en Breda. Ook naar mijn auto's en het asfalt dat ik gezien heb. Het is maar goed dat ik rijden leuk vind, want zo stond me niks in de weg om bij Marleen te zijn, samen te fietsen en haar alles te laten horen over het promoveren en vervolgens van haar te horen dat alles goed zou komen. En dat kwam het.

About the author

Casper van der Avoort was born in Tilburg, the Netherlands, in 1977. After an education in Mechanical Engineering at the University of Twente, the work in his Master's thesis on acoustical signal processing (2001) inspired Casper to do research in a related field. The occurrence of wave theory and inversion in the subject of synthesis imaging made him a suitable candidate for filling a Ph.D.-position in the Interferometry workgroup in the Netherlands Institute for Space Research (SRON) in Utrecht, the Netherlands, led by Jan-Willem den Herder with professor Joseph Braat from the Optics research group in Delft as promotor. In the first year, Casper attended the *Michelson Summerschool on long baseline stellar interferometry* at the Harvard center for Astrophysics in Cambridge, Masachusetts. After this year, the centroid of activities was transferred to the Delft University of Technology, where the work on imaging was found to be benefiting from the ongoing activities in nulling interferometry and aberration retrieval. The research performed in this group led to this thesis. Large parts of the work have been presented at international conferences in San Diego, Munich, Glasgow and Toulouse.

List of refereed publications

C. van der Avoort, J.J.M. Braat, P. Dirksen and A.J.E.M. Janssen, "Aberration retrieval from the intensity point-spread function in the focal region using the extended Nijboer-Zernike approach," *Journal of Modern Optics*, Volume **52**, Number 12, August 2005, pp. 1695–1728.

C. van der Avoort, J.W.A. den Herder, S.F. Pereira and J.J.M. Braat, "Optimum synthetic-aperture imaging of extended astronomical objects," *submitted to J. Opt. Soc. Am. A.*

C. van der Avoort *et al.*, "Comparison of beam combiners for the DARWIN imaging mode," *in preparation.*

List of conference contributions

C. van der Avoort, L.A. d'Arcio and J.W.A. den Herder, "Numerical Simulations on Dynamical Aspects of the DARWIN Constellation while Imaging," *ESA Special Publication* **539**, pp. 333–339, 2003.

C. van der Avoort, A.L. Mieremet and J.J.M. Braat, "Nulling interferometry using delay lines only," *European Optical Society topical meeting in advanced imaging techniques*, Delft, the Netherlands, 20 October 2003.

Casper van der Avoort, Hedser van Brug, Luigi d'Arcio, Jan-Willem den Herder, Joseph Braat, Rudolf le Poole, "Experimental validation of homothetic mapping," *SPIE Astronomical Telescopes*, New frontiers in stellar Interferometry, 2004.

Casper van der Avoort, Arjan Mierement, Joseph Braat, "Nulling interferometry without achromatic phase shifters," *SPIE Astronomical Telescopes*, New frontiers in stellar Interferometry, 2004.

C. van der Avoort, J.W.A. den Herder and J.J.M. Braat, "Comparison of blind imaging performance of Fizeau and Michelson type arrays for a partially resolved object," *Proc. SPIE* Vol. **5905**, pp. 206–218, Techniques and Instrumentation for Detection of exoplanets II; Daniel R. Coulter (editor), August 2005.

Pierre-Marie Gori, Casper van der Avoort, Rudolf S. Le Poole and Hedser Van Brug, "Delft Testbed Interferometer: homothetic mapping and astrometric performances," *Proc. SPIE* **5491**, pp. 1011–1020 (2004).

Hedser van Brug, Bastiaan Oostdijck, Bart Snijders, Casper van der Avoort and Pierre-Marie Gori, "Homothetic mapping as means to obtain a wide field of view: the Delft Testbed Interferometer," *Proc. SPIE* **5491**, pp. 1598–1607 (2004).

Peter Giesen, Bas Ouwerkerk, Hedser van Brug, Teun C. van den Dool and Casper van der Avoort, "Mechanical setup for optical aperture synthesis for wide-field imaging," *Proc. SPIE* **5528**, pp. 361–372 (2004).